# Exploring Challenges of Observing Exoplanet Spectra at High Resolution


Annabella Meech

Somerville College

University of Oxford

A thesis submitted for the degree of

*Doctor of Philosophy*

Michaelmas 2023

*It's a dangerous business, Frodo, going out your door.*
*You step onto the road, and if you don't keep your feet,*
*there's no knowing where you might be swept off to.*

— J.R.R. Tolkien, *The Lord of the Rings*

# DECLARATION

The work of this thesis is comprised both of work that I completed independently and in collaboration at the University of Oxford, between October 2019 and August 2023. I carried out this work under the supervision of Professor Suzanne Aigrain. This research was entirely funded by the Science and Technologies Facilities Council (STFC). I declare that no part of this thesis has been accepted or is currently being submitted for any degree, diploma or certificate or other qualification at the University of Oxford or elsewhere. Here I clarify the contributions to each chapter.

Chapter 3 is my own work, which has not yet been published. I contributed the majority of this work and wrote the manuscript. The study is based on data collected externally by the SPIRou Legacy Survey (PI: Dr Jean-François Donati) and the ATMOSPHERIX consortium (PI: Dr Florian Debras); I obtained this data via private communication. For the data reduction I extended and further developed a code written by Dr Florian Debras and Dr Baptiste Klein, and published in Klein et al. (2023). The remainder of the analysis and work was completed by myself, under guidance of Dr Baptiste Klein and Prof Suzanne Aigrain.

Chapter 4 is my own work, which has not yet been published. It is work completed under the supervision of Prof Suzanne Aigrain and Dr Baptiste Klein. I extended and further developed a code written by Dr Baptiste Klein, to forward model stellar spectra under different scenarios. The analysis is my own work.

Chapter 5 is based on the peer-reviewed publication **Meech, A.,** Aigrain, S., Brogi, M., Birkby, J. L., (2022). Application of a Gaussian Process Framework for Modelling of High-Resolution Exoplanet Spectra. *MNRAS*, 512:2:2604-2617, for which I am the principal author. I completed the majority of this work and wrote the manuscript, under the guidance of Prof Suzanne Aigrain This work used public data from the ESO archive, first published in Birkby et al. (2013) and Brogi et al. (2013). I obtained the pre-processed data from the corresponding authors by private

communication. The remainder of the analysis was my own work. In particular, while the GP framework used publically available codes, the entirety of the GP formalism was my own work, completed under the guidance of Prof Suzanne Aigrain. Prof Jayne Birkby and Dr Matteo Brogi were co-authors on the publication, having provided the data for this work, and they contributed comments to the manuscript.

*There is nothing more truly artistic than to love people.*

— Vincent Van Gogh, *1888*

# ACKNOWLEDGEMENTS

I am delighted to conclude that I have thoroughly enjoyed my time as a DPhil student, performing the research enclosed in this thesis. Though there have been difficult and stressful periods, my joy in studying the astrophysics of exoplanets has never waivered. I consider that a blessing, and testament to the incredible support network around me, and those in the field – my colleagues at Oxford in particular. It has been such an honour to work in Oxford, among so many greats. My heartfelt gratitude goes to one of them, my supervisor, Prof Suzanne Aigrain. Suzanne is an inspirational scientist and advisor, and manages her busy schedule with excellence, while maintaining care for her students. I am extremely grateful to have had the opportunity to work with her over the past 4 years. Suzanne, thank you for always having time for us and the patience to explain, what is often for you, the basics. I have learnt a great deal from you which I will carry forward into my career. Thank you for your mentorship and support.

One of the main reasons I love doing science is being able to work with so many amazing scientists, and I thank all of the other Oxoplanet members. I have been truly grateful for the wonderful community of exoplaneteers we have at Oxford. Your diligence and passion never failed to inspire me onward. Special thanks go to Dr Baptiste Klein, Dr Oscar Barragán, Dr Jake Taylor and (soon-to-be Dr!) Sophia Vaughan. Oscar and Baptiste, thank you for being my academic big brothers! Baptiste, thank you for your endless insight and knowledge, for your enthusiasm and encouragement. It has been a privilege to work with you. Our whiteboard brainstorming sessions are amongst my cherished memories of my time at Oxford, and I will miss them. Oscar, thank you for your encouragement, and all the super wraps! Our time in Chile was one of the highlights of my PhD, and I couldn't have asked for a better travel buddy and observing mentor. Thanks for sharing your wisdom and experience of academia, and being such a genuinely generous, caring friend. Jake,

thank you for encouraging me out of my comfort zone (science-wise and with all the karaoke sessions) and pushing me to be creative and confident with my science. Sophia, thank you for all chats (/rants) over coffee, the debugging sessions, oh and for always having biscuits! Here's to all the proposal ideas we had (and killed!). I am honoured to call such amazing scientists my colleagues, but more so, friends. I would also like to thank Prof Jayne Birkby, and Dr Matteo Brogi. Thanks Jayne for truly treating us PhDs as colleagues, for listening to and encouraging our ideas. To Matteo, thank you for your advice and encouragement, particularly when I was deciding to pursue the PhD – without it I wouldn't have had the confidence to apply!

I would like to thank Dr Joyce Abernethy, my school physics teacher and my first role model as a woman in science. You demonstrated and gave me the confidence to enter a male-dominated field.

To my viva committee members, Prof Chris Lintott and Dr Jens Hoeijmakers, thank you for your thorough reading of my thesis and engaging with my work.

On a practical note, I thank the Science and Technologies Facilities Council for funding this research, and to the Oxford MPLS for Covid-related extension funding. I have been privileged to travel extensively during my PhD, thanks to funding from the Oxford physics department, IAU, ESO and RAS.

To my dear friends Ezzy, Hannah and Claire, thank you for keeping me sane, and supporting me during the intense last few months. For being the most loving, caring, generous friends I could have wished for during my short time in Oxford. I am so blessed to call such empowering, strong women my friends.

To my family, thank you for your love and encouragement, and crucially maintaining my perspective. William, you have so kept me grounded and I am thankful that you always push me to explain the motivation of my science. Thank you for supporting me no-matter-what, for never failing to cheer me up, and reset my perspective. Mum and Dad, thank you for your never-ceasing encouragement to pursue what I enjoy, while pushing me to challenge myself. Not forgetting that the majority of this PhD was completed under lockdown during the Covid-19 pandemic – thank you for putting up with me! Mum, thank you for never disuading me from pursuing physics, for pushing me to excellence. I wouldn't be where I am today had you not pushed me. 사랑해요 엄마. Dad, thank you for taking an interest in my work, for asking questions. For attending all those science lectures with me. For willingly turning the channel over to Sky at Night (who would have thought that Chris Lintott would end up as my viva examiner all these years later!). For all the proof-reads over the years. And your steadfast support and stability. I am so grateful to have such a supportive family, cheering me onward.

Finally, my faith has carried me through the ups and downs of the last 4 years, and my praise goes to my God. I consider it an honour to be able to study your creation every day.

*— Annabella, August 2023*

# ABSTRACT

In recent years, exoplanet spectroscopy has become a hot topic of research, towards the characterisation of other planets and fuelled by the existential question of extraterrestrial life. Ground-based high-resolution spectroscopy, whereby individual planetary spectral lines can be detected, affords unique characterisation opportunities. Compared to other astrophysical fields, high-resolution spectroscopy for the detection of exoplanet atmospheres is in its infancy, since it was only established a decade ago. Yet, the high-resolution cross-correlation spectroscopy technique has yielded tremendous insight into hot Jupiter and warm Saturn atmospheres. Despite its success, there are challenges that remain, which should be addressed if we are to progress towards more demanding targets. In this thesis I explore a number of such challenges.

First, I investigated the near-infrared transmission spectrum of the young sub-Neptune AU Mic b, analysing high-resolution spectra with standard cross-correlation techniques. Though the real data yielded null detections, I demonstrate that the data would be sensitive to a variety of atmospheric scenarios. I thus place a number of constraints on the atmospheric content of AU Mic b, with a highlight conclusion being that the atmosphere is unlikely to be in chemical equilibrium.

Then, I investigated the impact of stellar heterogeneities on high-resolution analyses. In this simulation-based study, I forward-modelled a number of stellar spectral time-series considering stellar rotation and magnetic phenomena, and compared the recovery of planet atmospheres. I found that the Rossiter-Mclaughlin effect can completely obscure planetary atmosphere detections – it is thus advisable to correct for this phenomenon explicitly in high-resolution analyses. I also investigated the impact of unocculted and occulted photospheric spots, concluding that occulted spots are likely to pose more of a danger in high-resolution cross-correlation spectroscopy.

Finally, I developed an alternative methodology to cross-correlation technique, namely the employment of Gaussian process regression to sequentially model the distinct spectral components. This bypasses cross-correlation and the associated issues such as spurious noise features in the cross-correlation maps, and statistical interpretation of a detection signal-to-noise. I applied this technique to archival high-resolution spectral data of canonical hot Jupiters HD 189733 b and 51 Pegasi b. While the Gaussian process framework was not sensitive to the real signals, previously detected at $\sim 5\sigma$ significance with cross-correlation analyses, it was sensitive to slightly amplified signals.

# Contents

**List of Figures** **xix**

**List of Tables** **xxiii**

**List of Abbreviations** **xxv**

**1 INTRODUCTION** **3**

1.1 Exoplanets . . . 3
1.1.1 Exoplanets: an ancient science . . . 3
1.1.2 A definition . . . 6
1.1.3 Detection methods . . . 7
1.1.4 Exoplanet detections: recent past, present and future . . . 9
1.2 Exoplanet atmospheres . . . 11
1.2.1 A brief history . . . 11
1.3 Open questions . . . 12
1.4 Motivation . . . 13
1.5 Thesis outline . . . 16

**2 BACKGROUND MATERIAL** **17**

2.1 The composition of an exoplanet . . . 18
2.1.1 Composition from the interior to the atmosphere . . . 18
2.1.2 Unveiling the history of an exoplanet . . . 20
2.1.3 Atmospheric modelling . . . 22
2.1.4 An exoplanet zoo . . . 26
2.2 Observing exoplanet atmospheres . . . 27
2.2.1 Space-based vs ground-based observations . . . 32

2.3 High-resolution spectroscopy . . . 34
2.3.1 Observations . . . 35
2.3.2 Data reduction methods . . . 36
2.3.3 Search for the exoplanet spectrum . . . 38
2.3.4 Advantages . . . 40
2.3.5 The history of the technique . . . 42
2.3.6 Current status of the field . . . 43

**3 OBSERVING YOUNG ATMOSPHERES AT HIGH RESOLUTION 47**
3.1 Introduction and motivation . . . 48
3.1.1 Context . . . 48
3.1.2 The young sub-Neptune AU Mic b . . . 51
3.2 The observations . . . 54
3.3 Data reduction . . . 56
3.3.1 Blaze correction, normalisation and alignment . . . 56
3.3.2 Telluric and stellar spectrum removal . . . 58
3.4 The search for atmospheric molecules . . . 61
3.4.1 Atmospheric modelling . . . 61
3.4.2 Cross-correlation with real data . . . 64
3.4.3 Injection and recovery tests . . . 65
3.5 An active star . . . 73
3.5.1 Checking for signatures of stellar flares . . . 74
3.5.2 Stellar spots . . . 77
3.5.3 Assessing the Rossiter-McLaughlin Effect . . . 80
3.6 Alternative atmospheres . . . 84
3.6.1 Impact of flare events on atmospheric composition . . . 84
3.6.2 Cloudy atmospheres and disequilibrium chemistry . . . 85
3.7 Future work . . . 86
3.7.1 Future observations of AU Mic b . . . 86
3.7.2 Atmospheric retrievals . . . 88
3.8 Conclusions . . . 89

**4 THE IMPACT OF STELLAR INHOMOGENEITIES ON TRANSMISSION SPECTROSCOPY 91**
4.1 Introduction and motivation . . . 92
4.1.1 The Rossiter-Mclaughlin effect . . . 93
4.1.2 Stellar spots . . . 95
4.1.3 Centre-to-limb variation . . . 98
4.2 Theoretical formalism . . . 99

4.3 Spectral forward model . . . 100
4.3.1 Forward model structure . . . 100
4.3.2 Test cases . . . 103
4.3.3 Prescribed star-planet archetypes . . . 104
4.4 A K dwarf case study: HD 189733 . . . 105
4.4.1 The RM effect . . . 107
4.4.2 The impact of (only) unocculted spots . . . 111
4.5 An M dwarf case study: AU Mic . . . 112
4.5.1 The RM effect . . . 113
4.5.2 The impact of unocculted and occulted spots . . . 113
4.5.3 Comparison to theoretical formalism . . . 117
4.6 Future work . . . 119
4.6.1 Making the code public and publication . . . 119
4.6.2 Faculae . . . 119
4.6.3 Spectra of inhomogeneities . . . 120
4.6.4 Accounting for heterogeneities in high-resolution studies . . . 120
4.7 Conclusions . . . 122

**5 GP MODELLING OF HIGH-RESOLUTION SPECTRA 125**
5.1 Introduction and motivation . . . 126
5.2 Gaussian processes . . . 129
5.2.1 A definition . . . 129
5.2.2 Gaussian process regression . . . 130
5.2.3 Choosing a mean and covariance function . . . 131
5.2.4 Advantages and disadvantages of Gaussian processes . . . 133
5.3 GP framework formalism . . . 134
5.3.1 The telluric component . . . 137
5.3.2 The planet component . . . 139
5.4 The data and reduction . . . 140
5.5 HD 189733 b . . . 144
5.5.1 Removal of the stellar spectrum . . . 144
5.5.2 Telluric modelling . . . 144
5.5.3 Recovery of the planet spectrum . . . 145
5.6 51 Pegasi b . . . 147
5.6.1 Telluric spectrum . . . 149
5.6.2 Recovery of the planet spectrum . . . 149
5.7 Exploring the sensitivity of the planet GP . . . 150
5.7.1 Limiting assumptions of the GP framework . . . 150
5.7.2 Using alternative telluric correction methods . . . 153
5.8 Possible Extensions . . . 157

5.8.1 A simultaneous modelling approach . . . 157
5.8.2 Modelling of (only) tellurics . . . 160
5.9 Conclusions . . . 160

**6 CONCLUSIONS** **163**
6.1 Thesis summary . . . 163
6.2 Future work . . . 166
6.2.1 Observing young planet atmospheres . . . 166
6.2.2 Characterising sub-Neptune atmospheres . . . 167
6.2.3 Further use of Gaussian processes for high-resolution spectroscopy . . . 168
6.3 Final remarks . . . 170

**A ADDITIONAL METRICS FROM THE ANALYSIS OF THE AU MIC b SPECTRA** **171**
A.1 Data reduction diagnostics . . . 171
A.2 Impact of clouds on chemical equilibrium injection tests . . . 172

**B IMPACT OF STELLAR HETEROGENEITIES** **175**
B.1 Derivation of spot contamination factor on observed transit depth . 175
B.2 Forward-modelled spectra . . . 179

**C ADDITIONAL METRICS USED IN THE GP HIGH-RESOLUTION SPECTROSCOPY FRAMEWORK** **181**
C.1 Recovering an injected planet signal . . . 181
C.2 SYSREM optimisation . . . 183

**Bibliography** **185**

# List of Figures


1.1 Population diagrams of detected exoplanets . . . 7
1.2 Compilation image of some of the planets and moons in the Solar system . . . 14
1.3 Planet Earth . . . 15

2.1 The structure of the giant Solar system planets . . . 21
2.2 The different atmospheric processes considered in exoplanet atmosphere modelling . . . 24
2.3 A summary of detected atmospheric chemical species . . . 27
2.4 Discovered exoplanet population on a mass-density diagram . . . 28
2.5 Orbital geometry of a transiting exoplanet . . . 29
2.6 An *HST* spectrum of K2-18b and a *JWST* spectrum of WASP-39 b . . . 32
2.7 The cross-sections of some key atmospheric molecules which can be probed with *JWST* . . . 33
2.8 Sodium absorption lines resolved with FORS2 and ESPRESSO . . . 34
2.9 Concept of high-resolution spectroscopy . . . 35
2.10 Forward-modelled exoplanet spectra . . . 39
2.11 Cross-correlation map showing a detection of CO in HD 209458 b and $\tau$ Boötis b . . . 40
2.12 A visual summary of the high-resolution spectroscopy studies of exoplanets to date . . . 44

3.1 Bimodality of the size of small planets as a function of age . . . 50
3.2 Mass-radius diagram of known exoplanets, highlighting a sample of young planets . . . 51

3.3 Radius-age diagram of well characterised exoplanet population, showing AU Mic b in context . . . 53
3.4 Observational parameters of the IGRINS and SPIROU transits of AU Mic b 55
3.5 Reduction of the IGRINS and SPIRou time-series spectra of AU Mic b 57
3.6 Alignment of individual lines in the IGRINS AU Mic data . . . 59
3.7 FASTCHEM AU Mic b abundance-pressure profiles . . . 63
3.8 Cross-correlation of self-consistent atmospheric models with the transit data of AU Mic b . . . 63
3.9 Effect of density on forward-modelled planet atmospheric spectra . 65
3.10 The position of AU Mic b relative to the theoretical boundary between $CH_4$ and CO dominance, in chemical equilibrium . . . 66
3.11 A high VMR CO transmission spectrum of AU Mic b, and its resulting cross-correlation map . . . 66
3.12 Detection significances from the AU Mic b injection tests . . . 68
3.13 Comparing models injection strengths in the IGRINS vs SPIROU AU Mic b data . . . 69
3.14 Impact of grey cloud decks at different altitudes on the transmission spectrum of AU Mic b, assuming chemical equilibrium . . . 71
3.15 Re-scaled constraints on chemical equilibrium cases, when including cloud decks at different pressures . . . 72
3.16 Constraints on VMR of species in the atmosphere of AU Mic b, in the presence of an opaque cloud deck . . . 73
3.17 Flux across activity indicator lines in SPIROU transit of AU Mic b . 75
3.18 Standard deviation across activity indicator lines in SPIROU transit of AU Mic b . . . 76
3.19 Flux and standard deviation across the Br $\gamma$ line within the IGRINS transit of AU Mic b . . . 77
3.20 Impact of unocculted spots on the signal-to-noise of a water detection for AU Mic b . . . 79
3.21 Rossiter-Mclaughlin time-series forward model . . . 82
3.22 Impact of the RM-induced Doppler shadow on planetary CCFs . . . 83
3.23 The predicted transmission spectrum of AU Mic b, acquired with *JWST/NIRCam* . . . 86
3.24 The transmission spectra of different aerosols, within the bandpasses of *JWST* instruments . . . 88

4.1 The interior structure and atmosphere of the Sun . . . 93
4.2 Impact of stellar rotation on a stellar spectral line . . . 95
4.3 A schematic of the transit light source effect . . . 96
4.4 Stellar grid schematic for forward model . . . 101

4.5 Schematic to show the stellar coordinate system used in the stellar forward models . . . 101
4.6 Example stellar surface maps used to forward model stellar spectra 105
4.7 Atmospheric forward models of HD 189733 b . . . 105
4.8 Cross-correlation trail of the RM-only forward model, for the HD 189733 archetype . . . 106
4.9 The impact of the RM effect on the search for molecules in the atmosphere of HD 189733 b . . . 108
4.10 Testing the ability to recover a CO and $H_2O$ exoplanet spectrum, in the presence of the RM effect, for the HD 189733 archetype . . . 110
4.11 Recovered detection significances for the HD 189733 spot case, with a spot temperature of $T_{spot} = 3700$ K . . . 111
4.12 Recovery of AU Mic b $H_2O$ and CO atmospheres, in the presence of the RM effect . . . 113
4.13 Cross-correlation trail plots for the AU Mic archetype, with photospheric spots . . . 114
4.14 Impact of occulted spots on the detection of water in the atmosphere of AU Mic b . . . 115
4.15 The isolated spot cross-correlation signatures of the AU Mic archetype 117
4.16 Comparison of the forward-modelled impact of spots to the theoretical formalism . . . 118

5.1 A demonstration of Gaussian process regression . . . 132
5.2 Samples from different GP kernels . . . 134
5.3 GP framework workflow . . . 135
5.4 Cross-correlation maps for $H_2O$ and CO atmospheres with HD 189733 b and 51 Peg b . . . 141
5.5 HD 189733 spectral matrix from CRIRES detector 1 . . . 142
5.6 51 Peg spectral matrix from CRIRES detector 3 . . . 143
5.7 The pipeline-reduced CRIRES fluxes of HD 189733 and 51 Peg . . . 145
5.8 Recovery of the dayside spectrum of HD 189733 with the GP framework 146
5.9 Posterior distributions from evaluation of the planet GP . . . 148
5.11 Comparing the GP recovery of injected planetary signals, having employed different telluric corrections. . . . 156
5.12 Simultaneous GP modelling of a demonstrative simulated dataset containing a stellar and Doppler-shifting planet spectrum . . . 159

A.1 Dispersion of the AU Mic spectra over course of the reduction routine 172
A.2 Impact of a cloud deck at $\log_{10} P_c = -4$ on the constraining power of the chemical equilibrium injection tests for AU Mic b . . . 174

B.1 Residuals of the RM-only spectral time series, for the HD 189733 archetype. . . . . 178
B.2 Residuals of the spotted star spectral time series, for the AU Mic archetype. . . . . 179

C.1 Assessing the recovered planet radial velocity as a function of injection strength, with the GP high-resolution spectroscopy framework . . . 182
C.2 Optimising SYSREM iterations with the GP framework . . . . . 184

# List of Tables


2.1 Spectrographs used for exoplanet spectroscopy . . . . . 31

3.1 The collection of published mass and radius measurements of the planets in the AU Mic system . . . . . 54
3.2 Ancillary information concerning the IGRINS and SPIROU transit observations of AU Mic b . . . . . 56
3.3 Parameters for the forward modelling of AU Mic b . . . . . 62
3.4 Minimum and maximum extents of the integration window for AU Mic chromospheric activity indicator lines . . . . . 74

4.1 The characteristic parameters used in the stellar spectra forward modelling framework . . . . . 104
4.2 Detection of an atmospheric signal from HD 189733 b, for different stellar spectra cases . . . . . 109

5.1 Adopted parameters for both the HD 189733 and 51 Peg systems . . 140
5.2 Summary of the HD 189733 and 51 Peg CRIRES observations . . . . 140
5.3 Absorption line metrics to assess GP recovery . . . . . 158

A.1 The impact of an opaque cloud deck on the atmospheric constraints for AU Mic b . . . . . 173

# List of Abbreviations

**1-D, 2-D** . . . One- or two-dimensional, referring in this thesis to spatial dimensions in an image.

**CIA** . . . . . Collision-induced absorption.

**CLV** . . . . . Centre-to-limb variation.

**C/O** . . . . . Carbon-to-oxygen ratio.

**CCF** . . . . . Cross-correlation function.

**GP(s)** . . . . . Gaussian process(es).

**GPR** . . . . . Gaussian process regression.

**HST** . . . . . Hubble Space Telescope.

**HRCCS** . . . . High-resolution cross-correlation spectroscopy.

**JWST** . . . . . James Webb Space Telescope.

**LSF** . . . . . Line spread function.

**MCMC** . . . . Markov chain monte carlo.

**MLE** . . . . . Maximum likelihood estimate.

**nIR** . . . . . Near-infrared.

**PCA** . . . . . Principal component analysis.

**P-T** . . . . . Pressure-temperature.

**RV** . . . . . Radial velocity.

**RM(E)** . . . . Rossiter-Mclaughlin (effect).

**SNR** . . . . . Signal-to-noise ratio.

**TSM** . . . . . Transmission spectroscopy metric.

**TLSE** . . . . . Transit light source effect.

**TTV** . . . . . Transit timing variation.

**VMR** . . . . . Volume mixing ratio.

*...non si glorifica in uno, ma in soli innumerabili; non in una terra, un mondo, ma in diececento mila, dico in infiniti.*

*...He is glorified not in one, but in countless suns; not in a single earth, a single world, but in a thousand thousand, I say in an infinity of worlds.*

— Giordano Bruno, *De L'infinito Universo e Mondi (On the Infinite Universe and Worlds), 1584*
Translation by Dorothea Singer, *1951*

# CHAPTER 1

# INTRODUCTION

## Contents


**1.1 Exoplanets . . . . . 3**
1.1.1 Exoplanets: an ancient science . . . . . 3
1.1.2 A definition . . . . . 6
1.1.3 Detection methods . . . . . 7
1.1.4 Exoplanet detections: recent past, present and future . 9
**1.2 Exoplanet atmospheres . . . . . 11**
1.2.1 A brief history . . . . . 11
**1.3 Open questions . . . . . 12**
**1.4 Motivation . . . . . 13**
**1.5 Thesis outline . . . . . 16**


## 1.1 Exoplanets

### 1.1.1 Exoplanets: an ancient science

The posit of an infinite number of worlds, or *aperoi kosmoi*, has been present since early astronomical records. In ancient astronomy, the first astronomers deemed

the Earth to be at the centre of motion of all celestial bodies and indeed at the centre of the Universe, the *geocentric model*. The renowned ancient Greek and Roman philosophers including Plato, Aristotle, and Ptolemy concurred in this belief, promoting the Earth to be unique and humankind to be alone. Though they recorded observations of what we now know to be the planets of the Solar system, the ancient astronomers believed them to be simply another class of stars, *wandering* rather than fixed (Falkner, 2011).

Records of ancient astronomy from other global civilisations are scarcer, but nevertheless have proved to be of equal value in the progression of planetary astronomy. From Babylonia to the far East in China, Japan and Korea ($300 - 4$ BC; Dubs, 1958; de Jong, 2019), the orbital motions of the Solar system planets were studied. Of note in the middle East, the Islamic scholar al-Hassan Ibn al-Haytham ($945 - 1040$ AD) developed some of the fundamental ideas of celestial mechanics, to describe the orbital motion of the Solar system planets, later providing the basis for Copernicus and Kepler. Though the overwhelming consensus of ancient astronomy was the geocentric universe, there still existed a few who opposed the notion. Among them, Philolaus ($470 - 385$ BC), Hicetas ($400 - 335$ BC) and Aristarchus of Samos ($310 - 230$ BC), all who advocated the theory that the Earth was spherical, and in orbit around a central object. Despite opposing murmurings, the centralistic, unparalleled perspective of the Earth prevailed for more than one thousand years.

In the 16th century, Italian philosopher Giordano Bruno ($1548 - 1600$) promoted the *'plurality of worlds'* in his major philosophical work (Bruno, 1584):

> "In space there are countless constellations, suns and planets; we see only the suns because they give light; the planets remain invisible, for they are small and dark. There are also numberless earths circling around their suns. The countless worlds in the Universe are no worse and no less inhabited than our Earth. For it is utterly unreasonable to suppose that those teeming worlds which are as magnificent as our own, perhaps more so, and which enjoy the fructifying rays of a sun just as we do, should be uninhabited and should not bear similar or even more perfect inhabitants than our Earth."

This would have been a wildly unpopular opinion at the time[1]. An assessment of common belief up to and including that time would reveal a consensus of a finite physical universe, of which our world inhabited the centre. Bruno's ideas thus contradicted both the philosophical and general belief as well as the consensus of the established church, at a time when philosophy, religion and the natural sciences were viewed as intrinsically linked. Nicolaus Copernicus ($1473-1543$) had only recently published the new *heliocentric model* (Copernicus et al., 1543), postulating that the Earth was not at the centre of the Universe but that instead the Sun held this position. Of Copernicus, Johann Wolfgang von Goethe writes (Goethe, 1868)

> "Yet among all discoveries and convictions none may have produced a greater effect on the human spirit than the doctrine of Copernicus. Hardly had the world been acknowledged as spherical and closed in itself when it should abandon the enormous prerogative to be the centre of the universe."

Even this was radical, let alone the proposal that the Universe was infinite and that the Sun was one of many. Prior to the 16th century, the belief in worlds other than the Earth, *"mundos esse innumerabilis"*, was deemed heretical (by Philaster, Saint Jerome, and Saint Augustine and more recently Pope Gregory XIII to name a few). Bruno was executed in 1600 and his works forbidden and suppressed (even until 1966; Karolides et al. 2011).

Bruno's execution closely preceded the invention of the telescope at the beginning of the 17th century, the beginning of the scientific revolution and regarded by some as the genesis of modern astronomy. With it, Galileo Galilei ($1564-1642$) confirmed Copernicus' Sun-centred solar system, and discovered Jupiter's moons, the first confirmed orbit of a celestial body around another (Galilei, 1610). The existence of the Galilean moons corroborated Copernicus' heliocentric model. With physical laws that are still used to this day, Johannes Kepler ($1571-1630$) further refined this model, mapping the motion of the Solar system planets. Sir Isaac Newton ($1642-1726$) defined the laws of universal motion in *The Principia* (Newton, 1687),

[1]Some propose that Bruno's public declarations on the existence of other worlds were a component in his execution for heresy (Campbell, 2017).

and with them the law of gravitation. The consequent fuller understanding of the heliocentric model was pivotal in placing the Earth and the Solar system in a cosmic context. Far from being the centre of the Universe, we inhabit the fourth planet of an eight-planet system, in orbit around a mundane main sequence star. With such a reproducible structure, the posit of other worlds orbiting other suns no longer seemed so far-fetched, and so began the search for other planetary systems.

In 1952, Otto Struve ($1897-1963$) proposed two methods for indirect exoplanet detection: observing the wobble of a star induced by an orbiting planet, and the reduced light from a star due to a planet occultation (Struve, 1952). These are known in modern day as the 'radial velocity' (RV) and transit detection methods. As time would tell, this remarkable insight changed the course of exoplanet science. In 1992, the first extra-solar planet was discovered. A planetary-mass object was detected in orbit around the millisecond pulsar PSR 1257+12, by precision measurements of the induced deviation of the pulsar period (Wolszczan & Frail, 1992). It was not long before a planet was discovered around a Sun-like star; in 1995, Mayor & Queloz (1995) detected the radial velocity 'wobble' of G star 51 Pegasi, induced by an orbiting Jupiter-mass object. And so, our view of the cosmos and our position in it was irrevocably transformed. For millennia the human race has looked up at the heavens and pondered the existence of other worlds; with these planet detections we confirmed that our planetary system was not alone in the Universe.

### 1.1.2 A definition

The term *'planet'*, the Greek for 'wanderer' or 'wandering around', was first coined in the 17th century. Its definition has been necessarily refined since. The International Astronomical Union (IAU) formally defines a planet as a celestial body that fulfills three criteria: (i) it orbits the Sun; (ii) it has sufficient mass, and therefore self-gravity, to assume hydrostatic equilibrium; and (iii) it has cleared the neighbourhood around its orbit [2]. An *'extra-solar planet'* or *'exoplanet'* has no such formal definition, but is widely regarded as a celestial body in orbit around a star other than the

[2]Defined at the IAU 2006 General Assembly, Prague

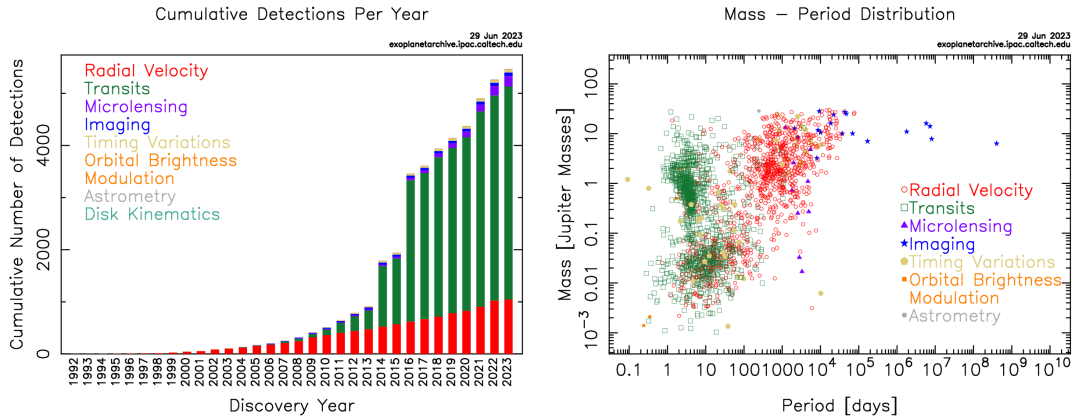


**Figure 1.1: Left:** Exoplanet discoveries throughout the years. **Right**: Detected exoplanets populating mass-period space. Figures from the NASA exoplanet archive.[3]

Sun, with mass insufficient to induce thermonuclear fusion. This mass threshold is usually defined at 13× the mass of Jupiter (Lecavelier des Etangs & Lissauer, 2022). However, this definition is contentious; it does not depend on formation mechanisms. Genuine planets form within a protoplanetary disk, either a product of the collapse of the protostellar nebula, or a supernova fallback disk. The latter can promote formation of planets around pulsars. It can then be difficult to distinguish planets from brown dwarfs, which form under gravitational collapse of a molecular gas cloud (Chabrier et al., 2007). Therefore, the above should be considered a working definition, to be refined should scientific evidence require it.

### 1.1.3 Detection methods

Since those first exoplanet discoveries in the mid-1990's, the radial velocity and transit methods have been used to successfully detect thousands of planets. Fig. 1.1 shows the population of exoplanets discovered, both the cumulative number discovered since 1992 and distributed in mass-period space. The different detection methods are distinguished; I briefly summarise the state-of-the-art methods used today to detect exoplanets.

The radial velocity method, otherwise known as Doppler spectroscopy, observes the 'wobble' of a host star induced by an orbiting planet, due its own orbit around the common centre of mass. The spectrum of the star is seen to Doppler shift,

[3] https://exoplanetarchive.ipac.caltech.edu/

detectable from the ground with precision spectrograph measurements. Then, Kepler's laws of motion may be used to infer the mass of the orbiting planets. From them we can derive a relation between the radial velocity, RV, of the stellar spectrum, as a function of time, $t$:

$$\mathrm{RV}(t) = K\Big[\cos\big(\omega + \nu(t)\big) + e\cos\omega\Big] \tag{1.1}$$

where $\omega$ is the argument of periastron, $\nu$ the true anomaly, $e$ the eccentricity. The semi-amplitude $K$ is equal to,

$$K = \frac{1}{\sqrt{1-e^2}}\frac{M_p \sin i}{(M_* + M_p)^{2/3}}\Big(\frac{2\pi G}{P}\Big)^{1/3} \tag{1.2}$$

where $M_*$ and $M_p$ are the stellar and planet masses, and $P$ is the orbital period of the planet (see Murray & Dermott, 2000, for a full derivation). From Equation 1.2, we can see that it is $M_p \sin i$ that is deduced, the minimum mass of the planet subject to the inclination of the planet orbit relative to the observer's plane, $i$. This was the method employed to detect the first exoplanet around a main sequence star; Mayor & Queloz (1995) used the ELODIE spectrograph at the Haute Provence Observatory to detect the hot Jupiter 51 Pegasi b.

Another dominant technique, the transit method, involves observing the decrease in flux from a host star as an orbiting planet passes in front, obstructing some of the stellar light from traversing to the observer. The consequent decrease in flux, $\Delta F$, is given by:

$$\frac{\Delta F}{F} \propto \left(\frac{R_p}{R_*}\right)^2, \tag{1.3}$$

where $R_p$ and $R_*$ are the radii of the planet and star. The transit duration is given by

$$T_{\mathrm{dur}} = \frac{P}{\pi}\sin^{-1}\left(\frac{\sqrt{(R_* + R_p)^2 - (bR_*)^2}}{a}\right) \tag{1.4}$$

where $a$ is the semi major axis. The impact parameter, $b$, is the projected, mid-transit distance between the planet and stellar disk centres, and is related to the semi-major axis by

$$b = \frac{a\cos i}{R_*} \tag{1.5}$$

(Deeg & Alonso, 2018). Thus, encoded in the shape of the transit light curve is both the size of the occulting planet relative to the size of the host star, and the orbital period of the planet.

Fig. 1.1 shows that these two methods have yielded the majority of exoplanet discoveries, constituting 95% of detections to date. It is important to clarify though that a number of other methods have been successful, such as microlensing events, direct imaging, and transit timing variations (TTVs; Gaudi, 2012; Batista, 2018; Pueyo, 2018; Agol & Fabrycky, 2018). The collection of methods used today is complementary since they are each sensitive to different regions of parameter space. For example, transit photometry and radial velocity detections are most sensitive to close-in, Jupiter-sized planets with edge-on orbits, while direct imaging is more effective for intrinsically warmer planets with low inclination at larger distances from their host stars. These methods then introduce detection biases which are important to acknowledge when performing population studies (Mousavi-Sadr et al., 2023; Bryson et al., 2020).

### 1.1.4 Exoplanet detections: recent past, present and future

From today's 21st century perspective, it is difficult to relate back to Bruno's time, when the plurality of worlds was an unorthodox belief. As of 2 July 2023, we have detected 5,463 confirmed planets, according to the NASA exoplanet archive[4]. Suffice to say, we have seen a revolution in exoplanet science.

A trickle of discoveries were reported following the first detections in the 1990s. Some of the key missions in the genesis of exoplanet discoveries included, *CoRoT*, *Kepler* and then later *K2*. The COnvection, ROtation and planetary Transits (COROT) spacecraft was launched in 2006 (Baglin et al., 2006; Boisnard & Auvergne, 2006). *CoRoT* was one of the first missions designed for the purpose of detecting exoplanets, and has led to a reported 34 exoplanet detections. Then, launched in 2009, *Kepler* and later the *K2* mission were highly successful in detecting transiting planets, far exceeding expectations regarding the number of exoplanet detections

[4] https://exoplanetarchive.ipac.caltech.edu/

(Borucki et al., 2009). The consequent dramatic increase in the number of confirmed planets post 2010 is clearly visible in Fig. 1.1.

Moving on to present day exoplanet detection missions, the Transiting Exoplanet Satellite Survey (*TESS*), launched in 2018, is systematically scanning more than 85% of the sky, observing bright stars for signs of transit events (Ricker et al., 2015). To date, it has led to the discovery of 379 confirmed exoplanets[5]. With regards to radial velocity studies, current operational instruments such as HARPS (both North and South), ESPRESSO, EXPRES, and NEID to name a few, are regularly used towards exoplanet detection (Petersburg et al., 2020). These high-resolution spectrographs are able to reach a radial velocity precision between 10–30 cm/s (Mayor et al., 2003; Pepe et al., 2021; Jurgenson et al., 2016). We can therefore expect to be sensitive to Sun-Earth analogues, which would incur a 10 cm/s radial velocity amplitude (Hall et al., 2018). However, it has become apparent that it is a stellar activity noise floor (such effects are outlined in Chapter 4, §4.1), rather than an instrumental limitation, inhibiting detection of smaller planets (Korhonen et al., 2015). The disentangling of stellar activity-induced signals has thus become an important focus of current-day radial velocity studies (see e.g., Zhao et al., 2022; Barragán et al., 2023).

Subsequent population studies have revealed a great diversity in characteristics, from Jupiter-sized planets so close to their host stars that the facing hemisphere reaches temperatures above 2000 K, to bare-rock worlds (Hoeijmakers et al., 2018a; Kreidberg et al., 2019). The quest for exoplanet discovery shows no signs of slowing down. Future missions such as *PLATO*, aim to push the limits of detection towards those necessary to discover an Earth twin, by being capable of detecting smaller planets with longer orbital periods (Rauer et al., 2016). Observing techniques have extensively advanced to the point where further characterisation has been made possible. The field has progressed beyond planet detection alone to now include detection of atmospheric chemical species, attempts to hunt for exomoons, detection of clouds in the atmosphere, measurement of the alignment of the planet orbit,

[5]As of 14/08/2023

mapping inhomogeneities across the different planetary hemispheres and more (see e.g., Seager, 2008; Kipping et al., 2015; Kreidberg et al., 2013; Gandhi et al., 2022).

## 1.2 Exoplanet atmospheres

### 1.2.1 A brief history

Methods to observe the atmosphere around an exoplanet were built upon the transit photometry and radial velocity methods explained in §1.1.3. Rather than the white light curve, one can observe the decrease in stellar disk-integrated flux as a function of wavelength during a planetary transit. Alternatively, one can observe the dayside of the planet with emission or reflection spectroscopy, either side of the secondary eclipse. These methods effectively resolves the opacity of the atmosphere, if one exists, at different wavelengths, from which one can deduce the atmospheric absorbers (Seager & Deming, 2009). I refer the reader to Chapter 2, §2.2 for a detailed overview of the techniques used to observe exoplanet atmospheres.

Charbonneau et al. (2002) reported the first detection of an atmosphere around a planet outside the Solar system, just two years after the first detection of an exoplanet transit event was reported (Charbonneau et al., 2000). With the Hubble Space Telescope (*HST*), they observed a deeper transit around 589 nm, the wavelength at which sodium preferentially absorbs light. The field has since blossomed. From space, *HST* has yielded numerous optical to near-infrared (nIR) exoplanet spectra since 2002, while the *Spitzer* space telescope provided photometric infrared data (2003-2010). From the ground, both high-resolution and low-resolution spectrographs such as HARPS, CRIRES and IGRINS, have also contributed to detections of atmospheric chemical species. There have been molecular detections of water, carbon monoxide, carbon dioxide, and methane, and atomic species such as sodium and iron (Benneke et al., 2019a; Kreidberg et al., 2020; Ehrenreich et al., 2020).

As of 2022, the James Webb Space Telescope (*JWST*) is now providing spectroscopic transit light curves of unprecedented precision, extending the wavelength

coverage available with *HST* to the mid-infrared. In Cycle 2[6], 32% of the available 5000 hrs were awarded to exoplanet programs. While space-based observations have and will continue to transform the knowledge parameter space of exoplanets, there are still rich information gains to be made from the ground. With the onset of the next generation observatories within the next decade, including the *TMT* (30 m), *GMT* (25.4 m) and *ELT* (39.3 m) (Madhusudhan, 2019), we expect to acquire exoplanet spectra to exquisite precision. ESO's 39 m diameter *ELT* is set for first light in 2027; with such a large aperture, we expect it to be sensitive to smaller exoplanets, further from their host stars.

In this thesis, I focus my studies on the detection of exoplanet atmospheres using the combined host star + planet light, as observed from the ground, rather than direct detection of the (isolated) planet.

## 1.3 Open questions

Since the first in 1992 (Wolszczan & Frail, 1992), each detection of an exoplanet has challenged our general understanding of planets. Jupiter-sized planets have been discovered so close to their host stars that they would exist inside the orbit of Mercury; so-called 'hot' or even 'ultra-hot Jupiters'. These have challenged our theories of giant planet formation; how can these giant planets form in such close proximity to their host stars? Simulations point to a migration history, whereby the giant planets form further out in their protoplanetary disk and then migrate through the disk towards the host star (Pollack et al., 1996).

Regarding slightly smaller planets, there is a dearth of Neptune-sized planets at short orbital distances; the 'hot Neptune desert'. Current instruments would be sensitive to such planets if in fact they exist, meaning that the dearth cannot be attributed to a detection bias. The cause of this desert is still under dispute (Mazeh et al., 2016; Vissapragada et al., 2022).

[6] https://www.stsci.edu/jwst/science-execution/approved-programs/general-observers/cycle-2-go

For even smaller-sized planets, there exists a further dearth of detected planets. This is colloquially named 'small planet radius valley', predicted by Owen & Wu (2013); Lopez & Fortney (2013) and then first observationally confirmed by Fulton et al. (2017). Statistical analysis of the *Kepler* survey exposed a bimodality of planet sizes either side of $\sim 2.1\,R_{\oplus}$, separating super-Earths from sub-Neptunes. Theoretical work had predicted such a valley due to atmospheric erosion, but the exact mechanism is debated. I refer the reader to Chapter 3, §3.1, for a detailed overview.

These are only a few examples of the open questions in exoplanet science; planetary physics is certainly not a closed book. We continue to discover extraneous and strange new worlds. With the characterisation of each new planet we add to the sample library from which we are able to refine our understanding of planetary systems.

## 1.4 Motivation

There are a number of motives driving the quest for observational exoplanet atmospheric characterisation:

(i) the atmosphere of a planet is a key property we can measure remotely with current methods. We can also measure the density and albedo of a planet, which informs us of bulk composition;

(ii) currently it is the leading hope for detection of extra-terrestrial life. Under current understanding, life can only exist within the safety of an atmosphere;

(iii) the atmosphere encodes information related to the formation and evolution history of the planet, thus observations are important for informing theoretical astrophysics.

Though we have proven one of Bruno's hypotheses to be true with the discovery of exoplanets, we have yet to fully concur with the extent of his musings, namely that life is not confined to the Earth. We are witnesses to an era in which, for the

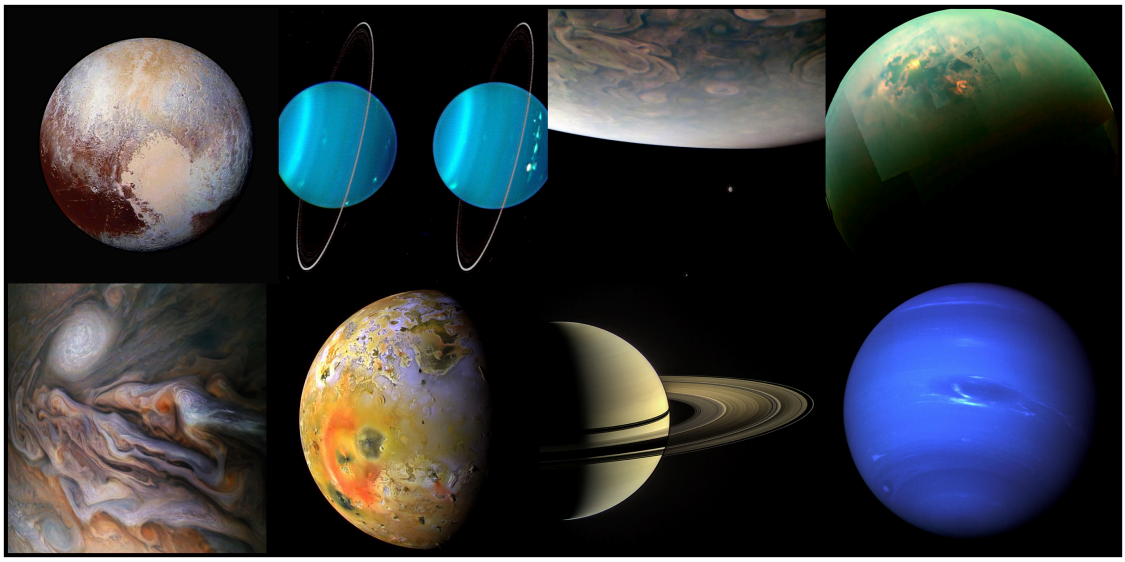

**Figure 1.2:** Compilation of images of some of the planets and moons in the Solar system. **Top row from left:** A New Horizons image of Pluto taken in 2015 (NASA, PIA19952); the Keck telescope images the two hemispheres of Uranus in 2004 (Lawrence Sromovsky, University Of Wisconsin-Madison/W.W. Keck Observatory); A Juno image of Jupiter taken in 2021, simultaneously capturing two of Jupiter's moons, Callisto and Io (NASA, PIA25019); A Cassini image of Titan, with sunlight reflecting from the northern polar seas (NASA, PIA18432). **Bottom row from left:** Clouds in the atmosphere of Jupiter, captured by the Juno spacecraft in 2018 (Gerald Eichstädt/Seán Doran/NASA/JPL-Caltech/SwRI/MSSS); Jupiter's moon Io as seen by the Galileo spacecraft in 1997 (NASA, PIA01667); Saturn captured by the Cassini spacecraft in 2010 (NASA, PIA12567); Neptune taken by Voyager 2, featuring the Great Dark Spot (NASA, PIA01492).

first time, scientists have a chance of detecting signs of life elsewhere in the Universe. The question of our loneliness in the Universe no longer remains purely philosophical, but starts to become empirical. The possible detection of extra-terrestrial life aside, planetary physics remains an important component of astrophysics to explore. With it we understand the context of our own Solar system, and begin to answer fundamental questions such as how we came to be here.

As we advance our detection capabilities towards characterising smaller, fainter and longer period planets, we must concentrate our efforts not only on the technology

**Figure 1.3:** Planet Earth (image credit to Robert Simmon, NASA Earth Observatory).

and instrument design and observing strategies, but also, with equal effort, on the data processing. The latter is the primary objective of this thesis – to explore and improve data handling techniques and methods that can be used to extract useful and meaningful information for exoplanet atmosphere study from ground-based observations. It will aim to address some of the inherent, current limitations of high-resolution spectroscopy.

While in the thesis I work with spectral data points, it is important to remind oneself of the objects being studied. In Fig. 1.2, I show some of the astounding, real images taken of the planets, dwarf planets and moons in the Solar system in situ. Far from being mundane rocks, remnants of stellar formation floating in the sky, these are dynamic, fierce and evolving worlds with weather, volcanoes, aurorae, and rings. While simplifying assumptions are necessary for now to make any progress, we should acknowledge that planets are gloriously more complex that our forward models can express. Planets are intricate, beautiful and diverse celestial objects.

Yet, amid all the beauty of the imaged Universe, the Earth stands out (Fig. 1.3). A particularly special planet, home to all known life in the Universe. One day we may well discover another Earth-twin, but for now there is certainly no planet B.

## 1.5 Thesis outline

This thesis is divided into the following chapters.

Chapter 2 provides some of the background material needed for the rest of the thesis.

Chapter 3 details the study of atmospheric transmission of the young sub-Neptune AU Mic b at high resolution. This study made use of the standard techniques detailed in chapter 2. The focus and main goal is to attempt to recover the first high-resolution transmission spectrum of a young planet. The work in this chapter is largely based on the publication Meech et al. (submitted).

Chapter 4 follows on from Chapter 3, aiming to characterise some of the challenges associated with high-resolution spectroscopy of planets in orbit around inhomogeneous stars.

Chapter 5 develops and explores an alternative technique for handling of high-resolution data, *viz* the application of Gaussian process regression. The work in this chapter is based on the publication Meech et al. (2022).

Finally, Chapter 6 provides the conclusions of the thesis.

*The scientist does not study nature because it is useful to do so. He studies it because he takes pleasure in it, and he takes pleasure in it because it is beautiful.*

— Henry Poincaré, *Science and Method, 1908*

# CHAPTER 2

# BACKGROUND MATERIAL

## Contents


**2.1 The composition of an exoplanet . . . . . 18**
2.1.1 Composition from the interior to the atmosphere . . . . 18
2.1.2 Unveiling the history of an exoplanet . . . . . 20
2.1.3 Atmospheric modelling . . . . . 22
2.1.4 An exoplanet zoo . . . . . 26
**2.2 Observing exoplanet atmospheres . . . . . 27**
2.2.1 Space-based vs ground-based observations . . . . . 32
**2.3 High-resolution spectroscopy . . . . . 34**
2.3.1 Observations . . . . . 35
2.3.2 Data reduction methods . . . . . 36
2.3.3 Search for the exoplanet spectrum . . . . . 38
2.3.4 Advantages . . . . . 40
2.3.5 The history of the technique . . . . . 42
2.3.6 Current status of the field . . . . . 43


In this chapter I endeavour to provide the background material needed to both understand the work in the following chapters, and place it in context within the current status of the field of exoplanet atmospheres.

## 2.1 The composition of an exoplanet

### 2.1.1 Composition from the interior to the atmosphere

Population studies of exoplanets have so far led to a definition of four distinct planet classes based on composition: gas giants, Neptunian-like planets (including so called 'sub-Neptunes'), super-Earths and terrestrial planets. Despite each class also displaying wide diversity, broad categories are helpful for understanding characteristics and tying them to the theory of planet formation. Regarding composition, though we make broad, sweeping generalisations, it is important to keep in mind that the actual planet compositions involve far more complexity; we would hope to improve the complexity of our models as our understanding and observational ability improves.

Typically, gas giant planets are similar to our own Saturn and Jupiter in terms of composition. For decades we have studied the composition of the Solar system planets, both remotely and via in situ probes. Though we shouldn't be lulled into a false sense of security regarding giant exoplanet composition, having Solar system analogues at least provides an initial basis for exploration. Our current theoretical understanding of the interior structure of the four Solar system giants is shown in Fig. 2.1. Jupiter is thought to host a small, dense core, overlaid with a comparably rarefied and larger core. Atop the 'core' is an extensive envelope of H/He-dominated gas. Saturn is thought to host no such compact core but rather a 'dilute' core, comprising a large fraction of the planet radius, and again, a H/He dominated envelope (Guillot et al., 2022; Helled et al., 2022). Despite in situ probes, the contribution of heavier elements is uncertain, as well as their distribution throughout the interiors of both giant planets.

Uranus and Neptune are thought to consist of a rocky core, surrounded by volatile ices such as water, ammonia and methane (Helled & Fortney, 2020). They also host H/He-dominated envelopes, but they constitute a smaller mass fraction than Jupiter and Saturn, while $CH_4$ is more prominent. The composition of Neptune-sized exoplanets is believed to be similarly populated by metals (Moses et al., 2013).

As an aside, I use the standard definition of 'metal' in exoplanet science, namely any element heavier than hydrogen or helium. The metallicity then denotes the relative abundance of these heavier elements. Stellar metallicity is usually presented as a log scale relative to solar abundances, that is

$$[\mathrm{X/H}] = \log_{10} \frac{[\mathrm{X/H}]_*}{[\mathrm{X/H}]_\odot} \tag{2.1}$$

where X and H represent the volume mixing ratios of species $X$ and hydrogen (Teske et al., 2019). Planet metallicity is presented similarly, with respect to either the host stellar or solar metallicity (Gandhi et al., 2023). Commonly used single species metallicity proxies include (e.g.,) [Fe/H], [C/H], and [$H_2O$/H]; these may not well represent the overall atmospheric metallicity, and thus it may be better to compute [m/H] where $m$ is a combination of two or more metals (Welbanks et al., 2019). Then, super-Earths are a class of planet unseen in the Solar system, slightly larger than the Earth. Atmospheres around these planets are not guaranteed, due to their smaller mass. Understanding of the composition of sub-Neptune/super-Earth atmospheres is still being developed, with observations indicating a wide diversity (Moses et al., 2013).

The final class encompasses everything equal in size and smaller than the Earth: the 'terrestrial' planet, of which we have Mercury, Venus, Earth and Mars in the Solar system. Of all the observed planets, we are inevitably most comprehensively informed about the interior of the Earth. The Earth has differentiated core, surrounded by mantle, a crust, hydrosphere and finally an outer atmosphere which comprises a negligible mass fraction (Baraffe et al., 2014). Though it has a somewhat similar interior, except for the lack of dynamo and tectonics, the atmospheric chemistry of Venus differs drastically from the Earth. In general, terrestrial planets are likely to be predominantly rocky, hosting thin, high mean molecular weight atmospheres, if at all. The hotter terrestrial planets, close to their parent stars, may host secondary atmospheres; any primary atmospheres are likely to have been ablated. Secondary atmospheres reflect the interior composition of the planet, and are formed post-formation as a result of outgassing processes. On the other

hand, primary atmospheres are accreted during the formation process, and have the same metallicity as the proto-planetary disk.

Atmospheres are fluids and are governed by four laws: the **Navier-Stokes equation** to describe the motion of fluid flow, the **continuity equation** for mass conservation, the **first law of thermodynamics** for conservation of energy, and the **equation of state** (EOS). Regarding the latter, for atmospheric physics we are interested in thermodynamic state variables temperature, $T$, pressure, $p$ and density, $\rho$ in particular. Under the ideal gas assumption,

$$p = \rho R T \tag{2.2}$$

where $R$ is the specific gas constant. In reality, planetary atmospheres are far from ideal gases. In particular, the ideal gas assumptions break down at high pressures since the intermolecular forces are important, and in the upper atmosphere where the gas becomes progressively collisionless (Heng & Showman, 2015; Heng, 2019; Owen, 2019). There are efforts to improve the EOS for exoplanet atmospheres, both from an experimental side, simulating conditions in a laboratory, and from the theoretical side (Baraffe et al., 2014; Zeng et al., 2022; Fortney et al., 2007). Both are difficult, and in practice the EOS contributes the highest uncertainty towards theoretical atmospheric modelling.

### 2.1.2 Unveiling the history of an exoplanet

As one of the motivations for planetary atmosphere characterisation, learning the composition of an exoplanet aids the understanding of its formation and evolution history. For giant planets, the primary contending formation theories are (i) core accretion and (ii) gravitational instability. In the core-nucleated accretion scenario, a $5 - 10\,\mathrm{M}_\oplus$ condensed core is built from km-sized planetesimals (Pollack et al., 1996). Once the gravitational energy is sufficiently greater than the thermal energy of the surrounding protoplanetary disk, the planetary embryo will begin to accrete material from the disk. A core of mass greater than $10\,\mathrm{M}_\oplus$ will induce runaway accretion, attracting a large gaseous envelope. On the other hand, gravitational

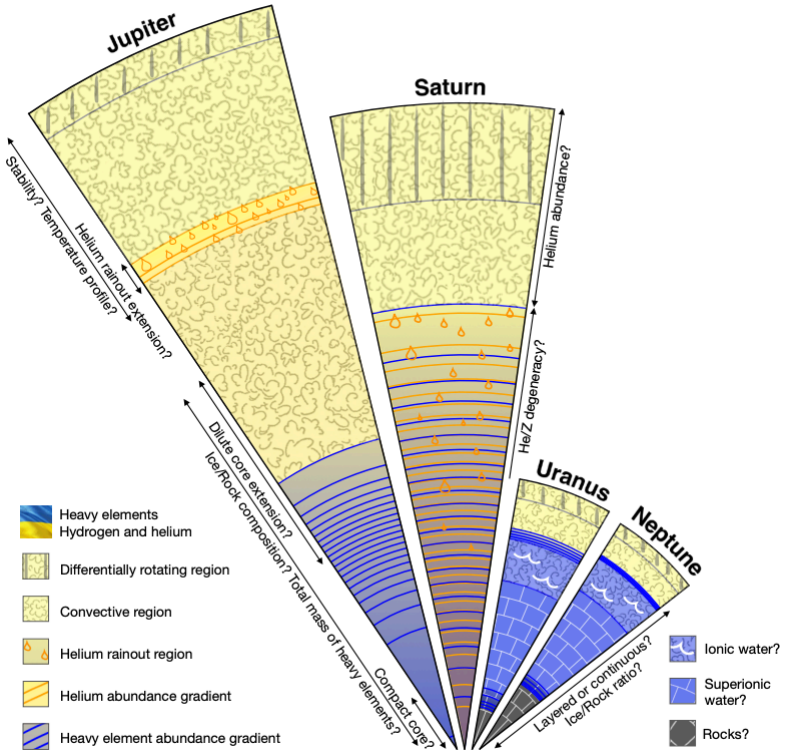


**Figure 2.1:** The theoretical structure of the four giant planets in the Solar system. Figure from Guillot et al. (2022).

instability posits that planets form from the disk in a similar fashion to formation of a star by collapse of a gas cloud (Boss, 2000). This has been proposed for giant planets at large distances from their host stars (D'Angelo & Lissauer, 2018). Notably, neither of these theories can advocate for the in situ formation of hot Jupiters, which exist in close proximity to their host star. Some form of migration must be invoked to marry the theory to observations.

The location and time of a planet formation event in the protoplanetary disk impacts the resulting chemical composition of the planet (Lothringer et al., 2021). The protoplanetary disk will have formed from the same molecular gas cloud as the central star, and so will have the same initial composition. Under the core accretion scenario (Pollack et al., 1996), if one assumes that there is then no interaction between the solid and gaseous zones in the formed planet, the observed composition of the atmosphere will be intrinsically linked to the location in the disk where the gas was acquired (Öberg et al., 2011). This is because there is a power-law

temperature profile in the disk, so different species condense at different radii from the host star; a 'snowline' in the disk is the distance from a host star at which a given volatile species freezes. The carbon-to-oyxgen (C/O) ratio is a useful diagnostic towards different formation scenarios; the two aforementioned formation theories form planets at different distances from their host stars. Of the volatiles with prominent spectral features, $H_2O$, CO and $CO_2$ are the major C- and O-bearing species. A C/O$<0.5$ would indicate formation within the $H_2O$ snowline, beyond which the relative carbon abundance, that is readily available for accretion, increases and the C/O becomes super-stellar (Madhusudhan et al., 2014).

In reality the picture is more complex. Firstly, the snowlines move in position, closer to their host stars, as the disk cools. The composition is therefore also a function of time. Moreover, the current-day atmospheric C/O ratio is subject to evolutionary processes, including that of the protoplanetary disk (Hoch et al., 2022). Then, there may be interaction between the solid material in the core and the gaseous atmosphere, or the infall of evaporating planetesimals, which impact the observed composition and introduce degeneracy in the inferred formation pathways. The C/H ratio can help to distinguish if the gas accretion was dominant, since there is relatively negligible solid hydrogen contribution (Öberg et al., 2011; Öberg & Bergin, 2016). Therefore, though there does not therefore exist a linear relation between C/O and formation location, measuring the planetary atmospheric C/O ratio relative to its host star can act as a useful metric, to constraint formation scenarios to first order (Öberg et al., 2011; Madhusudhan, 2012; Madhusudhan et al., 2014).

### 2.1.3 Atmospheric modelling

When building atmospheric forward models to construct exoplanet spectra, we must simplify the problem for computational tractability purposes. Madhusudhan et al. (2016) consider the most important parameters to be: gravity, elemental composition, insolation, internal heating, thermal structure and the strength of transport processes. Fig. 2.2 depicts some of these processes; I discuss each in turn.

The **gravitational field strength** controls the extent of an atmosphere which can be retained by a planet, as derived from its mass and radius. From it, we derive the atmospheric pressure scale height, $H$, given by

$$H = \frac{k_B T}{\mu m_H g} \tag{2.3}$$

where $k_B$ is Boltzmann's constant, $T$ is the planet temperature, $\mu$ is the mean molecular weight of the atmosphere, $m_H$ is the mass of a hydrogen atom, and $g$ is the acceleration due to gravity. It defines the extent of the atmosphere – formally the vertical distance over which the pressure and the density of the atmosphere is reduced by a factor of $e$, as

$$P(z) = P_0 \exp\{-z/H\} \tag{2.4}$$

(see Pierrehumbert, 2010, for a full derivation). It is thus a helpful parameter for predicting observability of an exoplanet's atmosphere, based on its extent (see the Transmission Spectroscopy Metric, TSM, discussed in §2.2; Kempton et al., 2018).

The **thermal structure**, the vertical variation in temperature as a function of pressure, plays an important role on the chemistry in the atmosphere. It dictates the formation of clouds depending on the condensation temperature of a given species. Another equilibrium condition that is often instated is radiative-convective equilibrium. This assumption enables a pressure-temperature (P-T) profile to be computed. Neglecting irradiation, a well-mixed atmosphere will follow the dry adiabatic lapse rate, given by

$$T(p) = T_0 \Big(\frac{p}{p_0}\Big)^{R/c_p}, \tag{2.5}$$

(9.8 °C/km for the Earth's atmosphere), where $(p_0, T_0)$ is a reference state and $R$ is the specific gas constant (Pierrehumbert, 2010). In retrieval codes, the P-T profile is typically parameterised (see e.g., Guillot, 2010). This has enabled detection of thermal inversions in hot Jupiter atmospheres, which can be invoked by a number of scenarios. An inversion may be caused by the presence of high-temperature absorbers, such as TiO and VO in oxygen-rich atmospheres, or hydrocarbons

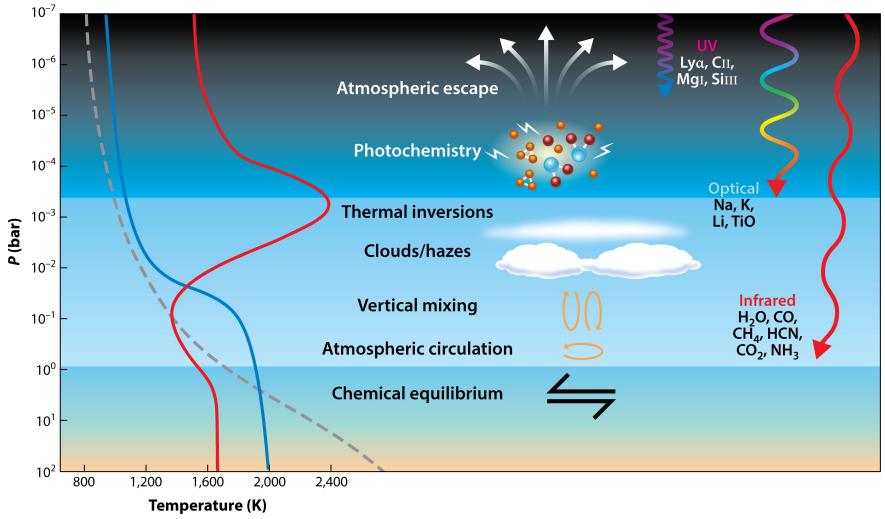


**Figure 2.2:** The dominant processes which govern an exoplanet atmosphere, at their relevant pressures. Towards the left of the plot are shown three exemplar P-T profiles in red, blue and grey. Shown towards the right are the typical depths reached by stellar radiation, along with the relevant chemicals with spectral features at each wavelength. Figure from Madhusudhan (2019).

when C/O> 1 (Madhusudhan, 2012). Other scenarios include insufficient cooling mechanisms and photochemically produced haze (Mollière et al., 2015).

The P-T profile also informs us of the **insolation**, the stellar flux incident at the top of a planet's atmosphere. The stellar irradiation can drive atmospheric escape and photochemistry in the upper layers of the atmosphere (see Fig. 2.2). Photochemical processes can deplete and supplement affected species, and produce aerosols in the form of haze or 'soot' (Zahnle et al., 2009). At even lower pressures in the exosphere, interaction with stellar particles can provide sufficient energy to an atmospheric particle towards escaping the gravitational influence of the planet.

**Internal heating** can influence the lower atmosphere and thereby the P-T profile. This tends to be more important for younger planets, with residual heat from formation. Its influence on atmospheric properties is inherently degenerate with the mixing processes, so it is a difficult parameter to constrain (Madhusudhan et al., 2016).

There are a multitude of **transport processes** occuring at any point in time in a planet atmosphere, such as vertical mixing due to diffusion, advection and circulation (Parmentier et al., 2013). Typically the strength of vertical mixing is

parameterised by the eddy diffusion coefficient, $K_{zz}$, which is difficult to constrain with observations. These processes can also contribute to disequilibrium chemistry. Atmospheric circulation impacts the temperature profile of an atmosphere, as well as heat transport around the planet. This impacts tidally locked planets in particular, enabling the redistribution of heat from the dayside to the nightside of the planet.

These all contribute to the expected **elemental composition** of an exoplanet atmosphere. Current forward modelling codes are able to include a wide range of atomic and molecular species – any for which we have laboratory-acquired spectral line lists (see e.g., EXOMOL; McKemmish et al., 2019; Yurchenko et al., 2020). (Thermo)chemical equilibrium may be employed as a starting assumption. By this we mean a steady-state chemistry which is dependent only on the atmospheric temperature and pressure, as well as elemental composition (Madhusudhan, 2019); we can use tools such as FASTCHEM (Stock et al., 2018) to compute the chemical abundances from elemental composition. However, at cooler temperatures and in the upper atmosphere, disequilibrium chemistry can become more important (Moses et al., 2013). Therefore, some choose to employ free chemistry in atmospheric retrievals. These impose no constraints on the chemical abundances, allowing the retrieval to be purely data-driven. However, this inevitably renders them subject to noise which can lead to unrealistic abundances (Heng & Lyons, 2016). There also exist codes to compute disequilibrium models (e.g., Tsai et al., 2017).

With the parameters above one can build a self-consistent model atmosphere[1]. Then, one may forward model a transmission, emission or reflection spectrum by solving the radiative transfer equation, which describes the interaction of the stellar flux as it interacts with the planet atmosphere. For a plane-parallel atmosphere, the radiative transfer equation is given by,

$$\mu \frac{\delta I_\lambda}{\delta \tau_\lambda} = I_\lambda - S_\lambda \tag{2.6}$$

where $I$ is the intensity, $S$ is the source function which includes all attenuation process, $\tau$ is the optical depth, each a function of wavelength, $\lambda$, and $\mu$ is the

[1] A self-consistent model atmosphere is one in which the radiative transfer, chemistry and structure are all consistent with each other (see Heng et al., 2016, for further detail.)

viewing angle, $\mu = \cos\theta$ (Heng & Marley, 2018). The optical depth describes the distance travelled of a photon before it interacts with matter, being absorbed or scattered, and is given by

$$\tau_\lambda = \int \kappa_\lambda \rho dz \tag{2.7}$$

where $\kappa$ is the absorption coefficient, or opacity, $\rho$ the mass density and $z$ the vertical distance through the atmosphere. There exists a library of algorithms which efficiently compute radiative transfer models (e.g., Heng et al., 2014; Irwin et al., 2008).

### 2.1.4 An exoplanet zoo

The current library of exoplanet atmosphere studies have revealed a diversity in exoplanet compositions, with further insight than the bulk composition estimates (§1.3); for a review see Roberge & Seager (2018). In Fig. 2.3 I reproduce a summary table of the detected atoms and molecules in the atmospheres of exoplanets, from Guillot et al. (2022). As a community, we have detected a vast array of chemical species, including volatiles, refractories, and silicates. As anticipated, hydrogen and helium are ubiquitous in the atmospheres of exoplanets (Nortmann et al., 2018), and in some cases, the detections of them at extended distances have been indicative of atmospheric escape (Orell-Miquel et al., 2023; dos Santos et al., 2020). The ultra-hot Jupiter population constitutes an extreme laboratory; atoms and molecules that are present in gaseous form only at extremely high temperatures, refractories such as Fe, TiO and VO, have been detected (Ehrenreich et al., 2020; Pelletier et al., 2023; Prinoth et al., 2022). Despite expecting $CH_4$ in equilibrium chemistry and the strong spectral features emcompassed by current spectrographs, the molecule has remained elusive at temperatures less than 1000 K until recently (see a recent detection by Madhusudhan et al., 2023). This may indicate that disequilibrium chemistry is more prominent in cooler planets (Moses et al., 2013). Moreover, scattering haze and opaque clouds have also been detected in a number of exoplanet atmospheres, including both hot Jupiters and warm Neptunes (Wakeford et al., 2017; Benneke et al., 2019a; Grant et al., 2023; Dyrek et al., 2023).

| | | Properties | | Bulk | | Ices | | | | Alkalis | | | Rocks | | | | | | | | | Isotope | References |
|---|---|---|---|---|---|---|---|---|---|---|---|---|---|---|---|---|---|---|---|---|---|---|---|
| | Planet name | Teq/ Teff (K) | M ($M_{Jup}$) | H | He | $H_2O$ | CO | $CH_4$ | HCN | Na | K | Li | Fe | Fe II | Mg | Ca II | Ca | Sc II | Si | Ti II | V | Cr | $^{13}CO$ | |
| Transiting planets | KELT-9b | 4048 | 2.88 | H | | | | | | | | | H | H | H | H | | L | | H | | | | 1,2,3,4,5,6,7,8,9 |
| | WASP-33b | 2781 | 2.1 | H | | L | L | | | | | | H | | | H | | | L | | | | | 2,10,11,12,13,111,115 |
| | WASP-189 | 2641 | 1.99 | | | | | | | | | | H | H | L | | | | | L | L | L | | 108,109,110 |
| | WASP-121b | 2359 | 1.18 | H | | M | | | | H | H | L | H | H | H | H | H | L | | | L | L | | 10,14,15,16,17,18,19,20 |
| | KELT-20b | 2255 | 3.38 | H | | L | | | | H | | | H | H | L | H | | | L | | | | | 21,22,23,24,25,26,115,116 |
| | WASP-76b | 2182 | 0.92 | | | L | | | | H | | L | H | | L | H | | | | | L | L | | 27,28,29,30,31,32,33,80 |
| | HAT-P-32b | 1801 | 0.58 | L | L | L | | | | | | | | | | | | | | | | | | 117,118 |
| | WASP-77Ab | 1741 | 2.29 | | | H | L | | | | | | | | | | | | | | | | L | 34,35 |
| | WASP-17b | 1698 | 0.78 | | | L | | | | L | | | | | | | | | | | | | | 36,37 |
| | HD209458 b | 1476 | 0.73 | L | L | H | H | L | L | C | | | | C | C | | | L | | | | | | | 38,39,40,41,42,43,44,45,46,47,48,11 |
| | WASP-127b | 1401 | 0.18 | | | L | | | | H | L | L | | | | | | | | | | | | | 49,50 |
| | XO-2b | 1327 | 0.566 | | | | | | | L | L | | | | | | | | | | | | | | 51 |
| | HAT-P-1b | 1322 | 0.525 | | | L | | | | L | | | | | | | | | | | | | | | 52,53 |
| | WASP-52 b | 1299 | 0.46 | L | | L | | | | H | L | | | | | | | | | | | | | | 54,55,56 |
| | WASP-96b | 1286 | 0.48 | | | L | | | | L | | | | | | | | | | | | | | | 57,58 |
| | HD189733b | 1192 | 1.13 | | H | H | H | | L | H | L | | | | | | | | | | | | | | 59,60,61,62,63,64,65,66,67,68,69,70 |
| | WASP-39b | 1120 | 0.28 | | | L | | | | L | | | | | | | | | | | | | | | 71,72 |
| | WASP-6b | 1093 | 0.37 | | | L | | | | H | H | | | | | | | | | | | | | | 73,74 |
| | WASP-69b | 988 | 0.29 | | L | L | | | | H | | | | | | | | | | | | | | | 75,55,76,77 |
| | HAT-P-12b | 957 | 0.21 | | | L | | | | L | | | | | | | | | | | | | | | 78,79 |
| | HAT-P-18b | 848 | 0.20 | | L | L | | | | | | | | | | | | | | | | | | | 81,55 |
| | HAT-P-11b | 829 | 0.084 | | M | L | | | | | | | | | | | | | | | | | | | 82,83,84 |
| | WASP-107b | 739 | 0.12 | | H | L | | | | | | | | | | | | | | | | | | | 85,86,87 |
| | GJ3470b | 604 | 0.043 | | L | L | | | | | | | | | | | | | | | | | | | 119, 120 |
| Non Transiting | Tau Bootis b | 1636 | 5.84 | | | C | H | | | | | | | | | | | | | | | | | | 88,89,90,91 |
| | HD179949b | 1552 | 0.92 | | | M | L | | | | | | | | | | | | | | | | | | 92,93 |
| | 51Peg b | 1260 | 0.46 | | | H | L | | | | | | | | | | | | | | | | | | 112,113 |
| | HD 102195b | 1053 | 0.46 | | | L | | L | | | | | | | | | | | | | | | | | 94 |
| Directly imaged | CQ Lupi b | ~2650 | 25 | | | L | L | | | | | | | | | | | | | | | | | | 95 |
| | Beta Pictoris b | ~1724 | 12.9 | | | H | H | | | | | | | | | | | | | | | | | | 96,97,98 |
| | TYC 8998-760-1b | ~1700 | 14 | | | L | L | | | | | | | | | | | | | | | | L | | 99 |
| | HR8799c | ~1100 | 8.1 | | | H | H | C | | | | | | | | | | | | | | | | | 100,101,102,103 |
| | HR8799b | ~900 | 5.8 | | | L | L | C | | | | | | | | | | | | | | | | | 104,105 |
| | 51 Eridiani b | ~760 | 9.1 | | | H | | H | | | | | | | | | | | | | | | | | 106,107 |

*Confidence level:*
High observed by at least 2 instruments
Medium: observed by one instrument multiple times
Low: observed once by one instrument
Controversial

*Note: only planets with at least two different species detected and only species that are detected in at least two planets are presented here. Photometric only detection are discarded.*

**Figure 2.3:** A summary of detected chemical species in the atmospheres of exoplanets, from Guillot et al. (2022).

## 2.2 Observing exoplanet atmospheres

The remote characterisation of exoplanets begins with their detection. From radial velocity measurements, we can infer masses of orbiting planets, and the depth of transit light curves provide the size of the planet relative to its host star. Combine the two, and we have a density estimate. Fig. 2.4 is a mass-density diagram populated with the known, well-characterised exoplanet population (as of 2018). Included in Fig. 2.4 are a suite of composition lines, consistent with each density solution. What I hope is clear from this diagram is that density alone can only inform us of bulk composition and does little to reveal the richness of exoplanet composition. That is not to detract from the useful scientific output of mass and radius measurements; other than their inherent information, they provide an estimate of the atmospheric scale height (see Equation 2.3), which acts as an important predictor for atmospheric study feasibility.

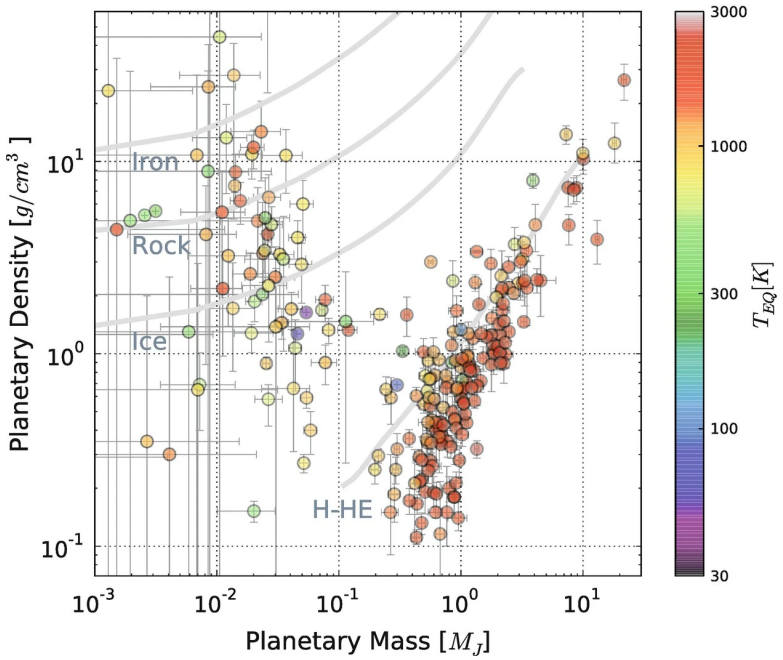


**Figure 2.4:** The population of discovered exoplanets with precise mass and radius constraints, coloured according to predicted equilibrium temperature. Over-plotted are some exemplar model pure composition lines. Figure from Laughlin (2018).

To further the characterisation of a planet and break the composition degeneracy, we might aspire to probe the interior structure (see §2.1). We are, of course, limited in what we can achieve with remote sensing. A more recent development is the innovation of methods to remotely observe the atmospheres around exoplanets (Charbonneau et al., 2002). Volatile chemical species which exist in gaseous form will interfere with, scattering or absorbing, incident stellar light, imparting a spectrum which can be detected from the Earth, assuming appropriate instrumental sensitivity (Kreidberg, 2018).

One can choose to observe the planet at various positions in its orbit (see Fig. 2.5). During a transit event, an atmosphere around the occulting planet will impart a **'transmission spectrum'**. With the same premise as the transit light curve detection method (Equation 1.3), during transit, a planet with an atmosphere would partially block a portion of the incident stellar light. Since the different atmospheric atomic and molecular species absorb light at different, characteristic wavelengths, the opacity of the planet, or its opaque radius, may be observed as a function of

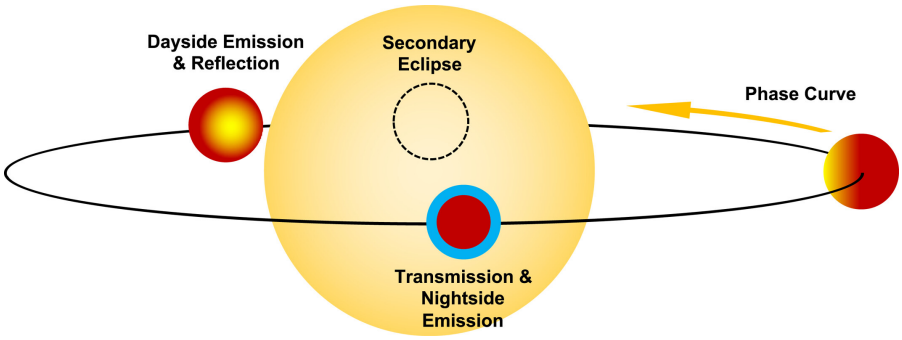


**Figure 2.5:** The orbital path of a transiting exoplanet (black) around its host star, with specific locations that enable atmospheric study indicated. Figure from Gao et al. (2021).

wavelength, in order to trace back to the absorbing chemical species. Each atom and molecule has its own characteristic absorption (and emission) spectrum; we compare the observed spectra to theoretical template spectra, which are based on laboratory-acquired 'line lists', the wavelengths at which a given species absorbs (emits) light. Towards prioritising targets for atmospheric characterisation, Kempton et al. (2018) developed the Transmission Spectroscopy Metric:

$$\mathrm{TSM} = A_s \times \frac{R_p^3 T_{\mathrm{eq}}}{M_p R_*^2} \times 10^{-m_J/5} \tag{2.8}$$

where $A_s$ is a scale factor, $R_p$ and $M_p$ the mass and radius of the planet, $R_*$ the stellar radius, $T_{\mathrm{eq}}$ the predicted planet equilibrium temperature and $m_J$ the J-band magnitude of the host star. This considers that a high signal-to-noise of transmission features ($\propto R_p H/R_*$, Kempton et al., 2018), and a bright host star will increase the prospect of detecting an atmosphere. It was originally derived to quantitatively compare targets for space-based observations, and so does not consider important parameters for ground-based high-resolution spectroscopy, such as the radial velocity of the planet (see §2.3). Yet, it is still a useful metric for first order comparison, and I refer to it throughout this thesis.

Traverse to the opposite side of the orbit, and you reach secondary eclipse, when the planet passes behind its host star. If the planet has its own thermal contribution and/or is tidally locked, the flux of the planet-star system will significantly decrease during secondary eclipse. The planet's own contribution, radiation from the hot dayside, may be inferred by comparing flux of the phases either side of the secondary

eclipse to the flux during the occultation event. Again, study this as a function of wavelength and one acquires an **'emission spectrum'**. This time, the decrease in flux is given by

$$\frac{\Delta F}{F} \simeq \frac{\mathcal{B}(\lambda, T_{p,\lambda})}{\mathcal{B}(\lambda, T_{*,\lambda})} \left(\frac{R_p}{R_*}\right)^2, \tag{2.9}$$

where $\mathcal{B}$ is the Planck function, dependent on the relevant brightness temperature $T$ at a given wavelength, $\lambda$ (Kreidberg, 2018). The planet emission originates from the $\tau \simeq 1$ 'surface', the altitude at which the atmosphere becomes transparent, which varies according to $\kappa_\lambda$ (see Equation 2.6, Gandhi & Madhusudhan, 2018). If there exists a change in temperature $T_{p,\lambda}$ with altitude of the $\tau \simeq 1$ surface, the observed change in opacity with wavelength allows us to probe the temperature structure with emission spectroscopy. At this configuration, the **'reflection spectrum'** of the planet may also be observed, if the planet has sufficiently high albedo as to scatter the incident stellar spectrum. This usually dominates over emission at optical wavelengths.

For tidally locked systems, the flux of the planet-star system can be observed across a larger phase range, or even the entire orbit, known as a **'phase curve'**. Considering first an orbiting bare rock, during transit one would observe the cold, or 'night', side of the planet. The 'dayside' would comprise the full projected hemisphere of the planet during secondary eclipse, as it aligns perfectly along the line of sight from observer to the star. The substellar point at any point in time is the latitude/longitude on the planet which receives the most stellar flux. In this scenario, the substellar point would be in full view and would induce a maximum in the phase curve during secondary eclipse. An atmosphere can enable heat redistribution around the tidally locked planet, and consequently shift the maximum flux contribution away from the substellar point. Studying the shape of phase curves therefore enable a probe into (i) the existence of an atmosphere and (ii) the winds in the atmosphere causing the redistribution of heat.

**Table 2.1:** A list of the major spectrographs used for exoplanet spectroscopy.

| Spectrograph | Telescope | Location | Resolution, R | Wavelength coverage (microns) |
|---|---|---|---|---|
| **High-resolution** | | | | |
| ESPRESSO | VLT | Paranal, Chile | 120000–140000 | 0.3–0.7 |
| HIRES | Keck I Telescope | Mauna Kea Observatory, Hawaii | 25000–85000 | 0.3–1.0 |
| UVES | VLT | Paranal, Chile | 80000–110000 | 0.3–0.5; 0.42–1.1 |
| PFS | Magellan II Telescope | Las Campanas Observatory, Chile | 38000–190000 | 0.391–0.734 |
| HORUS | Gran Telescopio Canarias | Roque de los Muchachos Observatory, La Palma | 25,000 | 0.38–0.69 |
| HARPS | ESO 3.6m | La Silla, Chile | 120,000 | 0.377–0.691 |
| HARPS-N | TNG | Roque de los Muchachos Observatory, La Palma | 115,000 | 0.378–0.691 |
| MAROON-X | Gemini North | Mauna Kea Observatory, Hawaii | 80,000 | 0.500–0.92 |
| HDS | Subaru | Mauna Kea Observatory, Hawaii | 165,000 | 0.62–0.88 |
| CARMENES | 3.5m | Calar Alto Observatory, Spain | 80000–100000 | 0.52–0.96; 0.96–1.71 |
| HPF | Hobby-Eberly Telescope | McDonald Observatory, Texas | 55,000 | 0.8–1.27 |
| GIANO-B | TNG | Roque de los Muchachos Observatory, La Palma | 50,000 | 0.9–2.45 |
| SPIRou | CFHT | Mauna Kea Observatory, Hawaii | 70,000 | 0.9–2.5 |
| NIRPS | ESO 3.6m | La Silla, Chile | 90000–100000 | 0.95–1.8 |
| CRIRES+ | VLT | Paranal, Chile | 80,000 | 0.95–5.3 |
| NIRSPEC | Keck | Las Campanas Observatory, Chile | 25,000 | 0.95–5.5 |
| IRD | Subaru | Mauna Kea Observatory, Hawaii | 70,000 | 0.97–1.75 |
| iSHELL | NASA IRTF | Mauna Kea Observatory, Hawaii | 75,000 | 1.1–5.3 |
| IGRINS | Gemini South | Cerro Pachon, Chile | 45,000 | 1.4–2.4 |
| **Low-resolution** | | | | |
| FORS2 | VLT | Paranal, Chile | 260–2600 | 0.33–1.1 |
| GMOS | Gemini North; Gemini South | Mauna Kea Observatory, Hawaii; Cerro Pachon, Chile | 210–8800 | 0.36–1.03 |
| LDSS3C | Magellan II Telescope | Las Campanas Observatory, Chile | 860–1810 | 0.38–1.0 |
| WFC3 | HST | Space | 70–210 | 0.8–1.7 |
| NIRSpec | JWST | Space | 100–2700 | 0.5–5.0 |
| NIRCam | JWST | Space | 1,600 | 0.6–2.3; 2.4–5.0 |
| MIRI | JWST | Space | 100–160 | 5.0–27.9 |
| NIRISS | JWST | Space | 700 | 0.6–2.8 |

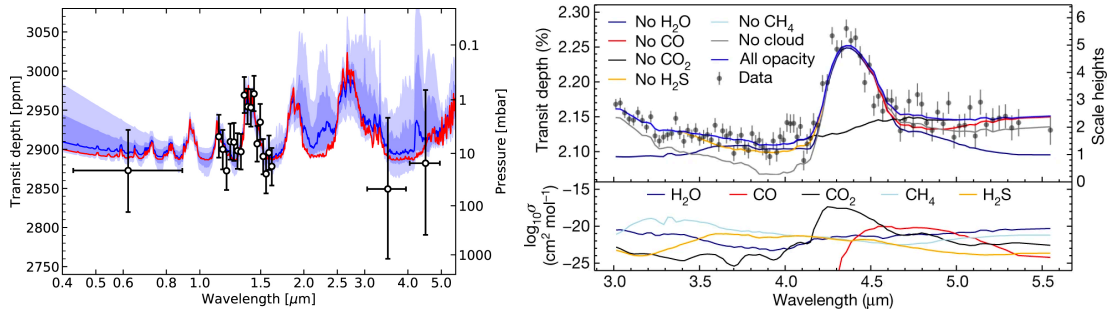


**Figure 2.6:** Space-based observations of exoplanet atmospheres. **Left:** The combined spectrum of K2-18 b, as seen with *WFC3* on *HST* and *Spitzer*. The 1.4μm water absorption feature is clearly resolved. Figure from Benneke et al. (2019b). **Right:** The *JWST/NIRSpec* transmission spectrum of WASP-39 b, showing clear $CO_2$ absorption. Figure from Team et al. (2023).

### 2.2.1 Space-based vs ground-based observations

Observations of exoplanet atmospheres can be made from space, with instruments like *HST* and now *JWST*, or from the ground. Spectrographs mounted on space-based telescopes are necessarily low-resolution, in order to meet size and weight payload requirements. As an example, *WFC3* on *HST* affords spectra at a maximum resolving power of $R = \frac{\lambda}{\Delta\lambda} \sim 210$; see Table 2.1 for a comparison in resolution between different instruments. Such instruments have been very successful in yielding atmospheric spectra. Fig. 2.6 shows an example transmission spectrum of the sub-Neptune K2-18 b, acquired with *HST/WFC3*, with additional photometric data points from *Spitzer*. The water band head is resolved within the data uncertainties, from which Benneke et al. (2019b) retrieved a water abundance consistent with $0.6 - 162\times$ that expected with a solar elemental abundance. Spectra of similar quality have been recovered for other sub-Neptunes and hot Jupiters (see e.g., Benneke et al., 2019a; Wakeford et al., 2018). *JWST* has now changed the game with its exquisite precision, and broad near-infrared (nIR) wavelength coverage; see Fig. 2.7 for a schematic of the wavelength coverage of the *JWST* instruments relative to bandheads of crucial atmospheric molecules. An example transmission spectrum from *JWST/NIRSpec* is shown in the right panel of Fig. 2.6, with the bandheads for various molecules shown in the bottom panel. The broad nIR wavelength coverage of *NIRSpec* is particularly apt for the main carbon bearing

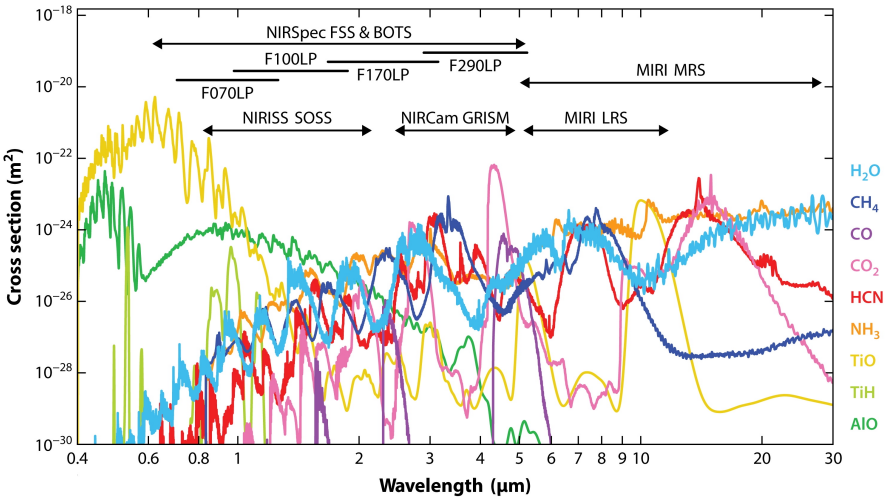


**Figure 2.7:** The cross-sections of some key atmospheric molecules which can be probed with *JWST*. The spectral coverage of the four instruments on *JWST* are shown. Figure from Madhusudhan (2019).

molecules (Alderson et al., 2023). The combination of high stability, telescope aperture, resolution and wavelength coverage of the *JWST* spectrographs make them very powerful instruments for exoplanet spectroscopy.

Ground-based low-resolution spectroscopy continues to contribute to exoplanet characterisation (e.g., Kirk et al., 2021; Diamond-Lowe et al., 2018; Espinoza et al., 2019; Gibson et al., 2013; Nikolov et al., 2018). An obvious, undesired contaminant is the absorption due to the Earth's atmosphere, known as 'telluric' absorption. The strategy of low-resolution spectroscopy is to simultaneously observe a separate standard star, within the same field of view, in order to correct for the tellurics. In Fig. 2.8, I show an optical, low-resolution spectrum of WASP-96 b acquired from the ground, with the FORS2 instrument on the VLT. Measuring the sodium, lithium and potassium abundances, Nikolov et al. (2018) were able to constrain the metallicity of WASP-96 b to $\log(Z_p/Z_\odot) = 0.4^{+0.7}_{-0.5}$, which was consistent with the host star.

Then, with a plethora of stable high-resolution spectrographs such as ESPRESSO and CRIRES+, high-resolution[2] spectroscopy has been very successful enabling atmospheric detections in recent years (see e.g., Line et al., 2021; Pelletier et al., 2021; Prinoth et al., 2022; Nugroho et al., 2021). At high resolution one can begin to

[2]In this thesis, I refer to spectra with resolving power $R > 10,000$ as high resolution.

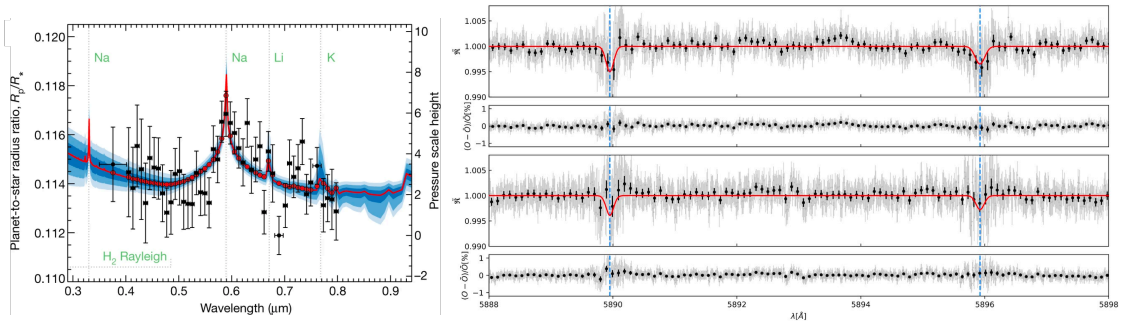


**Figure 2.8:** Ground-based observations showing sodium absorption in the atmosphere of **left:** WASP-96 b as seen with VLT/FORS2 and **right:** hot Neptune WASP-166 b, as seen by VLT/ESPRESSO. Figures from Nikolov et al. (2018) and Seidel et al. (2022) respectively.

resolve individual exoplanet spectral lines from the continuum; in Fig. 2.8 I show an example transmission spectrum obtained with ESPRESSO of the hot Neptune WASP-166 b (Seidel et al., 2022). In this thesis, I focus on ground-based high-resolution observations; I proceed to provide further details on high-resolution spectroscopy.

## 2.3 High-resolution spectroscopy

Since the pioneering work of Snellen et al. (2008) and Brogi et al. (2012), high-resolution spectroscopy has been a dominant workhorse in the detection of exoplanet atmospheres from the ground. The field has progressed from nIR detections of carbon-bearing molecules in the atmospheres, to resolving specific limb atmospheric contributions of transiting planets, and probing day-to-night winds (Birkby et al., 2013; Brogi et al., 2014; Line et al., 2021; Gandhi et al., 2022). Here, I detail the standardised, present day method.

The assignment of observing an exoplanet spectrum is quite a challenging one. An exoplanet's transmission or emission spectrum is typically a few orders of magnitude weaker than that of its host star. One technique involves the suppression of the stellar flux, using a 'mask' on the instrument of choice, before cross-correlation of an atmosphere template with each pixel. This is known as molecular mapping, and is only effective for planets which are sufficiently separated from their host star to not be hidden underneath the focal plane mask (e.g., Snellen et al., 2014; Hoeijmakers et al., 2018b). Integral field spectroscopy has been performed at low

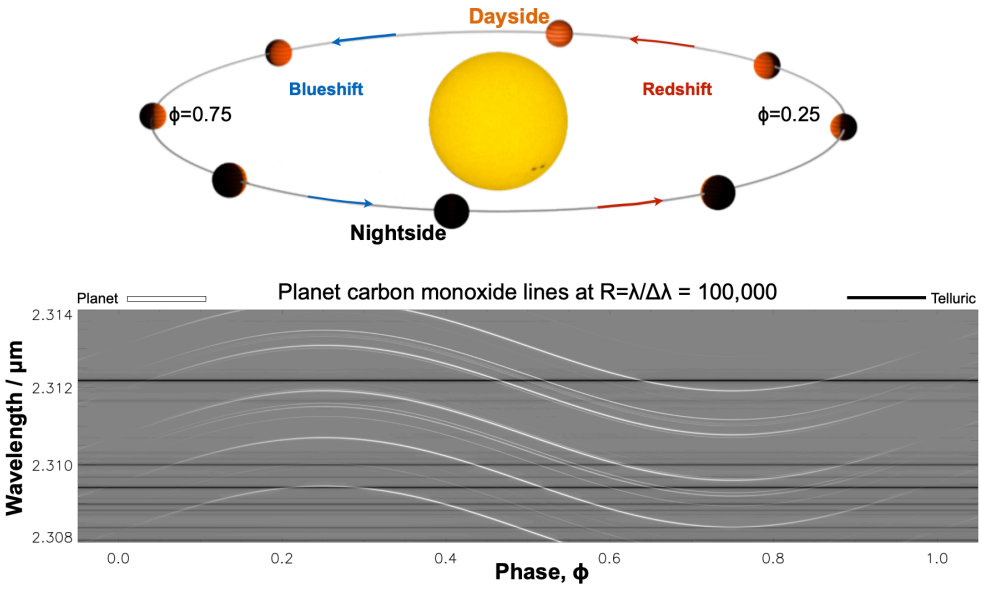


**Figure 2.9:** Schematic for the concept of high-resolution spectroscopy: the exoplanet spectrum Doppler-shifts during the planet's orbit (top panel), creating a sinusoidal signal in the spectral time-series (bottom panel). Figure from (Birkby, 2018).

to high resolution (see e.g., Zhang et al., 2021; Patapis et al., 2022; Tannock et al., 2022). For closer in planets, there is no choice but to observe the star simultaneously. The task is then to distinguish the stellar and planet spectra. From the ground, there is the additional nuisance signal input from the Earth's atmosphere. The key insight is that the planet's spectrum Doppler shifts as the planet orbits its host star, at least to some order, unless the orbital plane is perpendicular to line of sight. The stellar and telluric spectrum remain stationary in their respective rest frames. Therefore, though the stellar and telluric spectra are completely dominant, one can attempt to uncover the Doppler shifting planet signal, assuming sufficient velocity shift is observed. This insight is visualised in Fig. 2.9.

### 2.3.1 Observations

Such data will consist of a sequence of exposures, spectroscopically observing the star as a function of time. There are a few considerations to be made when planning these observations. Typically, the chosen targets have measured mass and periods, thus their orbital velocity may be estimated. Most high-resolution observations are taken during transit, or pre or post-eclipse. At quadrature, the radial velocity

component of the planet is at a maximum, but since only half of the dayside hemisphere is visible, this configuration presents more of a challenge; there have been few detections using such geometry (e.g., Finnerty et al., 2021).

Regardless of the phases observed, one must choose an exposure time which allows one to amply sample the planet velocity trail. While longer exposures augment the signal-to-noise, one must be careful to avoid 'Doppler smearing', whereby the planetary lines are broadened as a result of movement during the prolonged exposure. Finer time sampling is thus preferred. When choosing from the various available high-resolution spectrographs (see Table 2.1), one must consider the wavelengths that would be important to answer the scientific questions of interest. This depends on the type of spectrum desired; for example, the reflection component of an exoplanet's spectrum dominates at optical wavelengths, while the emission spectrum is increasingly prominent in the nIR. Concurrently, one must consider the valuable wavelengths for the sought chemical species and atmospheric effects. The resolution of the chosen instrument must also be factored in, since the planet spectral lines must shift across multiple resolution elements over the observed phase range in order to be distinguished from the stationary nuisance signals.

### 2.3.2 Data reduction methods

Once the spectral sequence has been acquired, it is usually subject to pre-processing steps such as bad-pixel correction, and alignment of the spectra to correct for instrumental jitter. It is also common practice to perform background subtraction. For échelle spectrographs, a standard observing technique is to nod the telescope along the slit, collecting photons at two distinct positions: A and B. One then acquires a sequence of exposures in an ABBA pattern. By combining these exposures into one 'frame', you effectively remove the background imprint. The task at hand is then to remove the telluric and stellar signals. So-called 'self-calibrated', high-resolution observations do not use simultaneous (or close in time) observations of a standard/calibration star. It follows that the first detrending step is often normalisation of the spectral continuum, correcting for the instrumental throughput

and the atmospheric variability. Then, depending on the wavelength and stellar type, one will dominate over the other, and so the order of removal will depend on the properties of the data at hand.

### Stellar removal

Towards the removal of the stellar spectrum, it is often assumed to be constant in time, and so a simple division by a reference stellar spectrum is standard. For transit observations, it is preferable to use out-of-transit frames to construct the reference spectrum (Seidel et al., 2020; Gibson et al., 2021). These frames are known not to contain the planet, and therefore there is little risk of partially dividing out the planet signal. Alternatively, if the star is well-characterised, a synthetic stellar model spectrum, interpolated from one of the plethora of stellar model grid libraries, may sufficient (e.g., Husser et al., 2013; Witzke et al., 2021). This type of treatment has historically been adequate, with the majority of high-resolution cross-correlation studies focusing on bright FGK stars, where the time variations are negligible. In reality however, most stars are not homogeneous, well-behaved disks in the sky, but rather constantly evolving. The impact of stellar non-uniformity is likely to increase with fainter, smaller stars (Genest et al., 2022); I discuss this extensively and explore alternative approaches in Chapter 4.

### Telluric removal

The task of removing telluric imprint is a substantially harder problem. Though the absorbers in the Earth's atmosphere are well characterised, turbulence, seeing, and clouds, amongst other weather patterns, render telluric behaviour unpredictable and difficult to model. There is a plethora of methods used to model and remove tellurics, a topic which has been extensively discussed in the literature (Langeveld et al., 2021; Meech et al., 2022; Cheverall et al., 2023; Gibson et al., 2021). There exist theory-based tools which compare synthetic models to the acquired spectral data. Example tools include MOLECFIT, TELFIT, TAPAS and TERRASPEC (Smette et al., 2015; Gullikson et al., 2014; Bertaux et al., 2014; Bender et al., 2012). These theoretical-based strategies tend to perform better at optical wavelengths where

telluric absorption is weaker and micro-tellurics are more prevalent. Micro-tellurics might not necessarily be easy to detect, and so knowledge of their locations is helpful. In the nIR, there is heavier telluric absorption, with wide absorption bands and even saturation. These tend to be more directly impacted by atmospheric behaviour, so empirical detrending methods are usually favoured. Principal Component Analysis (PCA) is a widely used method. Based on singular value decomposition, it exploits the stationary nature of telluric features to model common trends in time. Another popular algorithm is SYSREM (Mazeh et al., 2007; Tamuz et al., 2005), a variation of PCA which incorporates weighting by individual data point uncertainties. These are iterative processes, identifying strong time correlations first, and progressively more minor trends in later iterations. Both require a user-defined number of components to remove. Use too few iterations and you risk leaving telluric residuals in the data. Too many iterations and the algorithms start to pick up on trends unrelated to the tellurics. This can potentially put the planet signal at risk; the shift of planet spectrum is inherently continuous, while we observe at discrete time stamps, thus the sub-pixel shifts can cause the detrending algorithm to falsely identify the planet spectrum as a common trend. There has been some discussion in the literature addressing this concern (e.g., Cheverall et al., 2023); the number of iterations can be somewhat subjective, and there is a lack of a robust method to optimise the balance between adequate telluric removal and maintaining the planet signal.

### 2.3.3 Search for the exoplanet spectrum

Once all other sources of noise have been detrended out of the data, ideally one would be left with photon noise and the Doppler-shifting exoplanet spectrum. With high-resolution spectroscopy, one does not explicitly observe the exoplanet spectrum, except in the case of strong atomic lines in the optical, such as sodium (see Fig. 2.8). We thus require an estimate of the expected exoplanet spectrum and a method to compare it to the data. I have detailed the construction of atmospheric models in §2.1.3; there is an extensive collection of algorithms built to forward model exoplanet spectra. Codes such as PETITRADTRANS, PICASO and HELIOS incorporate planetary

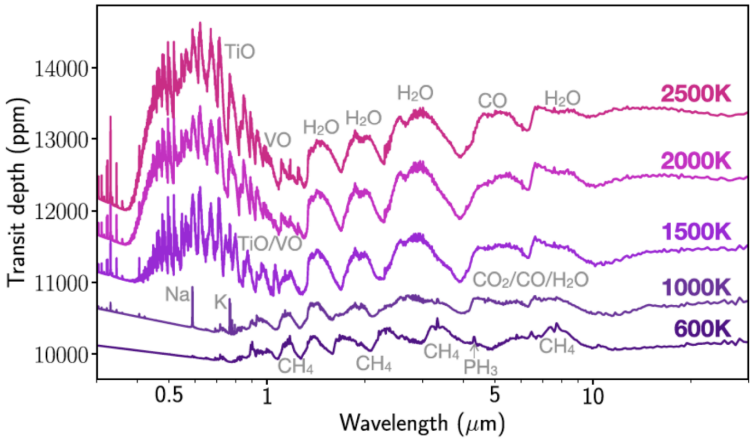


**Figure 2.10:** An example of forward-modelled exoplanet spectra over the 0.3–11 micron wavelength range, at different equilibrium temperatures. A number of spectroscopic features of key molecules are labelled. Figure from Goyal et al. (2019).

atmosphere physics to construct a model atmosphere, and perform radiative transfer (Mollière et al., 2019; Batalha et al., 2019; Goyal et al., 2019). Inputs typically include the atmospheric chemical composition, including both species and their abundances, planet gravity and orbital distance, and sometimes a parameterisation of the pressure-temperature, or 'P-T', profile. The output is a transmission, emission or reflection spectrum, an example of which is shown in Fig. 2.10.

To compare the forward-modelled spectrum to the data, we employ the 'cross-correlation' technique, a metric to constrain the degree to which the data is well-represented by the atmosphere in question. In statistics, the cross-correlation, $C(s)$, is normalised, as given by

$$C(s) = \frac{R(s)}{\sqrt{s_f^2 s_g^2}}. \tag{2.10}$$

In our case, we evaluate $C(s)$ for each velocity shift, $s$. $R(s)$ is the cross-covariance between the data, $f(n)$, and the model evaluated at different velocity shifts, $g(n-s)$. Then, $s_f^2$ is the variance of the data, and $s_g^2$ the variance of the model. To clarify,

$$\begin{aligned} R(s) &= \frac{1}{N}\sum_n f(n)g(n-s); \\ s_f^2 &= \frac{1}{N}\sum_n f^2(n); \\ s_g^2 &= \frac{1}{N}\sum_n g^2(n-s) \end{aligned} \tag{2.11}$$

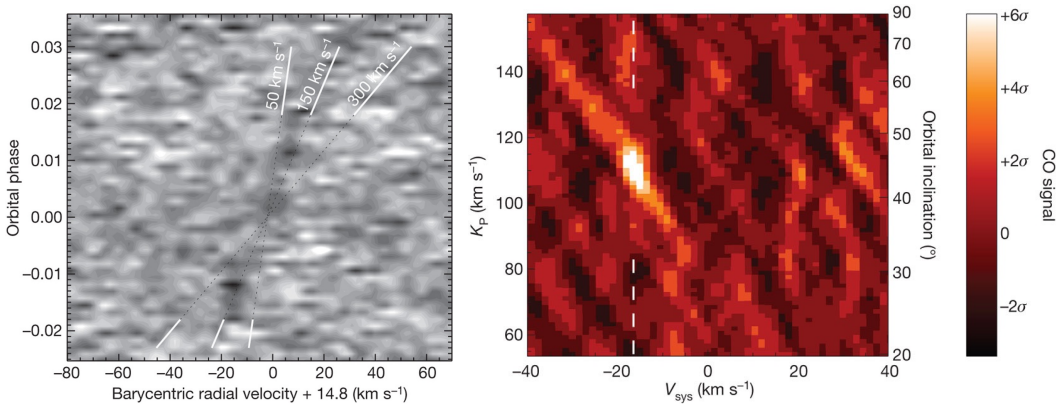


**Figure 2.11: Left:** Time-series of cross-correlation values from Snellen et al. (2010) for HD 209458 b. Each row is a cross-correlation function output having compared a spectrum with a template spectrum. **Right:** Map of peak cross-correlation coefficients as a function of planet orbital velocity and systemic velocity, having cross-correlated $\tau$ Boötis b spectra with a CO model. This plot would have been generated by summing the cross-correlation time-series (e.g., as shown in the left panel) along different velocity gradients. Figure from Brogi et al. (2012).

where each is the result of summation over every pixel $n$, and $N$ is the total number of pixels. The template is shifted in velocity across the data, and the cross-correlation coefficient computed at each velocity shift, constructing a cross-correlation function (CCF). This cross-correlation function effectively encodes the information from all the spectral lines, their positions and relative shapes. Doing this for a time-series of detrended spectra, builds up a time-series of cross-correlation functions, an example of this is shown in the left panel of Fig. 2.11. The idea is then to sum the CCFs along the time axis, for a given planet velocity solution. One can construct a cross-correlation 'velocity map' by displaying the peak correlation coefficient for each velocity solution, as shown in the right panel of Fig. 2.11. Typically these are converted to a signal-to-noise: one select a region away from the expected location of the planet in velocity space, computes the standard deviation of the correlation values in said region, and divides the entire map through by this value. In Fig. 2.11, this signal-to-noise is represented by the colourmap.

### 2.3.4 Advantages

High-resolution cross-correlation spectroscopy (HRCCS) affords a number of advantages over other techniques to detect exoplanet atmospheres. By nature, as one

increases the resolution of spectra, individual absorption lines begin to distinguish themselves from the continuum. In the context of exoplanet spectra, these individual spectral absorption lines encode a wealth of information:

(i) each atomic and molecular chemical species has its own distinct spectrum, a spectral 'fingerprint';

(ii) the depth of spectral lines from a given species corresponds to the abundance of said species;

(iii) the detected velocity shifts of these spectral lines encode information of the planet velocity, affording insight on both the orbital velocity and local velocity effects such as atmospheric winds and, for transit observations, contributions from different planetary limbs;

(iv) distortions in the line profiles including broadening can also be indicative of atmospheric dynamics.

Thus considering the ability of higher resolution spectrographs to resolve the unique individual spectral lines, there is a gain in information. Should the high-resolution spectrum be obtainable, there is a reduction in degeneracy of retrievals of different species since the lines are not blended together. This also means atomic species are retrievable. There is an additive benefit over low-resolution spectroscopy in the case of clouds. Cloud decks render the atmosphere opaque, below the cloud deck altitude. In the cores of spectral lines, the opacity, $\kappa_\lambda$, is high. With reference to Equation 2.7, it then follows that for a given optical depth, the traversed path length is shorter (fulfilled higher up in the atmosphere). This is then why the distinction of the cores of spectral lines at high resolution allows one to probe lower pressures. A low-altitude cloud deck which would flatten a low-resolution spectrum, would only act to truncate a high-resolution spectrum, as demonstrated by Hood et al. (2020) and Gandhi et al. (2020).

### 2.3.5 The history of the technique

At its conception in Snellen et al. (2010) and Brogi et al. (2012), high-resolution cross-correlation spectroscopy used simply a cross-correlation function to assess the significance of a template matched to the data. Their claims of CO absorption were based on an observed peak in the cross-correlation values close to the expected velocity trail of the planet, shown in Fig. 2.11. While Snellen et al. (2010) showed only the summed the cross-correlation time-series for one planet velocity, Brogi et al. (2012) extended this to show the summation over multiple velocity solutions, compiling a cross-correlation 'velocity map' (right panel of Fig. 2.11). They assigned significance to the detection by computing the standard deviation of the map away from the expected location of the planet, and dividing the entire map by this value, thus mapping each cross-correlation coefficient to an $X\sigma$ value. To this day, this technique is still used to report detections of atomic and molecular species.

There is another verification method used in Brogi et al. (2012), based on the Welch $t$-test. The cross-correlation values are divided into two samples: those that belong to the planet radial velocity 'trail' in the cross-correlation time-series, and those that do not. They test the null hypothesis that these two samples are drawn from the same parent distribution using the Welch $t$-test; Brogi et al. (2012) rejected the null hypothesis at the $6\sigma$ level. Again, this method assumes both Gaussianity of the cross-correlation values, and that they are independent. Though initially replicated, this method has been deemed by the field as unreliable: it is highly sensitive to the user-defined width of the planet trail (Cabot et al., 2019). Selecting too wide a trail and you may weaken the significance of the planet signal. Alternatively, a trail that is too narrow reduces the sample size. As a consequence, this method is not often used now.

Beyond first order detections, there has been a desire to pursue abundance measurements of atmospheric species. At low-resolution, abundances have been gathered via 'atmospheric retrievals' since 2009 (Madhusudhan & Seager, 2009; Line et al., 2012). Low-resolution spectroscopy yields an actual spectrum which can be compared to a forward-modelled atmosphere with a straight-forward least-squares

minimisation. With high-resolution spectroscopy the picture is more complex; one does not acquire a distinct spectrum, since it is buried in the noise. Further, the current 'detection' metric, a signal-to-noise measurement, does not easily lend itself to a comparison metric. The breakthrough came in 2019; Brogi & Line (2019) and Gibson et al. (2020) separately developed a mapping from cross-correlation value to a likelihood, which could then be easily evaluated in a Bayesian framework. The likelihood of Brogi & Line (2019) is given by

$$\log(L) = -\frac{N}{2} \log \left[ s_f^2 - 2R(s) + s_g^2 \right] \tag{2.12}$$

where $N$ the number of spectral channels, and the other variables are as given in Equation 2.10. This method assumes the data are Gaussian distributed, and that each data point is independent of the others. It is also quite computationally expensive, since $s_g^2$ must be re-evaluated for each new forward model tested. The method of Brogi & Line (2019) has been successfully implemented to retrieve abundance measurements from high-resolution observations (see e.g., Brogi et al., 2023; Gandhi et al., 2022; Boucher et al., 2023).

### 2.3.6 Current status of the field

The field of high-resolution spectroscopy has been developed extensively since 2010, both in theoretical and observational work. Fig. 2.12 displays a summary of detections using high-resolution spectroscopy, and includes an insert of the cumulative number of detections over the years (for an updated figure, see Savel et al. 2022). Many of these chemical detections have been corroborated by low-resolution observations. Brogi et al. (2017) proposed the benefits of combining low- and high-resolution observations, and there have since been a number of studies which have demonstrated joint low-/high-resolution retrievals in practice (Boucher et al., 2023; Wang et al., 2023).

The community is fortunate to have access to a plethora of quality high-resolution spectrographs with which to attempt exoplanet observations. Current operational instruments are listed in Table 2.1. High-resolution optical spectrographs such as

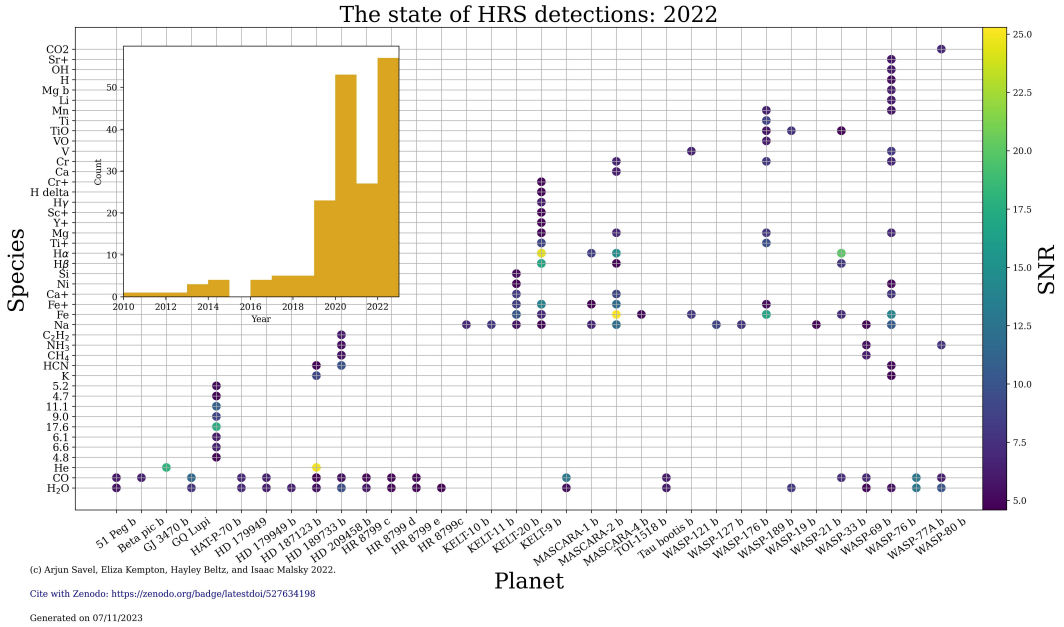


**Figure 2.12:** A summary of the exoplanet atmosphere detections using high-resolution spectroscopy. For each planet, the species detected are indicated by coloured circles, where colour marks the signal-to-noise of the reported detection. Inserted is the cumulative number of detections over the years. Figure credit to Savel et al. (2022).

ESPRESSO and HARPS are particularly good for detection of atomic species (see e.g., Pelletier et al., 2023). In the nIR, CARMENES, CRIRES+ and SPIROU offer wavelength coverage amenable to absorption features by the main carbon- and oxygen-bearing species (Webb et al., 2022; Yan et al., 2023; Pelletier et al., 2021). A visiting instrument on Gemini South, IGRINS has recently been successfully used to observe the emission spectra of hot Jupiters (Line et al., 2021; Brogi et al., 2023).

In the past four years, since commencing this thesis research, the field of high-resolution spectroscopy has advanced further still, thanks to these instruments. Recent HRCCS studies have achieved measurements of chemical abundances with precisions down to 0.1 dex for hot Jupiters (Line et al., 2021; Brogi et al., 2023). Giacobbe et al. (2021) used TNG/GIANO-B to detect five carbon- and nitrogen-bearing molecules, and successfully constrain the C/O ratio of the canonical hot Jupiter HD 209809 b. Ultra-hot Jupiters, with dayside temperature exceeding 2000 K, have yielded detections of atomic and even ionised metals (Prinoth et al., 2022; Pelletier et al., 2023). Focused study of ultra-hot Jupiters has also led to distinct of

different limb contributions (e.g., Ehrenreich et al., 2020), enabling the observational validation of the 3-D nature of exoplanets (Beltz et al., 2022, 2023). Towards a completely distinct population of exoplanets, we are starting to see successful high-resolution spectroscopy of directly imaged planets, such as HR 8799 c (Wang et al., 2023). To that end, direct imaging is well suited to detect young planets at larger orbital periods, thanks to their residual internal heat radiation. To date, atmospheric detections of young planets with high-resolution spectroscopy have been limited to the directly imaged population, due to the challenges associated with young stars (e.g., Palle et al., 2020). Cooler, smaller planets are more challenging to characterise with high-resolution spectroscopy; despite efforts, atmospheric detections mostly remain tentative or elusive (Orell-Miquel et al., 2022; Ridden-Harper et al., 2023).

In the imminent future, with current instruments and in preparation for the ELTs in the pipeline, there are a number of outstanding challenges in high-resolution spectroscopy which we should try to resolve. On the atmospheric modelling side, we must ensure the line lists we employ are accurate. Depending on the line lists used (e.g., HITEMP[3], EXOMOL[4]), the spectral line positions in the template can vary, which leads to differing cross-correlation results. We must understand these differences and form a universal agreement. Regarding data treatment, telluric and stellar removal becomes ever more crucial for slowly shifting planets. As we search for atmospheres around smaller planets, current detection sensitivity pushes us to smaller stars, giving rise to the so-called 'M dwarf opportunity'. Currie et al. (2023) found that the ELTs should be sensitive to $CO_2$ and $CH_4$, and maybe even $H_2O$ and $O_2$, in the atmospheres of terrestrial planets around M dwarfs. However, M-dwarf stars present inherent challenges by way of activity, rotation effects and centre-to-limb variations. We must be careful to understand the impact of these on atmospheric studies and use appropriate detrending to remove their effects.

In this thesis, I address some of these and other limiting factors in high-resolution spectroscopy.

[3] https://hitran.org/hitemp/
[4] https://www.exomol.com/data/

*Assumptions are dangerous things to make, and like all dangerous things to make – bombs, for instance, or strawberry shortcake – if you make even the tiniest mistake you can find yourself in terrible trouble.*

— Lemony Snicket, *A Series of Unfortunate Events: The Austere Academy, 2000*

# CHAPTER 3

# OBSERVING YOUNG ATMOSPHERES AT HIGH RESOLUTION

## Contents


**3.1 Introduction and motivation . . . . . 48**
3.1.1 Context . . . . . 48
3.1.2 The young sub-Neptune AU Mic b . . . . . 51
**3.2 The observations . . . . . 54**
**3.3 Data reduction . . . . . 56**
3.3.1 Blaze correction, normalisation and alignment . . . . . 56
3.3.2 Telluric and stellar spectrum removal . . . . . 58
**3.4 The search for atmospheric molecules . . . . . 61**
3.4.1 Atmospheric modelling . . . . . 61
3.4.2 Cross-correlation with real data . . . . . 64
3.4.3 Injection and recovery tests . . . . . 65
**3.5 An active star . . . . . 73**
3.5.1 Checking for signatures of stellar flares . . . . . 74
3.5.2 Stellar spots . . . . . 77
3.5.3 Assessing the Rossiter-McLaughlin Effect . . . . . 80
**3.6 Alternative atmospheres . . . . . 84**
3.6.1 Impact of flare events on atmospheric composition . . . 84
3.6.2 Cloudy atmospheres and disequilibrium chemistry . . . 85

**3.7 Future work** . . . . . **86**
3.7.1 Future observations of AU Mic b . . . . . 86
3.7.2 Atmospheric retrievals . . . . . 88
**3.8 Conclusions** . . . . . **89**

---

The data for this chapter was contributed by the ATMOSPHERIX consortium, and I contributed the analysis of the data. I led the interpretation of the results, with input from the collaboration.

## 3.1 Introduction and motivation

### 3.1.1 Context

Though the sub-Neptune population of planets is currently thought to be the most numerous (Borucki et al., 2011; Batalha et al., 2013), there are significantly fewer atmospheric detections for this class. There are a few possible reasons for this. The dearth of hot Neptunes (see, Mazeh et al., 2016) means that the majority of detected Neptunes are cooler than their hot Jupiter counterparts, leading to smaller scale heights and hence smaller atmospheric transmission signals (Equation 2.3). Secondly, these cooler Neptunes orbit further from their star. Crucially for the high-resolution cross-correlation technique, this means their radial velocity trail is slower, making it harder to distinguish from the stationary stellar and telluric signals. Cooler temperatures also increase the likelihood of condensate clouds. A number of space-based low-resolution observations of Neptunes have been published, with the majority presenting flat, featureless spectra (e.g., Kreidberg et al., 2013; Knutson et al., 2014). Clouds in the upper atmospheres have been the hypothesised cause, since they would act to suppress broad-band molecular features. In this regard, high-resolution spectroscopy may help to combat the obscurity of atmospheric aerosols (see §2.3.4).

There are a number of motives fuelling the study of young sub-Neptunes in particular. Stastistical analysis of the KEPLER sample has revealed that the small planet population is bifurcated into two size classes, the so-called 'sub-Neptunes' and 'super-Earths' (see Fig. 3.1 and Fulton et al., 2017; Van Eylen et al., 2018).

The **small planet radius valley**, otherwise known as the 'evaporation valley', was predicted prior to the observational confirmation (Owen & Wu, 2013; Lopez & Fortney, 2013), as a consequence of evolutionary mechanisms, whereby sub-Neptune planets lose their extended envelopes through atmospheric escape. They consequently morph into remnant, stripped cores. Advocating for this theory, the detection of a clear, distinct valley suggests that the core compositions of the two classes are the same; distinct core compositions would act to smear out the radius gap (Owen & Wu, 2017). Analysis of the slope of the radius valley has largely ruled out an opposing theory of gas-poor formation, wherein super-Earths form post dispersal of protoplanetary disk, thus making them a completely separate, inherently rocky population to the sub-Neptunes (Van Eylen et al., 2018). On the other hand, evaluating the slope distinctly in the case of red dwarf host stars, Cloutier & Menou (2020) uncovered a slope with an inverse gradient compared to that of Sun-like stars. This may be indicative of a different formation scenario, or alternatively, inefficient atmospheric mass loss for planets around smaller stars. All in all, the understanding of the small planet radius valley is far from complete.

There are two leading theories for the principal drivers of the radius valley-inducing atmospheric mass loss: photo-evaporation, which is driven by the X-ray and UV (XUV) irradiation of the host star, and core-powered mass loss, wherein the residual intrinsic interior energy powers a cooling luminosity to radiate away the atmosphere (Owen & Wu, 2017; Owen & Schlichting, 2023; Gupta & Schlichting, 2019). Further study separating the sample of small planets into age categories shows that the 'super-Earth' class is comparably underpopulated at young ages, and grows over time, as shown in Fig. 3.1. This would support the hypothesis that it is an evolutionary rather than a formation process which shapes the bimodal distribution. Young planets at the upper boundary of the small planet radius valley, and similarly the hot Neptune desert, are expected to be experiencing ongoing atmospheric loss. Core-powered mass loss and photo-evaporation are predicted to operate on different timescales. Photo-evaporation is thought to be more dominant in the first 100 Myr of the star's lifetime, when its XUV radiation is at a maximum,

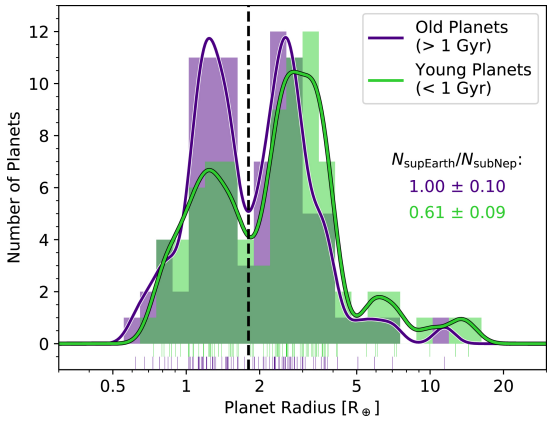


**Figure 3.1:** The bimodality of the size distribution of small planets changes with time. Figure from Berger et al. (2020).

while core-powered mass loss tends to work over longer, about 1 Gyr timescales (Berger et al., 2020; Owen & Wu, 2017). Not only do we gain insight into the early planetary lifetime, but by sampling planets across these crucial ages, we can directly probe early evolutionary mechanisms and consequent impact on the atmosphere.

The formation history of a planet is encoded in its atmospheric makeup (see §2.1.2). In particular, the C/O ratio is an important parameter to constrain, and can be measured with HRCCS by quantifying key carbon and oxygen-bearing molecules. Though the formation pathways of Neptune-sized planets are thought to be similar to their hot Jupiter counterparts, they are less well constrained. For hot Neptunes, formation at current day location has not been ruled out (Batygin et al., 2016); in this scenario we would expect to observe a low C/O ($< 0.5$), characteristic of the composition of the former protoplanetary disk at this location. Alternatively, formation at further distances and subsequent migration would lead to higher present day C/O (Madhusudhan et al., 2014; Rogers et al., 2011). The presence of the radius gap is suggestive of in situ formation for these smaller planets; if they formed beyond the main snowlines, we would expect accretion of large amounts of volatile ices (Van Eylen et al., 2018). On the other hand, any enrichment due to e.g., infalling planetesimals has a proportionately larger impact on the metallicity of the atmosphere, less extended than those of the hot Jupiter population (Crossfield & Kreidberg, 2017). Young planets offer a unique, closer insight into formation history,

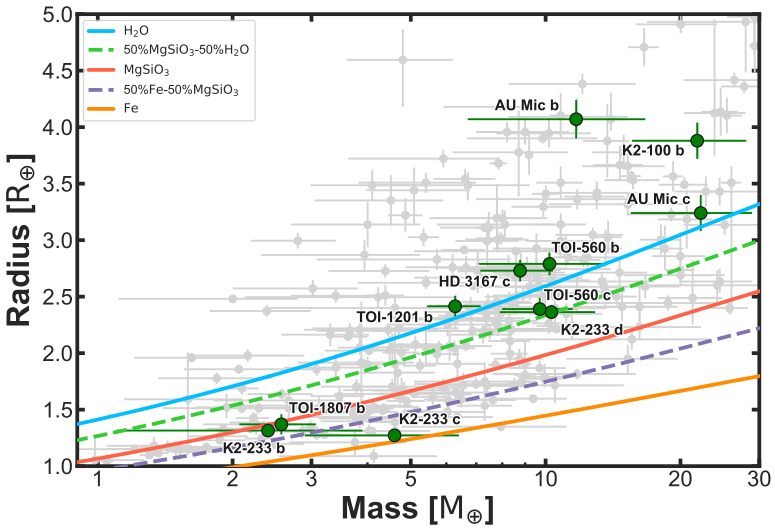


**Figure 3.2:** The AU Mic planets in context: population of exoplanets with both a mass and a radius measurement (grey), with a few young planets highlighted. Overplotted are a few bulk composition density lines, including pure $H_2O$ and pure Fe. Figure adapted from Barragán et al. (2023).

as their atmospheres are more likely to closely match primordial composition, and less likely to have experienced contamination processes and impact.

### 3.1.2 The young sub-Neptune AU Mic b

AU Mic is one of the brightest M stars in the Southern sky, with a V-band magnitude of 8.6[1]. It is a young star, at an estimated age of 22 Myr; contrary to many stars, its age is known precisely because AU Mic is a member of the Beta Pic moving group (Messina et al., 2016; Mamajek & Bell, 2014; Malo et al., 2014). In 2020, Plavchan et al. (2020) detected one transiting planet (b) in the AU Mic system, in the *TESS* lightcurves. A second, outer transiting planet (c) was detected by Martioli et al. (2021). There has been a collection of intensive follow-up studies seeking to further characterise the two planets in the system (e.g., Martioli et al., 2020; Zicher et al., 2022; Klein et al., 2022; Szabó et al., 2022; Gilbert et al., 2022; Rockcliffe et al., 2023).

At time of writing, we have a sample of only a few dozen young systems with planets which have precise radius and mass measurements, some of which are shown in Fig. 3.2. Young stars are notoriously unruly, with strong magnetic fields

[1] http://simbad.u-strasbg.fr/simbad/sim-basic?Ident=au+mic

(∼kG) and rapid rotation rates (Donati et al., 2014; Johns-Krull & Valenti, 1996). These provoke magnetic activity phenomena, such as stellar heterogeneities in the photosphere and chromosphere, and flaring events, all of which have hampered detections of orbiting planets. Transit and radial velocity (RV) measurements thus require careful disentangling of stellar activity signals present in the data. Advances in the modelling of transit and RV data have managed to push the detection floor down to smaller planets around young stars, namely the use of Gaussian process regression to disentangle stellar activity signals from that induced by the planet (see e.g., Barragán et al., 2019, 2022).

The story of AU Mic has developed since those first detections. Zicher et al. (2022) performed an intensive radial velocity follow-up campaign with ESO 3.6 m/HARPS to accurately measure the masses of the two Neptunes in the AU Mic system. They implemented a GP framework to measure the masses of planet b and c to $11.7 \pm 5.0$ and $22.2 \pm 6.7\,M_\oplus$ respectively. There have also been mass constraints from transit timing variation (TTV) detections: Wittrock et al. (2022) reported a mass for planet c of $10.8^{+2.3}_{-2.2}\,M_\oplus$. Some claims have been made towards a third planet in the system, exterior to the other two at a 33 day orbit (planet e, Donati et al., 2023) and even between them (planet d, Wittrock et al., 2023). Additional observations are needed to validate the existence of the candidates planets d and e. I summarise the published mass and radii of the planets in the AU Mic system in Table 3.1.

These precise mass and radius measurements have paved the way for atmospheric characterisation. The proximity ($9.72 \pm 0.04$ pc, Gaia Collaboration et al., 2018) of the system and favourable planet-to-star radius ratio of both Neptune-sized planets make them excellent targets for transmission spectroscopy. Indeed, they both have high Transmission Spectroscopy Metrics (TSMs, see Equation 2.8 and Kempton et al., 2018). At time of writing, there has been no claim of detection of the high-resolution transmission spectrum of any young planet ($< 1$ Gyr, see Fig. 3.3). For stringent constraints on atmospheric forward models, precise measurements of both mass *and* radius are necessary.

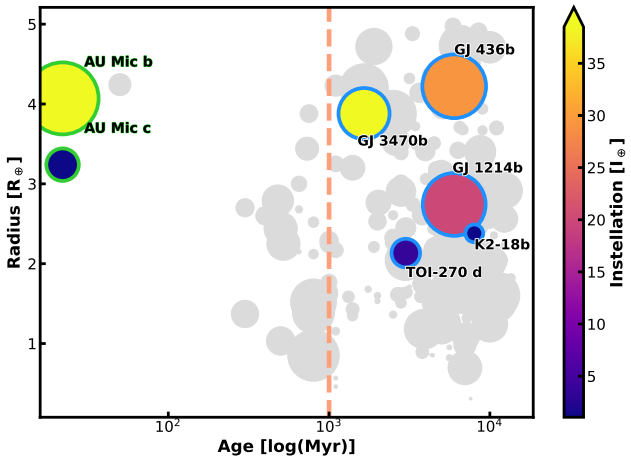


**Figure 3.3:** The age distribution of well characterised planets, with some sub-Neptunes highlighted in blue whose transmission spectra have been observed. The AU Mic planets are highlighted in green, at an age in stark contrast to those previously studied. The data points are coloured according to their experienced instellation, relative to Earth's insolation, and sized according to their TSM (Kempton et al., 2018).

**AU Mic b** is the inner of the two confirmed, Neptune-sized planets orbiting the young, M1V star AU Mic. Various follow-up observations of AU Mic b have sought to characterise the planet further. Martioli et al. (2020) measured the planet's obliquity, the angle between the planet spin axis and stellar spin axis, deducing AU Mic b to be well-aligned (see also, Addison et al., 2021; Palle et al., 2020; Hirano et al., 2020). Then, using far-UV *HST* observations of AU Mic, Feinstein et al. (2022) inferred that the activity of the host star is likely to induce a mass loss rate of $10^8\,\mathrm{g\,s^{-1}}$ for planet b. More recently, Rockcliffe et al. (2023) detected atmospheric escape in one *HST* Ly-$\alpha$ transit, but reported a non-detection in a second transit. They proposed that the time variability could be a result of photo-ionisation of the escaping hydrogen, due to a stellar flare event. Other than this hydrogen detection, the further atmospheric make-up of AU Mic b has not yet been measured, despite a number of attempts (see Palle et al., 2020). In Fig. 3.3, I show the AU Mic planets in age-radius space, where the size of the data points has been scaled according to the TSM. Of the young sub-Neptunes with well characterised mass and radius, AU Mic b has the highest TSM. It therefore currently offers the best opportunity to observe a young planet atmosphere, closest to its time of formation.

**Table 3.1:** The collection of published mass and radius measurements of the planets in the AU Mic system.

| Mass of planet b | Technique | Reference |
|---|---|---|
| $20.12^{+1.57}_{-1.72}\,M_\oplus$ | RVs and GPs | Cale et al. (2021) |
| $17.1^{+4.7}_{-4.5}\,M_\oplus$ | Doppler imaging | Klein et al. (2021) |
| $11.7 \pm 5.0\,M_\oplus$ | RVs and GPs | Zicher et al. (2022) |
| $10.2^{+3.9}_{-2.7}\,M_\oplus$ | RVs and Doppler imaging | Donati et al. (2023) |
| **Mass of planet c** | | |
| $9.60^{+2.07}_{-2.31}\,M_\oplus$ | RVs and GPs | Cale et al. (2021) |
| $10.8^{+2.3}_{-2.2}\,M_\oplus$ | TTVs | Wittrock et al. (2022) |
| $22.2 \pm 6.7\,M_\oplus$ | RVs and GPs | Zicher et al. (2022) |
| $14.2^{+4.8}_{-3.5}\,M_\oplus$ | RVs and Doppler imaging | Donati et al. (2023) |
| **Radius of planet b** | | |
| $4.20 \pm 0.20\,R_\oplus$ | Transit photometry | Plavchan et al. (2020) |
| $4.07 \pm 0.17\,R_\oplus$ | Transit spectroscopy RM | Martioli et al. (2021) |
| $4.36 \pm 0.18\,R_\oplus$ | Transit photometry | Szabó et al. (2021) |
| $4.19^{+0.24}_{-0.22}\,R_\oplus$ | Transit photometry | Gilbert et al. (2022) |
| $3.55 \pm 0.13\,R_\oplus$ | Transit photometry | Szabó et al. (2022) |
| **Radius of planet c** | | |
| $3.24 \pm 0.16\,R_\oplus$ | Transit spectroscopy RM | Martioli et al. (2021) |
| $2.79^{+0.31}_{-0.30}\,R_\oplus$ | Transit photometry | Gilbert et al. (2022) |
| $2.56 \pm 0.12\,R_\oplus$ | Transit photometry | Szabó et al. (2022) |

In this chapter, I present work aiming to place constraints on the atmospheric composition of the young sub-Neptune AU Mic b, using high-resolution, ground-based transmission spectroscopy. The contents of this chapter are mostly based on the publication Meech et al. 2023 (submitted).

## 3.2 The observations

We analysed high-resolution spectra of AU Mic, observed with IGRINS on Gemini South and SPIROU on the CFHT, acquired as part of the ATMOSPHERIX program and SPIROU Legacy Survey. Both spectroscopic observations captured a transit of the inner planet b. The IGRINS time-series was obtained on the 18th December 2021 (program ID: GS-2021B-Q-135, PI: Florian Debras). For the purposes of high-resolution cross correlation spectroscopy with échelle spectrographs, a standard

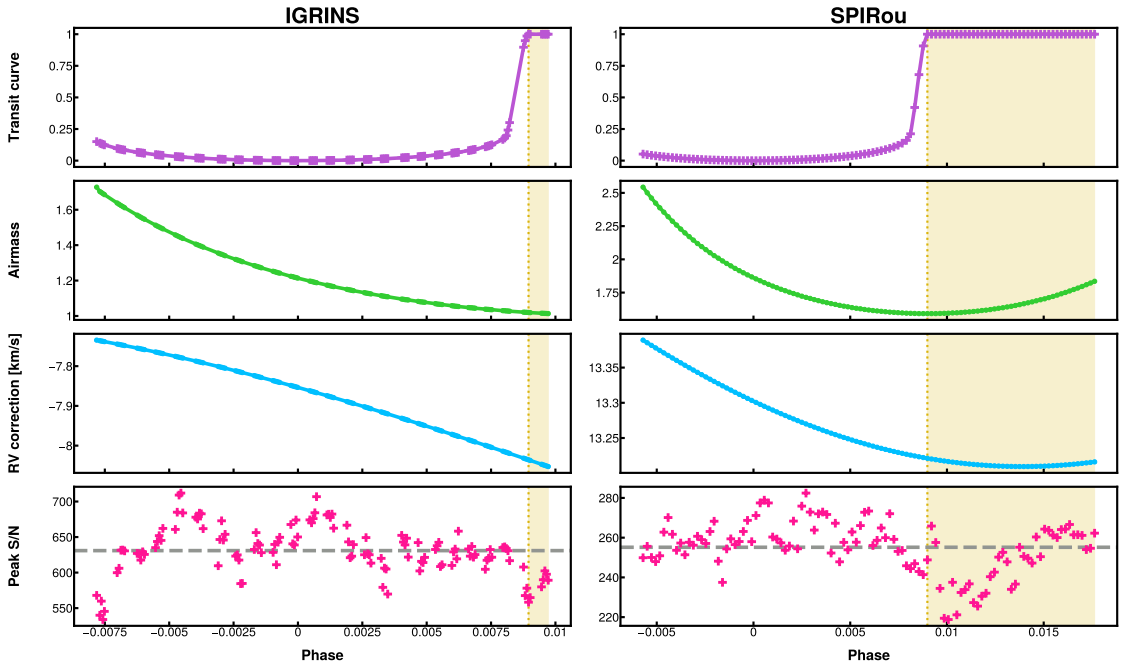


**Figure 3.4:** The IGRINS and SPIROU observations: with panels from the top **(i)** the simulated transit light curve using BATMAN, **(ii)** measured airmass over the course of the observation, **(iii)** the barycentric radial velocity correction and **(iv)** the average SNR across all orders. The yellow shaded regions indicate out-of-transit frames.

observing technique is to nod along the slit in an ABBA pattern in order to remove the background. With the IGRINS observations, an AAAAABBBBB nodding pattern was used to balance the overheads and exposure time of such a bright target, considering the 8.1 m aperture of Gemini South. I used the IGRINS pipeline data products (Sim et al., 2014). I combined each A frame with the corresponding B frame in the subsequent group of 5, to produce one 'exposure'. Thus, the output was 118 in-transit 'exposures', and 7 out-of-transit. The corresponding humidity, airmass and phases were averaged across the collated AB pair. The SPIROU data were acquired through the CFHT large program, ID 19AP42, as part of the SPIROU Legacy Survey (SLS, PI: Jean-François Donati), on 16th June 2019. These consisted of 75 in-transit frames, and 41 out-of-transit frames. Due to low S/N, I removed the first 7 in-transit spectra for our analyses, with a remaining 68 in-transit frames. These data were published as part of a Rossiter-Mclaughlin analysis in Martioli et al. (2020), who measured the sky-projected obliquity of AU Mic b to be $0^{+18}_{-15}$ degs, which would be consistent with an aligned orbit.

**Table 3.2:** Ancillary information concerning the IGRINS and SPIROU transit observations of AU Mic b.

| Instrument | Date | Phases Observed | Mid-transit time [JD] |
|---|---|---|---|
| **SPIRou** | $16-06-2019$ | $[-0.006, +0.018]$ | 2458651.9845 |
| **IGRINS** | $04-08-2021$ | $[-0.0078, +0.00972]$ | 2459430.5805 |
| | **Airmass mid-transit** | **Exposure time [s]** | **No. of frames [in/out]** |
| **SPIRou** | 1.868 | 122.6 | 68/41 |
| **IGRINS** | 1.214 | $5.0-20.0$ | 118/7 |

A number of characteristic properties of the two transits are shown in Fig. 3.4, and additional information in Table 3.2. Unfortunately, neither captured ingress. Nevertheless, I proceeded to see what we could extract from these data.

## 3.3 Data reduction

Both datasets were processed preliminarily with their corresponding instrumental pipelines. The SPIROU data were processed with the APERO pipeline (Cook et al., 2022), which performs an initial telluric correction via the TAPAS algorithm (Bertaux et al., 2014). The IGRINS data were similarly pre-processed with the public PLP pipeline (Sim et al., 2014). Though this pipeline performs a bad pixel correction, alignment and wavelength calibration, it does not attempt to model and/or remove tellurics. Here I detail the further corrections applied to the data. Beginning with the data products output from the respective pipelines, I applied a data reduction routine adapted from that detailed in Klein et al. (2023), a work published as part of the ATMOSPHERIX program. I perform the reduction on an order-by-order basis.

### 3.3.1 Blaze correction, normalisation and alignment

The 'raw' (by which here I mean pre-processed) spectral data products from both pipelines displayed the imprint of the instrumental blaze function; example orders are shown in the top panel of Fig. 3.5. I thus began by removing this blaze function imprinted onto the spectra. I iteratively fit a high order polynomial to each spectrum in turn, excluding data points below a given threshold level in order to locate the continuum rather than the spectral absorption features.

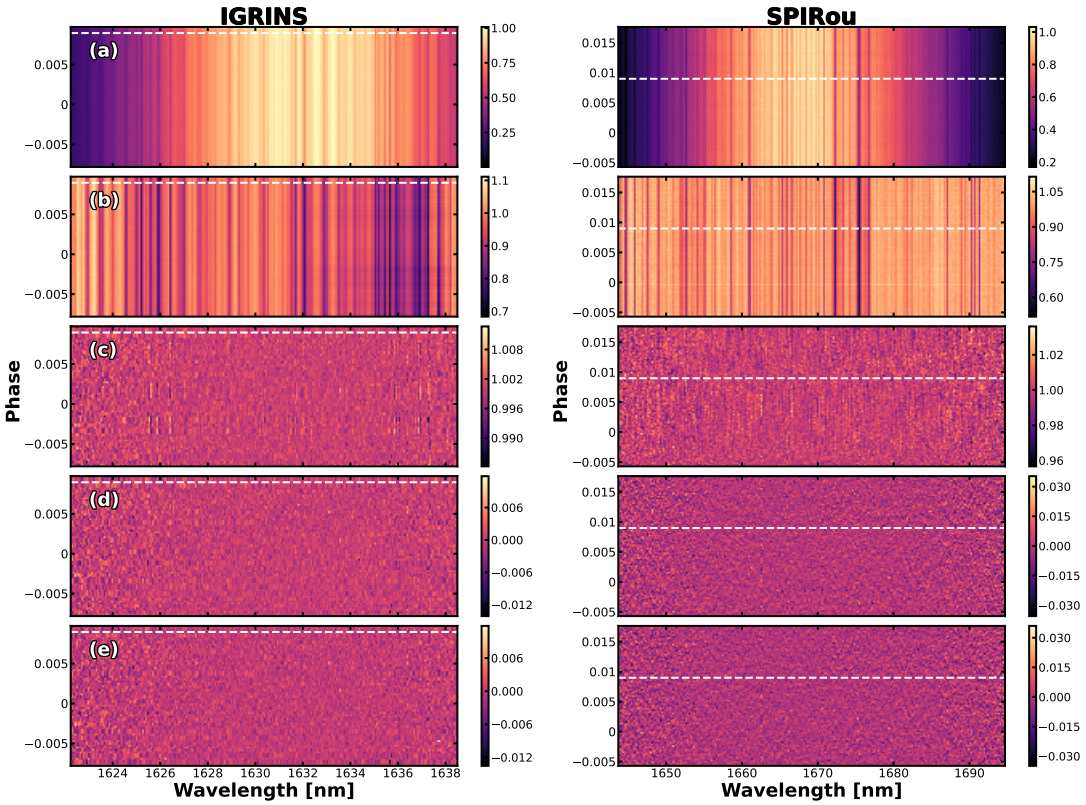


**Figure 3.5:** Successive data reduction method shown for exemplar order 15 for IGRINS **(left)** and order 33 with SPIRou **(right)**. In each panel, time is on the y-axis, so each row is an individual spectrum, where colour indicates the flux level. The triangle marker on the y-axes indicate the phase of egress. **Panel (a)** shows the extracted data products from each instrumental pipeline, having divided through by the maximum flux in each spectrum. Then, the blaze-corrected and normalised spectra are shown in **panel (b)**. In **panel (c)**, I show the result having detrended out the airmass trend, and **panel (d)** post PCA processing. The last panel, **panel (e)**, shows the end result of the detrending process, having sampled residuals at locations of strong telluric lines.

Interestingly, I observed that some of the spectral lines of the IGRINS pipeline-corrected fluxes were not well aligned, particularly in the redder orders. It did not seem to be a global shift but rather an abrupt stretching of the wavelength solution at the 62nd frame. This was apparent when looking in individual lines, and I demonstrate for example wavelengths the change in flux in Fig. 3.6. The change in flux shown is the flux in the line at each frame having subtracted the mean flux from the first 62 frames; the abrupt shift is apparent, since we would expect the change in flux to be homogeneous if the spectra were well aligned. The spectra must be correctly aligned for the remainder of the data reduction. I attempted an

alignment of the 'raw' spectra: I choose the highest signal-to-noise spectrum of the first 62 frames, $\mathcal{S}_1$. For each frame, I apply a stretch and shift to the wavelength solution, interpolate the spectrum back to the original wavelength solution before comparing to the reference spectrum $\mathcal{S}_1$. With least-squares minimisation I optimise the scaling parameters, and interpolate the spectra to the corresponding new wavelength solution. The resulting change in flux post alignment are shown in green in Fig. 3.6. I found that applying the blaze correction (and additional normalisation step) beforehand achieved a much cleaner alignment, shown in blue. Since this alignment routine introduces interpolation noise, I identified the orders that were truly in need of aligning, with typical wavelength shifts ranging from 0.29–0.35 nm. I applied this step only to orders redder than order 47 in the IGRINS data.

Then, I remove a first pass at the static spectrum by dividing out the median spectrum, in the Earth/stellar rest frame first in the case of IGRINS/SPIROU spectra, given the dominant contamination for these. As standard for high-resolution cross-correlation analyses, I continuum-normalise each spectrum to correct for varying throughput. This removes broad-band continuum information. I apply a basic bad pixel correction, via sigma clipping. Examples of the spectra following these steps are shown in panel (b) of Fig. 3.5.

### 3.3.2 Telluric and stellar spectrum removal

The subsequent steps are similar to that detailed in Klein et al. (2023). A dominant contaminator in the near-infrared, the telluric spectrum is far from constant in time. Its exact time-variation is difficult to parameterise, and is wavelength-dependent. That said, we know tellurics to vary exponentially with airmass (Allart et al., 2022). I therefore remove this airmass variation directly. Since the airmass variation is linear in log space, I fit an $n$-degree polynomial to the log of the residual fluxes from panel (b) (Fig. 3.5). Testing the degree of polynomial, I found $n = 2$ to be most effective at suppressing telluric contamination. Again, the resulting spectra are shown in Fig. 3.5, panel (c).

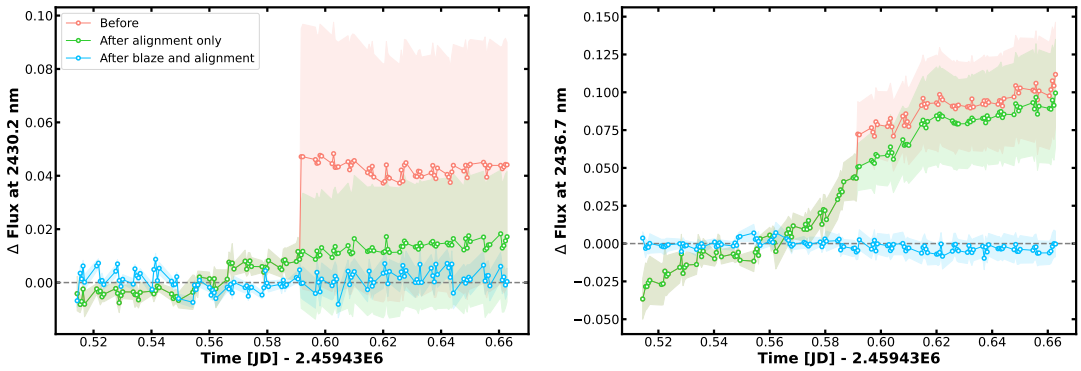


**Figure 3.6:** Investigating the alignment of spectral lines in the IGRINS data in order 49. The change in flux shown is the difference between the flux in each line and the mean flux from the first 62 frames, prior to the wavelength shift. In the flux channels corresponding to wavelengths **left:** 2430.2 nm and **right:** 2436.7 nm, the differential flux is measured in the pipeline spectra (red), after applying the alignment routine to the pipeline spectra (green) and after applying a blaze correction, normalisation and alignment routine (blue). The shaded regions correspond to the standard deviation of the change in flux in a 10 pixel window around the line.

To attempt to conquer the residual time-variability, I applied Principal Component Analysis (PCA). This is a popular algorithm for battling tellurics in high-resolution analyses (see e.g., Line et al., 2021). A noted challenge with using PCA is deducing the optimal number of components to remove; one would wish to remove as much static (in wavelength) contamination as possible, while preserving the Doppler-shifting planetary spectrum (see §2.3.2). In reality, given the finite, discrete resolution of the spectrograph and time sampling, the planet spectrum will experience sub-pixel shifts. Once the PCA algorithm has identified and removed the telluric and stellar residuals, it will begin to remove the planet-induced common modes, thus degrading the planetary signal. This has been commented upon in the literature as an issue, and template-matching methods now include a synonymous degrading of the model template in order to account for the detrending process. However, it's clearly not optimal to degrade the planetary signal. A standard method in the literature involves an injection of the model template, prior to reduction (and PCA application), and then observing the recovered signal-to-noise of the injected model as a function of PCA components removed. The 'optimal' number of components is then taken to be that which recovers the highest signal-to-noise in

the cross-correlation. This method is model-dependent, and subject to the spurious, poorly understood noise features in cross-correlation space. Cheverall et al. (2023) explore in more detail the issues with such an optimisation. They found that it can even artifically increase the detection significance, leading to false positives (see also Cabot et al., 2019). Klein et al. (2023) developed a novel PCA-tuning method, applying it to SPIROU data. I adopt this method; I construct a white noise map for each order, with the residual noise properties of the current status fluxes. I amplify each map by the order-specific instrumental blaze function, to account for the increased noise at order edges. Then, deconstructing each map with PCA into its eigenvalues and vectors, I store the highest eigenvalue, henceforth $e_{\mathrm{T}}$. For each order, I average $e_{\mathrm{T}}$ over several noise realisations. Since this eigenvalue should account for the dominant noise contribution, I apply this as a threshold level to the real data: any components with eigenvalues higher than $e_{\mathrm{T}}$ are removed. I also tested this method following a planetary model injection, and found it reported a very similar $e_{\mathrm{T}}$. The advantage of this tuning method over the standard aforementioned approach is the independence with model selection. The result having applied PCA is shown in panel (d) of Fig. 3.5.

As a final cleaning step, I sampled the pixel channels of known strong telluric lines. Using an ESO SKYCALC[2] (Noll et al., 2012) telluric model as a reference, I identified the strong telluric absorption lines for each order. Within a 3 pixel-wide window, I fit a low-order polynomial to the residuals in each marked line, to model the remaining residual temporal variation. I then combine these polynomials and remove the resulting trend from the entire spectral matrix. This suppressed the rms of the residuals by an average factor of 0.2 and 0.017 for the IGRINS and SPIROU spectra respectively; see Appendix A. The resulting final cleaned spectra are shown in panel (e) of Fig. 3.5, after which I masked any remaining spurious pixel channels. I refer the reader to Appendix A, §A.1 for more details on the data reduction diagnostics.

[2] https://www.eso.org/observing/etc/doc/skycalc/helpskycalc.html

## 3.4 The search for atmospheric molecules

Having reduced the spectra, we would expect them to consist predominantly of noise and a buried, Doppler-shifting planetary signal. In order to extract the transmission spectrum of the planet, I employ the high-resolution cross-correlation spectroscopy (HRCCS) technique. For this I require a set of forward-modelled planetary spectra, the modelling of which is next discussed.

### 3.4.1 Atmospheric modelling

To approximate the expected spectrum of AU Mic b I leverage the radiative transfer package PETITRADTRANS Mollière et al. (2019). I employ the open-source code FASTCHEM to calculate the relative abundances of each species. FASTCHEM is a radiative transfer code which accepts as input a P-T profile and elemental abundances, and outputs the self-consistent volume mixing ratios (VMRs) of the sought species, as a function of pressure (Stock et al., 2018). For the first set of models, I assume chemical equilibrium with a $H_2$/He-dominated chemistry, a standard starting assumption for analysis of exoplanet atmospheres. The temperature structure is fixed to the analytic model of Guillot (2010); I compute the P-T profile based on an equilibrium temperature of 593 K and an internal temperature of 200 K. I use an estimate for the internal temperature, considering the cooling curve relations presented in Linder et al. (2019). Then, the chemical abundances are are evaluated at each of a defined set of 130 equally spaced (in log-pressure) atmospheric layers, for a set of pressures ranging from $10^{-10}$ to $10^{2}$ bar with FASTCHEM. I produce models for a range of metallicities and C/O ratio, as given in Table 3.3, recomputing the equilibrium chemistry in each case. The metallicity scales all of the elemental abundances except hydrogen and helium, while the C/O is set by scaling the oxygen abundance (Mollière et al., 2015). The metallicities chosen are consistent with the mass-metallicity relation of Welbanks et al. (2019), considering the mass measurement of AU Mic b published by Zicher et al. (2022). Fig. 3.7 displays some of the output profiles from FASTCHEM. Using these abundances, I produce two sets of models:

| Parameter | Value |
|---|---|
| Chemical species | $H_2O$, $CO_2$, CO, $CH_4$, $NH_3$ |
| Metallicites [w.r.t. solar] | 1–100× |
| C/O ratio | 0.2–1.5 |

**Table 3.3:** Parameters for the forward modelling of AU Mic b, for the set of chemical equilibrium models.

- Full chemistry models: absorbing species listed in Table 3.3 [3] at the FASTCHEM abundances, embedded in $H_2$/He background gas.
- Single-specie models: $H_2$/He background gas with one extra absorbing molecule, at the abundances from the full chemistry FASTCHEM output. We produce one of these for each species listed in Table 3.3.

For each of these, I include the impact of Rayleigh scattering due to species $H_2$, He and $N_2$ and collision-induced absorption (CIA) by $H_2$-$H_2$, $H_2$-He, and $N_2$-$N_2$. Also consistent across all of the models is the selected line list for each species: I employ HITEMP for $H_2O$, $CO_2$ and CO (Rothman et al., 2010), and EXOMOL for $CH_4$ and $NH_3$. For the chemical equilibrium models, I compute clear atmospheres only.

To address the caveat of chemical equilibrium, I create a third set of single species, $s_i$, models with abundances between $\mathrm{VMR}[s_i] = 10^{-6}$ to $10^{-1}$, embedded in a solar abundance $H_2$/He background gas. Simultaneously, to constrain the range of parameter space to which we would be sensitive if there were condensate clouds in the atmosphere, I add an opaque cloud deck to the forward model. I vary the cloud deck pressure from $P_{\mathrm{cloud}} = 10^{=1}$ to $10^{-6}$ bar. Therefore, for each species I compile a set of 36 distinct forward models. The species considered are the same as those in the chemical equilibrium models (Table 3.3). These allow me to test for abundances of species which might either be absent (low abundance) at the equilibrium temperature used to derive the chemical equilibrium models, or those which would be present if there were significant disequilibrium processes occurring in the atmosphere of AU Mic b.

[3] Chosen based on previous studies of sub-Neptune atmospheres (see e.g., Moses et al., 2013; Gandhi et al., 2020)

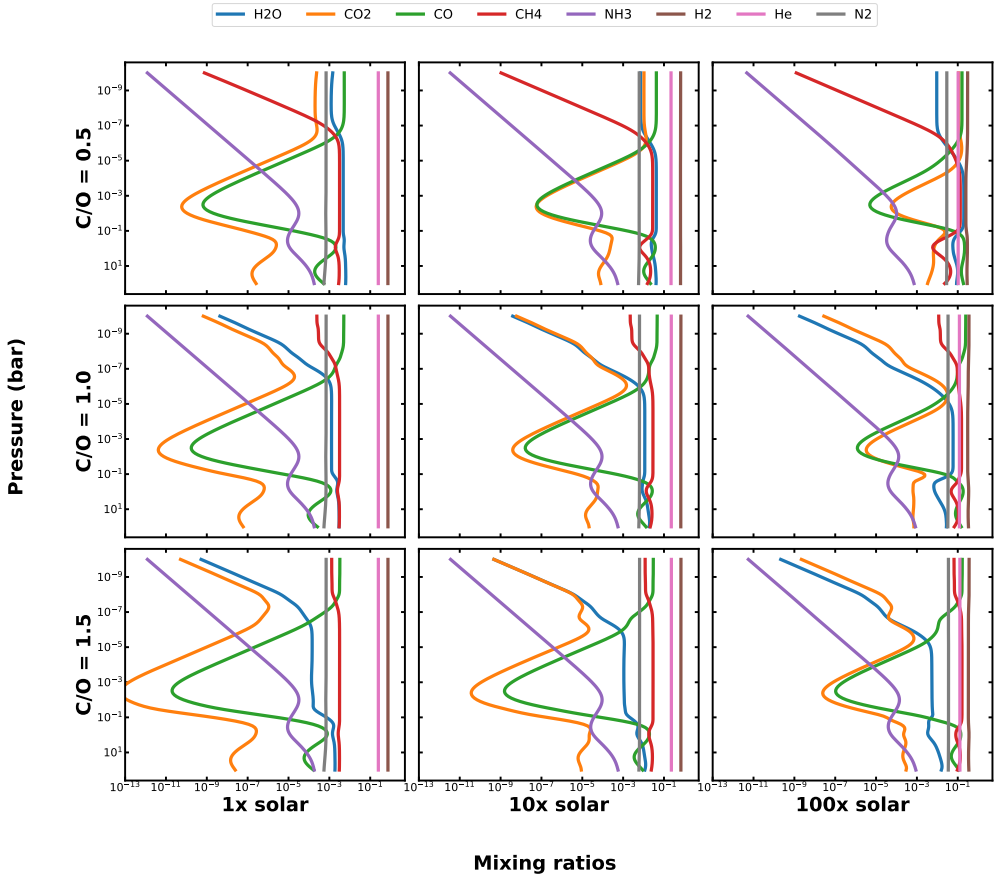


**Figure 3.7:** Abundance profiles for AU Mic b, computed for a range of metallicity and C/O with FASTCHEM. I include species $H_2O$, $CO_2$, CO, $CH_4$, and $NH_3$ for the fiducial atmospheres.

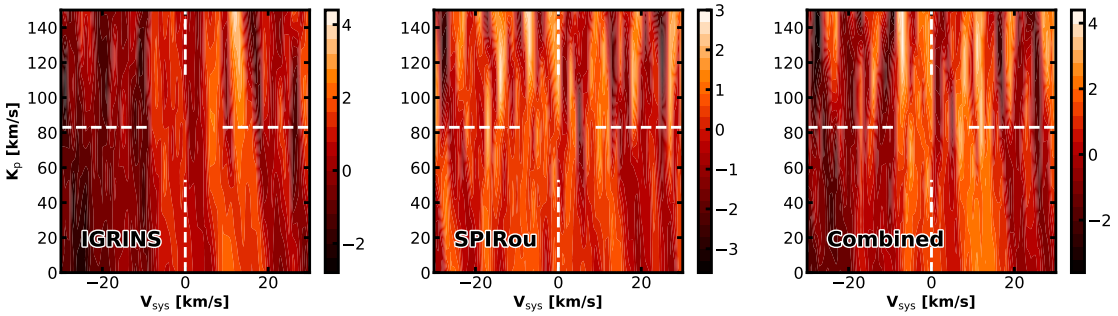


**Figure 3.8:** Velocity colour maps of cross-correlation coefficients for the IGRINS **(left)**, SPIROU **(middle)** and combined **(right)** datasets, having cross-correlated a full chemistry, self-consistent model at solar metallicity, with C/O of 1.0. The white dashed lines point towards the expected velocity location of the planet, in orbital velocity $K_p$ and systemic velocity $V_{\rm sys}$.

### 3.4.2 Cross-correlation with real data

I cross-correlate each of the models described in §3.4.1 with the reduced data spectral time-series, to attempt to detect the atmosphere of AU Mic b. The results of cross-correlating the full chemistry, self-consistent models to the real data are shown in Fig. 3.8 (at solar metallicity, and C/O of 1.0 as an example). I report non-detections in both datasets, across all models compared. These non-detections were consistent across variations of the data reduction, for different combinations of spectrograph orders (which had varying noise levels, mostly due to differing telluric contamination and instrumental systematics), and region selected to compute the standard deviation of the noise map. The next step was then to assess if the non-detection was a due to (i) insensitivity of the data to the expected atmospheric signals, either inherently or as a result of insufficient data reduction or modelling, or (ii) such atmospheric constituent molecules not being present in the atmosphere of AU Mic b at the tested abundances.

Towards ruling out scenario (i), I begin by testing the extrema of the mass and radius measurements of AU Mic b. The mass of AU Mic b in particular is not very precisely constrained. The mass estimate is only used for the forward model, and predominantly affects the scale height of the atmosphere (see Equation 2.3, Chapter 2), and thus the amplitude of the planetary spectral lines. Fig. 3.9 demonstrates the amplitude change of the self-consistent spectral model, between the basis model and implementing the lowest derived density, using the extrema of the mass and radius measurements (within the reported $1\sigma$ uncertainties). For some of the lines we observe a factor of 3 increase in the amplitude. I cross-correlate the real data with the full set of self-consistent models, reproduced for the lowest density estimate: alas no detection.

The models tested so far have considered only chemical equilibrium. Given the estimated equilibrium temperature of AU Mic b, we would expect most of the carbon to be sequestered in $CH_4$ (see Fig. 3.7). However, there exists an uncertainty on the equilibrium temperature, which could nudge AU Mic b across the theoretical boundary shown in Fig. 3.10, into the CO-dominated regime. On the

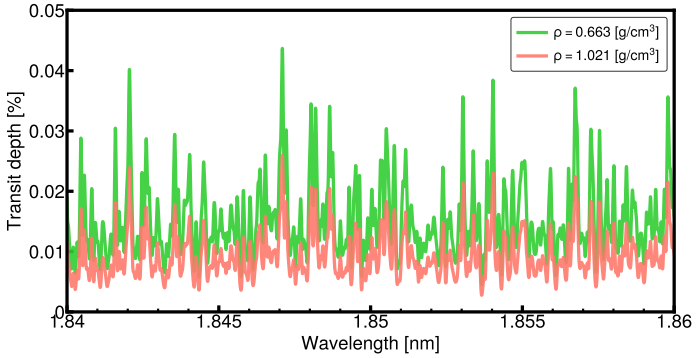


**Figure 3.9:** Effect of mass and radius measurements on the forward-modelled transmission spectrum. The pink spectrum indicates the basis model used in this work, based on the mass measurement from Zicher et al. (2022) and radius of Martioli et al. (2021). Then, the green shows that expected for the lowest density estimate consistent with the same mass and radius, within $1\sigma$.

other hand, the lack of $CH_4$ could also be a result of chemical disequilibrium processes. Therefore, as a test against these scenarios, to search for CO independently of the above assumptions, I cross-correlate the single species models with high VMR (VMR[CO] = $10^{-2}$) and no cloud deck. I used the aforementioned lowest density estimate to maximise the scale height. The forward-modelled spectrum and the cross-correlation result, from the combined datasets, are shown in Fig. 3.11. For the cross-correlation analysis, I also attempted combining only the frames known to host strong CO features. Either way, I report a null detection once again.

### 3.4.3 Injection and recovery tests

Therefore, to test the sensitivity of our data to the expected atmospheric signals of AU Mic b, I perform a series of injection and recovery tests. This involves injecting the forward-modelled atmosphere into the spectroscopic data at the pipeline-reduced stage, performing the same data reduction steps, and cross-correlating with the injected model to assess recovery-ability, knowing with certainty that such a signal exists in the data. I ran three sets of tests:

**TEST 1** injections of the full-chemistry, chemical equilibrium, self-consistent models for the metallicities and C/O ratios explored in §3.4.2, and cross-correlating with the same models;

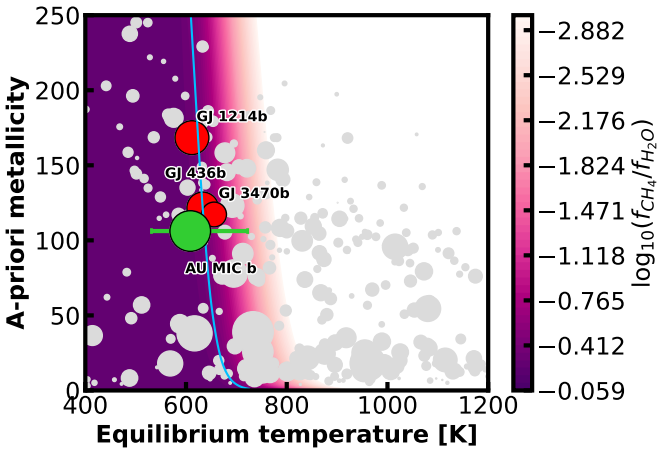


**Figure 3.10:** The expected metallicity of AU Mic b (green) compared to some other previously studied, evolved sub-Neptunes (red) and the rest of the well characterised small exoplanet population (with $M_p > 0.1\,M_J$, $R_p < 12\,R_J$, and $T_{\rm eq} < 1200\,K$, grey). Each data point is scaled according to its TSM, (Kempton et al., 2018). The propagated uncertainty on the equilibrium temperature of AU Mic b is indicated. Where not yet measured, the metallicity is predicted based on the mass-metallicity relation given in Thorngren et al. (2016). The purple background gradient shows the $CH_4$-$H_2O$ ratio assuming chemical equilibrium, at a pressure of 1 mbar. The blue line shows the theoretical boundary between the $CH_4$-dominance regime (left of line) and CO-dominance (right of line). Figure adapted from a figure by Maria Steinrueck.

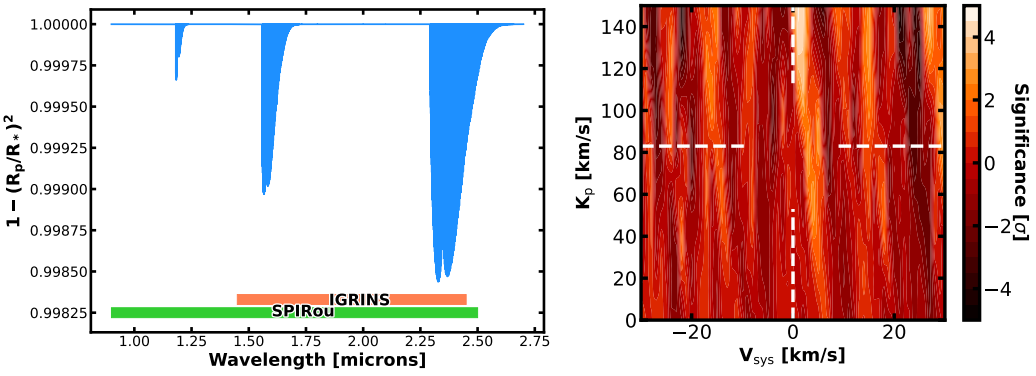


**Figure 3.11: Left:** The normalised CO transmission spectrum forward-modelled using the lowest density estimate of AU Mic b, with the IGRINS and SPIROU wavelength coverages indicated. **Right:** Result having cross-correlated the model on the left with combined reduced data from both instruments.

**TEST 2** injecting the same full-chemistry, chemical equilibrium, self-consistent models, then cross-correlating with models of individual species at $\mathrm{VMR}_i$ set by equilibrium chemistry;

**TEST 3** injecting the single species models, which consist of $\mathrm{VMR}_i$ independent of equilibrium chemistry and an opaque cloud deck, then cross-correlating with the same models.

The individual species models of **TEST 2** were created by first extracting the $\mathrm{VMR}_i$ of the species in question from the calculated FASTCHEM abundances (computed for self-consistent chemistry), then running PETITRADTRANS to produce a transmission spectrum of an atmosphere containing predominantly $H_2$ and He, and the single species, $i$, at an abundance set by $\mathrm{VMR}_i$. **TEST 2** allows us to investigate the detection threshold for each species individually though, crucially, not independently. A true exoplanet spectrum will include absorption features from a multitude of species, which will overlap and coalesce to form a composite spectrum. This then may make it more challenging to detect a given species since their spectral features may be masked by another's. By injecting the full spectrum rather than the spectrum of an individual species in **TEST 2**, I incorporate this reality into the injection tests. Having proceeded to the cross-correlation stage, I report the signal-to-noise of the velocity map at the injection velocity.

#### TEST 1 and 2

For **TEST 1** and **TEST 2**, I explore a range of metallicities relative to solar, and carbon-to-oxygen ratio (C/O), just as the models for the tests with the untouched data in §3.4.2. Fig. 3.12 shows the detection significances recovered for different injected models on both the datasets individually, as well as combined. Typically in high-resolution spectroscopy, a SNR of at least $5\sigma$ is required to claim a 'detection', while $3\sigma$ is considered more tentative. In Fig. 3.12, I grey-out the regions of parameter space with reported detections $< 3\sigma$. A detection of an injected model would suggest that the data would have been sufficiently sensitive to such an

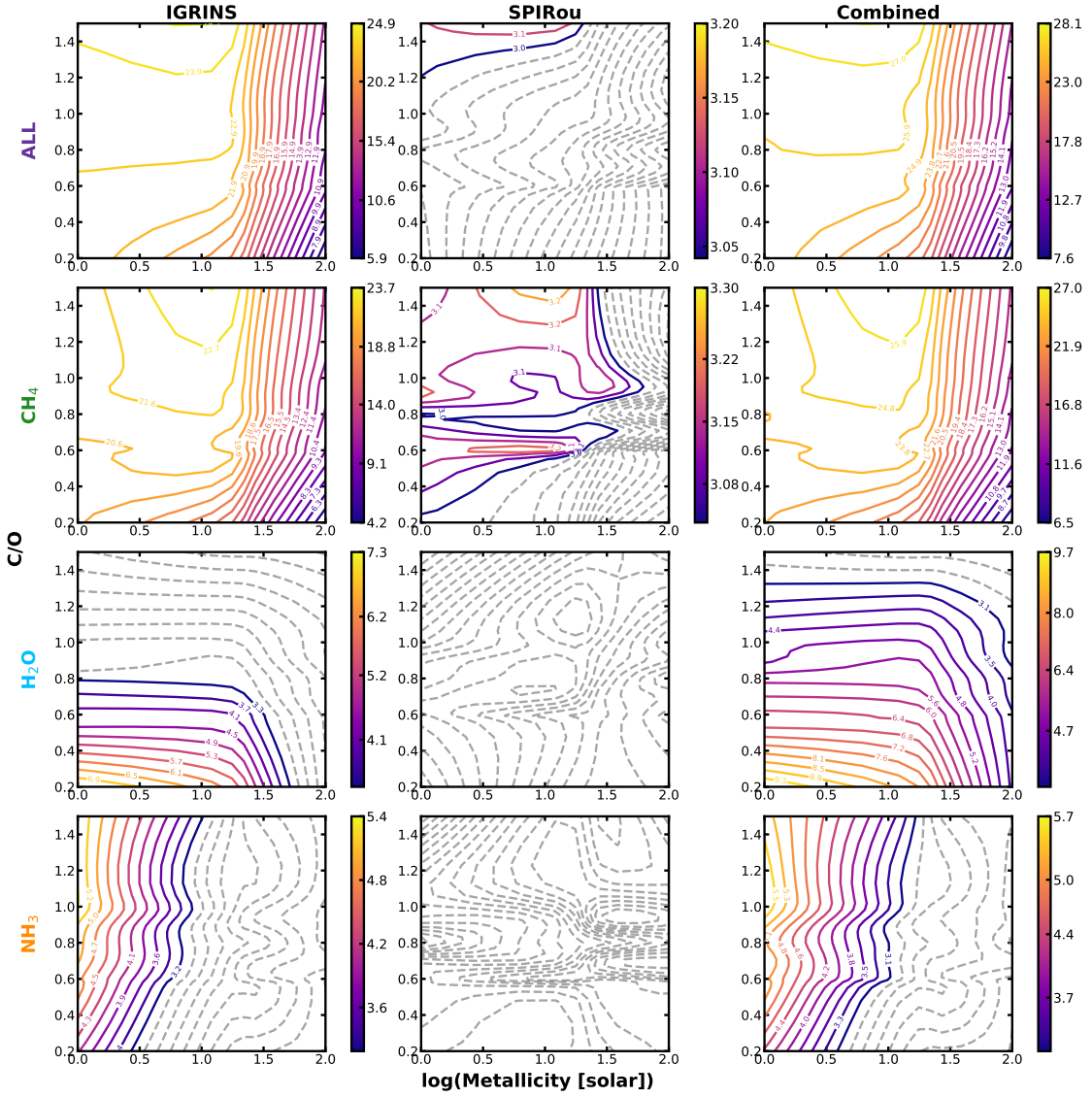


**Figure 3.12:** Equal detection significance contours from the series of injection-recovery tests. These are the signal-to-noise from the CCF velocity maps at the injection velocity. SNR$<3$ are greyed out in the dashed lines for an easier visual of the regions of parameter space we are able to rule out. In each case we inject the same full-chemistry, self-consistent model, but each row shows the result having cross-correlated with a different model (notably 'ALL' of the **top row** refers to the same full-chemistry model as that injected).

atmosphere; as such, I rule out atmosphere corresponding to the coloured regions in Fig. 3.12 to the significances inscribed on each contour.

Firstly, with the IGRINS data the full-chemistry atmosphere was well recovered consistently across the range of C/O and metallicities tested (**TEST 1**). This was seemingly driven by the $CH_4$, which was similarly recovered with significance $> 5\sigma$ across the board. I note that the SPIROU data were less sensitive to these

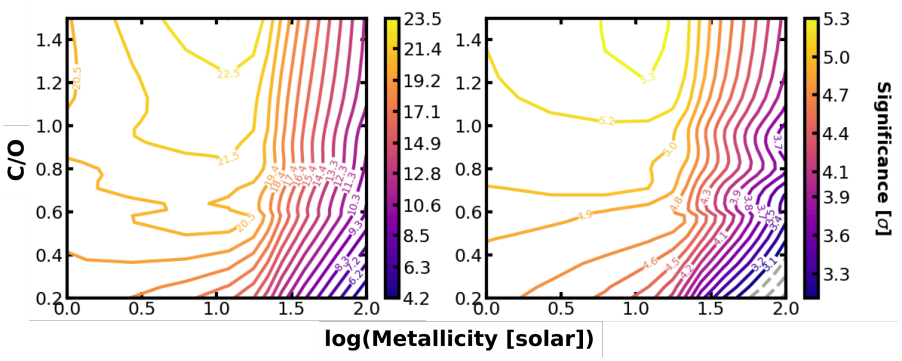


**Figure 3.13: Left:** IGRINS recovery of $CH_4$ models. **Right:** SPIROU recovery of the same $CH_4$ models, having amplified the amplitude of spectral features by a factor of 3.

injected models; I was only able to recover the high C/O, metallicity $< 1.5\times$ solar atmospheres at low SNR. This was a similar case overall: the IGRINS data were more sensitive to the atmospheres tested, and thus provided tighter constraints on the atmospheric composition of AU Mic b. Indeed, the IGRINS data were of sufficient quality to conclude with $> 7\sigma$ confidence that AU Mic b does not present $CH_4$ at the abundances corresponding to C/O$= 0.2 - 1.5$ and metallicities from $1 - 100\times$ solar assuming no clouds are present. The constraints on $H_2O$ and $NH_3$ were looser. At the $5\sigma$ level, I am able to rule out $H_2$/He-dominated, clear atmospheres including $H_2O$ at abundances $< 1.4\times$ solar, with C/O$< 0.4$. Reporting the same for $NH_3$, I rule out abundances $< 0.5\times$ solar for C/O$= 0.2 - 1.5$ inclusive. Neither datasets were sensitive to any of the CO or $CO_2$ atmospheres computed in **TEST 2** (not shown in Fig. 3.12).

To comment on the weaker constraining power of SPIROU, we might expect that the SPIROU data are less sensitive by a factor corresponding to the CFHT mirror size (3.4 m) compared to that of Gemini South (8 m). Indeed, by injecting an amplitude-scaled model into the SPIROU data, I was able to recover a similar range of atmospheres to the IGRINS data (see Fig. 3.13).

Though I did not explicitly repeat the cross-correlation tests with cloudy, chemical equilibrium models, I assessed the expected reduction in detection significance had I used such models. Fig. 3.14 shows the full chemistry, self-consistent, chemical equilibrium models, having included opaque cloud decks at different altitudes. I

calculate to first order the predicted reduction in detection significance as a result of these opaque cloud decks. In each observing band, I measure the reduction in strength and number of atmospheric spectral lines, $N_{\rm lines}$. From Birkby (2018),

$$\mathrm{SNR}_{\rm planet} = \left(\frac{S_p}{S_*}\right)\mathrm{SNR}_*\sqrt{N_{\rm lines}} \tag{3.1}$$

where $S_p/S_*$ represents the signal strength of the planet relative to the star, and $\mathrm{SNR}_*$ is the signal-to-noise of the observations. It follows that, all else being equal, the product of the reduction in the strength of the lines and the square root of $\Delta N_{\rm lines}$ is proportional to the reduction in cross-correlation detection significance. We can apply this product to re-scale the injection constraints of Fig. 3.12. For $N_{\rm lines}$, I count the number of peaks in the normalised forward-modelled spectrum above a given threshold, defined as 3% below the continuum level. The new constraints for cloud decks at altitudes with cloud top pressures in the range $-6 < \log_{10} P_c[\mathrm{bar}] < -2$ are given in Appendix A, Table A.1. To summarise, we lose all constraining power in the presence of cloud decks with altitudes higher than $P_c = 10^{-5}$ bar; at these cloud altitudes, the remainder of the spectral line is too shallow to be detected (see Fig. 3.14 for the relative lines strengths). For $H_2O$ and $NH_3$, the constraints quickly diminish when including a cloud deck even at $P_c = 10^{-2}$ bar, particularly at the $5\sigma$ threshold. More positively, $CH_4$, and the consequent full chemistry, equilibrium chemistry case, are detectable for a wide range of C/O and metallicity even in the case of an opaque deck at $P_c = 10^{-3}$ bar. In Fig. 3.15, I show the new constraints on the tested parameter space, in the presence of cloud decks at different altitudes, detected with significance greater than $3\sigma$ and $5\sigma$ respectively. I do not include CO here, since I was not able to detect it at chemical equilibrium abundances in **TEST 2**. We are still able to rule out some atmospheres in the presence of clouds. I give an example of an entire map in Appendix A, Fig. A.2, for a cloud deck at pressure $\log_{10} P_c[\mathrm{bar}] = -4$.

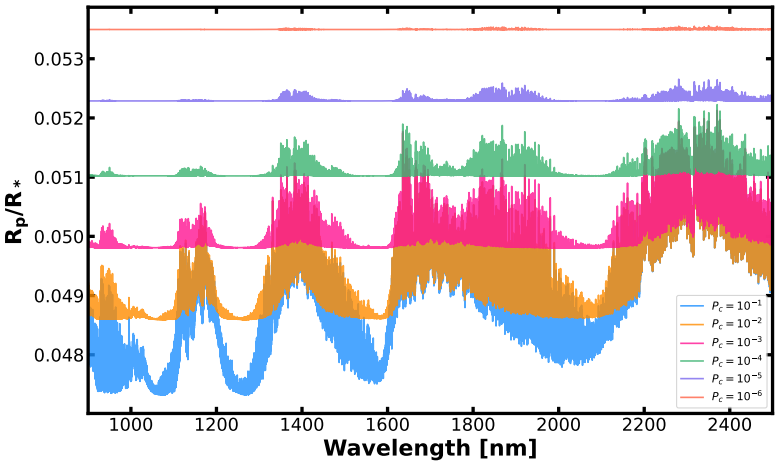


**Figure 3.14:** The impact of opaque cloud decks at different pressures, $P_c$ [bar], in the atmosphere of AU Mic b on its measured radius. Demonstrated here is the chemical equilibrium, forward-modelled atmosphere (in blue), and the subsequent truncation of spectral lines as cloud decks are added at progressively higher altitudes.

### TEST 3

Having ruled out some clear atmospheres, I turn to cloudy atmospheres independent of chemical equilibrium (**TEST 3**). These will enable me to explore chemical composition independently of equilibrium assumptions, while simultaneously accounting for an opaque cloud deck. For each species $i$, I inject models with $-6 < \log_{10} \mathrm{VMR}_i < -1$ and clouds with cloud top altitudes corresponding to pressures from $-6 < \log_{10} P_c[\mathrm{bar}] < -1$. I then assess the signal-to-noise peak cross-correlation at the injection velocity, having detrended the data. In Fig. 3.16, I show the parameter space at which a signal is recovered from the combined IGRINS and SPIROU data. The lightest contour shows the region wherein a signal is recovered to greater than $3\sigma$, and the darkest contour to greater than $5\sigma$. For reference, the chemical equilibrium profiles corresponding to these pressures are overplotted in dashed lines (from Fig. 3.7).

Cloud decks beyond $\log_{10} P_c < -5$ largely obstruct detections. This is not surprising given the truncation of the spectral lines with such a high altitude cloud, as shown in Fig. 3.14. Notably, the high abundance models with clouds $\log_{10} P_c < -5$ are retrieved, in the cases of $CH_4$ and $NH_3$. I rule out the largest parameter space

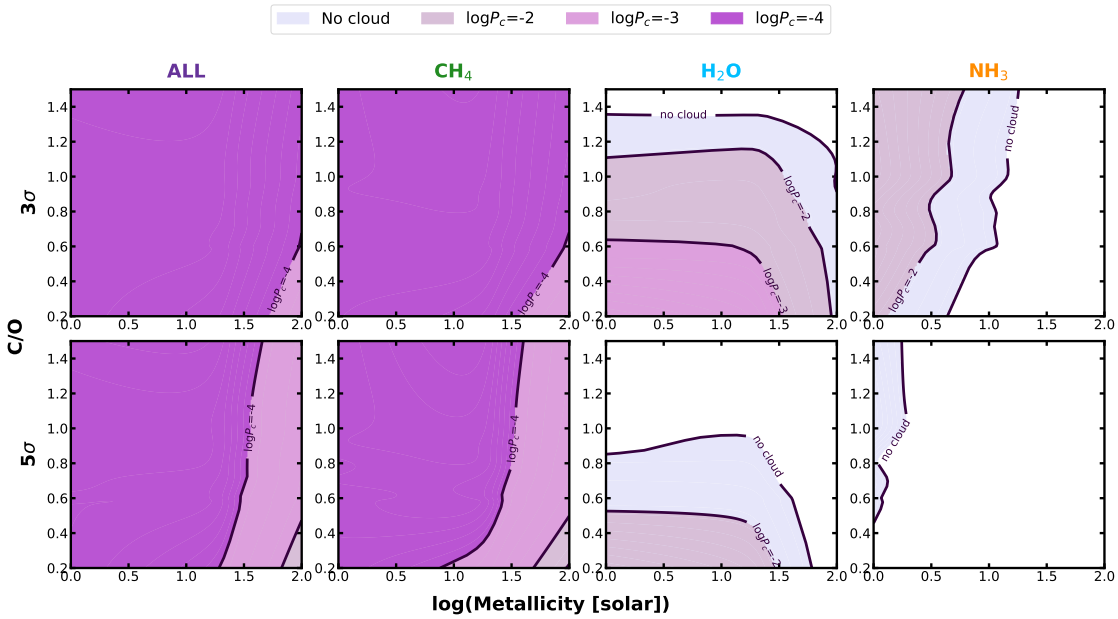


**Figure 3.15:** Re-scaled constraints on chemical equilibrium cases, when including cloud decks at different pressures, applying a **(top row):** $3\sigma$ and **(bottom row):** $5\sigma$ detection threshold.

for these molecules. The observed absence of $CH_4$ in the atmosphere of AU Mic b necessitates one of three mechanisms:

(i) under chemical equilibrium, AU Mic b inhabits the CO-dominated region, either because we have underestimated its equilibrium temperature, or the theoretical transition boundary (shown in Fig. 3.10) exists at a lower temperature than predicted;

(ii) there is an opaque cloud deck in the upper atmosphere of AU Mic b, while the abundance is lower than that corresponding to chemical equilibrium (lightest-coloured region of parameter space in the left-most panel of Fig. 3.16);

(iii) the chemical makeup of the upper atmosphere of AU Mic b is actually in disequilibrium, due to (e.g.,) photo-chemical-inducing irradiation, or vigorous mixing.

If the atmosphere of AU Mic b is in chemical equilibrium, it must be CO-dominated, or else host a high-altitude cloud deck. The injection tests ruled out the high-abundance, clear atmospheres for CO, as well as the cloudy case down to $\log_{10} P_c \gtrsim -3$

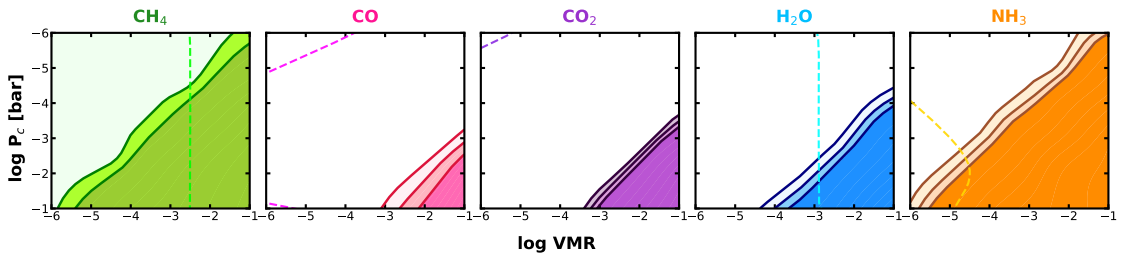


**Figure 3.16:** The parameter space excluded to $> 5\sigma$ in darker contours, with the $4\sigma$ and $3\sigma$ regions indicated in successively ligher contours, following injection tests of cloudy, single species models from **TEST 3** into the combined IGRINS and SPIROU data. Overplotted in the dashed lines are the chemical equilibrium FASTCHEM abundances at a metallicity of $1\times$ solar and C/O of 1, for reference (same as Fig. 3.7).

for abundances greater than $\log_{10}$ VMR $= -2$ (Fig. 3.16). So, regarding point (i), the CO would have to be present at abundances lower than $\log_{10}$ VMR $= -3$ in the case of a cloud-less atmosphere, and up to $\log_{10}$ VMR $= -1$ if there is a cloud deck higher than $\log_{10} P_c\,[\mathrm{bar}] \lesssim -3$. Regarding point (ii), condensate clouds are certainly a plausible scenario at an equilibrium temperature of $T_{\mathrm{eq}} \sim 600\,\mathrm{K}$ (see the condensation curves in Kitzmann et al., 2023); I only rule out a cloud deck at $\log_{10} P_c\,[\mathrm{bar}] = -6$ for high abundances of $CH_4$ and $NH_3$, but it could well be that another process is depleting these molecules. Then, point (iii) is very much a viable explanation. Disequilibrium chemical models are significantly more complex, and considered beyond the scope of the work in this chapter; I leave this to suggested future work.

## 3.5 An active star

Cooler, low-mass stars exhibit more signs of activity than their higher mass counterparts. With stronger magnetic fields induced by the stellar dynamo, there is a higher likelihood that magnetic phenomena such as photospheric spots and faculae, chromospheric plages, and flaring events will impact observations. Here, I explore the likelihood and impact of activity phenomena in the observations of AU Mic b.

| Line | Window minimum [nm] | Window maximum [nm] |
|---|---|---|
| He-I | 1082.82 | 1083.10 |
| Pa $\beta$ | 1281.72 | 1281.90 |
| Br $\gamma$ | 2165.40 | 2165.68 |

**Table 3.4:** Minimum and maximum extents of the integration window for each chromospheric indicator line examined in §3.5.1.

### 3.5.1 Checking for signatures of stellar flares

AU Mic is a highly active, young star, seen to flare on a regular basis. Gilbert et al. (2022) calculated a flare rate between $1-3$ flares per day, and a photometric peak-to-peak variability of 4%, from two sectors of *TESS* light curves. The event of a flare would likely be detrimental to any atmospheric study in transmission, considering the short transit duration and the time-scale of a flare (plus wind-down). There are a few key diagnostic tools in the nIR, covered by both IGRINS and SPIROU, which we can use to identify flare events. Near-infrared chromospheric lines such as the helium-I triplet and some hydrogen transition lines of the Paschen and Brackett series are thought to be useful proxies for stellar flaring events (Klein et al., 2021). The He-I triplet, Pa $\beta$ and Br $\gamma$ lines are all covered by the SPIROU bandpass, while the Br $\gamma$ line is the only proxy within the IGRINS wavelength range. We would expect the flux in each line to remain stable throughout the transit in the case of a quiet photosphere. For the relevant orders, I remove a mean out-of-transit spectrum, which would represent the mean stellar estimate. Since this is a first order approximation of the star, we are then left with residual stellar variations. For each line, I define a 'window' over which to integrate the flux (noted in Table 3.4); the light-curves for each indicator lines in the SPIROU spectra are shown in Fig. 3.17. We can see that 95% of the integrated fluxes are within $2\sigma$ of the mean: in the case of a flare event we would expect to see a large, sharp deviation in flux of these indicator lines. There is one visible outlier in the He-I light-curve at exposure 49; checking the offending exposure I observe residual OH

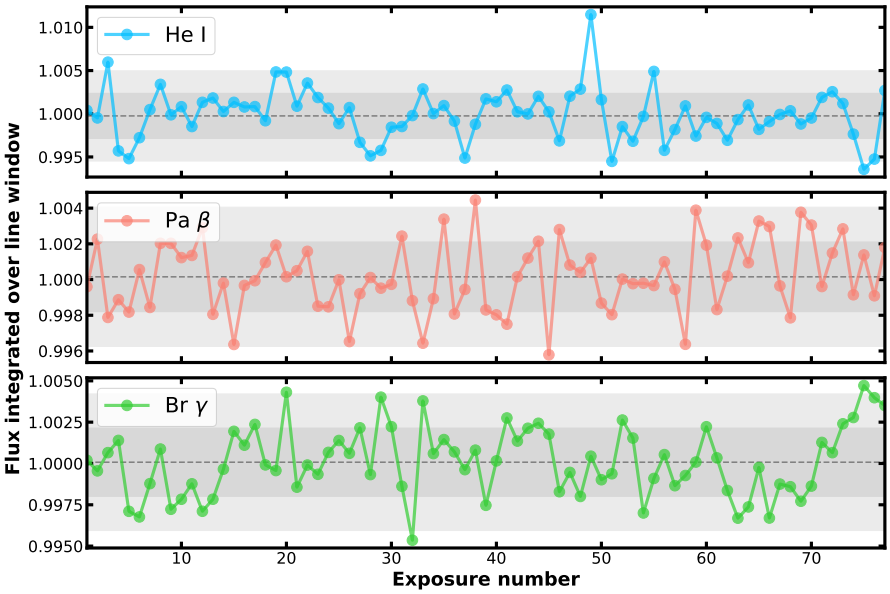


**Figure 3.17:** The integrated flux over a 0.2–0.3 nm-wide window around each chromospheric stellar line, for each SPIROU exposure, normalised by the median flux. The transit of planet b occurs between exposures 1 and 65 inclusive. The dashed line indicates the mean flux, with the 1- and 2-$\sigma$ intervals shaded.

emission, which is biasing the integrated flux. Also, in the event of a flare we would expect to see the same signature in all three indicators.

As an additional check, I also compute the standard deviation of the indicator line light-curve (Fig. 3.18). In the event of a flare, we would expect to see a significantly larger standard deviation of the flux within the line window, compared to the surrounding continuum, again for all three indicators. Upon first inspection, the Br $\gamma$ line standard deviation did not appear to be completely white noise, but this was resolved upon narrowing the integration window, to avoid any possible residual tellurics. Within the majority of exposures the standard deviation of the indicator line light-curves is comparable to the continuum light-curve. There are a few outliers to note, in particular exposure 49 in the He-I line (discussed above), and 23 and 34 in the Pa $\beta$ line. The latter two were manually checked, and there was nothing abnormal in the spectra; again, we would expect to see flare signals in all three lines, therefore I am confident to conclude that no detrimental flares occurred during the observed SPIROU transit.

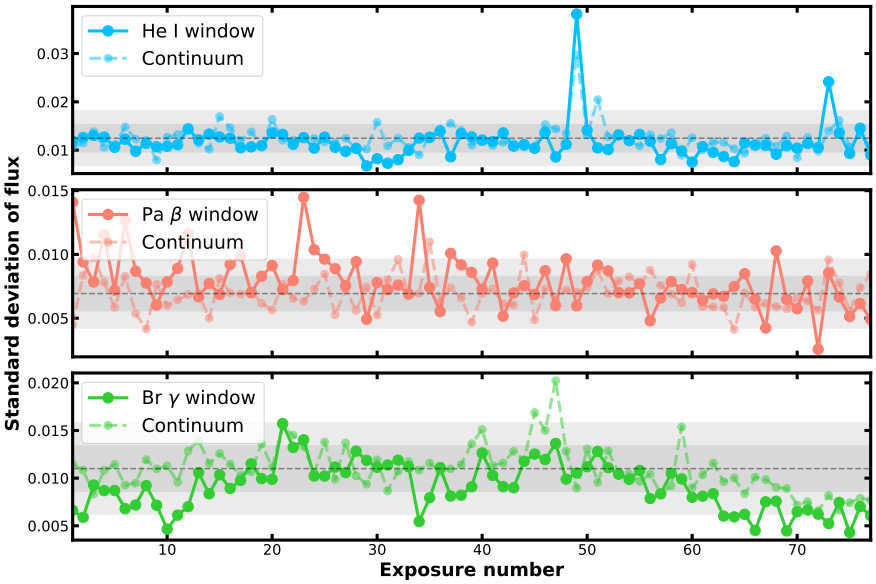


**Figure 3.18:** Standard deviation across the same 0.2–0.3 nm-wide window around each chromospheric indicator line as Fig. 3.17 (solid line), compared to the standard deviation of the rest of the spectrum in the corresponding order (dashed line).

I similarly check the IGRINS spectra, observing the Br $\gamma$ line at 2165 nm (the other two indicators are not captured by the IGRINS spectral coverage). It's important to remove the telluric lines, to isolate the variation of the stellar chromospheric indicator. The SPIROU pipeline removes a telluric template from the data, but the IGRINS pipeline-reduced data still includes telluric imprint. I start by fitting a blaze function to each exposure which simultaneously normalises the spectra. Then, I similarly remove the median out-of-transit spectrum, first in the Earth and then in the stellar reference frame. I checked visually for residual tellurics near the Br $\gamma$ line, narrowing the integration window as with the SPIROU data. I was satisfied that there was no telluric contamination left. The resulting integrated flux and standard deviation is shown in Fig. 3.19. The slight correlation in the integrated flux is thought to reflect the variation in SNR, and the standard deviation is completely within $2\sigma$ of that in the continuum. I am satisfied that the Br $\gamma$ line is dominated by noise rather than a flaring event.

I conclude that it is unlikely that either transit observations was affected by a stellar flare. I note, however, that the data information content are not sufficiently dense to rule out micro-flaring events.

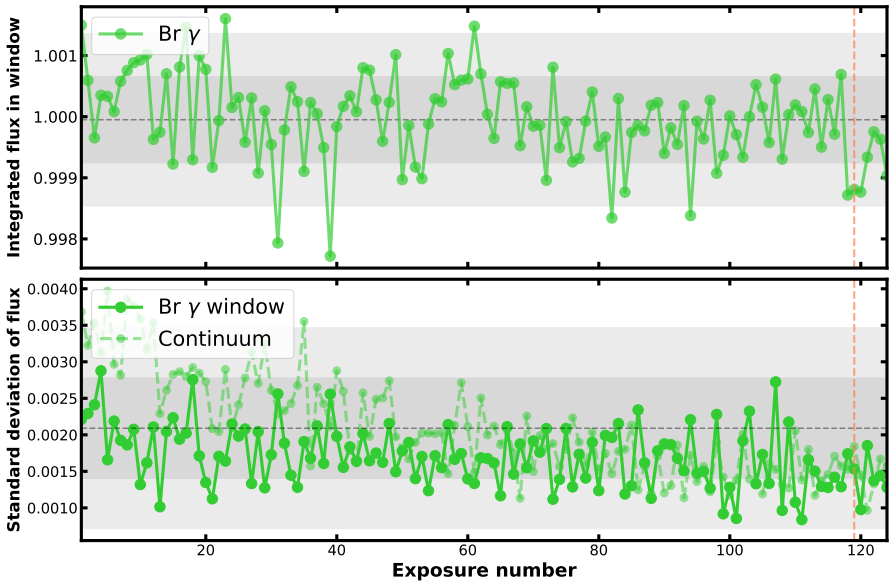


**Figure 3.19: Top panel:** The integrated flux and **bottom panel:** standard deviation of the Br $\gamma$ light-curve in the IGRINS data. I also show the standard deviation of the rest of the order exterior to the Br $\gamma$ line for comparison (dashed line **bottom panel**). The grey dashed line and intervals represent the mean and 1-/2$\sigma$ of the integrated flux **(top panel)**, and the continuum flux standard deviation **(bottom panel)**. The orange dashed line indicates the end of the transit.

### 3.5.2 Stellar spots

It is common in high-resolution spectroscopy to assume that the host star behaves as a perfectly homogeneous disk light source, behind the transiting planet. In fact, since high-resolution spectra are continuum-normalised, even limb darkening is often unaccounted for. It follows that the stellar spectrum is assumed to be constant during the transit, and a stellar removal involves simply dividing through by an average out-of-transit spectrum. To date, this has been a reasonable assumption for larger $R_p/R_*$, and closer-in planets. However, for smaller planets on longer orbits, and lower-mass stars, stellar inhomogeneities are more likely to have an impact on the observed spectra.

To quantify the impact of unocculted spots from a purely theoretical point of view, I expand on the ideas presented in Rackham et al. (2017). This formalism was derived specifically for low-resolution spectroscopy. So, applying it to high-resolution spectroscopy is not comprehensively representative of the impact of spots; I defer to Chapter 4 for a more detailed exploration of the impact of

stellar heterogeneities. Yet, this formalism can be used to derive an upper bound, worst-case scenario of the impact of difference spot coverages. Here, I complete preliminary tests to explore the likelihood that spots on the surface of AU Mic caused the reported non-detections in §3.4.2.

Rackham et al. (2018) reform Equation (11) in Rackham et al. (2017), which presents the observed transit depth, the true transit depth contaminated by the presence of stellar heterogeneities, assuming no spot (or faculae) crossing events. I reprint the derived contamination factor from Rackham et al. (2018) here

$$\varepsilon_\lambda = \frac{1}{1 - f_{het}(1 - \frac{F_{het}}{F_{phot}})} \tag{3.2}$$

where $f_{het}$ is the fraction of the stellar disk covered by heterogeneities (which includes both spots and faculae), and $F_{het}$ and $F_{phot}$ are the spectrum of the heterogeneity and photosphere respectively (see Chapter 4 for an extension of this to occulted heterogeneities). Equation 3.2 assumes that, at any point in time, the unocculted spectrum can be prescribed as

$$S_u = f'_{het}F_{het} + (1 - f'_{het})F_{phot} \tag{3.3}$$

where $f'_{het}$ is the fraction of the unocculted stellar disk covered by heterogeneities. This is given by $f'_{het} = f_{het}/f_u$ where $f_u$ is the fraction of the disk which is not occulted, i.e. $(\pi R_*^2 - \pi R_p^2)/\pi R_*^2 = 1 - D_\lambda$ where $D_\lambda$ is the transit depth.

I evaluate the contamination factor in Equation 3.2 for AU Mic, with different spot coverage fractions, $f_{het}$. For the two stellar spectra, $F_{phot}$ and $F_{het}$, I employ BT SETTL models at $\log g[\mathrm{cm/s^2}] = 4.5$. I assume the photospheric temperature to be 3700 K. The spot-to-photosphere temperature contrast is thought to be 0.86 for M dwarfs (Rackham et al., 2018); I employ a BT SETTL model at 3200 K for the spot contribution. In reality the spectra of heterogeneities are likely to diverge from cooler photospheric models, and this has been noted in the literature (Witzke et al., 2022). For the present illustration tests, this simplifying assumption suffices.

Concentrating on $H_2O$ and the relevant SPIROU orders, I create a noise matrix with similar properties to the observations analysed in this chapter (i.e., phase

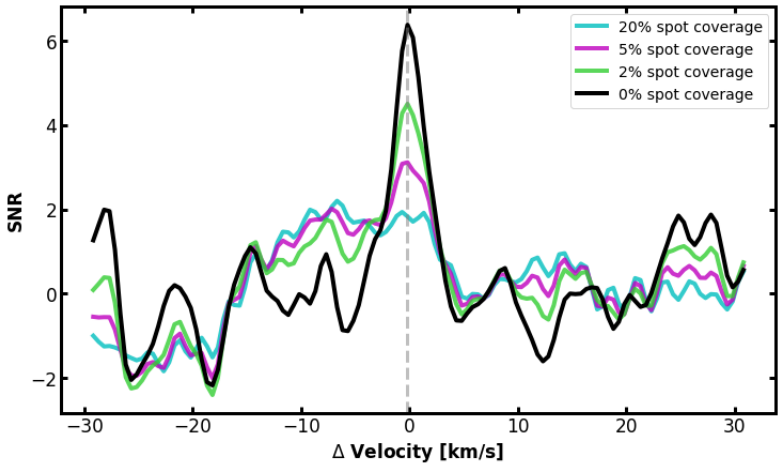


**Figure 3.20:** Cross-correlation of a water model with unocculted spot-contaminated spectra, for different spot coverage fractions, compared to an spot-free stellar spectrum (black). For the contamination spectrum, I evaluate the formulation of Rackham et al. (2018).

coverage, noise properties, wavelength coverage), scaled by the instrumental blaze function. I inject a planetary $H_2O$ model and apply the contamination factor, $\varepsilon_\lambda$. Assuming them to be removed completely, I neglect tellurics and the intrinsic stellar spectrum. I now have a time-series of 'spectra', i.e., contaminated planetary spectra, with which I cross-correlate the in-transit 'spectra' with the same (uncontaminated) $H_2O$ model as injected. Fig. 3.20 shows the collapsed CCFs for the three contamination factors tested: $2, 5$ and $20\%$. Averaged over several different noise realisations, I recovered the planetary $H_2O$ signal at $1.8\sigma$, $3.1\sigma$ and $4.5\sigma$ in the $20, 5$ and $2\%$ cases respectively. For reference, I show the cross-correlation result, having applied no contamination in Fig. 3.20 (solid black line): given the noise applied, I achieve a detection of $6.4\sigma$ in this case. Typically in high-resolution spectroscopy, a signal-to-noise of at least $5\sigma$ is required to claim a 'detection'. In our case, however, we observed no peak detections in our cross-correlation analyses, and are therefore interested if the presence of unocculted heterogeneities dampened the planetary atmosphere signal. From these tests, I conclude that only large spot covering fractions ($> 5\%$) would sufficiently dampen an atmospheric water signal if indeed water is present, to result in a complete non-detection. I note that I also check the impact of a larger heterogeneity-photosphere temperature

contrast; we would expect water features to strengthen with decreasing temperature. Lowering the $F_{het}$ temperature to 3000 K, I saw only a decrease of 1% in the aforementioned detection significances. Therefore, a larger temperature contrast would not impact our conclusions.

I consider the likelihood that AU Mic in fact displays a $f_{het}$ larger than 5%. Using SPIROU spectra collected between September and November 2019, Klein et al. (2021) were able to employ the Doppler imaging technique to estimate the spot coverage fraction of AU Mic to be 1.4% (see Kochukhov, 2016, for a comprehensive review of Doppler imaging). Then, Klein et al. (2022) derived spot coverages between 4.7 and 5.1% with one year of HARPS optical spectra. These are derived over the full stellar surface. Considering the upper limit of $f_{het} = 2.5\%$, i.e., the spot coverage of the projected stellar disk, Klein et al. (2022), our tests indicate that we would have still been able to detect $H_2O$ at a significance greater than $4\sigma$. To conclude, the presence of unocculted heterogeneities at the scale of previously published fractions cannot exclusively explain the null detection of water for AU Mic b.

I acknowledge that Equation 3.2 enfolds a number of simplifying assumptions. That said, Fig. 3.20 represents a pessimistic case, since the static-nature of the contamination factor in Equation 3.2 would mean it would be removed to some extent during the detrending of high-resolution spectra. This is not true of low-resolution spectroscopy; please refer to Chapter 4 for further thought extension to this work.

### 3.5.3 Assessing the Rossiter-McLaughlin Effect

Young stars are believed to experience higher rotation periods, due to their residual angular momentum from formation in the protostellar disk (Van Saders & Pinsonneault, 2013). Their rotation induces a broadening of the photospheric spectral lines. Add in a transiting planet, and different velocity contributions of the stellar disk are occulted at each point in time, manifesting as a time-variable bump in the stellar line profile, colloquially known as the 'Rossiter-McLaughlin Effect' (RME; Ohta et al., 2005; Winn, 2007). I explain this phenomenon in more detail in Chapter 4. Then, removing a 'static', time-invariant star spectrum may leave

behind a 'Doppler shadow' in the data, which follows the velocity of the planet. We are thus interested in whether the Doppler shadow of AU Mic b is sufficiently large to mask a planetary signal in the real data.

### A forward model

I simulate the problem to investigate the amplitude of the Doppler shadow. First, I initiate a limb-darkened stellar disk using the public code STARRY[4] (Luger et al., 2019, 2021a,b). Dividing the stellar disk into an $N \times N$ grid, I evaluate the blue/red-shift of the intrinsic stellar spectrum for the local radial velocity of each grid point. As a sanity check, I integrate the spectra over all the grid points, and as expected, I recover a broadened version of the intrinsic spectrum. Then, onto the planet impact; I simulate a transiting disk (no atmosphere at this stage) representing the transit observed on 16th June 2019. For each point in time, I disregard the occulted grid point(s), and integrate the remaining grid contributions. This simulation tool is developed and detailed in Chapter 4. I add noise akin to that of the reduced SPIROU spectra. The result is a time-series of forward-modelled stellar spectra with incorporated RME, $\mathcal{S}_{\rm RM}(\lambda, t)$. Our task is then to observe how this uncorrected RME manifests in cross-correlation space. I remove the out-of-transit mean spectrum, to represent a basic 'reduction' of the spectra, i.e., a detrending based on the assumption that the star is static in time. The residual time series is shown in Fig. 3.21.

To assess if the RME could mimic an atmospheric detection, I proceed to cross-correlate the time-series of residuals (in Fig. 3.21) with the planetary atmosphere models described in §3.4.1. I cross-correlate each spectrum in the time-series with (i) the self-consistent full chemistry model and separately (ii) the CO-only model with VMR[CO] $= 10^{-2}$. I chose to test CO alone, since we surmise that detections of species also present in the stellar photosphere are likely to be disproportionately impacted. The resulting cross-correlation functions, integrated in time, are shown

[4] https://starry.readthedocs.io/en/latest/

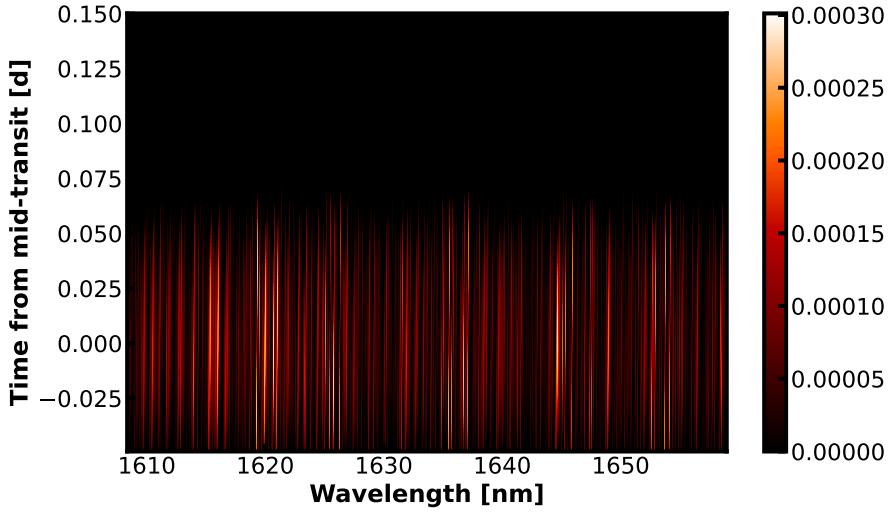


**Figure 3.21:** Time series of residual, forward-modelled stellar spectra, having removed the mean out-of-transit spectrum, i.e., $\mathcal{S}_{\rm RM}(\lambda,t)-\bar{\mathcal{S}}_{\rm RM}$. The RME remains post correction. This is an example forward model for the transit observed on $16-06-2019$, with spectral coverage corresponding to a SPIROU order with strong CO contribution.

in magenta in Fig. 3.22. I observe neither a statistically significant peak cross-correlation or anti-correlation across the velocities tested, let alone at the planet velocity. As a sanity check, I add a planetary model atmosphere into the forward model, prior to 'detrending'. This is purely an addition in spectral space; for a more complete model, see Chapter 4. Cross-correlations with the RME + planet model residual time-series are shown in green solid line in Fig. 3.22. I also create a static star + injected planet model case, shown in green dashed line. Both injection cases result in a $\sim 4\sigma$ peak detection, for the self-consistent atmosphere case as well as the CO-only case. This suggests that the Rossiter-Mclaughlin effect is unlikely to sufficiently dampen an atmospheric signal to explain a null detection.

### Preliminary empirical correction

We adapted the forward modelled RME simulation to try and correct for the RME at the spectral level. In the case of the SPIROU spectra, assuming the pipeline has removed the predominant telluric spectrum, we use the blaze-corrected out-of-transit mean as the master spectrum. We then use the above simulation to predict the Rossiter-Mclaughlin-induced distortions on the stellar spectral lines, according to the observational parameters. Thus, we forward model the RM-affected spectral

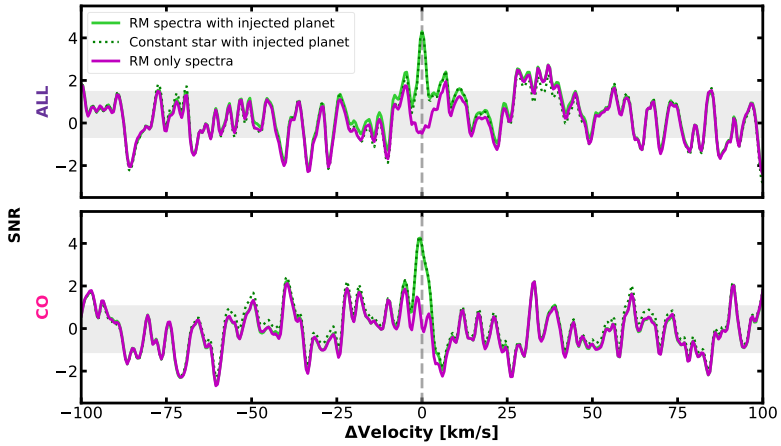


**Figure 3.22:** Cross-correlation function of the residual spectral time series, collapsed in time, with **(top panel:)** the full chemistry atmospheric model, and **(bottom panel:)** the CO-only model. The magenta solid line indicates the cross-correlation with the RME-only residual spectra. The result from the RME with injected planet signal time-series is shown in green solid line, with its $1\sigma$ interval shaded in grey. The green dashed line shows the result for the static star + planet case.

time-series, $\mathcal{S}_{\rm RM}(\lambda, t)$. To correct the observed, blaze-corrected SPIROU spectra, we scale each spectrum $\mathcal{S}_{\rm RM}$ and divide it out of the data.

The situation is a little more challenging for the IGRINS spectra, because the tellurics are not removed *a priori* (by the pipeline). It is therefore difficult to construct a master spectrum that contains stellar lines only. Towards a first order correction, we first distinguish stellar lines from telluric lines by considering that the variation of the former would be significantly lower than the latter during the course of the transit. We compute the standard deviation in each pixel in the spectral time-series. We define a threshold standard deviation, to separate telluric-dominated from stellar-dominated pixels. The threshold is defined as the standard deviation across all pixels of the SPIROU spectra, interpolated to the stellar rest frame. This is valid since we assume tellurics have been removed. Back to the IGRINS spectra, we assign pixels with a standard deviation below the threshold to the star category, with which we computed the master stellar spectrum. This is our input to the RM modelling simulation. The remainder of the model and correction is similar to that described above.

Having corrected the spectra, I return to the search for an atmospheric detection.

I again focus my attention on carbon monoxide. After applying the rest of the reduction method from §3.3, I cross-correlate the residuals with a CO-only, clear atmospheric model at VMR[CO] = $10^{-2}$. Still, the null detection prevails. This would agree with the above forward model results, namely that the RM alone cannot be the exclusive reason for the null atmospheric CO detections.

## 3.6 Alternative atmospheres

In §3.4.1, I assumed clear atmospheres, in chemical equilibrium and separately considered single species models with condensate clouds. Here, I discuss the potential alternative atmospheres, and the consequences on my conclusions.

### 3.6.1 Impact of flare events on atmospheric composition

From the tests performed in §3.5.1, I am satisfied that no major flaring event occurred during the course of the observations. However, AU Mic is known to be an active, frequently flaring M dwarf; I have not yet assessed the possibility that a past flare events has significantly altered the $H_2$/He primordial atmosphere around AU Mic b, to the extent that there is significant disequilibrium in the atmospheric chemistry. Venot et al. (2016) simulated the evolution of an atmosphere around two separate hypothetical planets around the notoriously active host AD Leo, at orbital distances corresponding to equilibrium temperatures of 412 K and 1303 K. I consider the 412 K case which, though cooler than AU Mic b ($T_{\rm eq}$ = 593 K), is the more similar of the two test cases. The majority of affected species experienced abundance variations in the mid layers of the atmosphere, to which high-resolution spectroscopy is less sensitive. The corresponding changes in absorption in the transmission spectra did not exceed 12 ppm and 40 ppm on longer timescales. These were mainly around the 3.3 µm region, due to the strong $CH_4$ absorption feature, and redward of 9 µm. In the $0.9 - 2.5$ µm region spanned by the AU Mic b observations analysed above, the changes in absorption did not exceed 3 ppm and 10 ppm. Therefore, even in the proximity of a star with a higher flaring rate (1 per 25 mins, as opposed to 5 per day for AU Mic, Gilbert et al. 2022), we would not expect the atmosphere to

display compositional changes which could be observed, considering the sensitivity of current facilities. In a similar study, Louca et al. (2023) simulated the environment of GJ 581 c, a sub-Neptune orbiting a M3V host star. The largest propagated change in the transmission spectrum was 1.1 ppm, again around 3.3 µm. I thus deem it very unlikely that the atmosphere of AU Mic b might be significantly impacted by preceding flares, to the extent that the forward models created in §3.4.1 are no longer a sufficient match to warrant detection by cross-correlation.

### 3.6.2 Cloudy atmospheres and disequilibrium chemistry

At the lower temperature of AU Mic b, atmospheric aerosols might be present and have the potential to impact observations (Kitzmann et al., 2023). Indeed, the cooler sub-Neptune population are predicted to be cloudier than there hotter counterparts (Heng, 2016). In §3.4, I consider opaque condensate cloud decks. These result in a grey opacity, which acts to truncate the atmospheric spectral lines (see Fig. 3.14). Another class of aerosols, not considered in the preceding sections, is photochemical haze. The role of haze and its dependencies on system parameters is still not well understood. Dymont et al. (2022) use the amplitude of the *HST/WFC3* water feature to investigate haze-planet property correlations empirically. For the variables considered, they tentatively concluded that younger planetary atmospheres with larger scale heights, and lower gravity are more likely to be hazy. It is then plausible that AU Mic b is host to substantial haze, though I note that there does not seem to be a clear consensus among the sub-Neptune population (Hörst et al., 2018). If produced by stellar irradiation, the $CH_4$ could be photochemically depleted, particularly at the pressures probed by these observations (see e.g., Benneke et al., 2019a).

Another mechanism which could result in a disequilibrium chemical state is the combination of high internal temperature and transport-induced quenching. This can hamper the chemical transformation of CO to $CH_4$. While tidal heating can invoke high intrinsic temperature (e.g., as proposed for canonical sub-Neptunes GJ 436 b and GJ 3470 b, Fortney et al., 2020), it is not expected to have a large

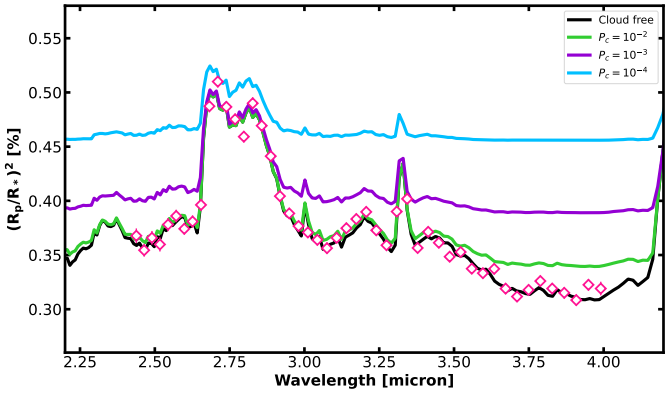


**Figure 3.23:** The transmission spectrum of AU Mic b with one transit observed by *JWST/NIRCam*. For reference, four distinct atmospheric models are overplotted - a clear atmosphere in black and those with an opaque cloud deck with cloud top pressure $P_c$ bar. At the sensitivity of *JWST* we would expect to distinguish between clear and cloudy scenarios. The noise on the *NIRCam* data points (pink diamonds) has been approximated using PANDEXO (Batalha et al., 2017); the errorbars are too small to be seen.

impact on AU Mic b given its eccentricity ($e < 0.1$, Zicher et al., 2022). That said, young planets are expected to have higher internal temperature, due to residual heat from formation. High levels of vertical mixing can then result in a quenching of the conversion of CO to $CH_4$ in the upper atmospheric layers probed by high-resolution spectroscopy (Prinn & Barshay, 1977; Madhusudhan et al., 2016). To conclude, a combination of these disequilibrium processes could elucidate the lack of observed $CH_4$.

## 3.7 Future work

### 3.7.1 Future observations of AU Mic b

The atmospheric compositions I have ruled out in this chapter provide constraints which are useful for informing future observations and associated retrievals of AU Mic b. The natural next step would be to observe AU Mic b from space. As previously mentioned, AU Mic b is the best target opportunity to observe a young sub-Neptune atmosphere, and thus is a sought-after target. We use CHIMERA (Line et al., 2013) to forward model the transmission spectrum of AU Mic b, considering the constraints presented in §3.4.3. We input the highest VMR possible in the case of each cloud deck pressure, from the $5\sigma$ contours in Fig. 3.16. Fig. 3.23 shows

the resulting predicted (clear) transmission spectrum of AU Mic b, which could be acquired by *JWST/NIRCam f322w2*[5] with one transit observation, using PANDEXO[6] (in addition to Gaussian noise) to estimate the noise level (Batalha et al., 2017). With a total science exposure time of 8.37 hrs, *NIRCam* would afford a datapoint-precision of 50–60 ppm. Such observations would enable one to distinguish between a clear and cloudy atmosphere, with cloud deck at $\log_{10} P_c[\text{bar}] = -2$ at a significance of $33\sigma$.

Future *JWST* observations may also help to distinguish some of the $CH_4$ depletion scenarios outlined above. Low-resolution space-based observations have the power to break the degeneracy between chemical abundances and cloud deck pressure seen with HRCCS. So then, towards confirming $CH_4$ depletion, the combination of the enhanced sensitivity of *JWST* and the wavelength coverage of *NIRSpec* should help to rule out the remainder of the parameter space in Fig. 3.16, i.e., the low abundance, high cloud deck scenarios. Then, it may offer the opportunity to further characterise the aerosol content of the atmosphere of AU Mic b; Fig. 3.24 shows the transmission spectra for different aerosol species. In reality though, deciphering the composition of aerosols is a challenge; often clouds host mixture compositions (Helling et al., 2006).

In *JWST* cycle 2[7], I was involved in two, ultimately unsuccessful, *JWST* proposals involving the target AU Mic b. The main concern of the time allocation committee is the impact of stellar activity on such (expensive) observations. This is a topical point of study at low-resolution (see Rackham & de Wit, 2023; Rackham et al., 2023); recent *JWST* observations of other active stars, albeit less active than AU Mic, have necessitated consideration of activity in atmospheric retrievals. *JWST* has such high photometric sensitivity that significant spot crossing events should be evident in the white light curves. Simultaneous photometry, e.g, with *CHEOPS*, can further help to constrain the spot coverage; optical photometry is thought to be particularly useful, since spot constrasts are larger at these wavelengths.

[5] *JWST/NIRSpec* cannot be used for AU Mic due to saturation limits.

[6] PANDEXO is distributed as part of the Exoplanet Characterisation Toolkit (https://exoctk.stsci.edu/), for the purpose of planning *HST* and *JWST* observations.

[7] https://www.stsci.edu/jwst/science-execution/approved-programs/general-observers/cycle-2-go

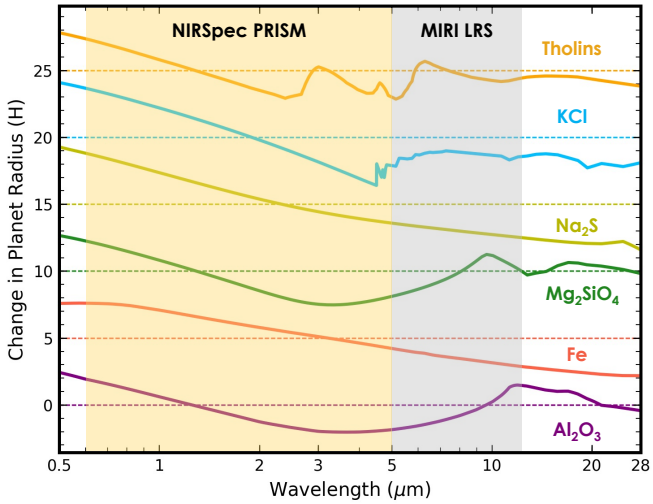


**Figure 3.24:** The transmission spectra of different aerosols, normalised and offset for clarity. The wavelength coverage of *JWST* instruments *NIRSpec prism* and *MIRI LRS* are shaded in yellow and grey respectively. Figure courtesy of Peter Gao, adapted from Gao et al. (2021).

Additionally, low-resolution retrievals are now equipped to simultaneously infer an (occulted) spot coverage fraction and temperature (see e.g., Mikal-Evans et al., 2023).

Future ground-based observations of AU Mic b are also in the pipeline; in collaboration with the ATMOSPHERIX consortium, we were awarded more telescope time to observe another transit with IGRINS. The hope is that more baseline spectra, simultaneous photometry and observations which capture the entire transit (including ingress) will help to tighten the constraints on AU Mic b's atmospheric composition.

### 3.7.2 Atmospheric retrievals

In this chapter, I concentrated only on data reduction and subsequent grid-based cross-correlation tests to attempt to detect an atmosphere. Similar works, with HRCCS detections, often progress to a grid-based or free atmospheric retrieval in order to quantify molecular abundances (e.g., Brogi et al., 2023). Since we did not detect an atmospheric signal in the real data via cross-correlation, there would be no purpose to merit a (computationally expensive) atmospheric retrieval here.

Yet, with additional high-resolution spectra, the data presented here could be used in combination for a future atmospheric retrieval.

## 3.8 Conclusions

In this chapter, I have analysed transit spectra of AU Mic, with the aim of characterising the atmosphere of the inner, transiting young sub-Neptune AU Mic b. I reported null detections of an atmosphere in chemical equilibrium, containing $H_2O$, $CH_4$, CO, $CO_2$ and $NH_3$. Similarly, the data are not sensitive to CO spectral features, corresponding to abundances $10^{-6} < \mathrm{VMR[CO]} < 10^{-1}$, even at the maximal possible scale height of AU Mic b. While the data yielded null detections, using standard HRCCS techniques, I was able to place useful constraints on the atmospheric composition of AU Mic b:

- Under the assumption of a clear atmosphere, completely free of haze beyond an altitude corresponding to $\log_{10} P_c = -2$, the IGRINS and SPIROU data together are able to rule out a self-consistent, $H_2$/He atmosphere following equilibrium chemistry, at a temperature of $T_{\mathrm{eq}} = 593\,\mathrm{K}$. This prevails for metallicities between $0.0 < \log_{10}[\mathrm{Fe/H}] < 2.0$ and C/O ratios between $0.2 < \mathrm{C/O} < 1.5$.

- The above parameter space is truncated when considering opaque cloud decks, at altitudes from $-2 < \log_{10} P_c < -6$. Still, I was able to retrieve injected atmospheres in chemical equilibrium, and individual species $CH_4$, $H_2O$ and $NH_3$, with stronger constraints over $CH_4$.

- Testing 'free abundance' models with opaque cloud decks, I extend the constrained parameter space to CO and $CO_2$.

- With the injection tests suggesting that the data would have been sensitive to $CH_4$, its lack may be a result of a shifted $CH_4$-CO boundary compared to the theoretical estimate, an underestimated equilibrium temperature, a high-altitude cloud deck beyond $\log_{10} P_c[\mathrm{bar}] < -4$, or in fact, chemical disequilibrium processes.

AU Mic b is a unique target, with many qualities towards a compelling science case. Future observations are inevitable and warranted, towards which I would hope the constraints presented in this chapter are useful.

*I suppose it is tempting, if the only tool you have is a hammer, to treat everything as if it were a nail.*

— Abraham Maslow, *Toward a Psychology of Being, 1962*

# CHAPTER 4

# THE IMPACT OF STELLAR INHOMOGENEITIES ON TRANSMISSION SPECTROSCOPY

## Contents


**4.1 Introduction and motivation . . . . . 92**
4.1.1 The Rossiter-Mclaughlin effect . . . . . 93
4.1.2 Stellar spots . . . . . 95
4.1.3 Centre-to-limb variation . . . . . 98
**4.2 Theoretical formalism . . . . . 99**
**4.3 Spectral forward model . . . . . 100**
4.3.1 Forward model structure . . . . . 100
4.3.2 Test cases . . . . . 103
4.3.3 Prescribed star-planet archetypes . . . . . 104
**4.4 A K dwarf case study: HD 189733 . . . . . 105**
4.4.1 The RM effect . . . . . 107
4.4.2 The impact of (only) unocculted spots . . . . . 111
**4.5 An M dwarf case study: AU Mic . . . . . 112**
4.5.1 The RM effect . . . . . 113
4.5.2 The impact of unocculted and occulted spots . . . . . 113
4.5.3 Comparison to theoretical formalism . . . . . 117

**4.6 Future work . . . . . 119**
4.6.1 Making the code public and publication . . . . . 119
4.6.2 Faculae . . . . . 119
4.6.3 Spectra of inhomogeneities . . . . . 120
4.6.4 Accounting for heterogeneities in high-resolution studies 120
**4.7 Conclusions . . . . . 122**

## 4.1 Introduction and motivation

Contrary to common treatment in high-resolution cross-correlation spectroscopy (HRCCS), stars are not homogeneous, steady-state disks in the sky. They are complex astrophysical objects, fusion reactors with complex structure. Stars are variables. Considering transmission spectroscopy (see Chapter 2, §2.2), the unocculted stellar spectral lines (and contribution from behind the planet) can vary in depth and shape over time due to (i) the occultation of the planet, and (ii) inherent short-term stellar time-variability. It is important to understand the contribution to the stellar spectrum both from the unocculted disk, and the occulted portion which illuminates the planet atmosphere, since our inferences about the transiting planet atmosphere are dependent on the stellar assumptions. Intrinsic stellar variability, such as granulation and oscillations (point (ii)), is independent of and occurs even without the occultation of a planet. This is sure to have an impact on transmission spectroscopy, but is challenging to model, requiring comprehensive magnetohydrodynamic simulations.

The technique of high-resolution transmission spectroscopy combines aspects of the transit and radial velocity detection methods, as detailed in Chapter 1, §1.1.3. Though the impact of activity on low-resolution spectroscopy has been thoroughly discussed in the literature (e.g., Rackham et al., 2023), there have been comparably fewer studies regarding high resolution. In this chapter, I endeavour to investigate some of the stellar-induced effects on high-resolution transmission spectroscopy measurements, by simulating a number of test cases. Here, I only consider variability caused by a planet occultation; these effects, encompassing

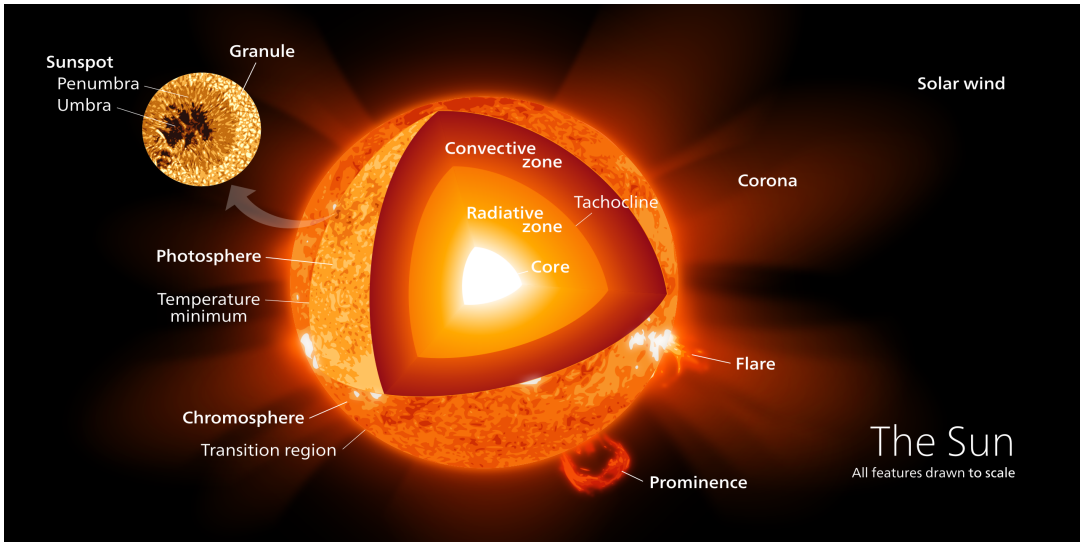


**Figure 4.1:** The interior structure and atmosphere of the Sun. Figure source: Wikipedia commons, Kelvin Song.

phenomena like the Rossiter-Mclaughlin (RM) effect, photospheric spot crossings and centre-to-limb variation (CLV), can have a higher impact on transmission spectroscopy and can be modelled. I introduce these stellar phenomena in turn below, and their expected impact on the stellar spectrum.

### 4.1.1 The Rossiter-Mclaughlin effect

The first stellar non-uniformity I consider in this study is the impact of the stellar rotation on the spectra. The spectral lines of a rotating star will be broadened compared to a non-rotating (or very slowly rotating) star. This is because each position on the stellar disk has a different radial velocity according to the $v \sin i$ of the star. The disk-integrated stellar spectrum is then an equal contribution of positive and negative radial velocities, translating to an equal number of red-shifted and blue-shifted components. The composite stellar line then is only broadened, and not shifted from its rest frame velocity.

The picture becomes more complex when introducing a transiting planet; over the course of the transit, the planet occults different velocity contributions, causing an asymmetry when integrating the remaining, unocculted stellar light. Fig. 4.2 demonstrates an exaggerated example, where the stellar rotation axis is

perpendicular to the line of sight. In this example, upon ingress, the planet occults the hemisphere of the stellar disk which is rotating towards the observer. The occulted stellar line is shown in blue – this would be missing from the disk-integrated spectrum and so the integrated unocculted spectrum would appear red-shifted. The same is true on reverse for egress. The stellar lines thus experience a distortion during the planet transit. This is a well known phenomenon, known as the Rossiter-Mclaughlin (RM) effect (Cegla et al., 2016); the position of the distortion of the stellar line is a function of the rotational period of the star, $P_{\rm rot}$, planet impact parameter, $b$, and transit duration, $T_{\rm dur}$. It follows that in radial velocity studies, whereby the stellar spectrum is cross-correlated with a template to derive its velocity shift, an additional signature is imparted atop of the radial velocity curve, mid-transit. This phenomenon is also a function of, and has been thus exploited to measure, the obliquity of a planet, the angle between the stellar rotation axis and the perpendicular to the orbital plane of the planet (see e.g., Martioli et al., 2020). Further, the occultation of the planet can be used to study the locally occulted stellar spectrum behind the planet. Such measurements can again be used to derive the sky-projected obliquity as well as the true obliquity (Cegla et al., 2016).

In HRCCS, we take advantage of the orbit-induced Doppler shift of the planet spectral lines. The total planet radial velocity in the stellar rest frame is given by:

$$v_p(t) = K_p \sin(2\pi\varphi) \tag{4.1}$$

where $K_p$ is the radial velocity semi-amplitude, and $\varphi$ are the orbital phases. Considering the stellar lines, they will experience a distortion due to the occultation of the planet. Firstly, it follows that the consequent 'variability' of the stellar spectrum will add noise to any subsequent cross-correlation analyses, no matter the chemical make-up of the planetary atmosphere. But, there is a specific problem when searching for a chemical species that exists both in the star and planet atmosphere. In this scenario, the distortion traverses the stellar line as a function of time, thus the RM directly interacts with the species probed, and can mimic (or mask) a planetary

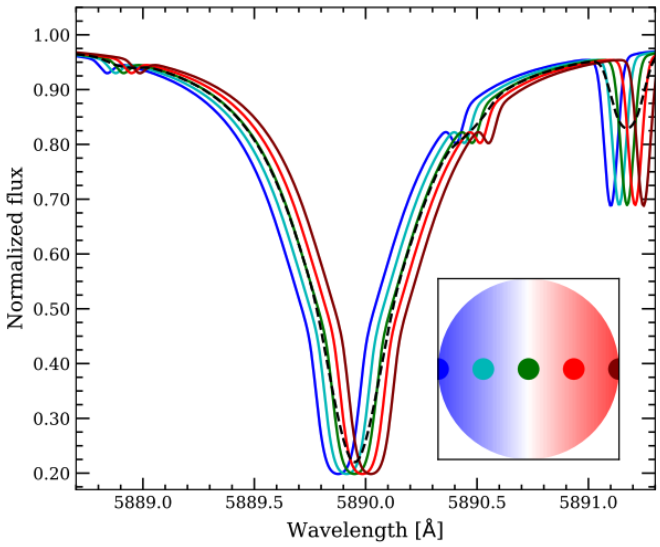


**Figure 4.2:** Impact of stellar rotation on a stellar spectral line. For different planet positions relative to the rotating stellar disk (sub-figure), the occulted stellar line contribution is shown in the corresponding colour. The out-of-transit disk-integrated stellar line is shown for reference in the black dashed line. Figure from Casasayas-Barris et al. (2020).

signal (Brogi et al., 2016). Typically, the apparent radial velocity semi-amplitude of the stellar line distortion, induced by the transiting planet, will be proportional to:

$$K_{\mathrm{RM}} \approx \frac{\mathrm{FWHM}}{\sin(2\pi\varphi_2) - \sin(2\pi\varphi_1)} \times \cos(\lambda_o) \tag{4.2}$$

where FWHM is the full-width half maximum of the stellar line, $\lambda_o$ is the sky-projected obliquity, and $\varphi_1/\varphi_2$ the phase of ingress/egress. Since the distortion is a 'bump', an obstruction of a velocity contribution, we might expect it to correspond to an anti-correlation in $\{K_p - v_{\mathrm{sys}}\}$ space, when cross-correlated with a planetary model. One could imagine this to be most problematic when the semi-amplitudes of the planet and RM effect are comparable, i.e., $K_p \sim K_{\mathrm{RM}}$.

I investigate the impact of the stellar rotation on high-resolution cross-correlation spectroscopy studies in this chapter, and the potential risks posed if left uncorrected.

### 4.1.2 Stellar spots

Stars are hosts to strong magnetic fields (potentially ranging from a few G to the order of ∼kG) as a result of their stellar dynamos; plasma fluid flow induces electric

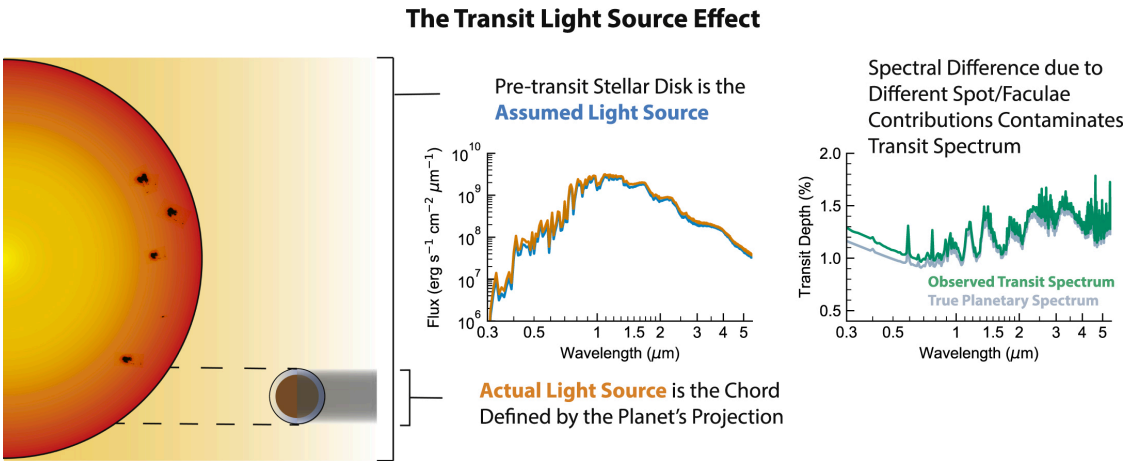


**Figure 4.3:** The transit light source effect, as presented by Rackham et al. (2018). **Left:** A schematic to show that the transmission spectrum of a planet atmosphere depends on the illumination by the occulted region of the star. **Middle:** The incident stellar spectrum (orange) can differ from the disk-integrated, out-of-transit spectrum (blue). **Right:** If the stellar disk is subject to spot/faculae, the observed transmission spectrum (green) can differ (as a function of time) compared to the true transmission spectrum (grey). Figure from Rackham et al. (2018).

current, which generates a magnetic field (for a comprehensive review of dynamo theory, see Rincon, 2019). These magnetic fields instigate various types of observable stellar activity phenomena, within the photosphere and chromosphere. Stellar spots are one such phenomenon, originating from the emergence of a magnetised flux tube from the photosphere. In these regions of locally amplified magnetic field, which dominates over stellar convection, the upwelling of plasma and the associated flux is suppressed. This leads to a localised cooling of the suppressed region, and, if strong enough, a darkening of the stellar photosphere. For comprehensive reviews of stellar spots, I refer the reader to Strassmeier (2009) and Berdyugina (2005).

Stellar spots imprint signatures in the stellar spectrum. Their own spectrum differs from that of the quiet photosphere, depending on the local magnetic field strength and spot temperature. The impact on the stellar spectrum may be studied by obtaining a spectral time-series; a dark spot will induce a 'bump' in a stellar line profile, traversing the profile as a result of the stellar rotation. This has been exploited for the purpose of mapping stellar surfaces, a technique known as 'Doppler imaging' (see Kochukhov, 2016, for a review).

Towards atmospheric characterisation, the effect and consequent attempts to account for stellar spots has recently been studied for low-resolution transmission spectroscopy (Rackham et al., 2018; Rackham & de Wit, 2023; Rackham et al., 2023). To account for occulted spots, current methodology simultaneously fits bumps in the transit light curve, from which the spot size and temperature can be inferred. The scenario is more challenging for unocculted spots, wherein there is not necessarily a distinct time variation on the spectra. The observed transmission spectrum is dependent on the spectrum (or light contribution) from the occulted region of the stellar disk, at each point in time along the transit, the so-called 'transit light source effect' (TLSE, Rackham et al., 2018). Assuming that the illuminating light source is equal to the stellar disk-integrated pre-transit spectrum can lead to inaccuraries in the transmission spectrum; this is demonstrated in the schematic of Fig. 4.3. Rackham & de Wit (2023) demonstrate with simulated *JWST/NIRSpec* and *JWST/PRISM* observations, that inaccurate stellar models can cause the stellar contamination correction to dominate the uncertainty budget of the acquired transmission spectrum. It is then important to understand the illuminating light source, and how it compares to the unocculted stellar disk contribution. Some have used photometric monitoring of the host star in order to constrain the (unocculted) spot coverage (e.g., Nascimbeni et al., 2015; Libby-Roberts et al., 2022). However, this approach would only be sensitive to variable rather than a constant level of spot coverage. Furthermore, it affords little information regarding spot distribution. Simultaneous photometry can be useful towards identifying spot crossing events, especially using photometric bands in which the spot contrast is greater.

In the high-resolution case, though the same theory of TLSE applies, we have much finer resolution, and so the impact of stellar heterogeneities is expected to be more acute. Moreover, we work in cross-correlation space, rather than on the spectra themselves. We are then concerned with the likelihood of inferring a non-existent atmosphere or incorrect atmospheric parameters, or the likelihood of inhomogeneities obstructing an atmospheric detection. This has not been extensively studied for high-resolution transmission spectroscopy, with only a handful of studies

in the literature (e.g., Genest et al., 2022), and fewer still towards low-mass stellar systems whereby the impact is likely to be larger, due to shared molecular lines between the star and planet.

### 4.1.3 Centre-to-limb variation

Limb darkening impacts the flux contributions from different regions of the projected stellar disk. This is a line-of-sight effect; as one observes the centre of the stellar disk, one probes deeper into the stellar photosphere compared to the depth probed at the limbs of the star, assuming the same optical depth. Further, the stellar surface is constructed with individual granules. Each granule is characterised by the convective heat transport within the photosphere, and therefore contributes a velocity effect as plasma material upwells and falls down towards and away from the observer (Nordlund et al., 2009). This contributes to the centre-to-limb variation (CLV) effect. The limb darkening of individual stellar spectral lines differs from the broad-band limb darkening of the continuum, affecting both their intensity and shape, as seen in Cegla et al. (2018). The impact of this effect on high-resolution, transmission cross-correlation spectroscopy was demonstrated in (e.g.,) Chiavassa & Brogi (2019) and Yan et al. (2017). Flowers et al. (2019) employed the 3-D simulation of stellar convection from Chiavassa & Brogi (2019), before forward modelling a time-series of stellar spectra. Applying these to correct archival CRIRES data of the stellar spectrum, Flowers et al. (2019) revealed an unambiguous, $> 7\sigma$ detection of CO from the atmosphere of the hot Jupiter HD 189733 b, previously only marginally detected having implemented a time-constant stellar correction (Brogi et al., 2016). To fully account for CLV, one would require intensive 3-D MHD simulations; we thus consider this beyond the scope of our study. In addition, the CLV effect is expected to have a smaller impact in observations of lower mass stars (Czesla et al., 2015). For these reasons, and since it has been studied in transmission before, I do not fully account for CLV here. I do, however, account for broadband continuum limb darkening.

## 4.2 Theoretical formalism

Rackham et al. (2018) derived a 'contamination factor', $\varepsilon_\lambda$, for the impact of unocculted stellar spots on the apparent transit depth $D_{\mathrm{obs},\lambda}$ compared to the intrinsic transit depth $D_\lambda$. They applied this contamination factor towards low-resolution spectroscopy. I reprint the formalism here:

$$D_{\mathrm{obs},\lambda} = \frac{D_\lambda}{1 - f_{het}(1 - \frac{F_{het}}{F_{phot}})} = \varepsilon_\lambda D_\lambda, \tag{4.3}$$

where $f_{het}$ is equal to the fraction of the **entire** projected stellar disk covered by spots, $F_{het}$ is the spot spectrum and $F_{phot}$ is the photospheric spectrum. They also noted that this formalism is easily extended to include the opposing impact of hotter faculae.

I reformed Equation 4.3, based on the same assumptions as Rackham et al. (2018), to derive the contamination factor from both unocculted *and* occulted stellar spots:

$$\varepsilon(\lambda, t) = \frac{f''_{het}(t) F_{het}(\lambda) + \left[1 - f''_{het}(t)\right] F_{phot}(\lambda)}{f_{het} F_{het}(\lambda) + \left[1 - f_{het}\right] F_{phot}(\lambda)}, \tag{4.4}$$

where $F_{het}$, $F_{phot}$ and $f_{het}$ have the same definitions as above, and $f''_{het}$ is the fraction of the **occulted** stellar disk covered by heterogeneities. The full derivation of Equation 4.4 is given in Appendix B.1. As a sanity check, Equation 4.4 reduces to the factor $\varepsilon_\lambda$ in Equation 4.3, for the case of zero spot occultation events, in which $f''_{het}(t) = 0.0$. I use this formalism as a first-order theoretical basis, and refer back to it in this chapter. I summarise the key terms to note, defined as follows:

$F_{het}$ the spectrum of the heterogeneity;

$F_{phot}$ the spectrum of the photosphere;

$f_{het}$ the total fraction of the **entire** projected stellar disk covered by heterogeneities;

$f'_{het}(t)$ the fraction of the **unocculted** stellar disk covered by heterogeneities;

$f''_{het}(t)$ the fraction of the **occulted** stellar disk covered by heterogeneities;

$f_{tc}$ the fraction of the **transit chord** covered by heterogeneities.

## 4.3 Spectral forward model

### 4.3.1 Forward model structure

We construct a framework to forward model a sequence of high-resolution spectra from a star-planet system, including the transit of a planet. The structure of the framework is as follows:

(i) First, we simulate a stellar disk.

(ii) We (optionally) add stellar spots to the disk, either opaque or with their own spectrum.

(iii) We simulate a transiting planet, either completely opaque or with an atmosphere.

(iv) We integrate the stellar and planetary spectral contributions as a function of time.

I refer the reader Fig. 4.4 for a schematic of this method. I proceed to detail further the additive components of our model.

**(i) Simulating the stellar disk.** We do so using the public, open-source PYTHON package STARRY[1] (Luger et al., 2019, 2021a,b). Instantiating a **map** object, STARRY allows us to divide the stellar disk into a grid map, with each stellar cell denoted with indices $ij$.

**(ii) Adding stellar spots.** We assume the following spot properties: the spot temperature, $T_{spot}$; number of spots, $N_{spot}$; the average spot size relative to the size of the stellar disk; and the maximum spot latitude. We then sample a random distribution to assign spot locations across the disk, removing any overlapping spots. At this stage, we can control the fraction of spots present in the transit chord. We define $f_{tc}$, the fraction of the transit chord covered by heterogeneities, i.e., $f_{tc} = 0.0$ would enforce zero spot-occultation events. Then, the spots are assigned either their own spectrum, set by $T_{spot}$, but otherwise matching parameters to the photospheric spectrum, or are completely opaque.

[1] https://starry.readthedocs.io/en/latest/

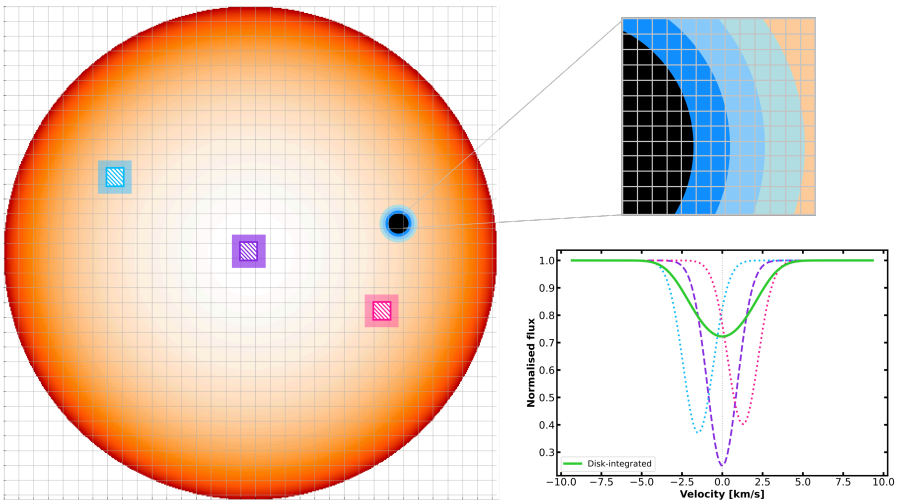


**Figure 4.4:** Schematic to demonstrate the process of the forward model, described in §4.3. **Left panel:** The visible stellar surface is divided into a grid, whereby the total stellar flux and spectrum is given by the integral of all unocculted grid points. If an atmosphere is included around the planetary core, this is simply an opacity as a function of wavelength (demonstrated by shades of blue in **top right panel**). Here, the atmospheric annulus has been exaggerated; in reality it is thinner. **Bottom right panel:** Line profile contributions from different stellar grid points (marked in the corresponding colour), as well as the disk-integrated profile (in green).

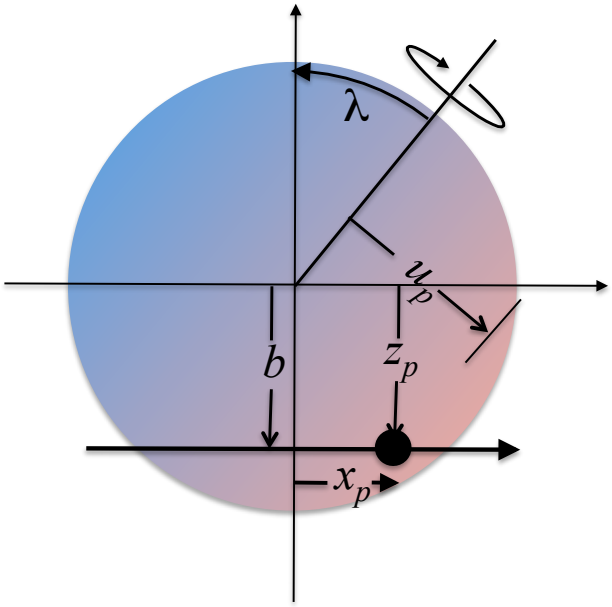


**Figure 4.5:** A visual of the stellar coordinate system and relevant geometry used in this chapter. The stellar hemisphere rotating towards/away from the observer is coloured in blue/red. The location of the transiting planet disk (in black) at any point in time is expressed by coordinate $(x_p, z_p)$. The angle $\lambda$ represents the sky-projected obliquity, the angle between the normal to the planet orbital plane and the stellar rotation angle. Figure from Collier Cameron et al. (2010).

**(iii) Adding a transiting planet.** We assume the following star-planet properties in order to simulate the transit: the semi-amplitude of the planet radial velocity, $K_p$; phase sampling; orbital period; nominal planet radius, $R_p$; semi-major axis; planet orbital inclination; planet impact parameter, $b$; planet eccentricity, $e$; argument of periapsis, $\omega$; and the projected spin-orbit angle or 'obliquity', $\lambda_o$. At each point in time, the co-ordinates $(x_p, z_p)$ of the planet are given by:

$$\begin{aligned} x_p &= r\sin(\nu + \omega - \pi/2) \\ z_p &= r\cos(\nu + \omega - \pi/2) \times \cos i \end{aligned} \tag{4.5}$$

where $r$ is the instantaneous distance between the star and the planet, $\nu$ is the true anomaly, and $i$ the stellar inclination (see Winn, 2014, for a full derivation and description of these equations). We project these co-ordinates to the stellar rest frame via,

$$\begin{aligned} u_p &= x_p\cos\lambda_o - z_p\sin\lambda_o \\ v_p &= z_p\cos\lambda_o + x_p\sin\lambda_o \end{aligned} \tag{4.6}$$

with respect to the stellar rotation axis (see Fig. 4.5).

In the cases where the planet is fully opaque, we block all flux contributions from cells occulted by $R_p^2$. Alternatively, if adding an atmosphere to the planet, we sub-sample each stellar cell $ij$, as visualised in Fig. 4.4. Assuming an 'injected' planet transmission model, pre-computed with PETITRADTRANS, we calculate the fraction of the stellar cell $ij$ occulted by the planet atmosphere as a function of wavelength. We are then able to recompute the stellar flux contribution from cell $ij$, considering that which is obstructed by the planet and atmosphere.

**(iv) Integrating all spectral contributions.** We can assign either a single line profile, or a full spectrum to each stellar cell. We then shift each spectrum according to the local velocity, $v_{ij}$. I demonstrate this for a line profile in the bottom right subset panel of Fig. 4.4 – the intrinsic line profile is Doppler-shifted, and scaled according to each grid-point projection and limb darkening. Once we have assigned each cell a stellar spectrum contribution (either spot or photosphere), and appropriately scaled it if there is also a planet contribution, then we turn to

integrating all the cell contributions. The output is a time-series of line profiles or spectra accounting for the above, $\boldsymbol{\mathcal{S}}(\lambda, t) = \{\mathcal{S}_1, ..., \mathcal{S}_V\}_{i=1}^{V}$.

Having forward-modelled the stellar (+ planet) spectra, I add noise to the spectra. I use a similar method to Hood et al. (2020); I begin by defining a signal-to-noise per resolution element, $\mathrm{SNR}_{\mathrm{res}}$. To convert this to a signal-to-noise per pixel, I multiply this by the square root of a normalised telluric spectrum, $\mathbf{T}$, and the number of resolution elements per pixel, $n_{\mathrm{res}}$, i.e., $\mathrm{SNR}_{\mathrm{pix}} = \mathrm{SNR}_{\mathrm{res}} \cdot \sqrt{\mathbf{T}(\lambda)} \cdot n_{\mathrm{res}}$. I then add noise to the spectra sampled from a Gaussian distribution as, $\mathcal{N}(0, 1/\mathrm{SNR}_{\mathrm{pix}})$. Finally, I convolve the spectra to the desired resolution. By way of 'detrending' the spectra, I limit the reduction to a division by the mean out-of-transit spectrum, and an optional PCA treatment, removing $\mathbf{N}_{\mathrm{PCA}}$ components. Example forward-modelled spectra are shown in Appendix B, in Fig. B.1 and Fig. B.2.

### 4.3.2 Test cases

This framework allows us to successively complicate the forward model, and observe the consequent degradation of the planet atmosphere signal. I thus compare the following cases:

**CASE 1** A homogeneous (static) star case, whereby all stellar time variability is neglected. I consider the stellar spectrum to be constant in time, and therefore easily removed by utilising the out-of-transit spectra. I then inject the planet atmosphere forward model, at the appropriate time-dependent velocity. In this case, we would expect the residuals to contain simply noise + the Doppler-shifting planet signal.

**CASE 2** A rotating star case, where the spectral contributions are shifted depending on the stellar rotation, $v \sin i$. Then, include a transiting bare rock to block select velocity contributions from the stellar disk. This is the Rossiter-Mclaughlin effect, and includes no planetary atmosphere signal.

**Table 4.1:** The characteristic parameters used in the forward modelling of archetypes listed in §4.3.3.

| Parameter | Unit | HD 189733 | AU Mic |
|---|---|---|---|
| Stellar type | – | K2 | M1 |
| $T_{phot}$ | K | 5000 | 3700 |
| $v \sin i$ | km/s | 3.5 | 7.8 |
| $R_p$ | $R_*$ | 0.15 | 0.05 |
| $K_p$ | km/s | 152.1 | 82.9 |
| Phase coverage | – | $[-0.0383, +0.0383]$ | $[-0.0154, +0.0154]$ |
| Impact parameter | – | 0.656 | 0.18 |
| Average spot size | Fraction of stellar disk area | 0.02 | 0.08 |
| Max spot latitude | Degrees | 50 | 80 |
| Number of spots | – | $10 - 15$ | $15 - 20$ |

**CASE 3** A rotating stellar disk, and an atmosphere around the transiting planet. Same as **CASE 2** with an atmosphere around an opaque planet core rather than a completely opaque disk.

**CASE 4** A rotating stellar disk with opaque spots, and an atmosphere around the transiting planet. Similar to **CASE 3** with addition of spots on the stellar disk. The spots do not evolve, with the exception of traversing the projected stellar disk with the stellar rotation period, and are completely static in size, shape and contrast.

**CASE 5** A rotating stellar disk with spots, and an atmosphere around the transiting planet. This is the same as **CASE 4** but here the spots have their own spectrum, defined by $T_{spot}$.

### 4.3.3 Prescribed star-planet archetypes

I test two distinct star-planet cases:

(1) an early K dwarf orbited by a hot Jupiter, akin to the HD 189733 system;

(2) a pre-main sequence star orbited by a sub-Neptune, with similar properties to the AU Mic system.

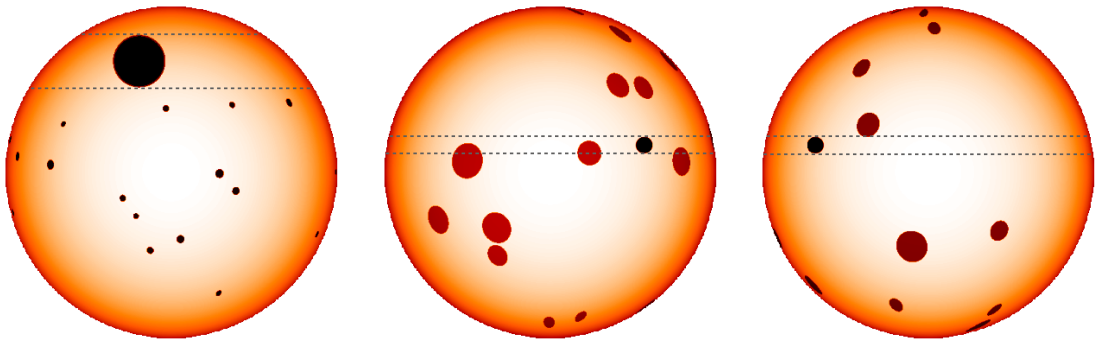

**Figure 4.6:** Example stellar maps for the three archetypes described in §4.3.3. **Left:** Spotted surface of HD 189733, where the fraction of spots in the transit chord, $f_{tc}$, is set to zero. Then, the spotted surface of AU Mic, with a spot distribution such that the transit chord contains a fraction of spots equal to **(middle:)** $f_{tc} = 0.1$, and **(right:)** $f_{tc} = 0.0$, i.e., no occultation events. In each case, the transit chord is shown bounded by dashed lines.

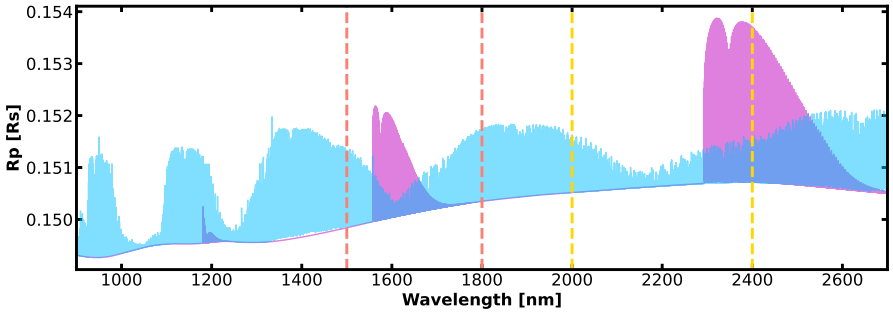


**Figure 4.7:** Atmospheric forward models of HD 189733 b, with $H_2O$ shown in blue and CO in magenta. The planetary radius is shown in units of stellar radii. The boundaries of the H and K-bands are shown in coral and gold dashed lines.

For each star-planet case, I test the 5 forward model cases, varying parameters such as the composition of the transiting planet atmosphere, and composition, distribution and coverage of spots. I provide a summary of the characteristic parameters used for each case in Table 4.1. Shown in Fig. 4.6 are some example stellar maps (which fulfill steps (i)-(iii) described in §4.3.1), used for the forward models. For each prescribed archetype, the transit coordinates are the same for every stellar surface map.

## 4.4 A K dwarf case study: HD 189733

I begin by demonstrating the successive test cases from §4.3.2, for the HD 189733 system. This star is a K dwarf and host to a canonical hot Jupiter (Bouchy et al.,

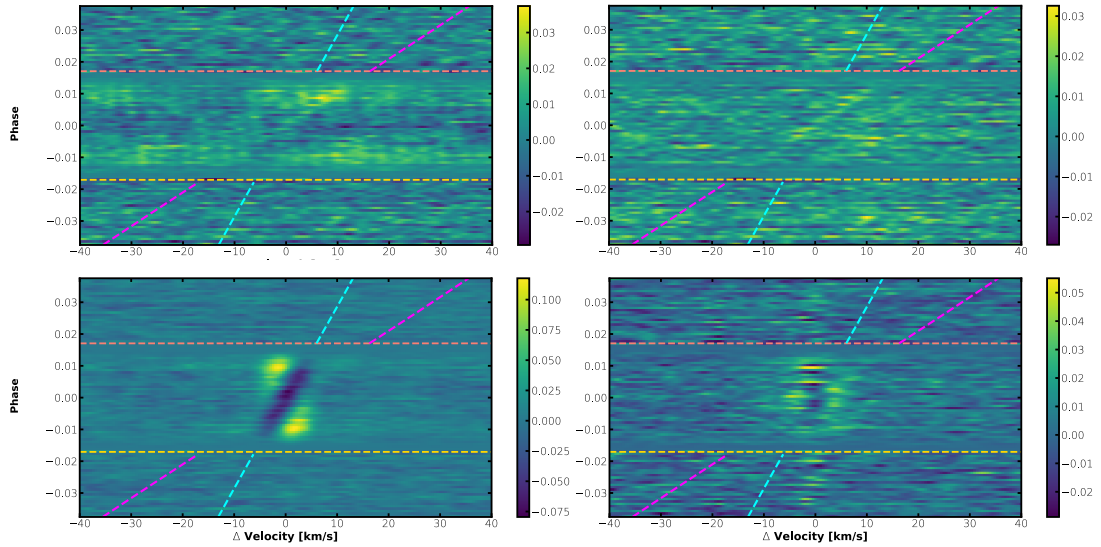


**Figure 4.8:** Cross-correlation trail of the **CASE 3** (RM) forward model, for the HD 189733 archetype, for a **(top row:)** $H_2O$ atmosphere in the H-band, at $SNR_{res} = 2000$, and **(bottom row:)** CO atmosphere in the K-band, at $SNR_{res} = 500$. In each cross-correlation coefficient colourmap, the phase is on the y-axis such that each row represents the cross-correlation function of the residual spectrum at that phase with the atmospheric spectral template. The ingress and egress phases are indicated by the yellow and coral dashed lines respectively. The out-of-transit dashed lines point to the (in-transit) expected radial velocity trail of (i) the planet signal in magenta, and (ii) the RM signal in cyan. The **left column** shows the result having applied no PCA detrending to the spectra (only removing the mean out-of-transit spectrum), and the **right column** shows the result having removed 5 PCA components.

2005), extensively studied at high resolution (e.g., Birkby et al., 2013; Rodler et al., 2013; Brogi et al., 2016, 2018; Flowers et al., 2019; Boucher et al., 2021). I focus on the two main species detected in the planet atmosphere, namely CO and $H_2O$. The transmission spectra of HD 189733 b, computed with PETITRADTRANS[2], for $H_2$/He-dominated atmospheres with chemical equilibrium abundances of CO (pink) and $H_2O$ (blue) are shown in Fig. 4.7. These are the atmospheres used for step (iii) for **CASE 3**, **CASE 4** and **CASE 5**. To provide a basis detection to which I can refer back, I cross-correlate the models with the residuals of **CASE 1**, the static star case. The results are indicated in Table 4.2; an example cross-correlation map is shown in Fig. 4.9, for CO in the H band.

[2] https://petitradtrans.readthedocs.io/en/latest/

### 4.4.1 The RM effect

As described in §4.1.1, the occultation of an (opaque) planet alone can mask a planetary atmosphere detection, since different stellar velocity contributions are obscured. I demonstrate its impact here; I use the simulator to forward model the **CASE 3** spectra, for the HD 189733 archetype, assuming a $v \sin i = 3.5\,\mathrm{km/s}$. For clarity, these spectra are derived from forward-modelling the rotating (spotless) stellar surface, transited by a planet with a $H_2$/He-dominated atmosphere and $H_2O$/CO at chemical equilibrium abundances (see Fig. 4.7 for the transit radius). I add noise to the spectra, and perform the basic 'reduction' (see §4.3.1 for details). The residual forward-modelled spectra for the CO case, having removed the out-of-transit mean, are shown in Fig. B.1 of Appendix B, as an example. Then, the time-series of cross-correlation functions for a $H_2O$ (top) and CO planet spectrum (bottom), in the H-band and K-band respectively, are shown in the left column of Fig. 4.8. Assuming a $v \sin i = 3.5\,\mathrm{km/s}$ and resolution element of width 2km/s for HD 189733, we would expect any RM-signature to have an effective radial velocity of $K_{\mathrm{RM}} \sim 56\,\mathrm{km/s}$ (Equation 4.2). The Doppler shadow induced by the RM effect is particularly evident in the case of CO, at the predicted characteristic radial velocity (cyan dashed line in Fig. 4.8). It dominates the cross-correlation map, obscuring the planet trail. Applying PCA starts to dampen the Doppler shadow (right column of Fig. 4.8), since the RM exists at a shallower velocity trail. In panel (c) of Fig. 4.9, I show the conversion to $\{K_p - v_{\mathrm{sys}}\}$ space, having collapsed the time series along different velocity solutions (for the $\mathbf{N}_{\mathrm{PCA}} = 0$ case). The $H_2O$ results shown (top row of Fig. 4.9) are for the $1500 - 1800\,\mathrm{nm}$ band, while for CO (bottom row of Fig. 4.9) I concentrated on $2300 - 2400\,\mathrm{nm}$. The planetary atmospheres are not detected for **CASE 3**, with this rudimentary reduction.

To show the RM cross-correlation signature, I cross-correlate **CASE 2** (a rotating stellar disk, with transiting opaque planet, with no atmosphere) with the planetary models. The results are shown in panel (b) of Fig. 4.9. In the case of carbon monoxide (bottom row in Fig. 4.9), there is a clear, defined RM signature in the correlation map, which closely matches the signature of panel (c). The peak

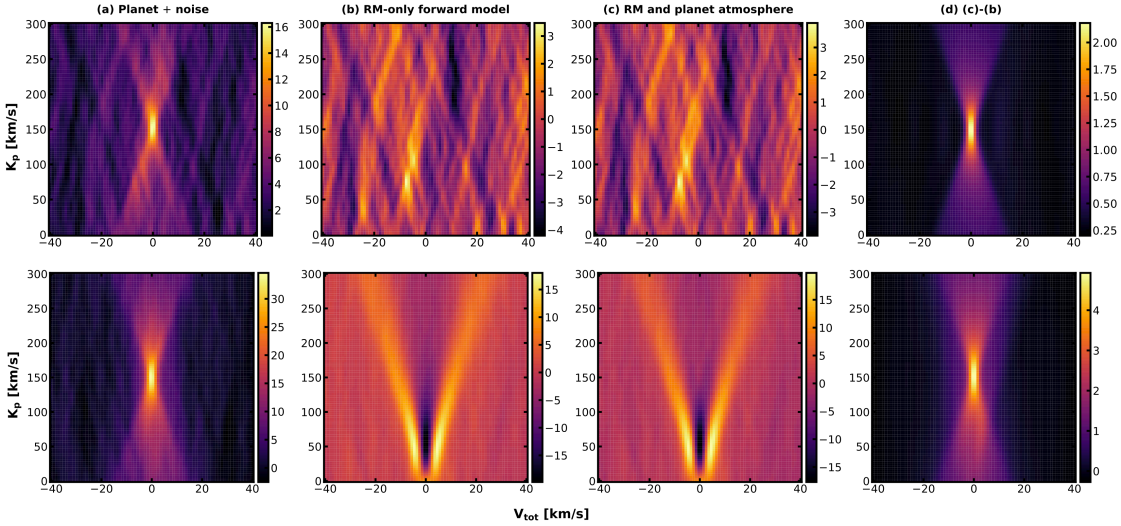


**Figure 4.9:** The cross-correlation significance colourmaps of **(top panel):** $H_2O$ and **(bottom panel):** CO for the HD 189733 archetype. **Panel (a):** The cross-correlation signature of the planet model, having injected into a noise map (described in §4.3.1), with constant stellar spectrum (**CASE 1**). **Panel (b):** Result of cross-correlating the planet model with the RM-only forward-modelled spectra, of **CASE 2**. This is the RM signature in cross-correlation space. **Panel (c):** Cross-correlating the planet model with the **CASE 3** spectra; the planet signal is obscured. **Panel (d):** The difference between map (c) and map (a). Removing the RM cross-correlation signature clearly reveals the planet atmosphere signal. The spectra for panels (a)-(c) included the same noise realisation, corresponding to $\mathrm{SNR_{res}} = 500$. The detrending of the spectra was limited to dividing out the mean out-of-transit and a normalisation; PCA was not applied to these spectra before cross-correlation.

anti-correlation can be seen at the predicted $K_{\mathrm{RM}} \sim 56\,\mathrm{km/s}$. On the other hand, the RM imprint is not a distinguished signature above the noise in the case of $H_2O$ (top row of Fig. 4.9). This is to be expected at the photospheric temperature of $T_{phot} = 5000\,\mathrm{K}$, wherein we would expect very little (if any) water. Yet, panel (c) of the top row in Fig. 4.9 shows that the RM effect still has the power to obscure an atmospheric signal of a molecule not present in the photosphere. All stellar spectral lines are distorted to some extent by the RM effect, which translates to additional correlated noise in $\{K_p - v_{\mathrm{sys}}\}$ space. In Fig. 4.9, this noise dominates over the cross-correlation signature of the planet $H_2O$ atmosphere. Panel (d) shows the subtraction of the **CASE 2** RM-only cross-correlation signature in panel (b), from the **CASE 3** cross-correlation map in panel (c). The planetary signal at $K_p \sim 153\,\mathrm{km/s}$ is uncovered, and matches the signature in panel (a), wherein I

**Table 4.2:** Detection of an atmospheric signal from HD 189733 b, for different stellar spectra cases (§4.3.2) at a resolution of $R \sim 100,000$ and a $\mathrm{SNR_{res}} = 1000$. I list the recovered significances having removed the mean out-of-transit spectrum, and 1 PCA component. **CASE 1** is the reference case (planet, static star and noise), so I also give the detection significances relative to this case. The **CASE 5** results are given for $f_{tc} = 0.0$ and $T_{spot} = 3700\,\mathrm{K}$.

| Molecule | Band | CASE # | Significance ($\sigma$) | Fraction of CASE 1 significance |
|---|---|---|---|---|
| CO | H-band | **CASE 1** | 33.56 | 1 |
| | | **CASE 3** | 6.83 | 0.20 |
| | | **CASE 4** | 6.85 | 0.20 |
| | | **CASE 5** | 6.82 | 0.20 |
| | K-band | **CASE 1** | 42.72 | 1 |
| | | **CASE 3** | 7.76 | 0.18 |
| | | **CASE 4** | 7.80 | 0.18 |
| | | **CASE 5** | 8.02 | 0.19 |
| $H_2O$ | H-band | **CASE 1** | 30.06 | 1 |
| | | **CASE 3** | 5.32 | 0.18 |
| | | **CASE 4** | 5.23 | 0.17 |
| | | **CASE 5** | 4.37 | 0.15 |
| | K-band | **CASE 1** | 8.97 | 1 |
| | | **CASE 3** | 3.53 | 0.39 |
| | | **CASE 4** | 3.52 | 0.39 |
| | | **CASE 5** | 3.63 | 0.40 |

tested the injection of the Doppler-shifting planetary signal into the same noise map.

The example shown in Fig. 4.9 is for $\mathrm{SNR_{res}} = 500$; I investigated the signal-to-noise at which the RM would dominate in the H and K bands, with the addition of PCA in the detrending. I vary the signal-to-noise, $\mathrm{SNR_{res}}$, and the number of PCA components removed, $\mathbf{N}_{\mathrm{PCA}}$. I then proceed to cross-correlate the original PETITRADTRANS atmospheric model used in the **CASE 3** forward model, producing maps like that in Fig. 4.9 for each combination of $\mathrm{SNR_{res}}$ and $\mathbf{N}_{\mathrm{PCA}}$. I assess the signal-to-noise of the peak cross-correlation at the injected planet velocity, by integrating over a 10 pixel square region around the peak. Fig. 4.10 summarises the recovered signal-to-noise for each band separately. In general, these tests demonstrate the ability of the Rossiter-Mclaughlin effect to dampen or even obscure a planetary atmosphere detection ($\mathbf{N}_{\mathrm{PCA}} = 0$ cases). It is evident that the search for atmospheric $H_2O$ is less impacted by the RM effect than CO at a photospheric temperature of $T_{phot} = 5000\,\mathrm{K}$; assuming a $5\sigma$ detection threshold, $H_2O$ could be recovered in the H-band at $\mathrm{SNR_{res}} > 1000$, even with no PCA detrending.

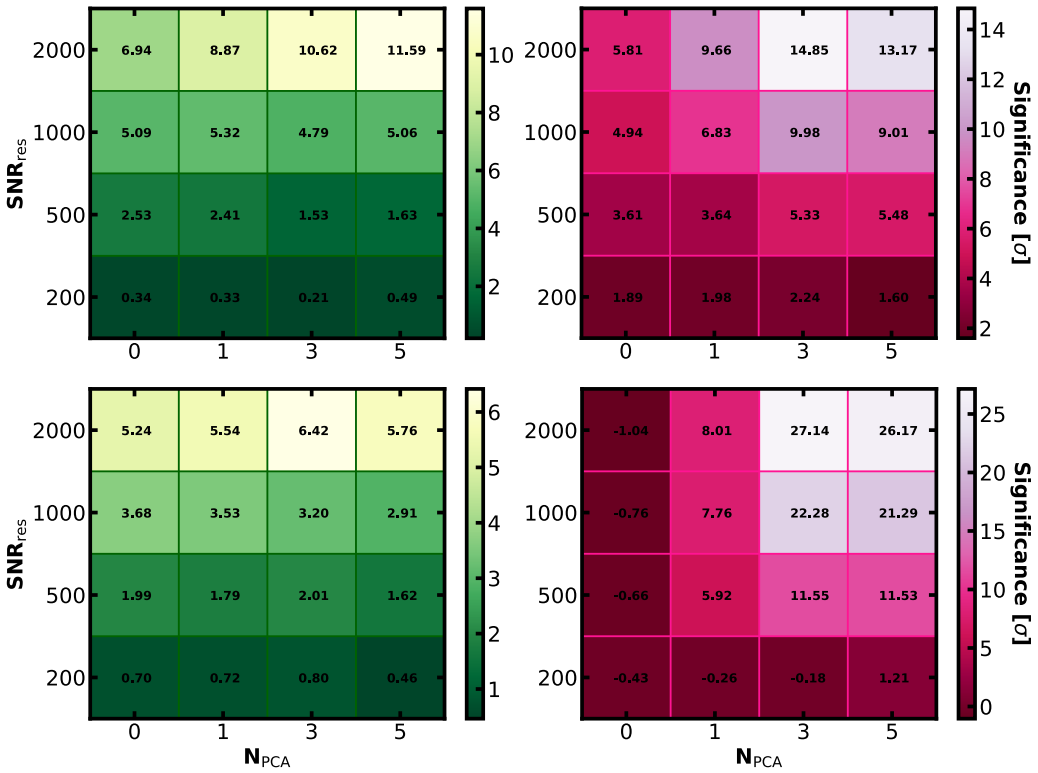


**Figure 4.10:** HD 189733 **CASE 3** tests for **left:** an $H_2O$ atmosphere (in green) and **right:** a CO atmosphere (in pink). At each signal-to-noise, I test the detection significance of each atmosphere, having removed $\mathbf{N}_{\mathrm{PCA}}$ PCA components in the detrending. The colourmaps indicate the signal-to-noise of the atmospheric detection in the cross-correlation map, at the simulated planet velocity (the values are also overwritten in units of sigma). The **top row:** shows the result in the H-band, and the **bottom row:** that in the K-band.

The depth of the $H_2O$ lines in the K-band are weaker, so a $\mathrm{SNR}_{\mathrm{res}}$ of 2000 was required for detection above the noise. For CO, the recovery is a little more dependent on the use of PCA detrending. At this photospheric temperature, we would expect a vast presence of CO, with very little $H_2O$. It is thus unsurprising that we see a large, correlated RM signature for CO. In the K-band, the RM completely dominates the CO cross-correlation when no PCA is applied (as in Fig. 4.9), hence the non-detections presented in the bottom right panel of Fig. 4.10. With successive detrending, PCA begins to remove the common modes in time, beginning with trends that are stationary in wavelength. Since the peak of the RM effect is located at $K_{\mathrm{RM}} \sim 56\,\mathrm{km/s}$ for HD 189733, the PCA will begin to remove this before the planetary signal (at a larger velocity). So, while the PCA does not

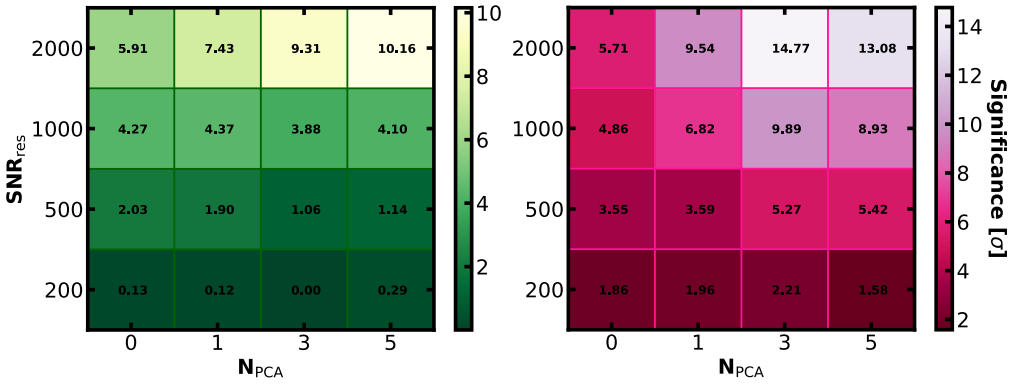


**Figure 4.11:** Recovered detection significances for HD 189733 **CASE 5**, with a spot temperature of $T_{spot} = 3700$ K. Same format as Fig. 4.10; **left:** result for $H_2O$, and **right:** CO, both in the H-band.

completely remove the cross-correlation RM signature, it dampens its amplitude, which unveils the weaker planetary peak at $K_p \sim 153$ km/s. Fig. 4.10 then gives the $SNR_{res}$ that would be necessary to detect $H_2O$ and CO in a HD 189733-like system, using only PCA to mitigate the RM effect.

### 4.4.2 The impact of (only) unocculted spots

The simulation framework presented in §4.3 allows one to define *a priori* the fraction of the transit chord covered by spots, $f_{tc}$. So, fixing $f_{tc} = 0.0$ enforces zero spot crossing events (an example stellar surface map for HD 189733 b is shown in the left panel of Fig. 4.6 for this case). Here, I test both **CASE 4** and **CASE 5** (a rotating, spotted stellar disk, transited by a planet with an atmosphere). Firstly, I consider opaque spots (**CASE 4**). Applying the same conditions as the baseline detection and Fig. 4.9, I report a detection of $H_2O$ in the H-band at a significance of $5.23\sigma$. Recalling that **CASE 4** builds upon **CASE 3**, I do not observe a significant decrease in the detection signal-to-noise across all tests performed when including opaque spots. This is somewhat predictable considering the relatively slow rotation of HD 189733; one would not expect unocculted, non-evolving, opaque spots to impact a planetary atmosphere detection. A persistent level of opaque spots would simply lower the stellar flux level[3]. In reality, however, any photospheric spots

[3]I note that this would not be true in the case of a faster rotational period, whereby the stellar rotation could induce a variable spot coverage over the duration of a planetary transit.

are very unlikely to be completely opaque.

I thus proceed to **CASE 5**, whereby each spot contributes its own spectrum. Based on Berdyugina (2005) and Afram & Berdyugina (2015), we might expect a realistic spot temperature that is 73% of the photospheric temperature, for K dwarfs; I thus assume a spot temperature of $T_{spot} = 3700\,\mathrm{K}$ for HD 189733. The results for $H_2O$ and CO in the H-band are shown in Fig. 4.11. Comparing this to H-band results for **CASE 3** (top row of Fig. 4.10), I observe a small decrease in the detection significance upon the inclusion of transparent spots. The detection of $H_2O$ shows a larger impact than CO. Moreover, decreasing the spot temperature to $T_{spot} = 3200\,\mathrm{K}$, had a smaller impact than the higher tested spot temperature. The spot-to-photosphere contrast is larger at lower spot temperatures, e.g., 0.67 compared to 0.51 in the H-band for $T_{spot} = 3200\,\mathrm{K}$ and $T_{spot} = 3700\,\mathrm{K}$ respectively[4]. With such a large contrast, we would expect this to dominate over the spectral line differences to the photosphere, effectively rendering the spot 'opaque' and more closely replicating **CASE 4** (Berdyugina, 2005).

## 4.5 An M dwarf case study: AU Mic

I proceed to test the AU Mic archetype. Introduced in Chapter 3, AU Mic is a young, active M1 star (Torres & Ferraz Mello, 1973; Rodono et al., 1986). It is then an ideal test case for the purpose of our investigation. Once again, I concentrated on the molecules CO and $H_2O$. As seen in Chapter 3, the chemical equilibrium abundance of carbon monoxide for AU Mic b, at a temperature of $T_{\mathrm{eq}} \sim 600\,\mathrm{K}$, is very low. I thus compute a high abundance CO model, for the purposes of these tests, with $\mathrm{VMR[CO]} = 10^{-2}$. The water model contains a $\mathrm{VMR}[H_2O]$ which is consistent with chemical equilibrium (see Fig. 3.7 in Chapter 3 for the appropriate profiles).

[4]Here I define the spot contrast level as $(T_{phot} - T_{spot})/T_{phot}$, rather than the absolute temperature difference.

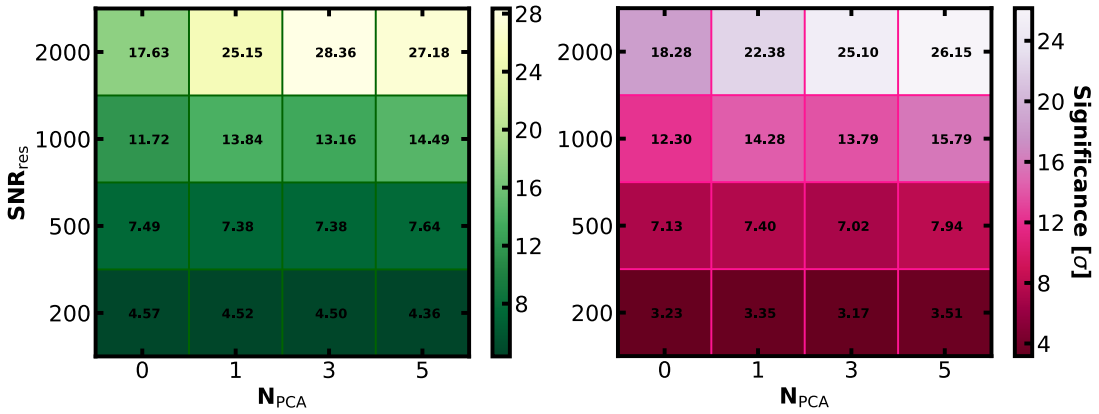


**Figure 4.12:** AU Mic **CASE 3** tests. Cross-correlation peak detection SNR shown for, **left:** $H_2O$ in the H-band, and **right:** CO in the K-band.

### 4.5.1 The RM effect

I repeated the **CASE 3** tests performed in §4.4.1, for the M1 archetype (akin to AU Mic). Using Equation 4.2, we expect the RM signature of AU Mic to peak at $K_{\rm RM} \sim 200\,{\rm km/s}$. Therefore, we would expect the RM cross-correlation signature *above* the planetary signal in velocity space ($K_p = 82.6\,{\rm km/s}$ for AU Mic b), the opposite of the HD 189733 archetype. The resulting detection significances of the $H_2O$ and CO atmospheres are shown in Fig. 4.12. Compared to the results for HD 189733 in §4.4.1, it is easier to disentangle the planetary signal, most likely due to the wider separation of the two signatures in velocity space. Both $H_2O$ and CO can be detected at $> 7\sigma$ significance, at ${\rm SNR_{res}} = 500$, even without PCA.

### 4.5.2 The impact of unocculted and occulted spots

Here, I explore the scenario of unocculted and occulted spots (under **CASE 5**). To quantify the spot occultation events, I re-introduce the parameter $f''_{het}(t)$, the fraction of the occulted portion of the stellar disk that is covered by spots (I refer back to §4.2). At any given time, all of the occulted grid points of the stellar disk are part of (i) a spot feature if $f''_{het} = 1$, or (ii) the photosphere if $f''_{het} = 0$. This is important, since it describes, as a function of time, the contribution of the background flux behind the planet from spots rather than the photosphere (see Fig. 4.3). Afram & Berdyugina (2015) predict that the average spot temperature

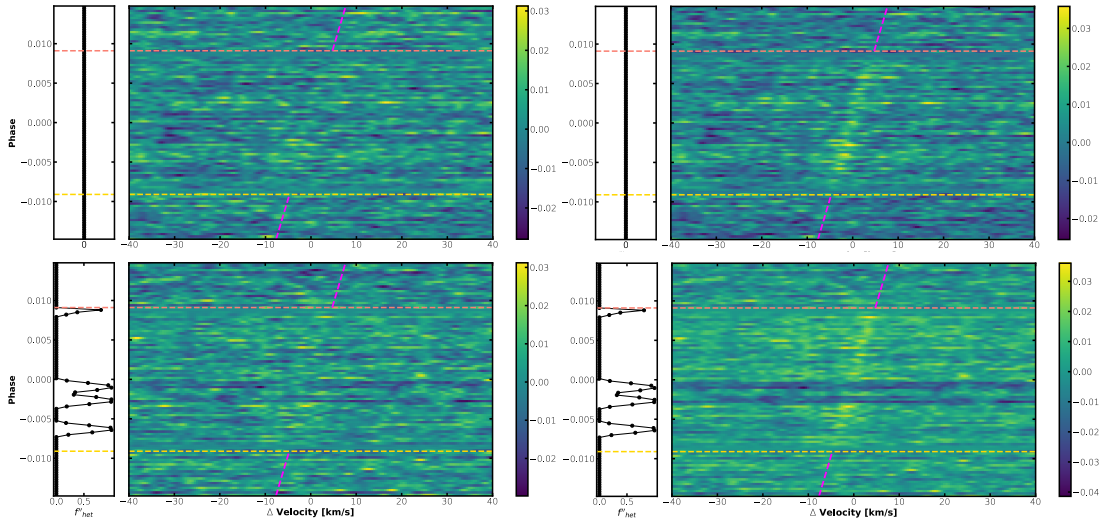


**Figure 4.13:** Cross-correlation trail plots for H-band **CASE 5** with the AU Mic archetype, including a $H_2O$ atmosphere, with **(left:)** $SNR_{res} = 200$ and **(right:)** $SNR_{res} = 1000$. I employed a spot temperature of $T_{spot} = 3000$ K, and different spot coverages. **Top panel:** only unocculted spots ($f_{tc} = 0.0$), and **bottom panel:** $f_{tc} = 0.2$. The dashed lines follow the same colour scheme as Fig. 4.8. For each panel, the **left subset panel** shows $f''_{het}(t)$ where a peak deviation from zero indicates spot occultation event.

for M dwarfs is 86% of the photospheric temperature; for AU Mic, I compute a stellar disk map using a spot temperature between $3000 < T_{spot} < 3200$ K. I also test various fractions of spot coverages within the transit chord, $f_{tc}$, while the total spot coverage over the disk, $f_{het}$, is kept constant. The middle panel of Fig. 4.6 shows an example map, for $f_{tc} = 0.1$, and the right panel $f_{tc} = 0.0$.

In Fig. 4.13, I demonstrate the cross-correlation trail plots for H-band assessment of $H_2O$, for a spotted, rotating AU Mic with $T_{spot} = 3000$ K (**CASE 5**). The top row shows an example with zero spot occultation events; there are no obvious spot signatures, despite the spot temperature likely cultivating water. An anti-correlation spot signature is evident in the case of occulted spots (bottom row of Fig. 4.13), in which $f_{tc} = 0.2$. As an example, the residual spectral time-series used for this cross-correlation map is shown in Appendix B, Fig. B.2. The collapsed cross-correlation velocity maps for occulted spot cases are shown in Fig. 4.14.

For the first case with $f_{tc} = 0.01$ (middle panel of Fig. 4.14), I do not observe a significant difference from the RM-only case (**CASE 3**). This is a low fraction of occultation events, so it closely resembles the $f_{tc} = 0.0$ (only unocculted spots) case,

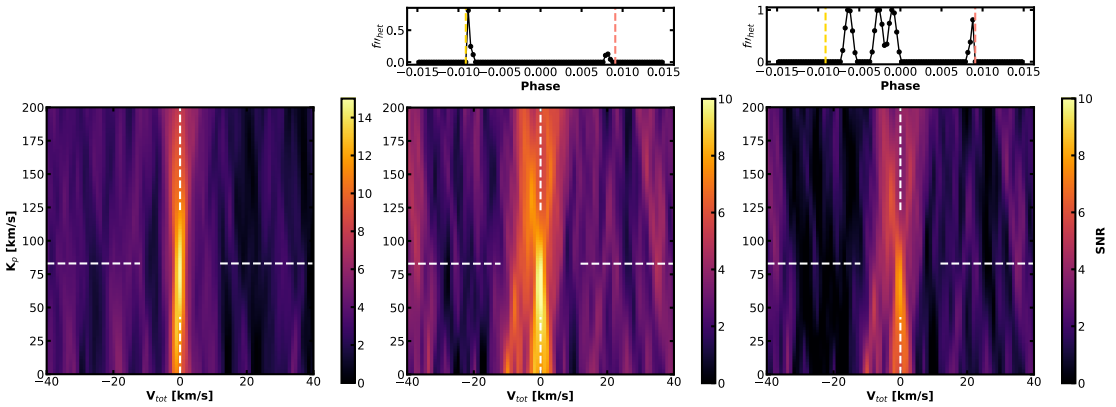


**Figure 4.14:** The impact of occulted spots on the detection of $H_2O$ in the atmosphere of AU Mic b. All three panels show the cross-correlation of H-band spectra with a planet water atmospheric model. **Left: CASE 1** homogeneous star case. The other two panels invoke **CASE 5**, with $T_{spot} = 3000$ K, $\mathrm{SNR_{res}} = 500$ and $\mathrm{N_{PCA}} = 3$. They each show the result for a different spot distribution (same total disk coverage, $f_{het}$), defined by the fraction of spots in the transit chord, $f_{tc}$; **middle:** $f_{tc} = 0.01$; **right:** $f_{tc} = 0.2$. In the spot cases, the above subset panel shows the value of $f''_{het}$ as a function of phase, where any peak indicates a spot crossing event, and the gold and pink dashed lines indicate ingress and egress respectively.

for which we previously observed very little difference in the recovered significance of the water detection. Though the example shown in Fig. 4.14 features spot crossing events close to the stellar limbs (see the subset panel), this was a consistent finding across different spot distributions. As one increases the fraction of occulted spots, while maintaining the total spot coverage of the stellar disk, the detection significance begins to diminish; in the right-hand panel of Fig. 4.14, I show the result for the $f_{tc} = 0.2$ case. We would expect water to be prevalent at this spot temperature, with much less at the photospheric temperature, as confirmed in synthesis of cooler photospheric models (Iyer et al., 2023). Further, since AU Mic is cooler than HD 189733, the spot contrast is significantly lower (0.329 compared to 0.506 in the centre of the H-band). We therefore expect to clearly observe the effects of the spot's spectrum; indeed, Afram & Berdyugina (2019) demonstrated the potential to extract spot properties from specific molecular M-dwarf spectral lines.

To investigate the cross-correlation signature of the spots themselves, I compare the **CASE 5** cross-correlation maps to those of **CASE 3**. The only difference between the two is the addition of spots on the stellar surface, so by subtracting

one from the other, we can isolate the cross-correlation template-dependent spot signature. In Fig. 4.15, I show the difference between the **CASE 5** and **CASE 3** cross-correlation signals, with the $H_2O$ atmospheric model, in the H-band. We can see that there is no such distinct feature in the case of only unocculted spots. In this case, the spot features are not 'probed' by the planet occultation. The only 'evolution' is that induced by the rotation of the star, namely the Doppler shift of the spot spectrum. While the spots have a distinct spectrum corresponding to $T_{spot} = 3000\,\mathrm{K}$, there is no apparent characteristic spot cross-correlation feature as a result. Rather, the contribution of unocculted spots appears to be more of an additive uncorrelated noise.

Proceeding to spot occultation cases, I show the $f_{tc} = 0.1$ and $f_{tc} = 0.2$ 'spot maps' in the central and right panels of Fig. 4.15. In these cases, the spot contribution is instead a pronounced anti-correlation centred on $v_{\mathrm{sys}} = 0\,\mathrm{km/s}$, and dispersed in $K_p$. Here, there are some shared absorption lines between the planet template and spot spectrum. It follows that we expect a phenomenon similar to the Rossiter-Mclaughlin effect. The anti-correlation can be explained by considering that during a spot occultation event, the spot contribution is obscured, resulting in a positive, time-isolated 'bump' in the integrated stellar line profile. Prior to the transit of the planet, the stellar spectrum is 'simply' a combination of the quiet photospheric spectrum, and the spot spectrum (which may share absorption lines with the planet atmosphere template). Then, during the planetary transit, with zero spot occultation events, the planet will induce the RM effect only on the spectral lines of the quiet photosphere. Instead, if the planet occults any spots during the transit, it will cause a suppression of the local spot spectral contribution. Therefore, the integrated spot spectrum will experience a time-dependent distortion akin to the RM effect.

Contrary to the Rossiter-Mclaughlin effect which is sampled over the full transit, spot occultations are discrete, sparse events. This is the most likely cause of the larger dispersion of the spot signature in $K_p$ space (central and right panel of Fig. 4.15). To clarify, in the unlikely, hypothetical scenario that the entire transit

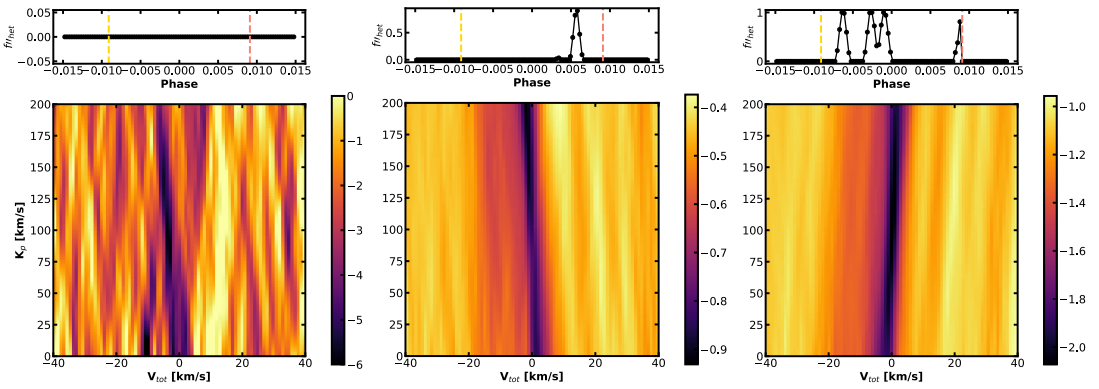


**Figure 4.15:** Isolating the spot cross-correlation signature. Each map is the difference between the cross-correlation map of the **CASE 5**, spotted star spectra ($T_{spot} = 3000\,\mathrm{K}$) with a water atmospheric model, and the **CASE 3**, RM-only case in the H-band, with $\mathrm{SNR_{res}} = 500$. **Left:** Unocculted spots ($f_{tc} = 0.0$); **middle:** $f_{tc} = 0.1$; and **right:** $f_{tc} = 0.2$ case. As in Fig. 4.14, the top subset panels show $f''_{het}(t)$, where a deviation from zero indicates a spot crossing event.

chord is occupied by spots ($f_{tc} = 1$), the planet transit would induce an RM effect on the spot spectral lines. I would expect that in the $f_{tc} = 1$ case, the apparent radial velocity of the spot cross-correlation signature would be more tightly constrained to $K_{\mathrm{RM}}$ (effectively **CASE 3**). All in all, the cross-correlation signatures of spots can be detrimental to the search for atmospheric signals, alterating the noise in the map and introducing anti-correlations in the vicinity of planet signatures.

### 4.5.3 Comparison to theoretical formalism

In §4.2, I introduced a theoretical formalism for the impact of stellar spots on the transmission spectrum, developed for low-resolution spectroscopy (Rackham et al., 2017, 2018). I test this formalism for the purposes of approximating the impact of spot features in high-resolution spectroscopy, by comparing it against my forward-modelled spectra.

First, I simulate a spotted stellar disk, assuming a spot temperature of $T_{spot}$, and forward model a spectral time-series, without any planet atmosphere contribution. I then inject a Doppler-shifting planet spectrum, atop of the stellar spectra. The injected planet spectrum is the normalised transmission spectrum, distorted by a factor $\varepsilon(\lambda, t)$. The factor $\varepsilon(\lambda, t)$, derived in Equation 4.4 (see §4.2), is a theoretical

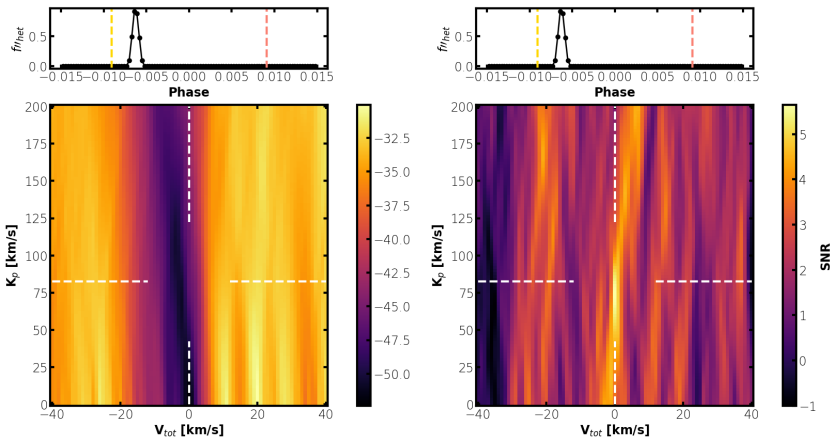


**Figure 4.16:** Comparison of simulation framework of §4.3, to the derived formalism of Equation 4.4 to describe impact of photospheric spots. The cross-correlation of an AU Mic b $H_2O$ atmosphere with **(left:)** a forward-modelled, spotted stellar spectral time-series, with injected $H_2O$ planetary spectrum, that was deformed by the factor $\varepsilon$ (see Equation 4.4), and **(right:)** a **CASE 5** full forward model, including the same $H_2O$ atmosphere. Both cases shown invoke the same spot distribution, with $f_{tc} = 0.05$, an additive noise at the level of $\mathrm{SNR}_{\mathrm{res}} = 500$, and no PCA detrending. As in Fig. 4.14, the subset panels show $f''_{het}$ as a function of phase.

contamination of the true transit depth, $D(\lambda)$, due to spots on the stellar surface. Finally, I add noise and normalise the spectra.

In Fig. 4.16, I show an example of the resulting cross-correlation, here for an $H_2O$ atmosphere with the AU Mic archetype, with spot temperature $T_{spot} = 3000\,\mathrm{K}$. For this example, there is one spot crossing event, with a total spot coverage in the transit chord of 5%. I apply no PCA detrending. The contamination approximation, (left-hand panel of Fig. 4.16), shows a strong anti-correlation signature centred on $v_{\mathrm{sys}} = 0.0\,\mathrm{km/s}$. These match the spot cross-correlation signatures shown in Fig. 4.15, though slightly broader. For comparison, I show in the same figure the cross-correlation of the same $H_2O$ model with the forward model from the simulator developed in this chapter. The right-hand panel of Fig. 4.16 shows that the planet water signature is still resolvable above the noise level, at an SNR of $\sim 5\sigma$, even without PCA. It is evident that though the contamination factor, $\varepsilon(\lambda, t)$, is able to replicate the signature of spots in cross-correlation space, it severely over-compensates, predicting a larger anti-correlation than observed in the more realistic simulator. Moreover, the detrending process cannot be accurately tested

on these spectral approximations, since the spots deformations encoded in the contamtination factor, $\varepsilon(\lambda, t)$, are stationary in the stellar rest frame. In reality, spot deformations are time-variable and, those induced by spot occultations in particular, are related to the planetary transit, with a characteristic radial velocity akin to that of the RM effect. The distortions resulting from the contamination factor, $\varepsilon(\lambda, t)$, therefore represent a worst-case scenario, and should only be used as a first-order approximation of the impact of a given spot coverage on high-resolution spectroscopy of exoplanet atmosphere signals.

## 4.6 Future work

### 4.6.1 Making the code public and publication

The algorithm written for the forward-modelling of stellar spectra in this chapter (detailed in §4.3.1) can be used to simulate any star, by input of the parameters listed in Table 4.1. I have demonstrated its application to archetype examples of a K2 dwarf (HD 189733), and M1 dwarf (AU Mic). It may widely useful to the field towards (e.g.,) justification in observing proposals, and development of correction approaches (see §4.6.4). To that end, we have plans to prepare the code for public release on `github.com`. We also plan to write up this work in a manuscript for publication.

### 4.6.2 Faculae

For the work in this chapter, my simulation tests went only as far to include photospheric spot features on the stellar disk. It has been theorised by simulation studies that M dwarfs stars tend to exhibit more spot features than faculae (Beeck et al., 2015; Panja et al., 2020). For earlier type stars, however, one would expect the contribution of faculae to be larger. Moreover, spot features are often accompanied by faculae on FGK stars, with Sun-like stars usually faculae dominated.

It would be relatively straight forward to add faculae to the forward model, in a similar manner to the addition of spots in **CASE 4** and **CASE 5**. Faculae are brighter, hotter regions in the photosphere, and so the contrast and faculae

spectrum would have the opposite effect to spots. It would thus be interesting and feasible to explore the additive aspect of faculae in hotter stars.

### 4.6.3 Spectra of inhomogeneities

In this work, I assigned the spots their own spectrum in **CASE 5**. I defined a spot temperature, $T_{spot}$, and then selected a synthetic stellar spectral model from the PHOENIX grid, with otherwise identical properties to the photospheric spectrum. In reality, the difference between spectra of heterogeneities and that of the photosphere is not only a contrast effect, and so it may not be accurate to simply use a cooler/hotter photospheric spectrum, derived from 1-D radiative-convective stellar models, as the spot/faculae model (Gully-Santiago & Morley, 2022). This is expected to be a worse approximation for faculae than spots (Witzke et al., 2022). Though this does not dominate the uncertainty budget, there is certainly scope to improve the model by employing more accurate spot (and faculae) spectra. There is currently ongoing development of models of heterogeneities (Rackham et al., 2023; Witzke et al., 2021); such work will have to wait until these models are ready.

### 4.6.4 Accounting for heterogeneities in high-resolution studies

Having seen the detrimental impact of stellar heterogeneities on HRCCS analyses, a natural next step would be to develop methods to correct for these effects, or account for them in real observations. Assuming the star to be stationary (and subsequent use of PCA detrending), can bias detection significances, which can be problematic if proceeding to atmospheric retrievals.

In §4.4.1, I showed that the Rossiter-Mclaughlin effect can dampen and even obscure a planetary atmosphere signal. It is thus recommended to consider the magnitude of the RM cross-correlation signature, depending on the atmospheric species sought, and attempt corrections for high-resolution studies. Chiavassa & Brogi (2019) demonstrated an RM correction, by simulating a 3-D stellar surface, accounting for granulation and the transit-induced RM effect. Unfortunately, we

currently have no such models for M dwarfs or young stars. It is thus imperative to formulate an empirical correction approach. One could consider a correction either in spectral or cross-correlation space. I demonstrated such a 'spectral-space' correction in Chapter 3 for the SPIROU AU Mic observations. A 'cross-correlation-space' correction would be dependent on the sought exoplanet atmospheric species. Correction of the so-called 'Doppler shadow' in cross-correlation space has been demonstrated in practice; for example, Prinoth et al. (2022) and Seidel et al. (2023) successfully fit and remove the Doppler shadow using a Gaussian profile. It has been shown to be effective, even in cases where the Doppler shadow overlaps with the planetary signature. This approach is sufficient for giant planets, and FGK stars, but smaller stars with less distinct RM signatures cannot be modelled in such a way, 'by eye'.

One could construct a **CASE 2** forward model, i.e., considering only a transiting bare rock, apply a spectral reduction and cross-correlate with an atmospheric spectrum template to build a forward-modelled RM-signature map (as in Fig. 4.9). One could then attempt to 'fit' this map to the cross-correlation map of the observations, and remove it. While this may help to unveil a previously obscured planet signal, we would have to proceed with caution if advancing to atmospheric abundance measurements. Such an approach would rely on accurate orbital ephemeride estimates and projected sky obliquity.

Both proposed empirical corrections are challenging in practice, predominantly because the forward model requires an input stellar spectrum, and $v \sin i$. One could use the mean out-of-transit stellar spectrum from the observations in hand as input to the forward model (as attempted in Chapter 3). However, the issue there is that the spectrum is already convolved due to the stellar rotation. Use of a synthetic (unconvolved) stellar spectrum would also be an option. These can often be an inaccurate match to observed spectra, particularly for lower mass stars, though there are focused efforts to improve these models (e.g., Iyer et al., 2023).

Correcting the impact of stellar spots is much more difficult; there is currently no example of such a correction in the literature. While it would be possible to forward-

model the cross-correlation signatures of spot features, as shown in this chapter, these are not only dependent on the cross-correlation template, but also the (i) assumed spot temperature, (ii) spot distribution and (iii) fraction of spots in the transit chord. There are therefore many degeneracies, which would make it challenging to constrain the cross-correlation signature in observations. It may instead be more feasible to apply a correction in spectral space. That said, more work is needed (and is currently ongoing) to fully understand the impact of spots on stellar spectra.

In any case, PCA (and other detrending methods which rely on stationary spectral features) is likely to be insufficient going forward.

## 4.7 Conclusions

In this chapter, I have described a purpose-built simulator for the forward-modelling of stellar spectra, impacted by stellar inhomogeneities. I explored the effects of the Rossiter-Mclaughlin effect and photospheric spots, in the case of a K dwarf/hot Jupiter archetype, and an M dwarf/sub-Neptune archetype. Regarding the hotter K dwarf archetype, I found that:

- the RM effect induces a strong anti-correlation signature, centred on $v_{\rm sys} = 0.0\,\mathrm{km/s}$, for species present in the photosphere. This signature peaks at a characteristic apparent radial velocity, which can differ from that of the planet;

- in the case of species under-represented in the photosphere, there is no such distinct correlation signature. However, the RM effect leads to a distortion of *all* stellar lines, which results in additive noise in cross-correlation space;

- considering realistic spot temperatures for K dwarfs, the spot contrasts are so high that the spot spectrum is virtually indistinguishable, effectively rendering the spots opaque. It follows that unocculted spots have very little impact on the recovery of atmospheric signals.

AU Mic is a good test case for young, active stars, with larger spot features and smaller spot contrasts. For the AU Mic-like cases, I reported:

- once again, an anti-correlation is introduced by the RM effect. Similarly to the HD 189733 case, cross-correlation with a CO yielded a more distinct RM signature than $H_2O$. The feature was less broadly distributed about $v_{\rm sys} = 0.0\,{\rm km/s}$ than that of HD 189733, presumably due to the higher rotational velocity. It was easier to distinguish the planet signal from the RM imprint, on account of a larger velocity separation;

- while the presence of unocculted spots (at a temperature of $T_{spot} = 3000\,{\rm K}$, 86% of the photospheric temperature) on the stellar disk introduces noise, they do not significantly impact the detection SNR of an $H_2O$ atmosphere, as they do not introduce anti-correlation preferentially in the vicinity of the planet signal;

- on the other hand, spots located in the transit chord introduce anti-correlation signatures centred on $v_{\rm sys} = 0.0\,{\rm km/s}$, when their spectra correlate somewhat with the planetary template spectrum. This results in a degrading of the planetary cross-correlation signal, decreasing further with increasingly numerous spot occultation events.

Going forward, it will be important to comprehensively quantify the impact of stellar heterogeneities on stellar spectra, in order to make correct inferences about the transmission spectrum of a transiting planet. This will become increasingly more crucial towards the study of young planets, and M dwarfs, which we are targeting in the pursuit of smaller planets.

*The important thing is not to stop questioning.*
*Curiosity has its own reason for existing.*

— Albert Einstein, *1955*

# CHAPTER 5

# GP MODELLING OF HIGH-RESOLUTION SPECTRA

## Contents


**5.1 Introduction and motivation . . . . . 126**
**5.2 Gaussian processes . . . . . 129**
5.2.1 A definition . . . . . 129
5.2.2 Gaussian process regression . . . . . 130
5.2.3 Choosing a mean and covariance function . . . . . 131
5.2.4 Advantages and disadvantages of Gaussian processes . . 133
**5.3 GP framework formalism . . . . . 134**
5.3.1 The telluric component . . . . . 137
5.3.2 The planet component . . . . . 139
**5.4 The data and reduction . . . . . 140**
**5.5 HD 189733 b . . . . . 144**
5.5.1 Removal of the stellar spectrum . . . . . 144
5.5.2 Telluric modelling . . . . . 144
5.5.3 Recovery of the planet spectrum . . . . . 145
**5.6 51 Pegasi b . . . . . 147**
5.6.1 Telluric spectrum . . . . . 149
5.6.2 Recovery of the planet spectrum . . . . . 149
**5.7 Exploring the sensitivity of the planet GP . . . . . 150**

5.7.1 Limiting assumptions of the GP framework . . . . . 150
5.7.2 Using alternative telluric correction methods . . . . . 153
**5.8 Possible Extensions . . . . . 157**
5.8.1 A simultaneous modelling approach . . . . . 157
5.8.2 Modelling of (only) tellurics . . . . . 160
**5.9 Conclusions . . . . . 160**

---

The work in this chapter is based on the peer-reviewed publication entitled *Application of a Gaussian Process Framework for Modelling of High-Resolution Exoplanet Spectra* (Meech et al., 2022). I led and completed this work, with guidance from Prof Suzanne Aigrain. The data analysed were contributed by Prof Jayne Birkby and Dr Matteo Brogi.

## 5.1 Introduction and motivation

In the previous chapters, I have introduced and demonstrated the state-of-the-art, widely used techniques to characterise exoplanet atmospheres at high-resolution. Yet, they are not without their issues and challenges. Prior to 2019, there was no robust method to assign abundances to molecular and atomic detections using high-resolution spectroscopy. 'Atmospheric retrievals' have revolutionised the low-resolution space-based technique for atmospheric characterisation (Madhusudhan & Seager, 2009). However, with high-resolution spectroscopy, it was not straightforward to couple the standard detection metric of signal-to-noise in velocity space (see e.g., §3.4) to a model comparison framework.

As mentioned in Chapter 3, the signal-to-noise metric is inherently subject to spurious noise features. The noise is computed as the standard deviation of the map of cross-correlation values, away from the expected planet location in velocity; I detail the method in §2.3.3. However, the noise level can vary across the map, and is very unlikely to be purely uncorrelated. On the data side, residual correlated noise from the detrending process, e.g., from tellurics and stellar effects, will pervade in the correlation map. Then, depending on the positions and strengths of the spectral lines of the atmospheric spectrum, there may be auto-correlation of the lines with

each other (see e.g., Borsato et al., 2023). This auto-correlation of aliasing signal could lead to an overestimation of the noise of the data. The calculation of the noise is highly dependent on the region of the map selected; the signal-to-noise is thus not a robust metric for anything beyond reporting a detection of a particular species, and even then requires an (informally community-agreed) $\sim 5\sigma$ threshold.

When it comes to comparing models and assessing their ability to describe the data, in an atmospheric retrieval, one would require some loss function. Since one does not directly observe the exoplanet spectrum with high-resolution cross-correlation spectroscopy, one cannot simply use a least squares minimisation (or another such optimisation). Then, Brogi & Line (2019) developed a cross-correlation-to-likelihood mapping, whereby they constructed a likelihood function, incorporating the cross-correlation coefficients from the template-matching process, as detailed in §2.3.5. This afforded a robust metric to implement a Bayesian analysis, and has led to multiple publications involving retrieved chemical abundances with high-resolution ground-based observations (e.g., Line et al., 2021; Brogi et al., 2023; Gandhi et al., 2023; Pelletier et al., 2023).

In an ideal scenario, one would extract the exoplanet spectrum from high-resolution observations. The challenge is in the noise level associated with ground-based optical and nIR spectroscopy: the planet signals are typically several orders of magnitude smaller than even the photon noise level, hence why we employ template-matching to extract the signals. Moreover, despite careful development of detrending techniques, often spurious noise remains in the spectra. Ruthless suppression of the noise can also hamper exoplanet detections, since the exoplanet signal itself may start to be removed. I will return to this point later in the chapter. What if there was a method to accurately model the noise in such data? Might direct extraction of the exoplanet signal be possible, say, for example, for the stronger signals of hot Jupiters?

Gaussian process (GP) regression has been pivotal in the recent advances of detection of exoplanets within astronomical time-series data. Though the number of exoplanet detections have grown exponentially since the 1990s as techniques

and instruments have developed, we have recently reached a boundary floor in the size of the smallest detectable planet using the radial velocity technique (Zhao et al., 2022; Korhonen et al., 2015). It is thought that stellar activity plays a significant role in the existence of this threshold, which is limiting our ability to advance towards detecting an Earth-like (in size, distance from host and host stellar type) planet. Smaller, cooler stars tend to have stronger dynamos, thus displaying stronger levels of magnetic activity. This manifests as fluctuations in flux, as well as spectral imprints, which therefore plagues exoplanet detection since the true planetary transit and radial velocity signatures are dwarfed by the stochastic activity signals. By using Gaussian process regression to model the imprinted stellar activity signals, several teams have been able to disentangle stellar activity signals from the true signals of orbiting planets (see e.g., Zicher et al., 2022; Barragán et al., 2022). Approaches range from simply applying a 1-D GP to either transit or RV data, modelling transit and RV data together, and even applying a multi-dimensional GP framework to RV data, whereby simultaneously collated 'activity indicators' constrain the GP model (see e.g., Barragán et al., 2023). Towards atmospheric characterisation, Gaussian process regression has been used to detrend spectroscopic light curves, modelling systematics in low-resolution transmission spectroscopy. This is a relatively straightforward problem: the observed light curves contain (i) the true stellar flux as a function of time, the signal we wish to uncover, plus (ii) systematics from the instrument, as well as (iii) fundamental noise, including photon noise, instrumental noise and residual noise from the Earth's atmosphere if observed from the ground. A model including the known information, i.e., the transit light curve, as well as a latent process, i.e., a Gaussian process, is well suited to this problem, and has been highly successful in detrending of exoplanet light curves (e.g., Kirk et al., 2021). To date, there has been no attempt to make use of Gaussian processes in high-resolution analyses. One of the major challenges is the computational expense given the multi-dimensionality and size of typical high-resolution exoplanet datasets.

Here, I explore the application of Gaussian process regression to high-resolution spectroscopy. The work in this chapter is mostly based on the publication Meech et al. (2022).

## 5.2 Gaussian processes

### 5.2.1 A definition

In order to explain our motivation, I first provide a brief, non-technical introduction to Gaussian processes. For comprehensive background and discussion of Gaussian processes, please see Rasmussen & Williams (2006).

Let us begin with a one-dimensional Gaussian distribution, which is wholly described by a mean $\mu$ and variance $\sigma^2$. We have a scalar variable $y$ which is drawn from this distribution, i.e.,

$$y \sim \mathcal{N}(\mu, \sigma^2), \tag{5.1}$$

and its probability density function would take the form

$$P(y) = \frac{1}{\sqrt{2\pi}\sigma} \exp\Big[-\frac{(y-\mu)^2}{2\sigma^2}\Big]. \tag{5.2}$$

Consider extending the above formalism to a bi-variate Gaussian distribution. For two jointly Gaussian distributed variables $\mathbf{y} = \begin{pmatrix} y_i \\ y_j \end{pmatrix}$ we now say they are drawn from a bi-variate Gaussian distribution defined as

$$\begin{bmatrix} y_i \\ y_j \end{bmatrix} \sim \mathcal{N}\left( \begin{bmatrix} \mu_i \\ \mu_j \end{bmatrix}, \begin{bmatrix} \sigma_i^2 & C \\ C & \sigma_j^2 \end{bmatrix} \right) \tag{5.3}$$

where $C$ is the covariance between the variables. Its probability density function is now given by

$$P(\mathbf{y}) = \frac{1}{\sqrt{(2\pi)^2|\boldsymbol{\Sigma}|}} \exp\Big[-\frac{1}{2}(\mathbf{y}-\boldsymbol{\mu})^{\mathrm{T}}\boldsymbol{\Sigma}^{-1}(\mathbf{y}-\boldsymbol{\mu})\Big] \tag{5.4}$$

where $\boldsymbol{\Sigma}$ is the covariance matrix. We could apply this same formalism to a collection of variables drawn from a multi-variate ($N$) Gaussian distribution, with a small adaption $\mathbf{y} \sim \mathcal{N}(\mathbf{m}, \mathbf{K})$ where $\mathbf{m}$ is the mean vector of length $N$ and $\mathbf{K}$ is the $N \times N$

covariance matrix. Extending this to an infinite number of variables, we arrive at a Gaussian process. We no longer have a Gaussian distribution over vectors and matrices, but rather a Gaussian distribution over functions:

$$f(\mathbf{x}) \sim \mathcal{GP}(\mathbf{m}, \mathbf{k}) \tag{5.5}$$

where $\mathbf{m}$ and $\mathbf{k}$ are now a parameterised mean function $m(\mathbf{x}; \boldsymbol{\theta})$ and a covariance function, $k(\mathbf{x}, \mathbf{x}'; \boldsymbol{\phi})$. We never deal with infinitely long vectors or matrices, since we only evaluate the mean and covariance functions at discrete locations. In summary, and by way of a formal definition, a Gaussian process is a "joint multi-variate Gaussian distribution over infinite variables" (Rasmussen & Williams, 2006).

### 5.2.2 Gaussian process regression

We can apply Gaussian processes to regression problems, to learn an unknown function from a set of data. In fact, Gaussian process regression is the extension of the most common regression technique, least-squares regression, to include correlated noise and affording non-parametric function inference (see Aigrain & Foreman-Mackey, 2022). We impose some covariance between the data points *a priori*, selecting a functional form for the covariance, the 'kernel', $k(\mathbf{x}, \mathbf{x}'; \boldsymbol{\phi})$. Any deterministic component of the model can be incorporated into the parameterised mean function, $m(\mathbf{x}; \boldsymbol{\theta})$. The parameters of the mean and covariance function $\boldsymbol{\Psi} = \{\boldsymbol{\theta}, \boldsymbol{\phi}\}$ are known as hyperparameters.

We can use Bayesian inference to derive a posterior distribution over the variables (see Parviainen (2018) for a reminder of Bayesian inference). Consider, we have $N$ observations $\{\mathbf{x}, \mathbf{y}\}$, our input 'training data', and we are interested in making predictions $\mathbf{y}_*$ at 'test' locations $\mathbf{x}_*$. If we assume our data are samples of a multi-variate Gaussian, we can introduce a log-likelihood function:

$$\log p(\mathbf{y}|\mathbf{x}, \boldsymbol{\theta}, \boldsymbol{\phi}) = -\frac{1}{2}(\mathbf{y} - \mathbf{m})^{\mathrm{T}}\mathbf{K}^{-1}(\mathbf{y} - \mathbf{m}) - \frac{1}{2}\log|\mathbf{K}| - \frac{N}{2}\log 2\pi \tag{5.6}$$

where $\mathbf{m}$ and $\mathbf{K}$ are evaluations of the mean and covariance function at the training inputs $\mathbf{x}$. A typical Gaussian process regression workflow is as follows:

(i) We construct a prior distribution over the function, $f(x)$, namely the functional form of the mean and covariance, paired with initial guesses of their hyperparameters;

(ii) we introduce the data, $\{\mathbf{x}, \mathbf{y}\}$ (left panel Fig. 5.1), and *train* the GP by computing the covariance matrix $\mathbf{K}$ and evaluating the log-likelihood;

(iii) and obtain a posterior distribution, $p(\boldsymbol{\theta}, \boldsymbol{\phi}|\mathbf{y}) \propto p(\mathbf{y}|\boldsymbol{\theta}, \boldsymbol{\phi})p(\boldsymbol{\theta}, \boldsymbol{\phi})$. It is the inherent properties of Gaussian distributions which enable the marginalisation over all of the unobserved variables, including $\boldsymbol{\phi}$;

(iv) we *condition* that distribution on our observations, $\mathbf{y}$;

(v) we use that posterior distribution to make predictions, $\mathbf{y}_*$, at new test locations $\mathbf{x}_*$ (right panel Fig. 5.1).

With regard to (v), the training and test sets are jointly Gaussian distributed:

$$p\left(\begin{bmatrix}\mathbf{y}\\ \mathbf{y}_*\end{bmatrix}\right) = \mathcal{N}\left(\begin{bmatrix}\mathbf{m}\\ \mathbf{m}_*\end{bmatrix}, \begin{bmatrix}\mathbf{K} & \mathbf{K}_*\\ \mathbf{K}_* & \mathbf{K}_{**}\end{bmatrix}\right) \tag{5.7}$$

where $\mathbf{m}_* = m(\mathbf{x}_*)$, $\mathbf{K}_* = k(\mathbf{x}, \mathbf{x}_*) = k(\mathbf{x}_*, \mathbf{x})$, and $\mathbf{K}_{**} = k(\mathbf{x}_*, \mathbf{x}_*)$. It follows that the predictive distribution, also Gaussian, is given by

$$p(\mathbf{y}_*|\mathbf{y}, k) = \mathcal{N}(\mathbf{m}_* + {\mathbf{K}_*}^{\mathrm{T}}\mathbf{K}^{-1}(\mathbf{y} - \mathbf{m}), \mathbf{K}_{**} - {\mathbf{K}_*}^{\mathrm{T}}\mathbf{K}^{-1}\mathbf{K}_*). \tag{5.8}$$

Notably, the predictive covariance is not dependent on observations $\mathbf{y}$, while the predictive mean is a linear combination of observations $\mathbf{y}$.

### 5.2.3 Choosing a mean and covariance function

When using Gaussian process regression, our modelling decisions are entirely contained in the parameterisation of the mean and covariance, or 'kernel', function. Any **deterministic** information on the functions to be modelled should be incorporated into the mean function, $m(\mathbf{x}; \boldsymbol{\theta})$. As an example, in the case of modelling systematics in transit light curves, the mean function can include the (parameterised) limb-darkening model (see e.g., Kirk et al., 2021). Conversely, the remaining **stochastic**

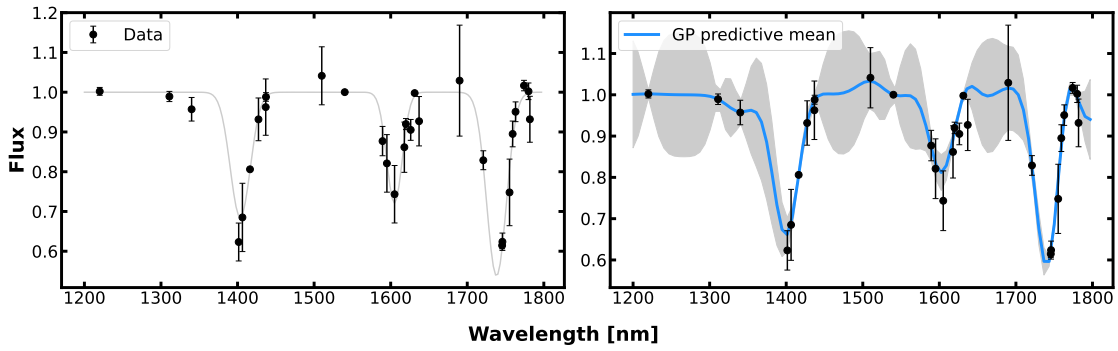


**Figure 5.1:** A demonstration of Gaussian process regression. **Left:** A set of noisy data $\{\mathbf{x}, \mathbf{y}\}$ (black data points), derived from a mock-up 'spectrum' (grey). **Right:** The GP predictive mean, $\mathbf{m}_*$ (blue solid line) and $1\sigma$ interval (grey) at test locations $\mathbf{x}_*$, having trained a GP with a squared exponential kernel on the data $\mathbf{x}$.

behaviour is entirely described by the covariance function, $k(\mathbf{x}, \mathbf{x}'; \boldsymbol{\phi})$. Prior to introducing the observations, one may be able to say something about the expected correlations between data, and thereby the family of functions to describe said data. One common property is *stationarity*; such kernels depend on relative rather than absolute locations, $|x_i - x_j|$. Another self-explanatory example property is *periodicity*; as an example that would merit a periodic kernel, a stellar-activity imprint on planet-induced radial velocity measurements are likely periodic, according to the stellar rotation (Rajpaul et al., 2015). The uncertainties of the observed data in question, $\sigma_i$, can be incorporated into the covariance such that

$$k(x_i, x_j) \rightarrow k(x_i, x_j) + \sigma_i^2 \delta_{ij}, \tag{5.9}$$

where $\delta_{ij}$ is the Kronecker delta function.

Ultimately, one can construct any kernel function, as long as it follows a couple of conditions. In order to be a valid kernel, the covariance function must be *positive semi-definite*, in order that $\mathbf{K}_*{}^{\mathrm{T}}\mathbf{K}^{-1}\mathbf{K}_* > 0$ and therefore $\mathrm{Var}(\mathbf{f}_*) \leq k(\mathbf{x}_*, \mathbf{x}'_*)$ where $\mathbf{f}_*$ is the GP predictive mean. It must also be symmetric, such that $k(x_i, x_j) = k(x_j, x_i)$. There are a few standard kernel functions. The **squared exponential** kernel function,

$$k(\tau; \boldsymbol{\phi}) = \alpha^2 \exp\Big[-\frac{\tau^2}{2\lambda^2}\Big], \tag{5.10}$$

where $\tau = |x_i - x_j|$, with amplitude $\alpha$ and characteristic length scale $\lambda$. It is commonly used due to its simplicity, and stationarity, and produces very smooth functions. Another family of kernels is the **quasi-periodic** kernel, typically of the form

$$k(\tau;\boldsymbol{\phi}) = \alpha^2 \exp\left(-\frac{\tau^2}{2\lambda_1^2} - \Gamma \sin^2\left[\frac{\pi\tau}{\lambda_2}\right]\right) \tag{5.11}$$

where $\boldsymbol{\phi} = \{\alpha, \Gamma, \lambda_1, \lambda_2\}$. It is useful for modelling a periodic signal, with period $\lambda_2$, which is variable over time according to a decoherence timescale $\lambda_1$. An alternative family of kernels is the **Matérn** kernel class, of the form

$$k(\tau;\boldsymbol{\phi}) = \alpha^2 \frac{2^{1-\nu}}{\Gamma(\nu)}\left(\frac{\sqrt{2\nu}|x_i - x_j|}{\lambda}\right)^{\nu} \mathbb{B}_\nu\left(\frac{\sqrt{2\nu}|x_i - x_j|}{\lambda}\right) \tag{5.12}$$

where $\nu$ denotes the degree of differentiability and thus the smoothness of the output functions, $\Gamma$ is now the Gamma function and $\mathbb{B}$ is the modified Bessel function. The squared exponential kernel is then a special case of this kernel, in the limit $\nu \to \infty$. The Matérn kernel simplifies nicely in the case of half-integer values of $\nu$; popular choices include $\nu = \{\frac{1}{2}, \frac{3}{2}, \frac{5}{2}\}$, with increasing 'smoothness'. For example, the Matérn-3/2 kernel is given by

$$k_{\mathrm{M32}}(\tau;\boldsymbol{\phi}) = \left(1 + \frac{\sqrt{3}\tau}{\lambda}\right)\exp\left[-\frac{\sqrt{3}\tau}{\lambda}\right], \tag{5.13}$$

and is the adopted kernel for the work in this chapter. Samples from each of these kernels are shown in Fig. 5.2. Each are stationary kernels, but the variation in smoothness is evident; the squared exponential and quasi-periodic produce smoothly varying functions, compared to the rougher behaviour of the Matérn kernels.

Typically, astrophysical applications use the above kernels (and others) in combination, via products and summations. For in depth discussions on kernel selection and construction see Aigrain & Foreman-Mackey (2022); Wilson & Adams (2013).

### 5.2.4 Advantages and disadvantages of Gaussian processes

We now have all the tools necessary to perform Gaussian process regression. Towards astrophysical applications, there are a number of benefits and disadvantages of

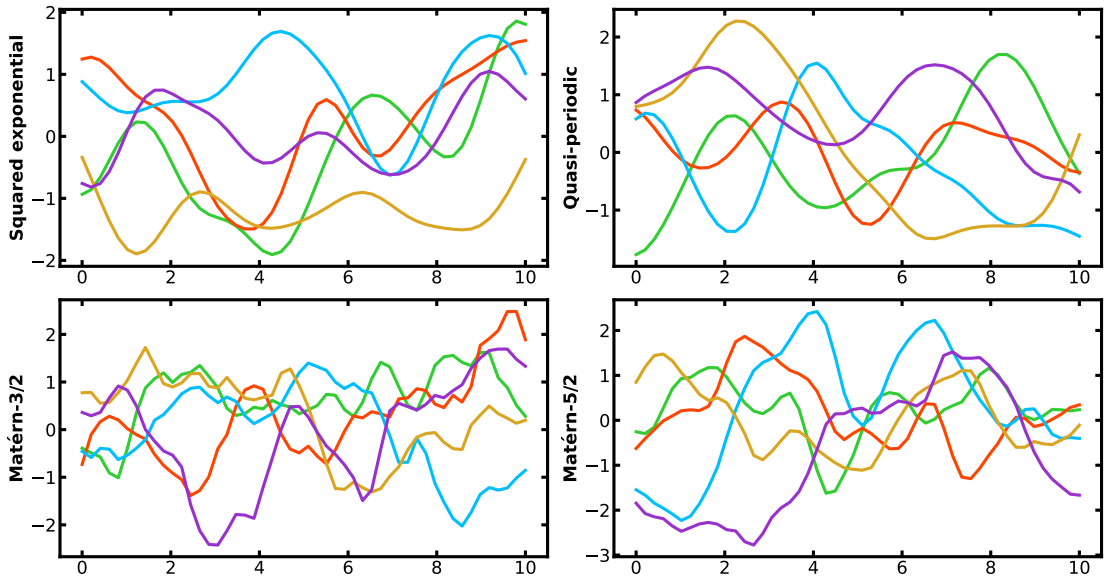


**Figure 5.2:** Samples from different GP kernels mentioned in §5.2.3. In each case $\lambda = 1$, with $\lambda_1 = 1$, $\Gamma = 0.1$, $\log \lambda_2 = 10$ for the quasi-periodic kernel. The mean function is set to zero in all cases.

employing GPR. A Gaussian process affords non-parametric (or actually infinite parameter) functions, which is beneficial for cases in which there is little known information regarding the relation between inputs and outputs. But, with such flexible models, we must be cautious not to over-fit the data. The GP log-likelihood (Equation 5.6) has a natural penalty term, $-\frac{1}{2}\log|\mathbf{K}|$, against more complex models. Additionally, GP regression lends itself easily to a Bayesian inference framework.

The computational cost of Gaussian process regression is high, predominantly due to the computation of the log-likelihood (Equation 5.6). Each evaluation requires inverting and calculating the determinant of the $N \times N$ covariance matrix $\mathbf{K}$. A common method to efficiently perform these computations is Cholesky decomposition, yet this still requires $\mathcal{O}(N^3)$ operations, quickly becoming intractable for large datasets.

## 5.3 GP framework formalism

We explore the application of Gaussian process regression to modelling of high-resolution exoplanet spectra. Consider we have a compiled set of $V$ observed

spectra, $\mathcal{D} = \{\mathcal{S}_1, ..., \mathcal{S}_V\}_{i=1}^{V}$. Each spectrum is given by $\mathcal{S}_i = \{(\lambda_{ij}, f_{ij}, \sigma_{ij})\}_{j=1}^{W}$, where $W$ is the total number of pixels, $\lambda_{ij}$ is the time-dependent wavelength, and $f_{ij}, \sigma_{ij}$ the corresponding flux and flux uncertainty. It follows that, at first approximation, each observed flux is given by:

$$f_{ij} = F_{\text{obs}} = \Big[F_{\text{planet}}(t_i, \lambda_j) + F_{\text{star}}(t_i, \lambda_j)\Big] \cdot T(t_i, \lambda_j) * P(\lambda_j) \cdot Q(\lambda_j) \tag{5.14}$$

where $F_{\text{planet}}$ and $F_{\text{star}}$ are the planetary and stellar spectra, $T$ is the telluric contribution, $P$ is the instrumental profile and $Q$ is the instrumental throughput (Vacca et al., 2003).

We wish to use a Gaussian process, trained on the high-resolution data, to forward model the spectral fluxes $f_{ij}$. In doing so, we recognise that there exists some correlation between flux uncertainties in the continuous domains wavelength and time, albeit locally, which can be specified via a parameterised covariance function. Naively, we wish to condition $f \sim \mathcal{GP}\Big(m(\lambda_{ij}), k(\lambda_{ij}, \lambda_{ij})\Big)$. We are interested in the distinct spectral components in Equation 5.14; we can marginalise over all variables except that of interest, namely $F_{\text{planet}}$. There are a number of obstacles to such a model. Firstly, high-resolution datasets typically consist of $> 10^5$ $(N)$ individual data points. With current publically available GP packages, this certainly translates to a bottleneck in computational time. This is predominantly due to the size of the $(N \times N)$ covariance matrix as mentioned above.

**Figure 5.3:** GP framework workflow.

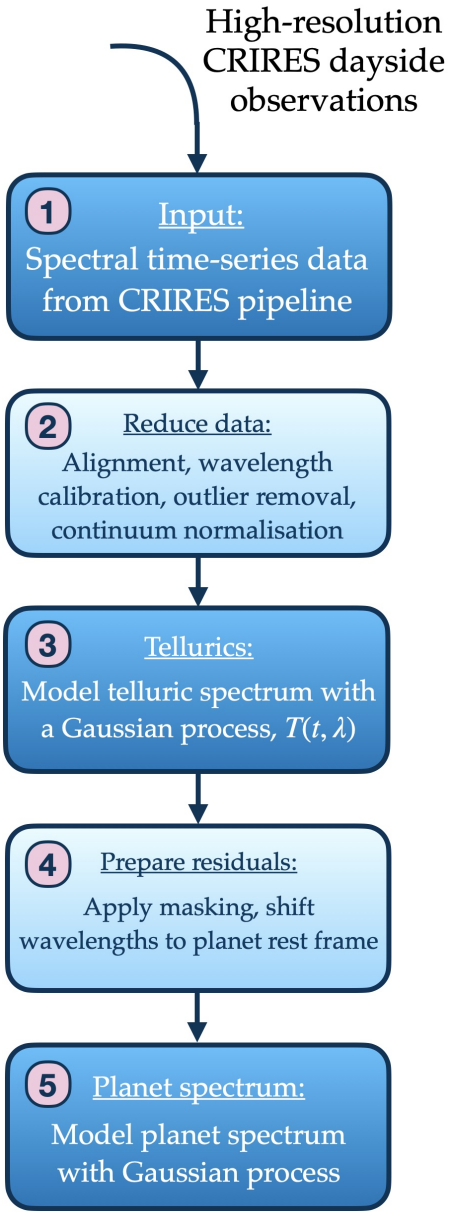

For the viability tests in this study, we concentrate on smaller datasets; we choose archival CRIRES datasets to work on, consisting of four separate orders, each with around 1000 pixels. CELERITE is a public PYTHON GP implementation. By restricting the form of the kernel to adaptable, stationary covariance functions, Foreman-Mackey et al. (2017) reduced the computational costs to $\mathcal{O} \sim N$ rather than the $\mathcal{O} \sim N^3$ from standard inversion and determinant computation methods. Therefore,

1. we adopt the CELERITE package for our GP implementation.

The form of specific forms of the CELERITE kernel limits its use to 1-D inputs. Therefore,

2. we develop a sequential modelling framework, to model each spectral component in turn.

Here begins our simplifications to, and assumptions for the GP forward model. The standard approach in literature is to continuum-normalise all spectra, thus effectively removing the $A$ component (Equation 5.14). While it is necessary to standardise all spectra, a disadvantage is that during the normalisation you lose broad-band feature information. We simplify our problem by

3. pre-continuum-normalising all spectra prior to using the data as a training set.

Another challenge in the complete modelling of Equation 5.14 is the combination of different operations, as a mixture of additive and multiplicative terms. The model would not be purely additive or multiplicative in either linear or log space. We are therefore limited in the components which we can forward model with GPs. In the nIR (wavelength coverage of CRIRES), the telluric spectrum dominates over the stellar spectrum as a contaminating factor.

4. We choose to sequentially model (i) first the telluric spectral component, then (ii) the planetary spectrum, assuming the stellar contribution has been sufficiently removed prior to application of the framework.

In reality, all components in Equation 5.14 are a function of time and wavelength, but for the sake of simplicity,

5. we have neglected the time component of the planet and stellar flux.

### 5.3.1 The telluric component

Assuming the stellar spectrum has been removed from the data, the dominant component is the telluric spectrum, $T(t, \lambda)$. Its relation to time is difficult to model; common techniques in literature for the removal of tellurics is the application of singular value decomposition of the spectral matrix (including the SYSREM algorithm and PCA methods) to remove common modes in each pixel. To first order, the telluric transmission is a function of the atmospheric path length. Following the Beer-Lambert law, the light intensity at the top of the atmosphere, $I_0(\lambda)$, is attenuated as:

$$I_\lambda = I_0(\lambda) \exp\Big[ - \sum^{j} \kappa(\lambda)\Big]. \tag{5.15}$$

$\kappa(\lambda)$ is the opacity function for each species $j$, as given by:

$$\kappa(\lambda) = -\sigma_j(\lambda) \cdot n_j \cdot z \tag{5.16}$$

where $\sigma_j$ represents the absorption cross-section of species $j$, $n_j$ its average number density, and $z$ is the path length (Allart et al., 2022). Assuming a plane-parallel atmosphere, a reasonable assumption for airmass $< 5$ (Vidal-Madjar et al., 2010), the telluric transmission spectrum follows:

$$T(t, \lambda) = \frac{I(\lambda)}{I_0(\lambda)} = \exp\Big[ - \tau(\lambda) a(t)\Big] \tag{5.17}$$

where $\tau$ is the optical depth at zenith, and $a = \sec z$, the airmass. We might then consider a telluric model of the form,

$$T(t, \lambda) = T_{\text{ref}}(\lambda)^{a(t)} \tag{5.18}$$

where $T_{\text{ref}}$ represents the telluric spectrum at zenith. A common approach in the literature is to derive $\tau$ by linear regression on the logarithm of fluxes $F_{\text{obs}}$, assuming

$T$ dominates (see e.g., Wyttenbach et al., 2015; Astudillo-Defru & Rojo, 2013; Langeveld et al., 2021). This is where our first GP modelling comes into play.

I use a GP predictive mean as the reference spectrum $T_{\rm ref}$. As the training set for the GP, I use the (pre-processed and normalised) fluxes, transformed as:

$$\mathbf{y} = \frac{\log F_{\rm obs}}{a(t)} \tag{5.19}$$

which correspond to Earth-frame wavelengths, $\mathbf{x} = \lambda_\oplus$. Here $F_{\rm obs}$ is the sorted, flattened array of all flux data points from a single order. We must model the tellurics in log-space, since GPs require affine transformations, which exponentiation is not. At this stage, I assume there is a common wavelength solution for each frame, given the prior alignment procedure. I note, though, that it would not be difficult to assign a wavelength solution per spectrum.

Regarding the GP itself, we make few assumptions in the model. The mean function is unassuming, set to $\mathbf{m} = \mathbf{0}$. I select the Matérn-3/2 kernel to model the covariance between data points, which takes the form:

$$k_{\rm M32}(\lambda_i, \lambda_j; \boldsymbol{\phi}) = \sigma^2 \left(1 + \frac{\sqrt{3}}{\rho}|\lambda_i - \lambda_j|\right) \exp\left[-\frac{\sqrt{3}}{\rho}|\lambda_i - \lambda_j|\right]. \tag{5.20}$$

This function is evaluated for each pair of wavelengths $(\lambda_i, \lambda_j)$. To detail the method, I evaluate the log-likelihood, $\log p(\mathbf{y}|\mathbf{x}, \boldsymbol{\phi})$, subsequently fixing the hyperparameters, $\boldsymbol{\phi} = \{\sigma, \rho\}$, to their maximum likelihood estimates. Evaluating Equation 5.20, I then have a covariance matrix $\mathbf{K}$. We are then interested in evaluation of the posterior distribution upon test locations, $\mathbf{x}_*$, for which I choose the universal wavelength solution of each order. As a final step, the resulting predictive mean, $\boldsymbol{\mu}_*$, is reformed into a reference spectrum. Our resulting telluric model is given by

$$T(t, \lambda_\oplus) = \exp\left[\boldsymbol{\mu}_*\right]^{a(t)}. \tag{5.21}$$

This methodology is visualised in Fig. ??.

### 5.3.2 The planet component

I proceed assuming the telluric spectrum has been removed, and therefore what remains is the planet spectrum buried within the intrinsic noise. As we remain in the telluric rest frame, the planet spectrum Doppler shifts over time as a result of its orbital motion. The total planet velocity is given by

$$v_p = v_{\rm bary} + v_{\rm sys} + K_p \sin 2\pi\varphi, \tag{5.22}$$

where $v_{\rm bary}$ and $v_{\rm sys}$ represent the barycentric correction and velocity of the stellar system, $K_p$ is the semi-amplitude of the planet radial velocity and $\varphi$ are the phases. I begin by assuming a $K_p$, shifting to the planet rest frame, and creating a composite planet+noise spectrum. To clarify, I concatenate the transformed wavelengths, providing a proper wavelength solution in the planet rest frame, $\lambda_p$, rather than interpolating the fluxes, avoiding the associated additive interpolation noise. The transformed wavelengths are given by $\lambda_p = \lambda_\oplus/(1 + \frac{v_p}{c})$. I use the residual fluxes and $\lambda_p$ as the training set $\{\mathbf{x}, \mathbf{y}\}$. The second GP presumes the same kernel and mean function as the first (§5.3.1).

Incorporating Equation 5.22 into our constructed log-likelihood function, I marginalise over $K_p$ together with the hyperparameters $\boldsymbol{\phi}$. I use the open-access sampling PYTHON package EMCEE (Foreman-Mackey et al., 2013) to explore the full, joint posterior distribution. EMCEE is a fast Markov Chain Monte Carlo (MCMC) sampling algorithm. For each parameter I assume uniform priors, with informative bounds only for (i) previous literature measurements of $K_{\rm p}$ and (ii) the spectrograph resolution in the case of $\rho$, which can be likened to a length scale. The priors are:

$$\begin{aligned} K_p &\sim \mathcal{U}(100, 200)\,\mathrm{km/s}; \\ \sigma &\sim \mathcal{U}(0, \infty); \\ \rho &\sim (\delta\lambda, \infty) \end{aligned} \tag{5.23}$$

where $\delta\lambda$ is the spectrograph resolution. As a final constraint, I only condition each GP on the subset of data within $10\rho$ of each test location, since we expect a rapid decline in correlation between test locations significantly separated.

**Table 5.1:** Adopted parameters for both the HD 189733 and 51 Peg systems.

| Parameter | Unit | Value | Reference |
|---|---|---|---|
| **HD 189733** | | | |
| $T_{\rm eff}$ | [K] | $4875 \pm 43$ | Boyajian et al. (2015) |
| $\log(g)$ | | $4.56 \pm 0.03$ | Boyajian et al. (2015) |
| Stellar metallicity | [Fe/H] | $-0.03 \pm 0.04$ | Bouchy et al. (2005) |
| $K_*$ | [m/s] | $205 \pm 6$ | Bouchy et al. (2005) |
| $R_*$ | $[R_\odot]$ | $0.766^{+0.007}_{-0.013}$ | Triaud et al. (2009) |
| $v_{\rm sys}$ | [km/s] | $-2.361 \pm 0.003$ | Bouchy et al. (2005) |
| $R_p$ | $[R_J]$ | $1.178^{+0.016}_{-0.023}$ | Triaud et al. (2009) |
| $K_p$ | [km/s] | $154^{+14}_{-10}$ | Birkby et al. (2013) |
| **51 Peg** | | | |
| $T_{\rm eff}$ | [K] | $5793 \pm 70$ | Fuhrmann et al. (1997) |
| $K_*$ | [m/s] | $55.65 \pm 0.53$ | Wang & Ford (2002) |
| $R_*$ | $[R_\odot]$ | $1.1609589^{+0.0222188}_{-0.0807567}$ | Gaia Collaboration et al. (2018) |
| $v_{\rm sys}$ | [km/s] | $-33.2 \pm 1.5$ | Brogi et al. (2013) |
| $R_p$ | $[R_J]$ | 1.2 | See section 5.6.2 |
| $K_p$ | [km/s] | $134.1 \pm 1.8$ | Brogi et al. (2013) |

**Table 5.2:** Summary of the observations.

| Object | Date | Phase coverage | Wavelength coverage [μm] | Exp. time [s] | No. of frames |
|---|---|---|---|---|---|
| **HD 189733** | 01-08-2011 | 0.383 – 0.475 | 3.1805 – 3.2659 | 150.0 | 48 |
| **51 Peg** | 16-10-2010 | 0.36 – 0.42 | 2.287 – 2.345 | 42.0 | 166 |
| | 17-10-2010 | 0.60 – 0.66 | 2.287 – 2.345 | 42.0 | 148 |
| | 25-10-2010 | 0.49 – 0.54 | 2.287 – 2.345 | 42.0 | 138 |

I define a 'detection' of a planet signal firstly based on recovery of an orbital velocity which agrees with the literature, or later injected, values. See Appendix C for this in practice. Secondly, I assess the recovery of the planetary lines, beginning with the strongest absorption.

## 5.4 The data and reduction

I apply our constructed GP framework to two datasets, both archival nIR CRIRES dayside observations of canonical hot Jupiters HD 189733 b and 51 Peg b. Both were collected with the CRyogenic Infra-Red Echelle Spectrograph (CRIRES, Käufl et al. 2004), which was mounted on the UT3 of the Very Large Telescope (VLT),

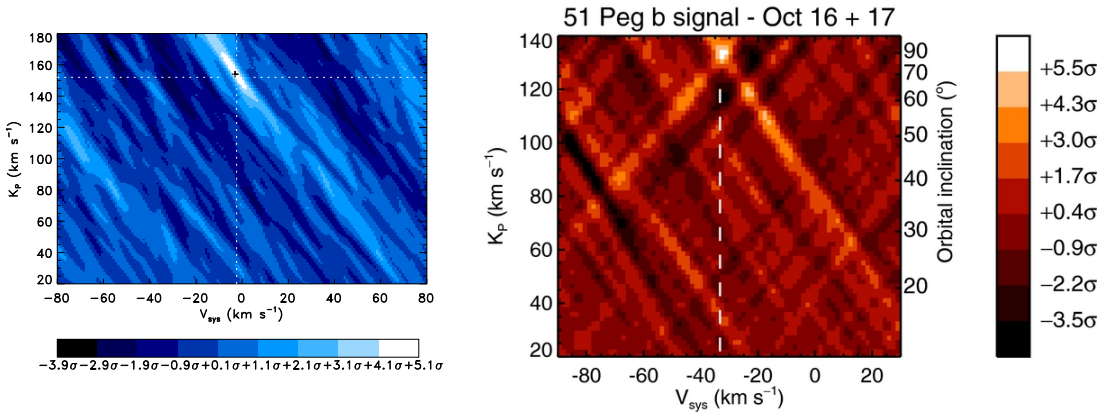


**Figure 5.4:** The cross-correlation maps of the original publications. **Left:** the detection of $H_2O$ in the atmosphere of HD 189733 b. Figure from Birkby et al. (2013). **Right:** the detection of atmospheric CO for 51 Peg b. Figure from Brogi et al. (2013). In each panel, the location of the highest significance correlation is pointed to with white dashed lines.

prior to the instrumental upgrade to CRIRES+ in 2014. The 51 Peg b observational bandpass centred on 2.4 µm, while the HD 189733 b observations were centred on 3.2 µm. A summary of the observations is given in Table 5.2.

We select these datasets for a number of reasons:

(i) both were sensitive to atmospheric detections using the cross-correlation method, specifically with detections of $H_2O$ and CO published in Birkby et al. (2013) and Brogi et al. (2013) respectively, providing a baseline against which to test our GP method. I show the detections reported by the original publications in Fig. 5.4;

(ii) the old CRIRES featured four detectors, producing on order of $4 \times 1000$ datapoints, which corresponds to tractable computational time of our GP framework;

(iii) the detections were made using standard detrending techniques; the observing conditions were not so complex as to require complex and tailored detrending.

The observation of HD 189733 was taken on August 1 2011, while there were three nights of observations for 51 Pegasi, October 16, 17 and 24 2010. Both programs were part of the ESO large Program ID. 186.C-0289 (PI: Snellen).

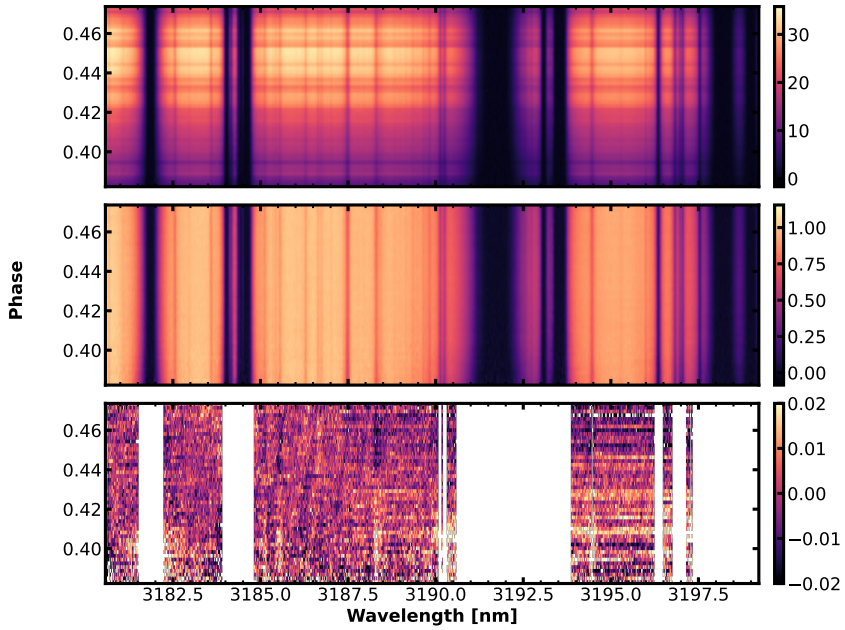


**Figure 5.5:** Spectral matrix for HD 189733, CRIRES detector 1. **Top panel:** Adopted pre-processed fluxes from Birkby et al. (2013), having been aligned, background and bad pixel corrected. **Middle panel:** Spectra post continuum-normalisation. **Bottom panel:** Residuals after removing the stellar model and GP telluric model, with deep telluric bands masked. In this panel the residuals have been weighted by the corresponding propagated uncertainties.

With regard to the preliminary data processing, I adopt the pre-processed spectra from the original publications (by private communications with the corresponding authors). The public instrumental (CRIRES-specific) pipeline was applied to both datasets, using versions v2.2.1 and v1.11.0 for HD 189733 and 51 Peg respectively. The authors of the original publications applied further processing algorithms to these pipeline products. Grouping the combined ABBA exposures into a single 'frame', they constructed a $V \times W$ spectral matrix as standard for each of the four CCD detectors ($V$ frames/epochs and $W$ pixels). They applied standard flat-fielding, bad pixel, background subtraction and alignment corrections; I adopt the spectra after these corrections. The proceeding corrections are the same for both datasets, except for the removal of the star in the case of the HD 189733 spectra, which I detail in the next section.

The first step is the normalisation of the spectra: I distinguish fluxes belonging to the continuum rather than absorption features by splitting each order into ten

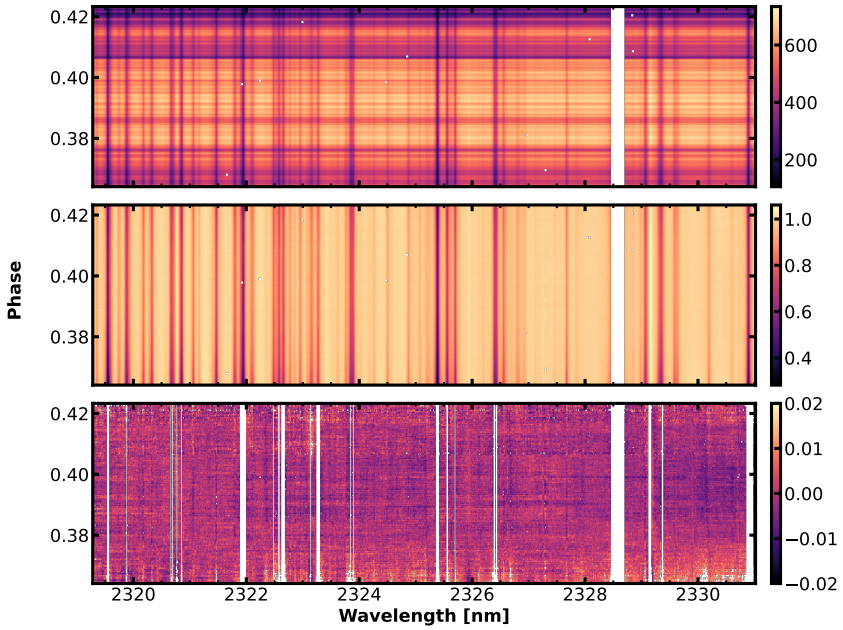


**Figure 5.6:** Spectral matrix for 51 Peg, CRIRES detector 3. I only display the fluxes from 16th October observation. Figure is the same format as Fig. 5.5, with the one exception being the lack of stellar treatment.

segments, and identifying the top 10% of fluxes in each segment. I then fit a low-order polynomial to these maximal fluxes to capture the broad-band variation, and divide through all fluxes by the result. I perform this normalisation independently for each spectrum. This concludes step 2 shown in the workflow Fig. ??.

Post telluric correction (step 3), I assess the residual dispersion in each pixel channel in order to apply appropriate masking to the fluxes, before searching for the planet signal. I compared the residual dispersion to that of the formal uncertainties from the CRIRES pipeline; in the pixels where the scatter was systematically larger, I applied an inflation scaling to the propagated uncertainties. Furthermore, if the dispersion surpassed a threshold factor of the median across the spectrum, I chose to entirely mask the column, usually corresponding to regions of strong or saturated telluric absorption.

## 5.5 HD 189733 b

I analyse one night of observation of HD 189733 b, spanning phases just prior to secondary eclipse (Table 5.2).

### 5.5.1 Removal of the stellar spectrum

In the original study of this dataset (Birkby et al., 2013), the investigators chose not to specifically remove the stellar spectral features in isolation. Instead, their reduction method involved use of PCA which, focusing on common modes in each pixel, would presumably simultaneously remove the negligibly shifting stellar lines. Our GP framework assumes complete stellar removal, given the form of the training set of the first GP in Equation 5.19. It is therefore necessary to explicitly remove the stellar spectral lines. I note that I attempted a first assessment of the adopted spectral matrices, applying the telluric model in Equation 5.21 to the fluxes as-is. Post telluric correction, I assessed the residual dispersion in each of the pixels expected to be affected by stellar lines with greater than 5% absorption. I found that these pixels showed higher time dispersion than the rest of the spectrum, up to a factor of 2.5. I therefore remove a synthetic stellar model from the data; I chose to use the PHOENIX stellar spectral library. PHOENIX is a stellar photosphere modelling code, capable of producing synthetic stellar spectra in the wavelength range $0.05 - 5\,\mu\text{m}$ at resolutions up to $R = 500,000$, for a range of stellar effective temperatures (Husser et al., 2013). I interpolated over the PHOENIX grid in three dimensions: the stellar effective temperature, gravity ($\log g$) and metallicity (Fe/H). I then evaluated the interpolation for the literature reported stellar parameters, given in Table 5.1. Finally, to fit the model stellar spectrum to the observations, I convolved it to the instrumental resolution and applied a scaling parameter, determined by the fit of two known, strong stellar lines.

### 5.5.2 Telluric modelling

There is significant water telluric absorption around the 3.2 µm band of these data. There are even some regions of complete saturation, seen as the dark vertical bands

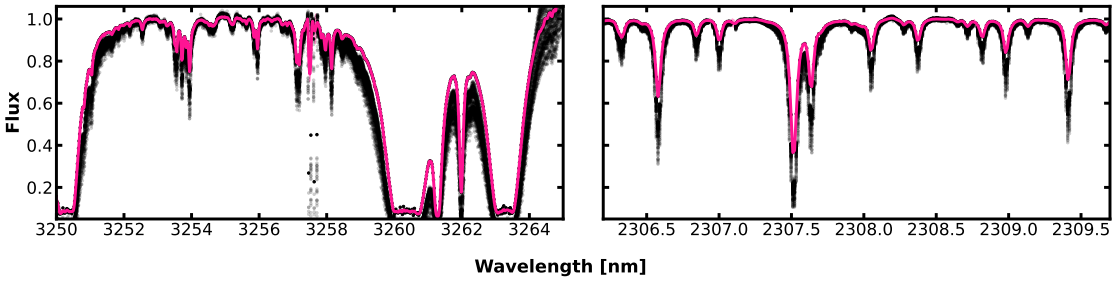


**Figure 5.7:** The pipeline-reduced fluxes of **left:** HD 189733 and **right:** 51 Peg from CRIRES detectors 4 and 2 respectively in black. Overplotted in pink is the GP telluric model of equation 5.21, with $1\sigma$ uncertainty shaded in pink, propagated from the GP predictive mean and covariance.

in Fig. 5.5. The predictive GP telluric model, $T(t, \lambda_{\oplus})$, is shown in Fig. 5.7, and example residuals, having removed this from the normalised fluxes, are shown for detector 1 in the bottom panel of Fig. 5.5.

### 5.5.3 Recovery of the planet spectrum

Having applied step 4 and 5 (Fig. ??), I report a null detection of any planetary spectrum. The reason was twofold: the MCMC did not converge for any of the three parameters $(K_p, \boldsymbol{\phi})$ (as determined by eye), and then an attempted evaluation of the predictive mean consisted purely of spurious noise features. I proceeded to explore the cause of the non detection; the Gaussian process is likely insensitive to the planet signal given the noise level, either (i) due to telluric residuals, a result of insufficient detrending, or (ii) the intrinsic photon noise level of the data. See §5.7.2 for the exploration of case (i). Regarding case (ii), I test the sensitivity of the data via injection-recovery tests.

Using HRCCS, Birkby et al. (2013) reported a detection of $H_2O$ at $4.8\sigma$ (Fig. 5.4). They used a forward-modelled spectrum, and thus pre-defined the shape and location of the planetary spectral lines. However, within our framework, we refrain from making assumptions[1] regarding the planetary spectrum *a priori*. A potential consequence may be a reduction in the sensitivity of the GP framework compared to HRCCS. Therefore, I inject the forward model which was recovered with highest

[1]I note that the one assumption we do make is the functional form of the covariance between the residual fluxes (Equation 5.20), inherent to Gaussian process regression.

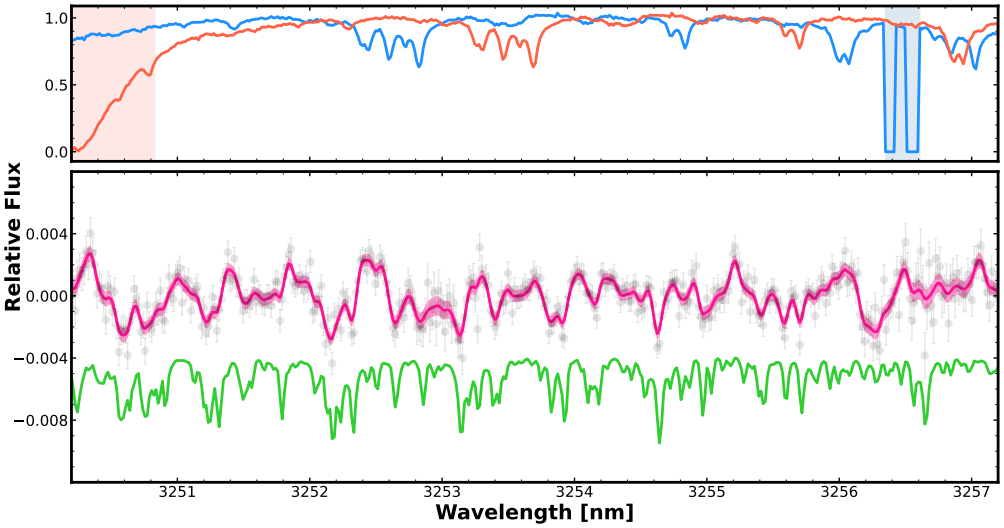


**Figure 5.8:** Recovery of an injected $H_2O$ planet spectrum, from the HD 189733 observations. **Top panel:** the position of the telluric spectrum, at its maximal shifts in the rest frame of the planet. The corresponding red and blue highlighted wavelengths are those that were masked in step 4. **Bottom panel:** The GP predictive mean and $1\sigma$ interval in pink, compared to the injected model in green. The residuals in the planet rest frame, having removed the GP telluric 'model' are also shown as transparent grey data points.

significance (bar a marginal $0.3\sigma$ increase with the inclusion of $CO_2$) in Birkby et al. (2013) and assess the recovery of said spectrum. To detail the atmospheric forward model, the planetary atmosphere was assumed to be $H_2$/He-dominated, with $H_2O$ at an abundance corresponding to VMR[$H_2O$] $= 10^{-5}$. The spectral lines were computed line-by-line based on the HITEMP line list (Rothman et al., 2010). The best fit temperature profile was linear, with $(T_1, P_1) = (1350\,\mathrm{K}, 10^{-1}\,\mathrm{bar})$ and $(T_2, P_2) = (500\,\mathrm{K}, 10^{-1.5}\,\mathrm{bar})$.

I inject the planet spectral model, $F_{\mathrm{model}}$, into the observed fluxes, $F_{\mathrm{obs}}$, prior to reduction as

$$F_{\mathrm{sim}}(t,\lambda) = F_{\mathrm{obs}}(t,\lambda) + F_{\mathrm{cont}}(t,\lambda)\left[n_{\mathrm{inj}} \cdot \frac{F_{\mathrm{model}}(t,\lambda)}{F_*(\lambda)}\left(\frac{R_p}{R_*}\right)^2\right] \tag{5.24}$$

where $R_p/R_*$ is the photometrically-derived planet-to-star radius ratio. This injection method is a take on the method of Brogi et al. (2013, 2014), adapted to use the observed flux continuum, $F_{\mathrm{cont}}$, to scale the injected planetary spectrum. As such, I circumvent 're-injection' of telluric absorption lines atop of the planetary

signal. For the scaling of the planetary model, I choose to use the blackbody fluxes for the stellar continuum $F_*(\lambda)$, derived for the published effective temperature (Table 5.1). The time variation of $F_{\rm model}(t, \lambda)$ is purely a Doppler-shift, induced by the planet orbital velocity, $v_p$ (Equation 5.22). Finally, $n_{\rm inj}$ is a scaling parameter which I use to amplify the planetary signal. Birkby et al. (2013) reported a 'zero-$\sigma$ detection' when injecting the $H_2O$ spectrum at $n_{\rm inj} = -0.56$, at the corresponding negative radial velocity. I operate on the basis that the real signal has nominal line strengths corresponding to $n_{\rm inj} = 0.56$, on the presumption that the null detection was a consequence of 'cancelling out' the real signal.

Having injected a planetary spectrum, I repeat the process in Fig. **??** for different $n_{\rm inj}$. The post-processing of the simulated fluxes, $F_{\rm sim}$, is identical to that applied to the real data. The lowest amplitude scaling for which we report a detection is $n_{\rm inj} = 1.8$; the recovered GP predictive mean is shown in Fig. 5.8. This was the minimum scaling factor at which I recovered a radial velocity that was consistent with the injection velocity $K_p = 154\,{\rm km/s}$ within $1\sigma$ (see Fig. C.1). The maximum likelihood estimate of the planet radial velocity was $K_p = 152.55 \pm 1.53\,{\rm km/s}$; the 1-D and 2-D posterior densities of $K_p$ and the two GP hyperparameters from step 5 are shown in Fig. 5.9, all of which converged well. In Fig. 5.8, I compare the recovered GP 'spectrum' (pink) to the injected spectrum (green). Though the recovered continuum is noisy, at $n_{\rm inj} = 1.8$ we begin to recover the deeper planet spectral lines. I convert the scaling parameter to a line contrast ratio: measuring the average line depth of the nominal $H_2O$ spectrum, $n_{\rm inj} = 1.8$ translates to an average line contrast of $\sim 4.37 \times 10^{-3}$. Therefore, the signal of the cross-correlation detection must be amplified by a factor of 3.2× to be detected by the GP framework, considering the noise properties of these data.

## 5.6 51 Pegasi b

I analyse three nights of spectral observations of 51 Peg, encompassing phases before prior to and post eclipse, and centred on 2.3 µm. With these dayside observations,

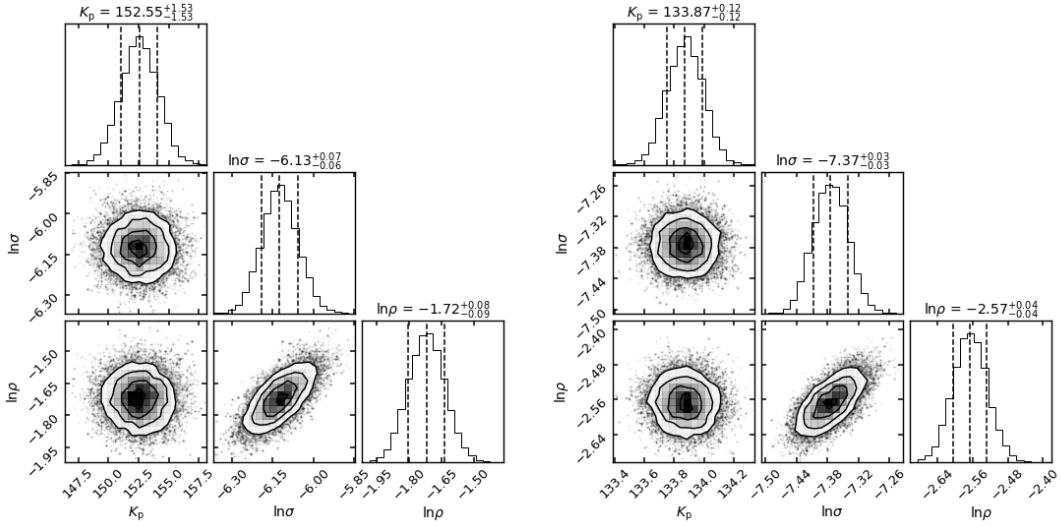


**Figure 5.9:** Posterior distributions of the three parameters varied in step 5 of the GP framework: planet radial velocity amplitude, $K_p$, and the two kernel hyperparameters, $\phi = \{\sigma, \rho\}$. The marginalised 1-D posterior distributions are shown on the diagonal. **Left:** the HD 189733 dataset and **right:** the 51 Peg dataset.

Brogi et al. (2013) reported a detection of an $H_2$/He-dominated atmosphere containing CO and $H_2O$ at a significance of $5.9\sigma$ (Fig. 5.4). This forward model assumed a non-inverted, linear temperature structure, with $(T_1, P_1) = (1250\,\mathrm{K}, 0.1\,\mathrm{bar})$ and upper bound $(T_2, P_2) = (500\,\mathrm{K}, 10^{-4}\,\mathrm{bar})$. The absolute abundances were fixed to $\mathrm{VMR[CO]} = 1 \times 10^{-4}$ and $\mathrm{VMR[H_2O]} = 3 \times 10^{-4}$, though I note that these are only weakly constrained, since Brogi et al. (2013) did not attempt to scale the amplitude of the lines. The line list used was the HITEMP data base (Rothman et al., 2010). Throughout our analyses, I adopt this atmospheric model as 'truth'.

Brogi et al. (2013) reported null detection of CO and $H_2O$ in the third night of data, proposing that stellar contamination could dampen the planetary signal, amongst other astrophysical causes. Contrary to the other two nights of data, the planet traversed superior conjunction on the 25th October 2010. As a consequence of the zero radial velocities, the planet and stellar spectral lines from the same species would overlap. This hypothesis was confirmed by Chiavassa & Brogi (2019), who were able to uncover the planetary signal in the third night of data, having implemented a more rigorous stellar correction. In this work, I begin at

step 2 (Fig. ??) with the stellar-corrected residuals from Chiavassa & Brogi (2019), acquired via private communication.

### 5.6.1 Telluric spectrum

I train the first GP on the stellar-corrected residuals; an example of the resulting GP predictive mean telluric model is shown in Fig. 5.7. I perform this telluric modelling on each night of data separately. Once again, the telluric-corrected residuals required masking. As well as the method described in §5.4, I manually masked a number of pixels centred on $\lambda \simeq 2328.5\,\mathrm{nm}$, which showed high dispersion and are known to contain a strong telluric line. An example order following this correction is shown in Fig. 5.6. Having corrected the tellurics, I combine the three nights of residual fluxes for the remaining analysis.

### 5.6.2 Recovery of the planet spectrum

I report a null detection of the planet signal reported in Brogi et al. (2013). Therefore, I proceed to perform injection tests using the same method as that detailed in §5.5.3. To clarify the inputs to Equation 5.24, I injected the $H_2O$ + CO model discussed above, which yielded the highest cross-correlation significance. As a non-transiting planet, the radius of 51 Peg b is not well constrained; I adopted a radius $R_p = 1.2\,R_J$, the average of all similar mass planets in the NASA exoplanet archive. This value is in agreement with the limits proposed by Scandariato et al. (2021) and Birkby et al. (2017).

The lowest injection amplitude at which I recover a detection was $n_{\mathrm{inj}} = 9.4$, with a reported $K_p = 133.88 \pm 0.12\,\mathrm{km/s}$ which is in agreement with the injection velocity, $K_p = 134\,\mathrm{km/s}$ (see Fig. 5.9 for the posterior distributions). The recovered GP 'spectrum' is shown in Fig. 5.10. Relative to the continuum, the injected spectrum corresponding to $n_{\mathrm{inj}} = 9.4$ exhibits an average line contrast of $\sim 1.39 \times 10^{-3}$. I note that Brogi et al. (2013) used a radius of $R_p = 1\,R_J$, inferred (but not measured) from the presence of secondary eclipses despite the non-transiting inclination of 51 Peg b. Also, as aforementioned, the detection reported in Brogi et al. (2013) does

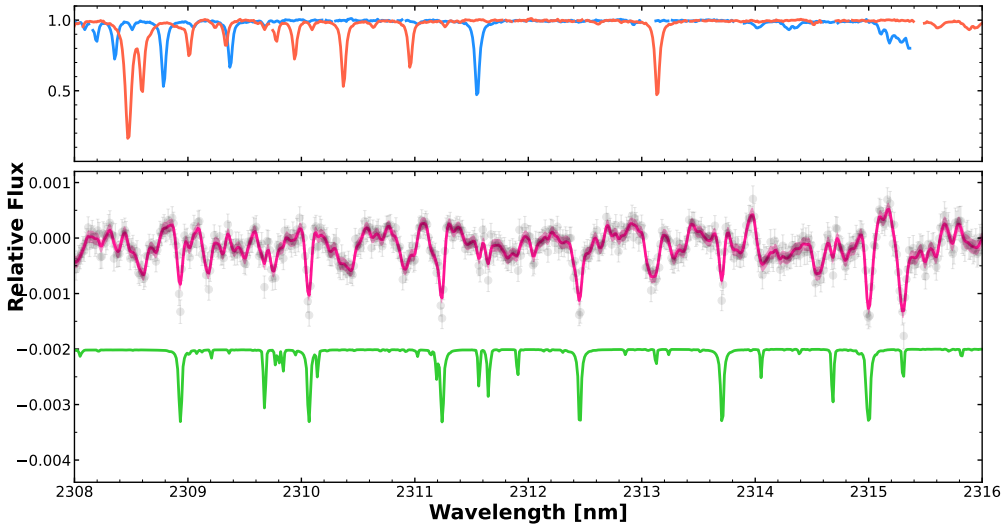


**Figure 5.10:** The smallest injection recovered planet spectrum of 51 Peg. Same format as Fig. 5.8.

not include a constraint on the line strength, and therefore species abundances, but only their presence. It is therefore difficult to directly compare the strength of the recovered signal using the GP framework to that recovered with cross-correlation. To first order, the cross-correlation technique is a factor 9.4× more sensitive than GP framework considering the noise properties of these data. However, we note that since $R_p$ and $R_*$ also scale the injected model (in Equation 5.24), had we implemented a larger planetary radius, the minimum scale factor, $n_{\rm inj}$, at which I recovered a spectrum would be reduced by the inverse square root of the same factor.

## 5.7 Exploring the sensitivity of the planet GP

Here, I discuss and explore the possible causes of the null detections of the presumably real, planet signals.

### 5.7.1 Limiting assumptions of the GP framework

I first detail the assumptions of our GP framework:

1. the spectral components (here the telluric spectrum and planet spectrum) are each a realization of an independent Gaussian process;

2. instrumental systematics have been perfectly removed via normalisation and wavelength calibration, prior to input at step 1 (Fig. ??);

3. the telluric variation corresponds logarithmically with airmass, while residual variation is minimal, below the intrinsic photon noise level;

4. the temporal variation of the planet spectrum corresponds only to a Doppler shift. The planet spectrum is otherwise constant in time;

5. the stellar spectrum is perfectly removed prior to step 1 (Fig. ??);

6. the exoplanet spectra detected in Birkby et al. (2013) and Brogi et al. (2013) are genuine.

Each of these assumptions has a non-negligible impact on the sensitivity of the GP framework to detect the planet spectrum. I proceed to address each assumption in turn, and impact of its violation.

1. Strictly speaking, a spectrum (of a star, telluric or planet) is not a Gaussian process. A Gaussian process is therefore not necessarily a natural model choice for a spectrum. I would issue caution in the case of inference over the wavelength domain, since the kernel hyperparameters are unlikely to be physically motivated. However, I am interested only with prediction in the GP framework presented. I therefore do not believe this to be a limiting factor in our analyses here, and the benefits of Gaussian process regression here outweigh the impact of this assumption. In addition, the spectral components handled above are certainly independent. I note that this might not necessarily be true in the extension of this framework to star-planet modelling of reflection spectra, wherein the planet's spectrum depends on the stellar spectrum.

2. The assumption of perfect systematics removal is standard practice in HRCCS. Misaligned spectra or an erroneous wavelength solution could cause (i) a reduced spectral feature to be recovered, or even overlooked and/or (ii) a broader $K_p$ posterior in the case of detection. In this case, the framework

above would have to be adapted to include a unique wavelength solution for each frame, which would be feasible, with little increase in computational time. I note here that resolution variability could result from an unstable line spread function (LSF), but again it is standard practice to assume stability.

3. The exponent relation between telluric variation and airmass is known to be true (see §5.3.1), and not in question. However, though airmass is one of the predominant factors, it is certainly not the only cause of the time variation of tellurics. Moreover, in the strong absorption regime, it is no longer true that the time variation corresponds linearly with airmass. This assumption is likely to be the limiting factor of our GP framework; I discuss it further in §5.7.2.

4. It is certainly possible that the planet spectrum varies over the observed phases. Theoretically predicted for a while, time variability has only recently been observed. For example, Ehrenreich et al. (2020) observed an asymmetric planetary iron trail, due to different limb contributions in transmission. In the case of emission spectroscopy, there is a change in the observed fraction of the dayside. However, this fractional change is minimal in the cases we present here. This assumption is in standing with that of standard cross-correlation studies, including the original works Birkby et al. (2013) and Brogi et al. (2013), which effectively sum the contributions from each epoch.

5. It is common to assume perfect stellar removal in HRCCS. As Chiavassa & Brogi (2019) showed, removing models which lack sufficient complexity can impede planetary detections. In the case of 51 Peg b, I am confident that this assumption is not obstructing a planet signal, given the detailed stellar treatment of Chiavassa & Brogi (2019) and their subsequent reported detection. For HD 189733 b, I handle the stellar removal myself, and assume only 1-D, homogeneous treatment. This may be insufficient, but I am certain that the impact of residual tellurics is more significant.

6. The original analyses reported detection significances of $4.8 - 5.1\sigma$ and $5.9\sigma$ (Birkby et al., 2013; Brogi et al., 2013); there exists a standard threshold of $5\sigma$ to claim a detection in HRCCS. It is therefore reasonable to presume these exoplanet signals exist in the data. In the unlikely event that there is no exoplanet atmospheric signal in the data, our injection tests are still valid, to indicate at what line contrast the GP framework would be able to distinguish such an atmospheric signal from the noise.

   The reported planetary radial velocities of the atmospheric signals have precisions of $2 - 14\,\mathrm{km/s}$ (see Table 5.1). Therefore, alternatively there is a possibility that the real signal is offset from the injection velocity. In this case, the injected and (slightly offset) real signals could coalesce to form a 'composite' planet signal, differing from the 'truth' model. This would act to confuse the GP search for the planetary signal, both due to a distortion of the lines compared to the model template, and an offset from rest frame velocity. Though this does not explain the null detections using the real data, it may impact the injection tests, since a higher injection amplitude would be necessary to overcome the intrinsic planet signal.

### 5.7.2 Using alternative telluric correction methods

I have acknowledged that the GP telluric model is non-ideal and a dominant limiting factor in our framework. Here I explore the use of other detrending techniques to isolate and examine the extent of the limitations of the GP telluric model. In order to directly compare the planet Gaussian process regression step to the cross-correlation sensitivity, I test the detrending methods employed in the original analyses.

#### SYSREM

Birkby et al. (2013) used the SYSREM algorithm to detrend the HD 189733 spectra. Originally developed to correct lightcurve systematics (Tamuz et al., 2005), SYSREM can be considered a take on PCA, with the addition of data-point uncertainty weighting. I begin by normalising the spectra, synonymous with §5.4, before

dividing through by the mean spectrum to leave only residual variation remaining. Before input to SYSREM I mask the wavelength channels with saturated tellurics (zero, or close-to zero, flux), using the same masks as that of Birkby et al. (2013). Similarly to PCA, SYSREM removes a user-defined number of components (see §2.3.2). Here I apply the same number of SYSREM iterations as Birkby et al. (2013): $\{8, 1\}$ for detectors 1 and 3, and then $\{5, 5\}$ for detectors 2 and 4, which were unused in the original analysis.

Using this technique to reduce the HD 189733 spectra, I endeavour to search for the true planet signal, starting at step 4 of Fig. **??**. I retrieve a null detection. I tried repeating the reduction for an alternative number of SYSREM iterations, identified using my own optimisation routine (see Appendix C), but to no avail. This may well support the claim that the telluric model is not the only cause of the null detection in §5.5.3. It may still be the *dominant* issue though. I therefore performed an injection test, to compare the sensitivity of the SYSREM to the GP reduction routine. Again injecting the $H_2O$ model into the pipeline-reduced fluxes using the same method as §5.5.3, I repeated the reduction and planet search. The lowest scale factor (Equation 5.24) for which I recover a planet detection was $n_{\rm inj} = 1.4$, retrieved with a marginal posterior mean $K_p = 155.62 \pm 1.76\,{\rm km/s}$.

### Linear regression

Brogi et al. (2013) used a tailored detrending technique to remove tellurics in the 51 Peg data, involving linear regression. Similar techniques were employed in Brogi et al. (2012, 2014); Schwarz et al. (2015). I apply this technique as follows: firstly, I normalise each spectrum using the same method as §5.4, then I explicitly removed the airmass variation in each pixel column (see e.g., §3.3)[2]. The residual variable behaviour in columns associated with known strong telluric lines was then measured, $s_k(t)$, where $k$ denotes the line index. I used an ESO SKYCALC[3] (Noll et al., 2012) telluric spectrum to compile a list of lines, $\lambda_k$, with absorption greater than 50%.

[2]As an aside, there remained visible telluric residuals after the first step of this technique, namely the explicit airmass removal, further confirming the shortfall of the GP telluric model.

[3]https://www.eso.org/observing/etc/doc/skycalc/helpskycalc.html

Then, I compiled a linear function of the combined $s_k$, and employed linear regression to fit this to the residuals in each wavelength column (before dividing it out). Finally, I applied a high-pass filter. These steps are analogous to Brogi et al. (2013). I choose to omit their final step, whereby they down-weigh any significantly noisy pixels by dividing out each column variance, since I wish not to modify the data variance. Thus, I instead opt for column masking where there is strong residual variability.

Having reduced the 51 Peg spectra using this technique, again I report a null detection of the real planet signal. I even attempted a reduction using the same $\lambda_k$ as those used by Brogi et al. (2013), but observed no improvement. From this I conclude that the GP telluric model of §5.3.1 is not the only cause of the null detection in §5.6.2. I proceeded with an injection of the CO+$H_2O$ model. I observed a reduction in the minimum recovered scale factor: at $n_{\rm inj} = 8.5$, I report a marginal posterior mean of $K_p = 134.13 \pm 0.14\,{\rm km/s}$.

In both detrending cases, the noise in the residuals expressed visibly better suppression having employed the original telluric correction methods. It is therefore unsurprising that a GP was able to recover planet spectra with marginally weaker line contrasts. The contrast is better expressed as a signal-to-noise: for 51 Peg b the $n_{\rm inj} = 8.5$ recovery using linear regression corresponds to a $\mathrm{SNR}_{\rm line} \sim 0.36$ for the strongest planet spectral lines. Then, the GP framework recovers a signal corresponding to $\mathrm{SNR}_{\rm line} \sim 0.29$, marginally smaller. In the next section, I explore the different detrending methods further.

### Comparison of detrending methods

For more comprehensive comparison of the above reduction methods, I apply all three to the 51 Peg dataset (all three nights) with a $n_{\rm inj} = 9.5$ injected planet model. I kept all other treatment the same between methods, including the masking of wavelength channels post detrending. The implementation of each method follows the above section. I optimised SYSREM using the method detailed in Appendix C. The recovered planet GP predictive mean using each detrending

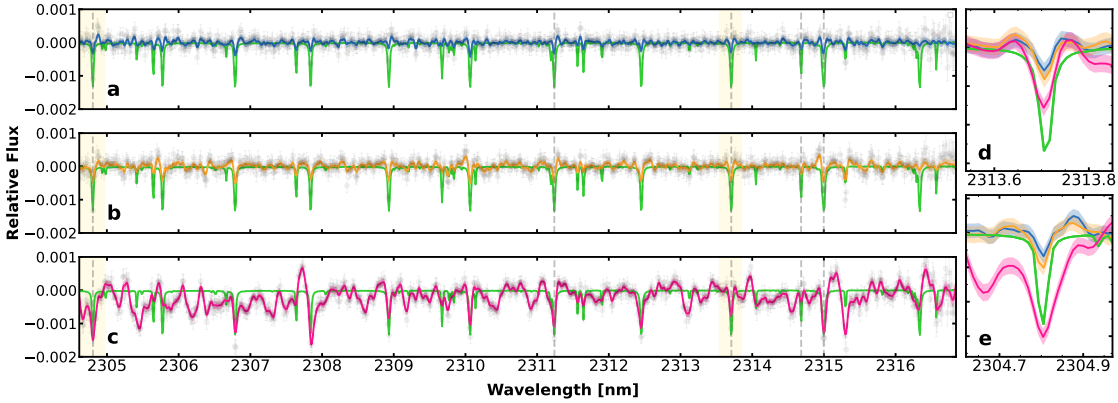


**Figure 5.11:** Recovery of an injected planetary signal using a GP, having detrended the data using different methods. The GP predictive mean and $1\sigma$ interval is shown compared to the injected model (green), having implemented **panel (a):** a linear regression detrending (blue), **panel (b):** the SYSREM algorithm (yellow) and **panel (c):** the GP telluric model (pink). The grey dashed lines indicate spectral lines which were measured to compare the three methods in §5.7.2. **Panels (d)** and **(e)** are magnified subsections of the recovered lines centred on 2313.709 and 2304.804 nm respectively, shaded yellow in panels **(a)-(c)**, with recoveries using all three methods shown in their respective colours.

method is shown compared to the injected model in Fig. 5.11, with the example of CRIRES detector 2 given.

At first glance, both SYSREM and the linear regression techniques tend to afford a cleaner planetary spectrum. This is a result of the better suppression of telluric noise. To offer a quantitative comparison, I target a number of line diagnostics, namely the amplitude (or depth) of the planetary spectral lines, their FWHM and the dispersion seen in the continuum exterior to absorption features. I measure these by fitting a Gaussian profile to a selection of deep planetary lines. For order 2, I demonstrate the metrics in Table 5.3, where the selected lines are highlighted by grey dashed lines in Fig. 5.11.

In general, the GP telluric method affords a noisy continuum, yet remains more faithful to the line depths. Both SYSREM and the linear regression technique significantly degrade the planetary signal, as seen in Fig. 5.11 panels (d) and (e). Regarding the lines given in Table 5.3, four lines were located in proximity to a strong telluric line ($> 95\%$ absorption): $\lambda \simeq 2311.241$ nm, 2313.709 nm (shown in panel (d) of Fig. 5.11), 2314.683 nm and 2314.999 nm. These each remain in regions of high telluric absorption throughout the observations; their lines are

more faithfully recovered with the GP technique. On the other hand, the line located at $\lambda \simeq 2304.804\,\mathrm{nm}$ traverses deep telluric line in more than 60% of the frames. It is shown in panel (e) of Fig. 5.11, and is poorly recovered with the GP method compared to the other two. These examples are representative of lines across the entire wavelength coverage, and I conclude that in regions of strong atmospheric opacity, or planetary lines which traverse telluric lines, the other two methods perform better. On the contrary, in regions of light telluric absorption, that GP telluric method affords a more faithful recovery of planetary lines. The line metrics indicate that SYSREM and the linear regression technique consistently eat away at both the wings and depth of the absorption lines. This highlights the dangers of harsh detrending: there is certainly a balance to be found between sufficiently removing the tellurics (GP method) and removing them too harshly so as to impact the planet spectrum (SYSREM and linear regression methods). Moreover, this confirms the importance of considering the impact of detrending on the planet signal when using HRCCS. It has the potential to lead to incorrect retrieval conclusions; it is thus crucial to mimic the artefacts of detrending on the cross-correlation model template (see Gibson et al., 2021).

## 5.8 Possible Extensions

### 5.8.1 A simultaneous modelling approach

I explore here the extension of the sequential method in Meech et al. (2022) to simultaneous GP forward modelling. This is a challenging step for several reasons. Firstly, (i) such a model would require three dimensions at a minimum (to include the planet, star and tellurics), and (ii) the number of data points of a high-resolution exoplanet observation quickly surpasses $\sim 1 \times 10^6$. Both of these are bottle-necks for the public, optimised GP codes (e.g., GEORGE, Ambikasaran et al. 2015). In addition, all three components will have different rest frame velocities, and so the input wavelength array, $\{\mathbf{x}\}$, will require different sorting for each. This is the limiting factor towards employing the extension of CELERITE to 2-D inputs presented by Gordon et al. (2020). Then, as given in Equation 5.14, the total spectrum is a

**Table 5.3:** Detection metrics assessing recovery of planetary spectral lines. The example given is that of a $n_{\rm inj} = 9.5$ injected CO model into the 51 Peg spectra. Each metric is the ratio between the recovered line and the injected line. The lines listed are indicated by grey dashed lines in Fig. 5.11.

| Wavelength [nm] | Airmass linear regression | SYSREM | GP telluric correction |
|---|---|---|---|
| **Amplitude** | | | |
| Average | $0.629 \pm 0.038$ | $0.680 \pm 0.038$ | $1.138 \pm 0.053$ |
| 2304.804 | $0.833 \pm 0.180$ | $0.919 \pm 0.139$ | $1.575 \pm 0.227$ |
| 2311.241 | $0.655 \pm 0.154$ | $0.692 \pm 0.118$ | $1.073 \pm 0.194$ |
| 2313.709 | $0.576 \pm 0.121$ | $0.628 \pm 0.095$ | $0.923 \pm 0.125$ |
| 2314.683 | $0.652 \pm 0.164$ | $0.636 \pm 0.184$ | $0.716 \pm 0.247$ |
| 2314.999 | $0.534 \pm 0.108$ | $0.549 \pm 0.103$ | $1.157 \pm 0.146$ |
| **FWHM** | | | |
| Average | $0.739 \pm 0.049$ | $0.808 \pm 0.047$ | $1.123 \pm 0.065$ |
| 2304.804 | $0.751 \pm 0.152$ | $0.805 \pm 0.131$ | $1.185 \pm 0.239$ |
| 2311.241 | $0.724 \pm 0.191$ | $0.758 \pm 0.147$ | $1.219 \pm 0.264$ |
| 2313.709 | $0.603 \pm 0.133$ | $0.637 \pm 0.102$ | $0.741 \pm 0.120$ |
| 2314.683 | $0.941 \pm 0.241$ | $0.923 \pm 0.269$ | $0.801 \pm 0.355$ |
| 2314.999 | $0.730 \pm 0.160$ | $0.795 \pm 0.147$ | $1.264 \pm 0.174$ |
| **Continuum standard deviation** | | | |
| | 1.622 | 1.726 | 3.747 |

mixture of additive and multiplicative components. All in all, these issues require further thought. Yet, one plausible extension would be a simultaneous GP modelling of the Doppler-shifting planet spectrum, as well as the stellar spectrum. Here, I performed a few preliminary basic simulation tests towards this extension.

I start here with a demonstrative, simulated high-resolution observations, of a narrow bandpass. I create a mock stellar 'spectrum', featuring a continuum and several absorption lines, around the 1.2 µm region and setting a resolution of $R = 45,000$. Then, I add in a comparably weaker planet spectrum, Doppler-shifting according to a velocity of $K_p = 200\,\mathrm{km/s}$, before adding noise equivalent to an SNR = 100. The stellar spectrum is assumed to remain stationary in wavelength.

For the GP implementation, I employ TINYGP[4]. This package is the successor to GEORGE; it allows multi-dimensionality, and moreover, supports GPU usage.

[4] https://tinygp.readthedocs.io/en/stable/

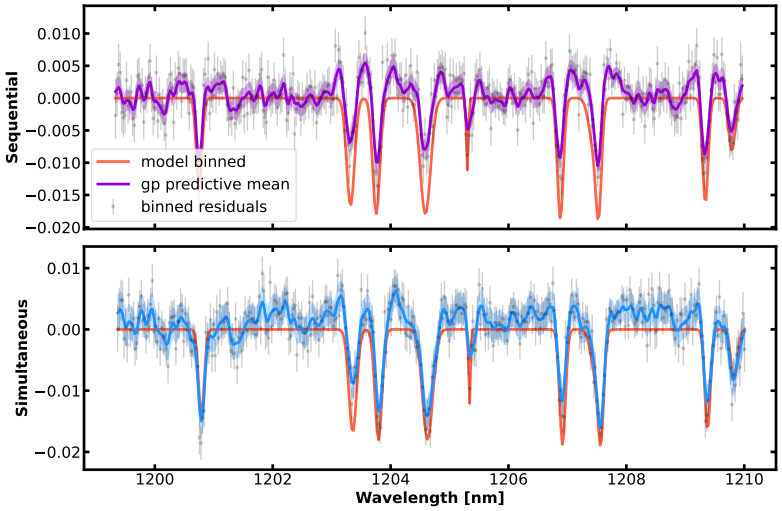


**Figure 5.12:** Simultaneous modelling **(bottom panel)** compared to sequential method from §5.3 **(top panel)** of a simple, demonstrative simulated dataset containing a stellar and Doppler-shifting planet spectrum. The residual fluxes, having removed the stationary spectral component corresponding to $k_1$, are shown as grey data points. The simulated planet 'spectrum', prior to adding noise, is shown in red, and the GP predictive mean in purple **(top)** and blue **(bottom)**.

The simultaneous model features a 2-D kernel, $k = k_1 + k_2$, where $k_1$ and $k_2$ are Matérn-3/2 kernels with their own hyperparameters. Kernel $k_1$ corresponds to the stationary (stellar) spectral component, and $k_2$ the Doppler-shifting component. Similarly to the sequential method, I marginalise over the GP hyperparameters and velocity $K_p$, and then make predictions with the trained GP at test locations. The resulting GP predictive mean is shown in the planet rest frame in the bottom panel of Fig. 5.12 (blue), compared to the original, noiseless planet 'spectrum' (red). For comparison, the GP predictive mean using the sequential modelling approach for the same test data is shown in the top panel of Fig. 5.12 (purple). I repeated this test for different spectra and noise realisations; in all cases the joint model yielded a more accurate spectrum.

This simple demonstration supports the claim that simultaneous modelling of a stationary and Doppler-shifting signal is beneficial, particularly towards the distinguishing of overlapping features from the different component spectra. This was seen as one of the shortfalls of the GP method in §5.7.2, compared to the other two methods examined. In practice, the computational cost of modelling an

entire high-resolution datasets using TINYGP is likely to be prohibitive. One would likely require high-performance computing, to perform GP regression, splitting the data into narrow bandpass chunks.

### 5.8.2 Modelling of (only) tellurics

The work of Meech et al. (2022) was modular; I separated out the modelling of the tellurics with a GP as the preliminary step. Since this work was for the purpose of a first step towards simultaneous modelling, our telluric model was purposefully simplistic. The modelling was across the spectral domain and we only allowed strict airmass variation in time. In reality though, tellurics display complicated behaviour in time, notoriously difficult to parameterise. Therefore, assuming airmass-only variation severely lacks complexity. I would propose one possible extension as the application of GPs to model the tellurics only, to be applied as a first correction akin to other detrending approaches (e.g. SYSREM). I leave this to future work.

## 5.9 Conclusions

In this chapter, I have presented a novel, alternative methodology to recover high-resolution planetary spectra, using Gaussian process regression. I adopted a sequential method, whereby I modelled the (stationary) telluric and (Doppler-shifting) planetary spectrum independently and in sequence. For computational efficiency reasons, I had to make a number of simplifying assumptions to the models. I then applied the framework to two archival CRIRES datasets, featuring dayside observations of two hot Jupiters. Despite reporting null detections of the previously published planetary signals, I was able to perform a useful set of injection-recovery tests to assess the sensitivity of the GP framework. I recovered injected planetary signals with scale factors which would be akin to realistic hot Jupiter line contrasts.

It is likely that the simplifying assumptions of the GP framework, combined with the inherent reduced sensitivity of Gaussian process regression compared to a cross-correlation, were the limiting factors in recovering the real signal. Towards the first, I explored two other telluric removal methods and compared the recovered

planet spectrum to that using the GP framework. These afforded 'cleaner' spectral recovery, i.e., in the continuum, but severely degraded the spectral lines. The tests confirmed that the GP telluric model lacked complexity in the time domain, and this is likely to be the dominant reason for insensitivity of this technique. More sophisticated treatment of tellurics would be necessary to develop this technique further. These tests also highlighted there is a need to balance sufficient detrending with treating the fluxes too harshly.

Though the methodology would require further advancement before we could apply it to direct use of Gaussian process regression for atmospheric detection, such an approach affords a number of advantages. Primarily, one obtains a tangible spectrum estimate, unseen with cross-correlation methods. This can be directly fed into a Bayesian retrieval framework, without the need of a conversion tool. Then, we consider the correlations between data, whereby cross-correlation methods unrealistically assume independence. Finally, our methodology is purely data-driven. Computational tractability is likely to be the limiting factor with development of this framework. Yet, the tests presented here show promise and there may be scope for integration of Gaussian process regression with the future analyses of high-resolution exoplanet spectra.

*So comes snow after fire, and even dragons have their endings.*

— J.R.R. Tolkien, *The Hobbit, 1937*

# CHAPTER 6

# CONCLUSIONS

## Contents


**6.1 Thesis summary . . . . . 163**
**6.2 Future work . . . . . 166**
6.2.1 Observing young planet atmospheres . . . . . 166
6.2.2 Characterising sub-Neptune atmospheres . . . . . 167
6.2.3 Further use of Gaussian processes for high-resolution spectroscopy . . . . . 168
**6.3 Final remarks . . . . . 170**


## 6.1 Thesis summary

In this thesis, I have explored the technique of high-resolution spectroscopy for exoplanet atmosphere characterisation, with the aim of investigating some of the challenges and issues we currently face, and exploring possible solutions. Ground-based high-resolution spectroscopy is a powerful technique for extracting close-in exoplanet spectra. It has led to a myriad of detections of atomic and molecular

species in the atmospheres of exoplanets, and is a highly complementary technique to space-based observations with (e.g.,) *JWST*.

In Chapter 3, I focused on a case study of the young sub-Neptune AU Mic b, with the aim of measuring its atmospheric content in transmission. There is a unique science case in favour of probing the atmospheres of young planets, since they are more likely to host atmospheres closer to their primordial compositions. However, young stars can be more active than their older counterparts; AU Mic is a notoriously active M dwarf. I reported null detections of an atmosphere in chemical equilibrium, as well as an atmosphere with a high abundance of carbon monoxide. Through a series of injection-recovery tests, I was able to explore the sensitivity of the IGRINS and SPIROU data used, and concluded that, in combination, they would have been sensitive to a chemical equilibrium atmosphere, a high abundance of methane in particular. I was also able to place constraints on individual molecules, independently of chemical equilibrium, and on the altitude of an opaque cloud layer. The highlight conclusion from this work was that the atmosphere of AU Mic b, if indeed it exists, is unlikely to conform to chemical equilibrium conditions. This necessitates some disequilibrium mechanism, to deplete the abundance of $CH_4$. I proposed several plausible processes, including photochemistry in the upper atmospheric layers due to stellar irradiation, and quenching induced by a high intrinsic temperature. Ultimately, additional observations will be essential towards the characterisation of this atmosphere, together with development of disequilibrium models.

Next, in Chapter 4, I performed a simulation-based study to explore the impact of stellar inhomogeneities on high-resolution transmission spectroscopy. Our conclusions on the atmospheres of exoplanets are inherently dependent on the assumptions we make about the host star, when studied in transmission. Often, high-resolution analyses assume the star to be homogeneous, which is ever becoming a more problematic assumption. In this thesis, I explored the impact of stellar rotation and then photospheric spots on the detection of key nIR molecules. As expected, both have the potential to degrade the signal-to-noise of a planetary cross-correlation detection by introducing anti-correlation signatures. Occultation of spots was seen

to have a larger impact than unocculted spots. Then, spots with temperatures such that the molecular species expected in the planet's atmosphere are also present in the spot's atmosphere pose the greatest danger to high-resolution spectroscopy, with the ability to dampen the significance below the standard threshold. Use of principal component analysis, which removes common modes in time, can somewhat mitigate the impact, but it will be important to develop robust correction tools in the future.

In Chapter 5, I developed a Gaussian process (GP) framework for the purpose of forward-modelling exoplanet spectra. Gaussian processes allow for modelling of the covariance between data, affording probability distributions over functions. To date, their application to high-resolution spectroscopy has been limited, primarily due to the computational time bottleneck. Using the publically distributed, fast implementation GP algorithm CELERITE, I modelled the telluric spectral component, and then the exoplanet spectrum in sequence. I applied this framework to two archival CRIRES datasets, both of which contains high-resolution spectral time series dayside observations of canonical hot Jupiters. I reported null detections of the real signals, previously retrieved using traditional cross-correlation analyses. To test the hypothesis that the insensitivity of the GP framework was due to the simplistic telluric model, I employed two other telluric correction techniques. Alas, the GP method was still not sensitive to the real signals. I proceeded to test injected signals, and found that implementing the more rigorous telluric treatment improved the sensitivity of the secondary GP to recover the planet signal (at realistic line strengths). These tests indicated that while the telluric modelling was not the sole cause of the null detections using the GP framework, it was a dominant factor. The telluric modelling would thus require refinement, should this technique be further developed.

Contrary to the standard cross-correlation technique for high-resolution spectroscopy, the GP framework does produce a direct estimate of the planetary spectrum. The main benefit of this is ease of integration into a retrieval framework, whereby standard Bayesian metrics can be used to compare theoretical models (akin to methods used in low-resolution spectroscopy). In Chapter 5, I used this product of

the framework to show the impact of different detrending methods on the planetary spectrum. Harsh detrending of the telluric and stellar spectral lines can degrade the planetary signal, specifically the wings and amplitudes of the absorption spectral features. The main takeaway here is that we must approach high-resolution data detrending with caution, and be sure to replicate the effects of detrending on the model templates used for cross-correlation.

## 6.2 Future work

As in any scientific field, much of the research completed unlocks more questions than it answers. It is natural, then, to ponder future work which would build upon the research in this thesis. However, it is important to focus, among the numerous possibilities, on those which (i) would offer the highest scientific output, and (ii) are reasonably achievable, considering current technology. Here, I outline a few suggestions of such work.

### 6.2.1 Observing young planet atmospheres

The work in Chapter 3 sought to probe the transmission spectrum of the young planet AU Mic b. As justified in §3.1, the ability to observe close to primordial state composition fuels the pursuit of young planetary atmospheres. In *JWST* cycle 2[1], there were no accepted exoplanet transmission spectroscopy programs involving young targets. The main concern and hurdle in the imminent future will be the handling of young stars, given their inherent high levels of activity; I have demonstrated the difficulty in interpreting high-resolution transmission spectra impacted by stellar inhomogeneities. Simultaneous photometry may offer aid in this regard. By monitoring the flux of the host star during the transit, one can identify spot-crossing events and, to some extent, constrain the variability and therefore the spot coverage. Space-based, optical photometry (e.g., with CHEOPS) is likely to be optimal for this purpose, since the spot contrast is higher in the optical

[1] https://www.stsci.edu/jwst/science-execution/approved-programs/general-observers/cycle-2-go

domain. However, the utility of these secondary observations is limited; one can only probe longitudinal variability, and small-scale spot-crossing events and the effect of unocculted spots may go undetected. In Chapter 4, I showed that the impact of unocculted spots is less severe at high resolution, therefore our efforts should focus on handling spot occultation events in high-resolution spectroscopy.

Low-resolution retrievals have recently started to include spot constraints, including spot and faculae coverage and average temperature of the hetergeneities (e.g., Mikal-Evans et al., 2023; Moran et al., 2023). Within high-resolution spectroscopy, we have yet to advance that far, with retrieval frameworks only in their genesis. Further study of the impact on the planetary spectrum (and individual lines) would be required before this could be achieved.

### 6.2.2 Characterising sub-Neptune atmospheres

AU Mic b is a young planet within the upper boundary of the small planet radius valley (see §3.1 in Chapter 3 for an overview). The sub-Neptune population *in general* has an enticing science case; there is much to learn regarding planet formation and evolution of the small planet population. To this end, I submitted a (ultimately unsuccessful) *JWST* proposal in cycle 2, to observe the transmission spectra of three sub-Neptunes, AU Mic b, TOI-560 b and GJ 3090 b, with NIRCAM and NIRSPEC. These targets span two orders of magnitude in ages (22 Myr, 480 Myr and 1 Gyr respectively). By probing a range of ages, one can observe the evolution of this population as a function of time, which would help to distinguish between theoretical causes of the radius valley (core-powered mass loss, photo-evaporation, and gas poor formation, Owen & Wu, 2013; Lopez & Fortney, 2013; Lopez & Rice, 2018).

Even the understanding of *evolved* sub-Neptunes is not fully resolved; low-resolution transmission spectroscopy has yielded mostly featureless spectra (Knutson et al., 2014; Kreidberg et al., 2013), the latest being GJ 1214 b with *JWST* (Kempton et al., 2023; Gao et al., 2023). In P112, I was awarded ESO time to observe the transmission spectrum of one such sub-Neptune, TOI-674 b (Murgas et al., 2021), with VLT/CRIRES+ (I.D. 112.25W3.001, P.I. Meech). This planet resides

in the hot Neptune desert, a dearth of Neptune-mass planets in close-in orbits ($P < 10$ days). The hot Neptune desert is thought to be shaped by similar processes as the small planet radius valley. There is then an compelling science case towards studying the atmospheric composition of a planet *within* the desert. If the desert is a result of atmospheric mass loss, any planets within its boundaries should be experiencing current-day mass loss. Moreover, measuring their C/O ratio would help to constrain the formation routes of this population. TOI-674 b was recently observed with *HST/WFC3*; Brande et al. (2022) presented tentative evidence toward an atmospheric water detection. However, they were unable to constrain the C/O ratio, due to the wavelength coverage of *WFC3*. The wavelength coverage of CRIRES+ is ideally suited to probing key carbon-bearing molecules ($CH_4$, CO and $CO_2$). In addition, high-resolution spectroscopy affords the ability to detect species above any present condensate cloud deck, consequently breaking the degeneracy between species abundance and cloud deck pressure (see §3.1 in Chapter 3 and Gandhi et al., 2020, for details). With three transit observations scheduled for 2024 in this program, we hope to be able to measure the abundance of key carbon-bearing molecules (to constrain the C/O ratio), and enable the first detection of $CH_4$ in a cool planet.

### 6.2.3 Further use of Gaussian processes for high-resolution spectroscopy

The work in Chapter 5, explored the use of Gaussian processes to model separate high-resolution spectral components. This was the first step towards a global model which could jointly model (and therefore distinguish) the telluric and stellar spectra from the planetary spectrum. Such a global model is challenging, predominantly due to the computational bottleneck for the large number of datapoints in high-resolution data. Yet, there is certainly scope for implementing GPs in analyses of high-resolution spectra going forward.

One idea that I would like to explore, is the improvement of the GP telluric model presented in Chapter 5. In that work, I used the GP to model the correlations in wavelength. It may instead be interesting to explore the use of GPs to model

correlations in time. Current-day detrending techniques, such as PCA, used throughout this thesis, rely on the insight that telluric and stellar spectra are quasi-stationary compared to the Doppler-shifting planetary spectrum. As the extent of telluric absorption varies over time due to (e.g.,) atmospheric turbulence, and airmass, this must be compensated for in any telluric model. Therefore, with each iteration, PCA removes the distinct trends in time. Using a GP would require care; GPs afford flexible models, which could capture sub-pixel common modes that are actually from the planet itself.

Another project idea is the construction of a joint GP model, made tractable by numerical rather than analytic optimisation, in an extension to the open-source package WOBBLE[2]. Developed by Bedell et al. (2019), WOBBLE is an algorithm built for data-driven modelling of time-series spectra, for the purposes of extracting stellar radial velocities. By using the data to directly infer the stellar and telluric templates, WOBBLE removes reliance on external spectral models, which may not be a good match for individual observations. They argue that the data themselves contain the information needed; it is *simply* a case of distinguishing the separate components. A set of regularisation parameters are used to adjust the relative weighting of the stellar to telluric components, and the time-variability of the telluric spectrum, but these are difficult to tune in practice. As an extension to this package, one could conceive the use of a GP prior over the spectral components, which would impose more realistic spectral characteristics such as smoothness. WOBBLE then uses numerical marginalisation to evaluate the flux at each wavelength. We could imagine, (i) evaluating the logarithm of the GP prior at each pixel value, (ii) combining those of each spectral component before, (iii) adding the result to the log-likelihood and then, (iv) using some numerical-based optimiser to handle the large number of free parameters. This proposal would hopefully improve the computational efficiency compared to using (e.g.,) GEORGE[3] or TINYGP[4] to construct a multi-dimensional GP model.

[2] https://wobble.readthedocs.io/en/latest/
[3] https://george.readthedocs.io/en/latest/user/gp/
[4] https://tinygp.readthedocs.io/en/stable/

## 6.3 Final remarks

Scientists have now discovered and confirmed well over 5000 extra-solar planets[5]. In the last couple of decades, the field has quickly progressed from detections to characterisation, with high-resolution spectroscopy now providing conclusive and precise measurements of exoplanet atmospheres. One day in the future, the human race may find signs of extra-terrestrial life in the Universe. Even if we do not, the discovery of the wide-ranging, wonderfully diverse collection of extra-solar planets and their complex properties is a hugely significantly scientific achievement, and I consider myself blessed to have been able to contribute (to whatever extent) to this field.

[5] 5052 according to the NASA exoplanet archive, as of 03/09/2023

# APPENDIX A

# ADDITIONAL METRICS FROM THE ANALYSIS OF THE AU MIC b SPECTRA

## A.1 Data reduction diagnostics

Here I offer a few of the diagnostics I used in §3.3 to assess the reduction of the AU Mic b IGRINS and SPIROU spectra. The detrending routine outlined in Chapter 3, §3.3 included a number of different steps, each with parameters to be tuned. Towards tuning the detrending process, I assessed the suppression of the noise in each order. Fig. A.1 shows the average dispersion in each IGRINS and SPIROU order, prior to and post PCA treatment in black and blue respectively, compared to the DRS-reported RMS in pink. These proved to be useful metrics in the diagnosis of quality of detrending.

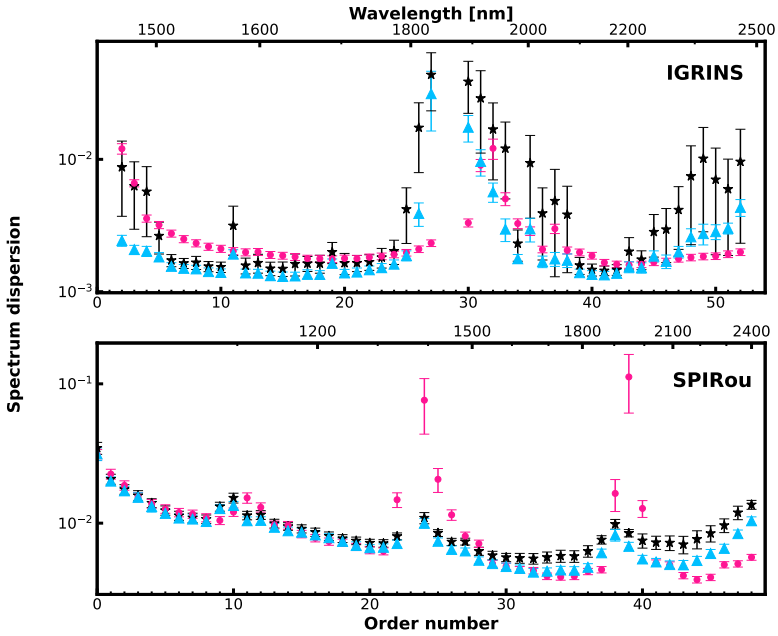


**Figure A.1:** RMS dispersion in the centre of each order, averaged over one hundred central pixels, pre (black stars) and post (blue triangles) PCA application. The RMS reported by the DRS is shown in pink for comparison.

## A.2 Impact of clouds on chemical equilibrium injection tests

In Chapter 3, §3.4.3, I extended the constraints from the chemical equilibrium injection tests to atmospheres with cloud decks at different pressures. In Table A.1 I give the constraints of the chemical equilibrium injection tests, scaled according to the impact of an opaque cloud deck at different altitudes. Additionally, in Fig. A.2 I show exemplar maps from the equilibrium chemistry cloud tests, for a cloud deck at a pressure of $\log_{10} P_c[\text{bar}] = -4$. The results of these tests are shown in §3.4.3, Fig. 3.15.

**Table A.1:** The impact of an opaque cloud deck on the constraints from §3.4.3.

| **Cloud top pressure** $\log_{10}(P_c\,[\mathrm{bar}])$ | **SNR$_p$ reduction factor** | **ALL** | | **CH$_4$** | |
|---|---|---|---|---|---|
| | | **3$\sigma$** | **5$\sigma$** | **3$\sigma$** | **5$\sigma$** |
| No cloud | 1 | – | 0.0<log([Fe/H])<2.0; 0.2< C/O<1.5 | – | 0.0<log([Fe/H])<2.0; 0.2<C/O<1.5 |
| -2 | 0.732 | – | 0.0<log([Fe/H])<2.0; 0.2<C/O<1.5 | – | 0.0<log([Fe/H])<2.0; 0.2<C/O<1.5 |
| -3 | 0.473 | – | 0.0<log([Fe/H])<2.0; 0.2<C/O<1.5 | 0.0<log([Fe/H])<2.0; 0.2<C/O<1.5 | 0.0<log([Fe/H])<1.6; 0.2<C/O<1.5 |
| -4 | 0.243 | 0.0<log([Fe/H])<2.0; 0.3<C/O<1.5 | 0.0<log([Fe/H])<1.5; 0.2<C/O<1.5 | 0.0<log([Fe/H])<2.0; 0.4<C/O<1.5 | 0.0<log([Fe/H])<1.5; 0.2<C/O<1.5 |
| -5 | 0.074 | None | None | None | None |
| -6 | 0.013 | None | None | None | None |
| | | **H$_2$O** | | **NH$_3$** | |
| | | **3$\sigma$** | **5$\sigma$** | **3$\sigma$** | **5$\sigma$** |
| No cloud | 1 | 0.0<log([Fe/H])<2.0; 0.2<C/O<1.3 | 0.0<log([Fe/H])<1.7; 0.2<C/O<0.9 | 0.0<log([Fe/H])<1.1; 0.2<C/O<1.5 | 0.0<log([Fe/H])<0.2; 0.2<C/O<1.5 |
| -2 | 0.732 | 0.0<log([Fe/H])<2.0; 0.2<C/O<1.1 | 0.0<log([Fe/H])<1.45; 0.2<C/O<0.52 | 0.0<log([Fe/H])<0.6; 0.2<C/O<1.5 | None |
| -3 | 0.473 | 0.0<log([Fe/H])<1.5; 0.2<C/O<0.6 | None | None | None |
| -4 | 0.243 | None | None | None | None |
| -5 | 0.074 | None | None | None | None |
| -6 | 0.013 | None | None | None | None |

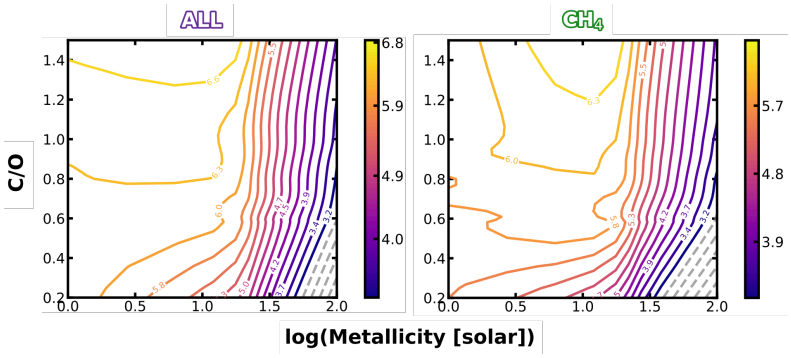


**Figure A.2:** The impact of a cloud deck on the chemical equilibrium injection tests. **Left:** Full chemistry model and **right:** $CH_4$ model, both with a cloud deck at pressure $\log_{10} P_c = -4$. The colourmap denotes signal-to-noise significance of an atmospheric detection.

# APPENDIX B

# IMPACT OF STELLAR HETEROGENEITIES

## B.1 Derivation of spot contamination factor on observed transit depth

Here, I give the full derivation of the spot contamination factor presented in Chapter 4 (Equation 4.4). This is the contamination factor of the depth of the wavelength-dependent transit light curve due to both occulted and unocculted spots. I first define:

$f_o$ the fraction of the **entire** stellar disk covered by the occulted spectrum, equivalent to the fraction of the disk which is occulted. This is time-dependent only due to the ingress/egress of the planet, since it is equivalent to $(R_p/R_*)^2$;

$f_u$ the fraction of **entire** stellar disk covered by unocculted spectrum **or**, in other words, the fraction of disk which is unocculted. On the reverse of $f_o$, this is

equivalent to $1-(R_p/R_*)^2$;

$f'_{het}$ the fraction of the **unocculted** stellar disk covered by heterogeneities;

$f''_{het}$ the fraction of the **occulted** stellar disk covered by heterogeneities.

In this derived formalism, $f_{het}$ has the same definition as the original derivation in Rackham et al. (2018), namely it is equal to the fraction of the **entire** projected stellar disk covered by heterogeneities. Similarly, $F_{het}$ and $F_{phot}$ assume the same definitions, as the spectrum of the heterogeneity and photosphere respectively. These are related as:

$$\begin{aligned} f_{het} &= f''_{het}f_o + f'_{het}f_u \\ &= f''_{het}(1-f_u) + f'_{het}f_u \\ &= f''_{het}D_\lambda + f'_{het}(1-D_\lambda). \end{aligned} \tag{B.1}$$

where $D_\lambda$ is the true transit depth. I note here that this differs already from Rackham et al. (2018), wherein only unocculted heterogeneieties were considered. That is to say, Rackham et al. (2018) considered that the transit chord only contained $F_{phot}$ and therefore $f'_{het} = \frac{f_{het}}{f_u}$. It follows that the total out-of-transit flux is given by

$$F_{out-of-transit} = f_{het}F_{het} + (1-f_{het})F_{phot}. \tag{B.2}$$

The in-transit flux is the combination of the total unocculted spectrum $S_u$ and the total occulted spectrum $S_o$,

$$\begin{aligned} S_o &= f''_{het}F_{het} + (1-f''_{het})F_{phot} \\ S_u &= f'_{het}F_{het} + (1-f'_{het})F_{phot}. \end{aligned} \tag{B.3}$$

In Rackham et al. (2017), Equation (11) states:

$$\left(\frac{R_p}{R_*}\right)^2_{\rm obs} = D_{\rm obs} = 1 - \frac{(1-f_u-D_\lambda)S_o + f_uS_u}{(1-f_u)S_o + f_uS_u} \tag{B.4}$$

where $D_{\rm obs}$ and $D_\lambda$ are the observed and true transit depths, and all other terms assume the same definitions as above. The denominator of the second term is equivalent to the out-of-transit flux, and the numerator is the same with the

subtraction of $D_\lambda S_o$, the occulted fraction. With some rearranging, eqn (B.4) is equivalent to

$$\begin{aligned} D_{\text{obs}} &= \frac{D_\lambda S_o}{(1-f_u)S_o + f_u S_u} \\ &= \frac{D_\lambda}{(1-f_u) + f_u \frac{S_u}{S_o}} \\ &= \frac{D_\lambda}{1 - f_u(1 - \frac{S_u}{S_o})}. \end{aligned} \tag{B.5}$$

I now substitute our new definitions of $S_o$ and $S_u$ from Equation B.3 into Equation B.5:

$$\begin{aligned} D_{\text{obs}} &= \frac{D_\lambda}{1 - f_u(1 - \frac{f'_{het}F_{het} + (1-f'_{het})F_{phot}}{f''_{het}F_{het} + (1-f''_{het})F_{phot}})} \\ &= \frac{D_\lambda}{1 - f_u\left[\frac{(f''_{het} - f'_{het})F_{het} - (f''_{het} - f'_{het})F_{phot}}{f''_{het}F_{het} + (1-f''_{het})F_{phot}}\right]}. \end{aligned} \tag{B.6}$$

Then, from Equation B.1 we have,

$$\begin{aligned} f_{het} &= f''_{het}(1-f_u) + f'_{het}f_u \\ &= f''_{het} - f_u(f''_{het} - f'_{het}) \\ f''_{het} - f'_{het} &= \frac{f''_{het} - f_{het}}{f_u}. \end{aligned} \tag{B.7}$$

Substituting Equation B.7 into Equation B.6 we have,

$$\begin{aligned} D_{\text{obs}} &= \frac{D_\lambda}{1 - \frac{(f''_{het} - f_{het})(F_{het} - F_{phot})}{f''_{het}F_{het} + (1-f''_{het})F_{phot}}} \\ &= \frac{D_\lambda}{\frac{f_{het}F_{het} + (1-f''_{het})F_{phot} + (f''_{het} - f_{het})F_{phot}}{f''_{het}F_{het} + (1-f''_{het})F_{phot}}} \\ &= \frac{D_\lambda}{\frac{f_{het}F_{het} + (1-f_{het})F_{phot}}{f''_{het}F_{het} + (1-f''_{het})F_{phot}}} \end{aligned} \tag{B.8}$$

where the contamination factor is now:

$$\varepsilon(\lambda) = \frac{1}{\frac{f_{het}F_{het} + (1-f_{het})F_{phot}}{f''_{het}F_{het} + (1-f''_{het})F_{phot}}}, \tag{B.9}$$

which, with some rearranging, becomes

$$\varepsilon(\lambda, t) = \frac{f''_{het}(t)F_{het}(\lambda) + \left[1 - f''_{het}(t)\right]F_{phot}(\lambda)}{f_{het}F_{het}(\lambda) + \left[1 - f_{het}\right]F_{phot}(\lambda)}. \tag{B.10}$$

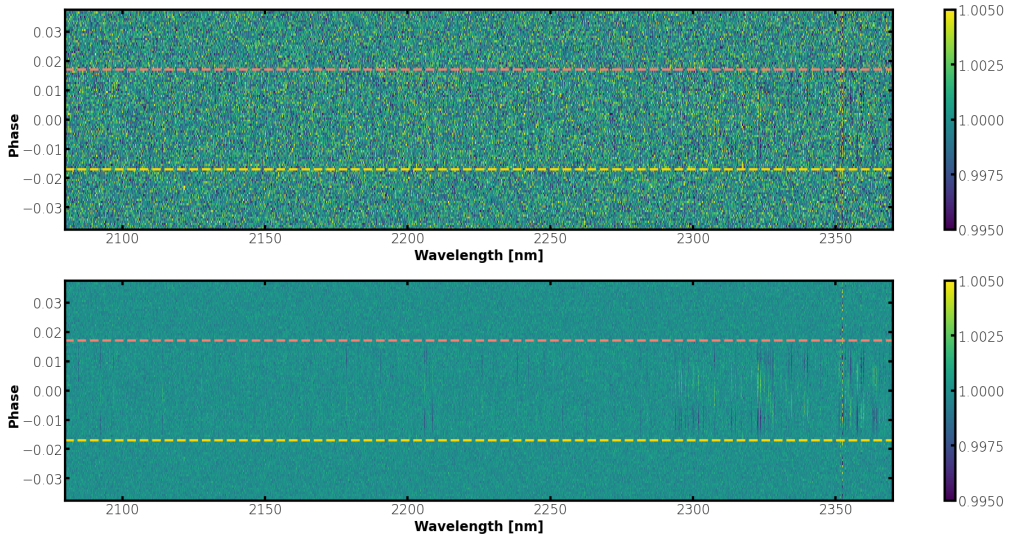


**Figure B.1:** Residuals of the **CASE 3** spectral time series, for the HD 189733 archetype with CO atmosphere around the planet, in the K-band. In each panel, I show the residual fluxes (indicated in colour), after having removed the mean out-of-transit spectrum. No PCA detrending has been applied. Each row represents one spectrum. The yellow and coral dashed lines indicate ingress and egress respectively. Each panel shows a different noise level, for the same forward-model spectral time series. **Top panel:** $\mathrm{SNR_{res}} = 500$ and **bottom panel:** $\mathrm{SNR_{res}} = 2000$; the RM residual imprint is more clearly visible in the latter.

I highlight that though $f_{het}$ is considered constant here, time dependence could be introduced if the spot coverage of the projected stellar disk evolves significantly over the duration of the observations.

One could construct a time-series of simulated spectra as follows:

$$\boldsymbol{\mathcal{F}}_{\mathbf{tot}}(\lambda, t) = \Big[\boldsymbol{\mathcal{S}}(\lambda, t) + D(\lambda)\varepsilon(\lambda, t)\Big] \times \mathbf{T}(\lambda, t) \tag{B.11}$$

where $\boldsymbol{\mathcal{S}}(\lambda, t)$ is the forward-modelled stellar spectra, including a transiting bare rock (completely opaque planet), and $\mathbf{T}(\lambda, t)$ is the telluric spectrum. The forward-model stellar spectra, $\boldsymbol{\mathcal{S}}(\lambda, t)$, consist of the contribution of the unocculted stellar disk. I refer the reader to Chapter 4, §4.5.3 for the use of this derived spot contamination factor.

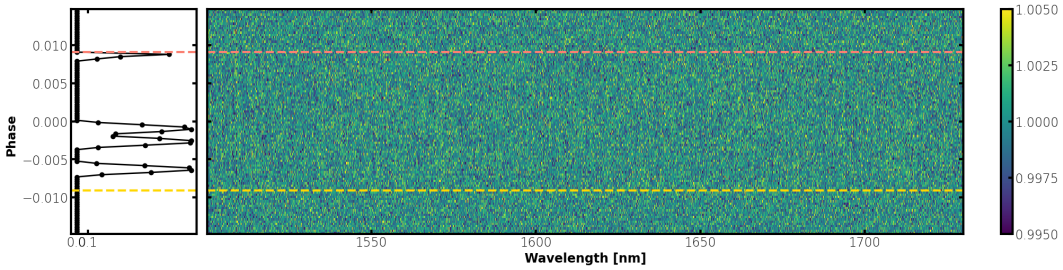


**Figure B.2:** Residuals of the **CASE 5** spectral time series, for the AU Mic archetype in the H-band. The right panel has the same format as Fig. B.1, with additive noise corresponding to $\mathrm{SNR_{res}} = 500$. Again, no PCA was applied. Shown in the **left panel** is $f''_{het}$, the fraction of spots in the occulted portion of the stellar disk; spot crossing events are seen as peaks over time.

## B.2 Forward-modelled spectra

In Chapter 4 of this thesis, I introduce a framework built to forward model stellar spectra, while considering stellar heterogeneities. To clarify some of the intermediate steps in the framework outlined in §4.3.1, I provide some example plots here.

In Fig. B.1, I demonstrate the residual imprint of the RM effect. These spectra are the **CASE 3** residual spectral time series for the HD 189733 archetype, having included a CO atmosphere around the transiting planet. I have removed the mean out-of-transit spectrum, to reveal the time variation. The $\mathrm{SNR_{res}} = 500$ case (top panel of Fig. B.1) are those used in the cross-correlation, to yield Fig. 4.9 in Chapter 4. The RM imprint is more clearly visible by eye in the $\mathrm{SNR_{res}} = 2000$ case (bottom panel of Fig. B.1), wherein its wavelength dependence is evident.

To demonstrate a spot case, in Fig. B.2 I show an example forward-modelled spectral time series for the AU Mic archetype. This example is for **CASE 5**, where the spots have an assigned temperature of $T_{spot} = 3000\,\mathrm{K}$, and $f_{tc} = 0.2$ (see §4.2 for definitions). An $H_2O$ atmosphere was included around the transiting planet in the forward model. These spectra are used for the cross-correlation shown in the right panel of Fig. 4.14 of Chapter 4.

# APPENDIX C

# ADDITIONAL METRICS USED IN THE GP HIGH-RESOLUTION SPECTROSCOPY FRAMEWORK

## C.1 Recovering an injected planet signal

Here I provide further details of how I defined a detection of a planet signal in the injection-recovery tests using the GP framework, in §5. When assessing the recovered planet 'spectrum', I monitor both the marginal posterior radial velocity $K_p$ as well as the GP predictive mean itself. I would expect that if the GP truly recovered the injected signal, the $K_p$, which dictates the Doppler shift of the spectral lines over time, should be in agreement with that of the injected signal. Fig. C.1 shows the divergence of $K_p$ for lower injection strengths, $n_{\rm inj}$, for both datasets of §5.4. The mean and $1\sigma$ uncertainties shown are estimated by fitting a Gaussian to the marginal posterior in each case. The reported $n_{\rm inj}$ of §5.5.3 and §5.6.2 are chosen

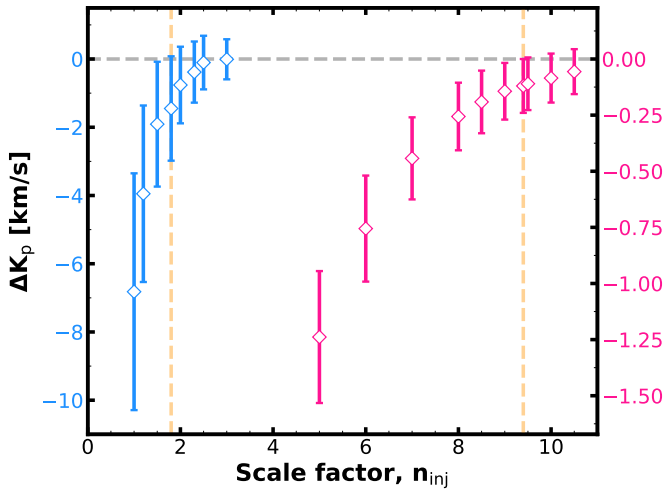


**Figure C.1:** Recovered marginal posterior radial velocity mean and uncertainty, applying the GP framework to the **left axis:** 51 Peg and **right axis:** HD 189733 datasets, from §5.4. Here, $\Delta K_p$ refers to the difference between the injected and recovered radial velocity. The yellow dashed lines indicate the minimum scaling factors reported in §5.5.3 and §5.6.2.

as the minimum scaling factor at which the recovered $K_p$ is in agreement with the injection velocity, within $1\sigma$ (as indicated by the yellow dashed lines in Fig. C.1).

The constraints on $K_p$ from the GP framework are an order of magnitude smaller than those of the original cross-correlation analyses (see Table 5.1). Theoretically, the limit on the constraints of $K_p$ would be a combination of the signal-to-noise of the spectra, range of phase coverage, number of (detected) lines and the spectrograph resolution. This assumes that the residual data consists only of pure photon noise and the planet signal, i.e., that the detrending was perfect. This is a unrealistic assumption; even with the most powerful detrending methods, correlated noise due to stellar, telluric and systematic signals will remain in the data. Looking again to Fig. C.1, it is then likely that at low $n_{\rm inj}$, where the $\Delta K_p$ is seen to diverge, the nuisance signals are dominating. If we were to pursue this methodology further, it would thus be important to reflect the nuisance signal noise in the estimation of the uncertainty on $K_p$. On the other hand, the uncertainties reported from HRCCS analyses are likely to be inflated due to interpolation noise.

## C.2 SYSREM optimisation

In Chapter 5, I leveraged the SYSREM algorithm to detrend high-resolution spectra. It is a powerful tool to identify common modes in wavelength, yet has the potential to be brutal if not carefully managed. The standard optimisation of SYSREM involves injecting a planetary signal into the data, and assessing the number of iterations at which it is recovered with highest significance within a cross-correlation map. I discuss in §2.3.2 and §3.3 the details and disadvantages of this method (see also Cheverall et al., 2023; Cabot et al., 2019). The line metrics assessed in §5.11 offer a natural comparison to an injected model, which circumvents the signal-to-noise metric from cross-correlation maps.

I test this on both datasets from §5.4. Firstly, I apply three iterations of SYSREM and train the planet GP on the stacked residuals. This affords a set of optimised hyperparameters and thereby covariance function, as well as radial velocity, $K_p$. Then, I apply eight iterations of SYSREM, evaluating the GP after each iteration. Following each iteration, I evaluate the metrics of §5.11, namely the recovered amplitudes and FWHMs of selected deep planetary lines and continuum standard deviation. The amplitudes and FWHMs are averaged over the lines in the order. I also combine the three metrics into one (normalised) metric. Each is normalised to afford the ratio of the recovered to the injected spectrum property.

In Fig. C.2, I show an example of this for the 51 Peg data from the 16th October 2010. The aim would be to minimise the difference between the injected and recovered spectrum. I select the number of SYSREM iterations which minimises the combined metric. If there are multiple solutions with minimal improvement, I select the lower number of iterations.

This is the method used to optimise SYSREM in §5.7.2. Unlike the standard cross-correlation map SNR method, this method avoids the issue of optimising noise rather than the planet signal itself. It follows that there is a reduced risk of a bias detection by optimising SYSREM on an order-by-order basis (hence the treatment of individual detectors above). Yet, this method still relies on model

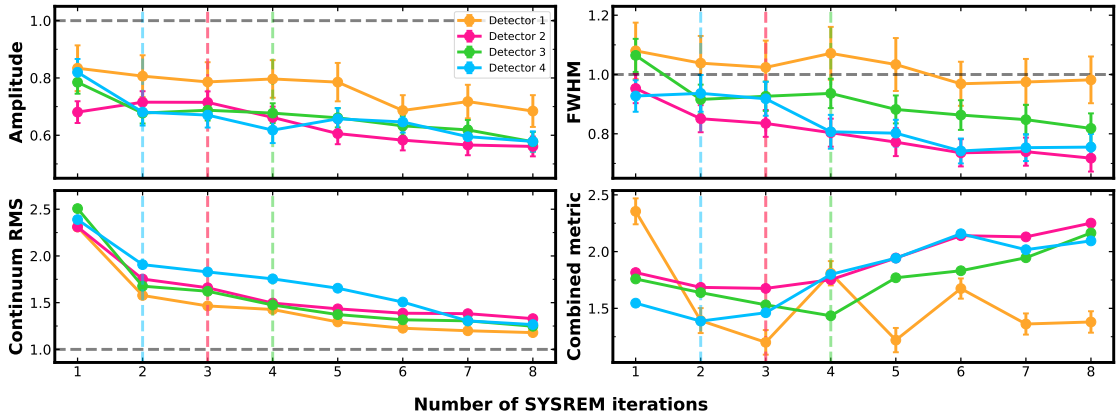


**Figure C.2:** Optimising the number of SYSREM iterations by assessing recovered planetary lines in comparison to an injected model. This example is for the 51 Peg observations acquired on the 16th October 2010, with CRIRES. Each of the orders are optimised separately, and shown in distinct colours. The coloured dashed lines indicate the iteration at which the combined metric is at a minimum.

injection, and is therefore model dependent. I refer the reader to Chapter 3, §3.3 for another (PCA) optimisation method which is model independent.

*If I have seen further it is by standing on the shoulders of Giants.*

— Sir Isaac Newton, 1675

# Bibliography


Addison B. C., et al., 2021, The Astronomical Journal, 162, 137

Afram N., Berdyugina S. V., 2015, Astronomy & Astrophysics, 576, A34

Afram N., Berdyugina S. V., 2019, Astronomy and Astrophysics, 629, A83

Agol E., Fabrycky D. C., 2018, in Deeg H. J., Belmonte J. A., eds, , Handbook of Exoplanets. Springer International Publishing, Cham, pp 797–816, doi:10.1007/978-3-319-55333-7_7

Aigrain S., Foreman-Mackey D., 2022, Gaussian Process Regression for Astronomical Time-Series, doi:10.48550/arXiv.2209.08940

Alderson L., et al., 2023, Nature, 614, 664

Allart R., et al., 2022, Astronomy & Astrophysics, 666, A196

Ambikasaran S., Foreman-Mackey D., Greengard L., Hogg D. W., O'neil M., 2015, IEEE Transactions on Pattern Analysis and Machine Intelligence, 38

Astudillo-Defru N., Rojo P., 2013, A&A, 557

Baglin A., et al., 2006, CoRoT: A High Precision Photometer for Stellar Ecolution and Exoplanet Finding

Baraffe I., Chabrier G., Fortney J., Sotin C., 2014, Planetary Internal Structures. eprint: arXiv:1401.4738, doi:10.2458/azu_uapress_9780816531240-ch033

Barragán O., et al., 2019, Monthly Notices of the Royal Astronomical Society, 490, 698

Barragán O., et al., 2022, Monthly Notices of the Royal Astronomical Society, 514, 1606

Barragán O., et al., 2023, Monthly Notices of the Royal Astronomical Society, 522, 3458

Batalha N. M., et al., 2013, February The Astrophysical Journal Supplement Series, 204, 2013

Batalha N. E., et al., 2017, Publications of the Astronomical Society of the Pacific, 129, 064501

Batalha N. E., Marley M. S., Lewis N. K., Fortney J. J., 2019, The Astrophysical Journal, 878, 70

Batista V., 2018, in Deeg H. J., Belmonte J. A., eds, , Handbook of Exoplanets. Springer International Publishing, Cham, pp 659–687, doi:10.1007/978-3-319-55333-7_120

Batygin K., Bodenheimer P. H., Laughlin G. P., 2016, The Astrophysical Journal, 829, 114

Bedell M., Hogg D., Foreman-Mackey D., Montet B., Luger R., 2019, The Astronomical Journal, 158, 164

Beeck B., Schüssler M., Cameron R. H., Reiners A., 2015, Astronomy and Astrophysics, 581, A42

Beltz H., Rauscher E., Kempton E. M. R., Malsky I., Ochs G., Arora M., Savel A., 2022, The Astronomical Journal, 164, 140

Beltz H., Rauscher E., Kempton E. M. R., Malsky I., Savel A. B., 2023, The Astronomical Journal, 165, 257

Bender C. F., et al., 2012, The Astrophysical Journal, 751, L31

Benneke B., et al., 2019a, Nature Astronomy, 3, 813

Benneke B., et al., 2019b, The Astrophysical Journal Letters, 887, L14

Berdyugina S. V., 2005, Living Reviews in Solar Physics, 2, 8

Berger T. A., Huber D., Gaidos E., van Saders J. L., Weiss L. M., 2020, The Astronomical Journal, 160, 108

Bertaux J. L., Lallement R., Ferron S., Boonne C., Bodichon R., 2014, Astronomy & Astrophysics, 564, A46

Birkby J., 2018, arXiv e-prints arXiv:1806.04617

Birkby J., de Kok R. J., Brogi M., de Mooij E. J., Schwarz H., Albrecht S., Snellen I. A., 2013, MNRAS Letters, 436, 1980

Birkby J., De Kok R. J., Brogi M., Schwarz H., Snellen I. A., 2017, The Astronomical Journal, 153, 138

Boisnard L., Auvergne M., 2006, CoRoT in Brief

Borsato N. W., Hoeijmakers H. J., Prinoth B., Thorsbro B., Forsberg R., Kitzmann D., Jones K., Heng K., 2023, Astronomy & Astrophysics, 673, A158

Borucki W., et al., 2009, KEPLER: Search for Earth-Size Planets in the Habitable Zone, doi:10.1017/S1743921308026513

Borucki W. J., et al., 2011, The Astrophysical Journal, 736, 19

Boss A. P., 2000, The Astrophysical Journal, 536, L101

Boucher A., et al., 2021, The Astronomical Journal, 162, 233

Boucher A., et al., 2023, CO or No CO? Narrowing the CO Abundance Constraint and Recovering the H2O Detection in the Atmosphere of WASP-127 b Using SPIRou (arxiv:2303.03232), doi:10.1093/mnras/stad1247

Bouchy F., et al., 2005, A&A, 444, L15

Boyajian T., et al., 2015, MNRAS, 447, 846

Brande J., et al., 2022, The Astronomical Journal, 164, 197

Brogi M., Line M., 2019, The Astronomical Journal, 157, 114

Brogi M., Snellen I. A., De Kok R. J., Albrecht S., Birkby J., De Mooij E. J. W., 2012, Nature, 486, 502

Brogi M., Snellen I. A., De Kok R. J., Albrecht S., Birkby J., De Mooij E. J. W., 2013, Astrophysical Journal, 767

Brogi M., De Kok R. J., Birkby J., Schwarz H., Snellen I. A., 2014, A&A, 565

Brogi M., De Kok R. J., Albrecht S., Snellen I. A., Birkby J., Schwarz H., 2016, The Astrophysical Journal, 817, 106

Brogi M., Line M., Bean J., Désert J.-M., Schwarz H., 2017, The Astrophysical Journal Letters, 839

Brogi M., Giacobbe P., Guilluy G., de Kok R. J., Sozzetti A., Mancini L., Bonomo A. S., 2018, Astronomy and Astrophysics, 615, A16

Brogi M., et al., 2023, The Astronomical Journal, 165, 91

Bruno G., 1584, On the Infinite Universe and Worlds. France

Bryson S., Coughlin J., Batalha N. M., Berger T., Huber D., Burke C., Dotson J., Mullally S. E., 2020, The Astronomical Journal, 159, 279

Cabot S. H. C., Madhusudhan N., Hawker G. A., Gandhi S., 2019, MNRAS, 482, 4422

Cale B., et al., 2021, The Astronomical Journal, 162, 295

Campbell M. B., 2017, in , Wonder and Science. Cornell University Press, Ithaca, NY, pp 113–150, doi:10.7591/9781501705069-007

Casasayas-Barris N., et al., 2020, Astronomy & Astrophysics, 635

Cegla H. M., Lovis C., Bourrier V., Beeck B., Watson C. A., Pepe F., 2016, Astronomy and Astrophysics, 588, A127

Cegla H. M., et al., 2018, The Astrophysical Journal, 866, 55

Chabrier G., Baraffe I., Selsis F., Barman T. S., Hennebelle P., Alibert Y., 2007, Gaseous Planets, Protostars, and Young Brown Dwarfs: Birth and Fate. eprint: arXiv:astro-ph/0602291, doi:10.48550/arXiv.astro-ph/0602291

Charbonneau D., Brown T. M., Latham D. W., Mayor M., 2000, The Astrophysical Journal, 529, L45

Charbonneau D., Brown T. M., Noyes R. W., Gilliland R. L., 2002, The Astrophysical Journal, 568, 377

Cheverall C. J., Madhusudhan N., Holmberg M., 2023, Robustness Measures for Molecular Detections Using High-Resolution Transmission Spectroscopy of Exoplanets, doi:10.48550/arXiv.2303.01496

Chiavassa A., Brogi M., 2019, A&A, 631

Cloutier R., Menou K., 2020, The Astronomical Journal, 159, 211

Collier Cameron A., Bruce V. A., Miller G. R. M., Triaud A. H. M. J., Queloz D., 2010, Monthly Notices of the Royal Astronomical Society, 403, 151

Cook N. J., et al., 2022, Publications of the Astronomical Society of the Pacific, 134, 114509

Copernicus N., Lerner M. P., Segonds A. P., Verdet J. P., Luna C., Savoie D., Toulmonde M., 1543, De Revolutionibus Orbium Coelestium. Paris: Les Belle Lettres Vol. 1, Johnson Reprint Corporation.

Crossfield I. J. M., Kreidberg L., 2017, The Astronomical Journal, 154, 261

Currie M. H., Meadows V. S., Rasmussen K. C., 2023, The Planetary Science Journal, 4, 83

Czesla S., Klocová T., Khalafinejad S., Wolter U., Schmitt J. H. M. M., 2015, Astronomy and Astrophysics, 582, A51

D'Angelo G., Lissauer J. J., 2018, in Deeg H. J., Belmonte J. A., eds, , Handbook of Exoplanets. Springer International Publishing, Cham, pp 2319–2343, doi:10.1007/978-3-319-55333-7_140

Deeg H. J., Alonso R., 2018, in Deeg H. J., Belmonte J. A., eds, , Handbook of Exoplanets. Springer International Publishing, Cham, pp 633–657, doi:10.1007/978-3-319-55333-7_117

Diamond-Lowe H., Berta-Thompson Z., Charbonneau D., Kempton E. M.-R., 2018, The Astronomical Journal, 156, 42

Donati J.-F., et al., 2014, Monthly Notices of the Royal Astronomical Society, 444, 3220

Donati J.-F., et al., 2023, Monthly Notices of the Royal Astronomical Society, p. stad1193

Dubs H. H., 1958, Journal of the American Oriental Society, 78, 295

Dymont A. H., Yu X., Ohno K., Zhang X., Fortney J. J., Thorngren D., Dickinson C., 2022, The Astrophysical Journal, 937, 90

Dyrek A., et al., 2023, Nature

Ehrenreich D., et al., 2020, Nature, 580, 597

Espinoza N., et al., 2019, Monthly Notices of the Royal Astronomical Society, 482, 2065

Falkner D. E., 2011, The Mythology of the Night Sky, doi:10.1007/978-1-4614-0137-7.

Feinstein A. D., et al., 2022, The Astronomical Journal, 164, 110

Finnerty L., Buzard C., Pelletier S., Piskorz D., Lockwood A. C., Bender C. F., Benneke B., Blake G. A., 2021, The Astronomical Journal, 161, 104

Flowers E., Brogi M., Rauscher E., M-R Kempton E., Chiavassa A., 2019, The Astronomical Journal, 157

Foreman-Mackey D., Hogg D. W., Lang D., Goodman J., 2013, PASP, 125, 306

Foreman-Mackey D., Agol E., Ambikasaran S., Angus R., 2017, The Astrophysical Journal, 154

Fortney J. J., Marley M. S., Barnes J. W., 2007, The Astrophysical Journal, 659, 1661

Fortney J. J., Visscher C., Marley M. S., Hood C. E., Line M. R., Thorngren D. P., Freedman R. S., Lupu R., 2020, The Astronomical Journal, 160, 288

Fuhrmann K., Pfeiffer M. J., Bernkopf J., 1997, A&A, 326, 1081

Fulton B. J., et al., 2017, The Astronomical Journal, 154, 109

Gaia Collaboration et al., 2018, Astronomy & Astrophysics, 616, A1

Galilei G., 1610, Sidereus, nuncius. in Paltheniano

Gandhi S., Madhusudhan N., 2018, Monthly Notices of the Royal Astronomical Society, 474, 271

Gandhi S., Brogi M., Webb R. K., 2020, Monthly Notices of the Royal Astronomical Society, 498, 194

Gandhi S., Kesseli A., Snellen I., Brogi M., Wardenier J. P., Parmentier V., Welbanks L., Savel A. B., 2022, Monthly Notices of the Royal Astronomical Society, 515, 749

Gandhi S., et al., 2023, The Astronomical Journal, 165, 242

Gao P., Wakeford H. R., Moran S. E., Parmentier V., 2021, Journal of Geophysical Research: Planets, 126

Gao P., et al., 2023, The Astrophysical Journal, 951, 96

Gaudi B. S., 2012, Annual Review of Astronomy and Astrophysics, 50, 411

Genest F., Lafrenière D., Boucher A., Darveau-Bernier A., Doyon R., Artigau É., Cook N., 2022, The Astronomical Journal, 163, 231

Giacobbe P., et al., 2021, Nature, 592, 205

Gibson N. P., Aigrain S., Barstow J. K., Evans T. M., Fletcher L. N., Irwin P. G. J., 2013, Monthly Notices of the Royal Astronomical Society, 428, 3680

Gibson N. P., et al., 2020, MNRAS, 493, 2215

Gibson N. P., Nugroho S. K., Lothringer J., Maguire C., Sing D. K., 2021, MNRAS, 000, 1

Gilbert E. A., et al., 2022, The Astronomical Journal, 163, 147

Goethe J. W., 1868, Goethes Werke. Bibliographisches Institut

Gordon T. A., Agol E., Foreman-Mackey D., 2020, The Astronomical Journal, 160

Goyal J. M., Wakeford H. R., Mayne N. J., Lewis N. K., Drummond B., Sing D. K., 2019, Monthly Notices of the Royal Astronomical Society, 482, 4503

Grant D., et al., 2023, JWST-TST DREAMS: Quartz Clouds in the Atmosphere of WASP-17b (arxiv:2310.08637)

Guillot T., 2010, Astronomy and Astrophysics, 520, A27

Guillot T., Fletcher L. N., Helled R., Ikoma M., Line M. R., Parmentier V., 2022, Giant Planets from the Inside-Out (arxiv:2205.04100)

Gullikson K., Dodson-Robinson S., Kraus A., 2014, The Astronomical Journal, 148

Gully-Santiago M. A., Morley C. V., 2022, The Astrophysical Journal, 941, 200

Gupta A., Schlichting H. E., 2019, Monthly Notices of the Royal Astronomical Society, 487, 24

Hall R. D., Thompson S. J., Handley W., Queloz D., 2018, Monthly Notices of the Royal Astronomical Society, 479, 2968

Helled R., Fortney J. J., 2020, Philosophical Transactions of the Royal Society A: Mathematical, Physical and Engineering Sciences, 378, 20190474

Helled R., Movshovitz N., Nettelmann N., 2022, The Nature of Gas Giant Planets (arxiv:2202.10046)

Helling Ch., Thi W. F., Woitke P., Fridlund M., 2006, Astronomy and Astrophysics, 451, L9

Heng K., 2016, The Astrophysical Journal, 826, L16

Heng K., 2019, Monthly Notices of the Royal Astronomical Society, 490, 3378

Heng K., Lyons J. R., 2016, The Astrophysical Journal, 817, 149

Heng K., Marley M. S., 2018, in Deeg H. J., Belmonte J. A., eds, , Handbook of Exoplanets. Springer International Publishing, Cham, pp 2137–2152, doi:10.1007/978-3-319-55333-7_102

Heng K., Showman A. P., 2015, Annual Review of Earth and Planetary Sciences, 43, 509

Heng K., Mendonça J. M., Lee J.-M., 2014, The Astrophysical Journal Supplement Series, 215, 4

Heng K., Lyons J. R., Tsai S.-M., 2016, The Astrophysical Journal, 816, 96

Hirano T., et al., 2020, The Astrophysical Journal, 899, L13

Hoch K. K. W., Konopacky Q. M., Theissen C. A., Ruffio J.-B., Barman T. S., Perrin M. D., Macintosh B., Marois C., 2022, Assessing the C/O Ratio Formation Diagnostic: A Potential Trend with Companion Mass (arxiv:2212.04557)

Hoeijmakers H. J., et al., 2018a, Nature, 560, 453

Hoeijmakers H. J., Schwarz H., Snellen I. A. G., de Kok R. J., Bonnefoy M., Chauvin G., Lagrange A. M., Girard J. H., 2018b, Astronomy & Astrophysics, 617, A144

Hood C. E., et al., 2020, The Astronomical Journal, 160, 198

Hörst S. M., et al., 2018, Nature Astronomy, 2, 303

Husser T.-O., Wende -Von Berg S., Dreizler S., Homeier D., Reiners A., Barman T., Hauschildt P. H., 2013, A&A, 553

Irwin P. G. J., et al., 2008, Journal of Quantitative Spectroscopy and Radiative Transfer, 109, 1136

Iyer A. R., Line M. R., Muirhead P. S., Fortney J. J., Gharib-Nezhad E., 2023, The Astrophysical Journal, 944, 41

Johns-Krull C. M., Valenti J. A., 1996, The Astrophysical Journal, 459, L95

Jurgenson C., Fischer D., McCracken T., Sawyer D., Szymkowiak A., Davis A., Muller G., Santoro F., 2016, ] 10.1117/12.2233002, 9908, 99086T

Karolides N. J., Bald M., Sova D. B., 2011, 120 Banned Books: Censorship Histories of World Literature, 2nd ed edn. Facts on File, Inc, New York, NY

Käufl H., et al., 2004, Society of Photo-Optical Instrumentation Engineers (SPIE) Conference Series, 5492, 1218

Kempton E. M.-R., et al., 2018, Publications of the Astronomical Society of the Pacific, 130, 114401

Kempton E. M. R., et al., 2023, Nature, 620, 67

Kipping D. M., Schmitt A. R., Huang X., Torres G., Nesvorný D., Buchhave L. A., Hartman J., Bakos G. Á., 2015, The Astrophysical Journal, 813, 14

Kirk J., et al., 2021, The Astronomical Journal, 162, 34

Kitzmann D., Stock J. W., Patzer A. B. C., 2023, FastChem Cond: Equilibrium Chemistry with Condensation and Rainout for Cool Planetary and Stellar Environments (arxiv:2309.02337)

Klein B., et al., 2021, Monthly Notices of the Royal Astronomical Society, 502, 188

Klein B., et al., 2022, Monthly Notices of the Royal Astronomical Society, 512, 5067

Klein B., et al., 2023, ATMOSPHERIX: I- An Open Source High Resolution Transmission Spectroscopy Pipeline for Exoplanets Atmospheres with SPIRou (arxiv:2308.14510)

Knutson H. A., et al., 2014, The Astrophysical Journal, 794

Kochukhov O., 2016, in Rozelot J.-P., Neiner C., eds, Lecture Notes in Physics, Cartography of the Sun and the Stars. Springer International Publishing, Cham, pp 177–204, doi:10.1007/978-3-319-24151-7_9

Korhonen H., Andersen J. M., Piskunov N., Hackman T., Juncher D., Jarvinen S. P., Joergensen U. G., 2015, Monthly Notices of the Royal Astronomical Society, 448, 3038

Kreidberg L., 2018, in Deeg H. J., Belmonte J. A., eds, , Handbook of Exoplanets. Springer International Publishing, Cham, pp 2083–2105, doi:10.1007/978-3-319-55333-7_100

Kreidberg L., et al., 2013, Nature, 505, 69

Kreidberg L., et al., 2019, Nature, 573, 87

Kreidberg L., et al., 2020, Technical report, Tentative Evidence for Water Vapor in the Atmosphere of the Neptune-Size Exoplanet HD 106315 c. (arxiv:2006.07444v1)

Langeveld A. B., Madhusudhan N., Cabot S. H. C., Hodgkin S. T., 2021, MNRAS, 502, 4392

Laughlin G., 2018, in Deeg H. J., Belmonte J. A., eds, , Handbook of Exoplanets. Springer International Publishing, Cham, pp 1357–1373, doi:10.1007/978-3-319-55333-7_1

Lecavelier des Etangs A., Lissauer J. J., 2022, New Astronomy Reviews, 94, 101641

Libby-Roberts J. E., et al., 2022, The Astronomical Journal, 164, 59

Linder E. F., Mordasini C., Mollière P., Marleau G.-D., Malik M., Quanz S. P., Meyer M. R., 2019, Astronomy & Astrophysics, 623, A85

Line M. R., Zhang X., Vaisht G., Chen P., Natraj V., Chen P., Yung Y. L., 2012, The Astrophysical Journal, 749, 93

Line M. R., et al., 2013, The Astrophysical Journal, 775, 137

Line M. R., et al., 2021, Nature, 598, 580

Lopez E. D., Fortney J. J., 2013, The Astrophysical Journal, 776, 2

Lopez E. D., Rice K., 2018, Monthly Notices of the Royal Astronomical Society, 479, 5303

Lothringer J. D., Rustamkulov Z., Sing D. K., Gibson N. P., Wilson J., Schlaufman K. C., 2021, The Astrophysical Journal, 914, 12

Louca A. J., Miguel Y., Tsai S.-M., Froning C. S., Loyd R. O. P., France K., 2023, Monthly Notices of the Royal Astronomical Society, 521, 3333

Luger R., Agol E., Foreman-Mackey D., Fleming D. P., Lustig-Yaeger J., Deitrick R., 2019, The Astronomical Journal, 157, 64

Luger R., Foreman-Mackey D., Hedges C., Hogg D. W., 2021a, The Astronomical Journal, 162, 123

Luger R., Foreman-Mackey D., Hedges C., 2021b, The Astronomical Journal, 162, 124

Madhusudhan N., 2012, The Astrophysical Journal, 758, 36

Madhusudhan N., 2019, Annual Review of Astronomy and Astrophysics, 57, 617

Madhusudhan N., Seager . S., 2009, The Astrophysical Journal, 707, 24

Madhusudhan N., Amin M. A., Kennedy G. M., 2014, The Astrophysical Journal, 794, L12

Madhusudhan N., Agúndez M., Moses J. I., Hu Y., 2016, Space Science Reviews, 205, 285

Madhusudhan N., Sarkar S., Constantinou S., Holmberg M., Piette A. A. A., Moses J. I., 2023, The Astrophysical Journal, 956, L13

Malo L., Doyon R., Feiden G. A., Albert L., Lafrenière D., Artigau É., Gagné J., Riedel A., 2014, The Astrophysical Journal, 792, 37

Mamajek E. E., Bell C. P. M., 2014, Monthly Notices of the Royal Astronomical Society, 445, 2169

Martioli E., et al., 2020, Astronomy & Astrophysics, 641, L1

Martioli E., Hébrard G., Correia A. C. M., Laskar J., Lecavelier des Etangs A., 2021, Astronomy & Astrophysics, 649, A177

Mayor M., Queloz D., 1995, Nature, 378, 355

Mayor M., et al., 2003, The Messenger, 114, 20

Mazeh T., Tamuz O., Zucker S., 2007, in Astronomical Society of the Pacific Conference Series, Vol 366. p. 119

Mazeh T., Holczer T., Faigler S., 2016, Astronomy and Astrophysics, 589, A75

McKemmish L. K., Masseron T., Hoeijmakers H. J., Pérez-Mesa V., Grimm S. L., Yurchenko S. N., Tennyson J., 2019, Monthly Notices of the Royal Astronomical Society, 488, 2836

Meech A., Aigrain S., Brogi M., Birkby J. L., 2022, Monthly Notices of the Royal Astronomical Society, 512, 2604

Messina S., Leto G., Pagano I., 2016, Astrophysics and Space Science, 361, 291

Mikal-Evans T., et al., 2023, The Astronomical Journal, 165, 84

Mollière P., van Boekel R., Dullemond C. P., Henning T., Mordasini C., 2015, The Astrophysical Journal, 813, 47

Mollière P., Wardenier J. P., van Boekel R., Henning T., Molaverdikhani K., Snellen I. A. G., 2019, Astronomy & Astrophysics, 627, A67

Moran S. E., et al., 2023, The Astrophysical Journal Letters, 948, L11

Moses J. I., et al., 2013, The Astrophysical Journal, 777, 34

Mousavi-Sadr M., Jassur D. M., Gozaliasl G., 2023, Revisiting Mass-Radius Relationships for Exoplanet Populations: A Machine Learning Insight (arxiv:2301.07143)

Murgas F., et al., 2021, Astronomy and Astrophysics, 653, A60

Murray C. D., Dermott S. F., 2000, Solar System Dynamics. Cambridge University Press, Cambridge, doi:10.1017/CBO9781139174817

Nascimbeni V., et al., 2015, Astronomy & Astrophysics, 579, A113

Newton S. I., 1687, Newton's Principia: Sections I. II. III.. Macmillan and Company

Nikolov N., et al., 2018, Nature, 557, 526

Noll S., Kausch W., Barden M., Jones A. M., Szyszka C., Kimeswenger S., Vinther J., 2012, A&A, 543

Nordlund Å., Stein R. F., Asplund M., 2009, Living Reviews in Solar Physics, 6, 2

Nortmann L., et al., 2018, Science, 362, 1388

Nugroho S. K., et al., 2021, The Astrophysical Journal, 910, L9

Öberg K. I., Bergin E. A., 2016, The Astrophysical Journal, 831, L19

Öberg K. I., Murray-Clay R., Bergin E. A., 2011, The Astrophysical Journal, 743, L16

Ohta Y., Taruya A., Suto Y., 2005, The Astrophysical Journal, 622, 1118

Orell-Miquel J., et al., 2022, Astronomy and Astrophysics, 659, A55

Orell-Miquel J., et al., 2023, Confirmation of an He I Evaporating Atmosphere around the 650-Myr-old Sub-Neptune HD235088 b (TOI-1430 b) with CARMENES, doi:10.48550/arXiv.2307.05191

Owen J. E., 2019, Annual Review of Earth and Planetary Sciences, 47, 67

Owen J. E., Schlichting H. E., 2023, Mapping out the Parameter Space for Photoevaporation and Core-Powered Mass-Loss (arxiv:2308.00020)

Owen J. E., Wu Y., 2013, The Astrophysical Journal, 775, 105

Owen J. E., Wu Y., 2017, The Astrophysical Journal, 847, 29

Palle E., et al., 2020, Astronomy & Astrophysics, 643, A25

Panja M., Cameron R., Solanki S. K., 2020, The Astrophysical Journal, 893, 113

Parmentier V., Showman A. P., Lian Y., 2013, Astronomy and Astrophysics, 558, A91

Parviainen H., 2018, pp 1567–1590 (arxiv:1711.03329), doi:10.1007/978-3-319-55333-7_149

Patapis P., et al., 2022, Astronomy and Astrophysics, 658, A72

Pelletier S., et al., 2021, The Astronomical Journal, 162, 73

Pelletier S., et al., 2023, Vanadium Oxide and a Sharp Onset of Cold-Trapping on a Giant Exoplanet, doi:10.48550/arXiv.2306.08739

Pepe F., et al., 2021, Astronomy and Astrophysics, 645, A96

Petersburg R. R., et al., 2020, The Astronomical Journal, 159, 187

Pierrehumbert R. T., 2010, Principles of Planetary Climate [Electronic Resource]. University Press, Cambridge

Plavchan P., et al., 2020, Nature, 582, 497

Pollack J. B., Hubickyj O., Bodenheimer P., Lissauer J. J., Podolak M., Greenzweig Y., 1996, Icarus, 124, 62

Prinn R. G., Barshay S. S., 1977, Science, 198, 1031

Prinoth B., et al., 2022, Nature Astronomy, 6, 449

Pueyo L., 2018, in Deeg H. J., Belmonte J. A., eds, , Handbook of Exoplanets. Springer International Publishing, Cham, pp 705–765, doi:10.1007/978-3-319-55333-7_10

Rackham B. V., de Wit J., 2023, Towards Robust Corrections for Stellar Contamination in JWST Exoplanet Transmission Spectra (arxiv:2303.15418)

Rackham B., et al., 2017, The Astrophysical Journal, 834, 151

Rackham B. V., Apai D., Giampapa M. S., 2018, The Astrophysical Journal, 853, 122

Rackham B. V., et al., 2023, RAS Techniques and Instruments, 2, 148

Rajpaul V., Aigrain S., Osborne M. A., Reece S., Roberts S., 2015, MNRAS, 452, 2269

Rasmussen C. E., Williams C. K. I., 2006, Gaussian Processes for Machine Learning. MIT Press Cambridge, MA

Rauer H., Aerts C., Cabrera J., PLATO Team 2016, Astronomische Nachrichten, 337, 961

Ricker G. R., et al., 2015, Journal of Astronomical Telescopes, Instruments, and Systems, 1, 014003

Ridden-Harper A., et al., 2023, The Astronomical Journal, 165, 170

Rincon F., 2019, Journal of Plasma Physics, 85, 205850401

Roberge A., Seager S., 2018, in Deeg H. J., Belmonte J. A., eds, , Handbook of Exoplanets. Springer International Publishing, Cham, pp 2063–2082, doi:10.1007/978-3-319-55333-7_98

Rockcliffe K. E., Newton E. R., Youngblood A., Duvvuri G. M., Plavchan P., Gao P., Mann A. W., Lowrance P. J., 2023, The Astronomical Journal, 166, 77

Rodler F., Kürster M., Barnes J. R., 2013, MNRAS, 432, 1980

Rodono M., et al., 1986, Astronomy and Astrophysics, 165, 135

Rogers L. A., Bodenheimer P., Lissauer J. J., Seager S., 2011, The Astrophysical Journal, 738, 59

Rothman L. S., et al., 2010, Journal of Quantitative Spectroscopy and Radiative Transfer, 111, 2139

Savel A., M.-R. Kempton E., Beltz H., Malsky I., 2022, Arjunsavel/Hires-Literature, Zenodo, doi:10.5281/zenodo.7065957

Scandariato G., et al., 2021, A&A, 646

Schwarz H., Brogi M., De Kok R. J., Birkby J., Snellen I., 2015, A&A, 576

Seager S., 2008, in Botta O., Bada J. L., Gomez-Elvira J., Javaux E., Selsis F., Summons R., eds, Space Sciences Series of ISSI, Strategies of Life Detection. Springer US, Boston, MA, pp 345–354, doi:10.1007/978-0-387-77516-6_25

Seager S., Deming D., 2009, The Astrophysical Journal, 703, 1884

Seidel J. V., Ehrenreich D., Pino L., Bourrier V., Lavie B., Allart R., Wyttenbach A., Lovis C., 2020, A&A, 633

Seidel J. V., et al., 2022, Monthly Notices of the Royal Astronomical Society: Letters, 513, L15

Seidel J. V., Prinoth B., Knudstrup E., Hoeijmakers H. J., Zanazzi J. J., Albrecht S., 2023, Detection of Atmospheric Species and Dynamics in the Bloated Hot Jupiter WASP-172~b with ESPRESSO (arxiv:2308.13622)

Sim C. K., et al., 2014, Advances in Space Research, 53, 1647

Smette A., et al., 2015, A&A, 576, 77

Snellen I. A., Albrecht S., De Mooij E. J. W., Le Poole R. S., 2008, A&A, 487, 357

Snellen I. A. G., de Kok R. J., de Mooij E. J. W., Albrecht S., 2010, Nature, 465, 1049

Snellen I. A. G., Brandl B. R., de Kok R. J., Brogi M., Birkby J., Schwarz H., 2014, Nature, 509, 63

Stock J. W., Kitzmann D., Patzer A. B. C., Sedlmayr E., 2018, Monthly Notices of the Royal Astronomical Society

Strassmeier K. G., 2009, The Astronomy and Astrophysics Review, 17, 251

Struve O., 1952, The Observatory, 72, 199

Szabó G. M., et al., 2021, Astronomy & Astrophysics, 654, A159

Szabó G. M., et al., 2022, Astronomy & Astrophysics, 659, L7

Tamuz O., Mazeh T., Zucker S., 2005, MNRAS, 356, 1466

Tannock M. E., Metchev S., Hood C. E., Mace G. N., Fortney J. J., Morley C. V., Jaffe D. T., Lupu R., 2022, Monthly Notices of the Royal Astronomical Society, 514, 3160

Team T. J. T. E. C. E. R. S., et al., 2023, Nature, 614, 649

Teske J. K., Thorngren D., Fortney J. J., Hinkel N., Brewer J. M., 2019, The Astronomical Journal, 158, 239

Thorngren D. P., Fortney J. J., Murray-Clay R. A., Lopez E. D., 2016, The Astrophysical Journal, 831, 64

Torres C. A. O., Ferraz Mello S., 1973, Astronomy and Astrophysics, 27, 231

Triaud A. H. M. J., et al., 2009, A&A, 506, 377

Tsai S.-M., Lyons J. R., Grosheintz L., Rimmer P. B., Kitzmann D., Heng K., 2017, The Astrophysical Journal Supplement Series, 228, 20

Vacca W. D., Cushing M. C., Rayner J. T., 2003, Publications of the Astronomical Society of the Pacific, 115, 389

Van Eylen V., Agentoft C., Lundkvist M. S., Kjeldsen H., Owen J. E., Fulton B. J., Petigura E., Snellen I., 2018, Monthly Notices of the Royal Astronomical Society, 479, 4786

Van Saders J. L., Pinsonneault M. H., 2013, The Astrophysical Journal, 776, 67

Venot O., Rocchetto M., Carl S., Hashim A., Decin L., 2016, The Astrophysical Journal, 830, 77

Vidal-Madjar A., et al., 2010, A&A, 523

Vissapragada S., et al., 2022, The Astronomical Journal, 164, 234

Wakeford H. R., Visscher C., Lewis N. K., Kataria T., Marley M. S., Fortney J. J., Mandell A. M., 2017, Monthly Notices of the Royal Astronomical Society, 464, 4247

Wakeford H. R., et al., 2018, The Astronomical Journal, 155, 29

Wang J., Ford E. B., 2002, MNRAS, 418, 1822

Wang J., et al., 2023, The Astronomical Journal, 165, 4

Webb R. K., Gandhi S., Brogi M., Birkby J. L., de Mooij E., Snellen I., Zhang Y., 2022, Monthly Notices of the Royal Astronomical Society, 514, 4160

Welbanks L., Madhusudhan N., Allard N. F., Hubeny I., Spiegelman F., Leininger T., 2019, The Astrophysical Journal Letters, 887, L20

Wilson A. G., Adams R. P., 2013, Gaussian Process Kernels for Pattern Discovery and Extrapolation (arxiv:1302.4245)

Winn J. N., 2007, ] 10.48550/arXiv.astro-ph/0612744, 366, 170

Winn J. N., 2014, Transits and Occultations (arxiv:1001.2010)

Wittrock J. M., et al., 2022, The Astronomical Journal, 164, 27

Wittrock J. M., et al., 2023, Validating AU Microscopii d with Transit Timing Variations (arxiv:2302.04922)

Witzke V., et al., 2021, Astronomy & Astrophysics, 653, A65

Witzke V., Shapiro A. I., Kostogryz N. M., Cameron R., Rackham B. V., Seager S., Solanki S. K., Unruh Y. C., 2022, The Astrophysical Journal Letters, 941, L35

Wolszczan A., Frail D. A., 1992, Nature, 355, 145

Wyttenbach A., Ehrenreich D., Lovis C., Udry S., Pepe F., 2015, Technical report, Spectrally Resolved Detection of Sodium in the Atmosphere of HD 189733b with the HARPS Spectrograph. (arxiv:1503.05581v1)

Yan F., Pallé E., Fosbury R. A. E., Petr-Gotzens M. G., Henning Th., 2017, Astronomy and Astrophysics, 603, A73

Yan F., et al., 2023, Astronomy and Astrophysics, 672, A107

Yurchenko S. N., Mellor T. M., Freedman R. S., Tennyson J., 2020, Monthly Notices of the Royal Astronomical Society, 496, 5282

Zahnle K., Marley M. S., Fortney J. J., 2009, Thermometric Soots on Warm Jupiters?, doi:10.48550/arXiv.0911.0728

Zeng L., Jacobsen S. B., Sasselov D. D., Petaev M. I., 2022, EOS Manual (arxiv:2211.06518)

Zhang Y., Snellen I. A. G., Mollière P., 2021, Astronomy and Astrophysics, 656, A76

Zhao L. L., et al., 2022, The Astronomical Journal, 163, 171

Zicher N., et al., 2022, Monthly Notices of the Royal Astronomical Society, 512, 3060

de Jong T., 2019, Archive for History of Exact Sciences, 73, 1

dos Santos L. A., et al., 2020, Astronomy and Astrophysics, 634, L4